Measurement of the Neutron Spin Polarization in Deuteron Photodisintegration Near Threshold

Thomas Charles Krahulik
Warwick, New York, U.S.A.

Bachelor of Science, Stony Brook University, 2017

A Dissertation presented to the Graduate Faculty of
the University of Virginia in Candidacy for the Degree of
Doctor of Philosophy

Department of Physics

University of Virginia
December 2024

Abstract

As the only known two-nucleon bound state, the deuteron offers a unique opportunity to study the interactions between nucleons. Nuclear theory has developed a number of models and theories to describe the strong nuclear force in the low energy regime of quantum chromodynamics (QCD). Contemporary theories have been fit to unpolarized nucleon-nucleon scattering cross sections rather successfully, lending credence to multiple approaches to modeling the nuclear force. Investigations of spin polarization degrees of freedom in nuclear reactions provide additional rigorous tests of nuclear theory. The spin polarization induced on the neutron in deuteron photodisintegration has been previously measured for insight into nucleon-nucleon interactions. These past measurements demonstrated notable discrepancies with theoretical predictions, prompting questions about the implications for either the experimental methodology or the underlying theory.

This dissertation details a measurement of the spin polarization of the neutron from deuteron photodisintegration performed at the High Intensity Gamma-Ray Source (HIGS) using a 16 MeV photon beam with circular polarization. It served as one of a series of measurements of this observable near the energy threshold for photodisintegration to investigate the long-standing discrepancies between previous experimental measurements and theoretical calculations. Innovations in accelerator technology and spin polarization techniques have offered new capabilities in obtaining a precise result. The experimental setup used a heavy water (^2H_2O) target surrounded by high-pressure gas ^{4}He-Xe polarization analyzers at laboratory reaction angles of interest. Liquid organic scintillator detectors on each side of an analyzer acted as neutron counting detectors, to measure the left-right scattering asymmetry of polarized neutrons from the analyzers. The neutron polarization was extracted from the scattering asymmetry for comparisons to theoretical predictions and previous measurements.

To Emil R. Krahulik and Charles A. Patneaude

Acknowledgements

I am a firm believer in acknowledging and recognizing the importance of people in our lives. I am grateful to have been surrounded by people who supported, encouraged, and challenged me throughout this journey.

My graduate advisor, Professor Blaine Norum has been an excellent guide and mentor during my graduate career. I am grateful to have had an advisor who could uniquely balance working closely with me when I needed guidance while simultaneously supporting me as an independent researcher. He has provided me with opportunities to be involved in every aspect of experimental research, enabling me to learn valuable skills and hone my capabilities as a scientist. Every step along the way, he has reminded me that the intuition and motivation behind the research are just as important as the skills or techniques.

Though our collaboration may have been small, I am fortunate to have had the opportunity to work with some excellent researchers on this experiment. Professor Rob Pywell of the University of Saskatchewan exhibited dedication and technical prowess, that proved invaluable to the success of our experiment. I learned a great deal of skills in instrumentation and data analysis through his guidance. Tanner Polischuk, the engineer-turned-physicist, brought an enthusiastic and hard-working attitude to the lab everyday. Working side-by-side with him on this experiment has been an enjoyable experience that I will dearly miss. He is a diligent problem-solver and is always happy to provide thoughtful answers to my many questions. I could not have asked for a better collaborator.

In preparation of the experiment, I had the honor of working with Professor Werner Tornow of Duke University. He graciously spent many hours sharing with me an incredible set of skills and knowledge to develop our neutron polarization analyzers. From organizing beam tests of detectors, to offering crucial physics insight into experimental data, Prof. Tornow's passion for research and eagerness to offer

guidance has been a meaningful contribution to my graduate career. I am eternally grateful for his mentorship.

I am also grateful for the other members of our research group at the University of Virginia, Matt Roberts and Haoyu Chen, for their mentorship and friendship throughout my time in the group.

Our experiment was also made possible by the hard work and collaborative spirit of the faculty, staff, and students of Duke University and TUNL including Prof. Calvin Howell, Maurice Pentico, Dr. Chris Westerfeldt, Brogan Thomas, and many others.

I owe a great amount of my success to the opportunities afforded to me by my undergraduate research advisors at Stony Brook University. Professor Abhay Deshpande and Dr. Nils Feege were instrumental in facilitating my road to this ultimate accomplishment. I am grateful to Prof. Deshpande for taking a chance on me early in my career and inviting me to join his research group. That opportunity has opened many doors for me to pursue research in a field about which I am passionate. The guidance and thoughtful instruction offered to me by Dr. Feege provided me a strong foundation in the technical skills required for experimental research. I cannot be more grateful for his willingness to share such knowledge and dedication.

I want to thank Prof. Dustin Keller, Prof. Stefan Baeßler, and Prof. Henning Mortveit for their time and energy in serving on my thesis defense committee and reviewing my dissertation.

I would like to express my appreciation for the administrative and technical staff in the University of Virginia Department of Physics, whose tireless work behind the scenes provided the needed support for my and many others' success. I would like to acknowledge the UVA Physics Machine Shop Foreman, Will Fariss. Will devoted his craftsmanship to the service of research. He created a welcoming and professional environment in the machine shop. He constructed the entire detector frame for the experiment of topic in this dissertation, as well as many other parts for projects in our lab. He also instructed me when I took the graduate student machine shop class, and he continued to mentor me in technical skills as I returned to him for help with

new projects. I am grateful for his hard work and joyful spirit, and I am honored to have had the opportunity to work with him.

I would also like to acknowledge the expertise and hard work of the other technical staff who were always willing to help: Larry St. John, Mike Beverage, Bryan Wright, and Al Tobias. I am grateful to Peter Cline, Beth Guyton, and Rick Marshall for everything they did to support the department and graduate students. A special thank you to "my office family", Beverly Martyn, Faye Safley, Dawn Shifflett, and Tammie Shifflett. My work days were always brighter when I got a chance to stop by the office to say hello.

The friends I have made before and during my time in Charlottesville helped me to have an enriching experience, providing a source of support, joy, and adventure throughout the years. Thank you to the friends I made at UVA: Jacob Higgins, Anna Hall, Marybeth Beydler, Sean Jeffas, Matthew Wampler, Miller Eaton, Arthur Conover, Adrian Gutierrez, Chris Jantzi, and many others. I was fortunate to have made friends throughout the Charlottesville community as well, connecting me to experiences beyond graduate school. I'd like to especially thank Lindsey "Lindy" Lipinski and Matthew "Champ" Fielding for the fun, laughs, and support during my time in Charlottesville. Thank you to Erynn McLeod for supporting me through thick and thin over the years. Thank you to Grace Cummings, whose encouragement and guidance helped me believe in myself and my abilities as a scientist. Her hard work and passion for the field inspire me everyday.

Finally, I would not be where I am today without the love, support, and devotion of my family. My parents have worked hard to raise me and provide me with opportunities that have allowed me to explore my passion for science. My mom, Christine Krahulik, has provided an endless supply of love and encouragement. I have been inspired by how hard she works to pursue her dreams and excel in her career while supporting her family, and I strive to bring that level of dedication to my work. My dad, Robert Krahulik, has always made sure to be available to help and support me anyway he can. He has taught me the value in continuing to learn new ideas and skills, and to never, ever give up on your goals. My sister, Katie Krahulik, has been my best friend for as long as I can remember. As much joy as I receive from the

laughs and adventures we share, I am inspired by her hard work, her perseverance, and her love of life. Everyday, she teaches me to go out and give it my all. I am grateful to have had the love and support of my grandmothers, Christel Krahulik and Geraldine Patneaude. I would like to offer one final thank you to all of the family and friends who have supported me over the years.

Contents

Abstract v

Acknowledgements ix

Contents xiii

List of Figures xvii

List of Tables xx

1 Introduction 1

1.1 Background . . . 1
1.2 The Deuteron . . . 1
1.3 Photodisintegration of the Deuteron . . . 3
1.3.1 History . . . 4
1.3.2 Emergent Problems in Deuteron Photodisintegration . . . 6
1.3.3 Deuteron Photodisintegration at HIγS . . . 12
1.4 Motivation . . . 14
1.5 The Measurement . . . 15
1.6 Document Overview . . . 16

2 Theoretical Background 17

2.1 The Strong Nuclear Force . . . 17
2.2 Meson Exchange Theory . . . 19
2.2.1 Yukawa Potential . . . 19
2.2.2 One Pion Exchange Potential . . . 21
2.2.3 One Boson Exchange Potential . . . 25
2.2.4 CD Bonn Potential . . . 29
2.3 Phenomenological Models . . . 31
2.3.1 Argonne v_{18} Potential . . . 33

2.4 Chiral Effective Field Theory . . . 35
2.4.1 Chiral Perturbation Theory . . . 37
2.5 Deuteron Photodisintegration . . . 40
2.5.1 Kinematics of $d(\gamma, n)p$ . . . 40
2.5.2 Polarization Observables in Deuteron Photodisintegration . . . 43
2.5.3 Additional Techniques in Photodisintegration Calculations . . . 45
2.6 Spin Polarization in Nuclear Reactions . . . 49
2.6.1 Spin Polarization . . . 49
2.6.2 Polarization in Nuclear Reactions . . . 50

3 Monte Carlo Simulation **53**
3.1 Monte Carlo Methods . . . 53
3.2 GEANT4: A Simulation Toolkit . . . 55
3.2.1 Particle Tracking in GEANT4 . . . 55
3.2.2 Physics Lists . . . 56
3.2.3 Detector Construction . . . 57
3.2.4 Primary Generation . . . 59
3.2.5 User Actions . . . 60
3.3 Event Generation . . . 60
3.3.1 Angular Distribution of Neutrons . . . 61
3.3.2 Photodisintegration Kinematics . . . 61
3.3.3 Geometric Effects . . . 62
3.3.4 Polarization of Neutrons . . . 63
3.4 Polarized Neutron Scattering in GEANT4 . . . 64
3.4.1 ParticleHP Model . . . 64
3.4.2 Polarization in ParticleHP . . . 65
3.5 Implementation of *nvec* Simulation . . . 67
3.5.1 Light Output Scaling . . . 68
3.5.2 Simulating Geometric Asymmetries . . . 68
3.5.3 Calculation of Effective Analyzing Powers . . . 68

4 Experimental Overview **71**
4.1 High Intensity Gamma Source . . . 72
4.1.1 Electron Beam Acceleration . . . 73
4.1.2 Free Electron Laser . . . 74

4.1.3 Gamma Ray Production . . . 74
4.1.4 Background Effect of HIγS Bunching Mode . . . 75
4.2 Methods in Particle Detection . . . 76
4.2.1 Scintillation . . . 76
4.2.2 Noble Gas Scintillators . . . 77
4.2.3 Organic Scintillators . . . 78
4.2.4 Pulse Shape Discrimination . . . 80
4.3 Polarization Analyzers . . . 82
4.3.1 Analyzer Design and Assembly . . . 82
4.3.2 Pressure Tests . . . 86
4.3.3 Surface Treatment . . . 88
4.3.4 Gas Handling Techniques . . . 92
4.3.5 TUNL Tandem van de Graaff Beam Test . . . 97
4.3.6 TUNL Tandem van de Graaff Timing Test . . . 101
4.4 Organic Scintillator Neutron Counters . . . 106
4.5 Electronics and Data Acquisition . . . 108
4.5.1 Discriminators . . . 109
4.5.2 Analog-to-Digital Converters (ADCs) . . . 109
4.5.3 Time-to-Digital Converters (TDCs) . . . 109
4.5.4 Scalers . . . 110
4.5.5 Data Acquisition Windows . . . 110
4.5.6 Trigger Logic . . . 112
4.5.7 Data Acquisition Software . . . 114

5 Data Analysis **115**
5.1 Software Packages . . . 115
5.2 Calibrations . . . 116
5.2.1 ADC Calibrations . . . 116
5.2.2 TDC Calibrations . . . 121
5.2.3 PSD Parameters . . . 124
5.3 Analyzing Event Selection . . . 129
5.3.1 Analyzer Hit Identification . . . 130
5.3.2 Analyzer-Cell Coincidences . . . 131
5.3.3 Time-of-Flight Analysis . . . 133
5.3.4 Pulse Shape Discrimination Analysis . . . 134

5.3.5 Light Output Cuts . . . 138
5.4 Systematic Corrections . . . 140
5.4.1 Multiplicity Correction . . . 141
5.4.2 Random Signal Subtraction . . . 141
5.4.3 Shifted Pedestal Correction . . . 143
5.4.4 PSD Cut Correction . . . 144
5.4.5 Relative Detector Efficiencies . . . 145
5.4.6 Instrumental Asymmetries . . . 147
5.5 Neutron Polarization Extraction . . . 149
5.5.1 Integrating Neutron Yields . . . 150
5.5.2 Calculating Asymmetries . . . 150
5.5.3 Extraction of Polarization Contributions . . . 151

6 Results and Discussion **153**
6.1 Results . . . 153
6.2 Discussion of the Results at $\theta_n = 45°$ . . . 156
6.3 Future Prospects . . . 158
6.3.1 Further Analysis of Current Experiment . . . 158
6.3.2 Potential Improvements to the Experimental Design . . . 158
6.3.3 Possibilities for Future Measurements . . . 160

7 Conclusion **161**

Bibliography **163**

A Input Parameters for Event Generation **171**
A.1 Photodisintegration Differential Cross Section . . . 171
A.2 Gamma-Ray Beam Parameters . . . 172

B Analyzing Powers in n-^{4}He Elastic Scattering **173**

C Data Tables of Presented Results **175**

List of Figures

1.1 Experimental Results of R. Nath et al 9
1.2 Historical P_y^n Measurements Compared to Theory 11
1.3 The Blowfish Detector Array 12

2.1 Ranges of Meson Contributions to Nuclear Potential 29
2.2 Hierarchy of Feynman Diagrams for Calculating Internucleon Forces . 39
2.3 Kinetic Energy of Photoneutron as a Function of Lab Reaction Angle 42
2.4 Feynman Diagrams for Meson Exchange Currents 46
2.5 Feynman Diagrams for Isobar Configurations 47

3.1 Visualization of Acceptance-Rejection Sampling 54
3.2 Diagram Demonstrating Tracking in GEANT4 55
3.3 Example of Material Definition in GEANT4 58
3.4 Sample Geometry Classes Available in GEANT4 59
3.5 Simulated Detector Geometry from GEANT4 67
3.6 Geometric Effects on Analyzing Power Uncertainties 70

4.1 Experimental Layout Diagrams 72
4.2 HIγS Facility 73
4.3 π-Electron Structure of Organic Molecules 79
4.4 Intensity of Light Output Over Time in Organic Scintillator 81
4.5 Original Analyzer Cell Design 83
4.6 Free Body Diagram of Analyzer Windows 84
4.7 Modified Analyzer Cell Design 85
4.8 Free Body Diagram of Analyzer Windows 86
4.9 Analyzer Pressure Test Setup 87
4.10 Reflective Layer Coating Procedure 89
4.11 Evaporative Deposition of Wavelength Shifter on Analyzer 90
4.12 Boat for Evaporation Deposition 91
4.13 LENA Gas Handling System 92

4.14 LENA Gas Filling Station Schematic 93
4.15 Gamma Vault Gas Handling System 95
4.16 TUNL Tandem van de Graaff Accelerator Floor Plan 97
4.17 Setup for Tandem Beam Test of Analyzers 98
4.18 ADC Spectrum of Pulse Integration from Analyzer Signals 99
4.19 ADC Spectrum of Neutron Events in Analyzer 100
4.20 ADC Spectra of Neutrons Scattering at Three Different Angles 101
4.21 Time Difference Between Signals in Analyzer 102
4.22 Time Difference Between Signals in Analyzer from Beam Test 103
4.23 Signal Timing Difference in Analyzer vs Gas Pressure 104
4.24 Fraction of Events Included in Analysis as a Function of the Cut Applied to the Time Difference 105
4.25 Diagram of Neutron Detector from Blowfish Array 106
4.26 Neutron Detector Cage Assembly 107
4.27 View of Detector Station from Target 108
4.28 Circuit Logic for Data Acquisition Windows 111
4.29 Master Trigger Logic 113

5.1 Sample Pedestal Spectra for ADC Channels 117
5.2 Sample Pedestal Spectra for ADC Channels with Shifted Pedestals . . 118
5.3 ADC Spectrum from Cs-137 Source for Gain Finding 119
5.4 Gain Scaling of Light Output Spectrum 121
5.5 Raw TDC Spectrum 122
5.6 TDC Offset 123
5.7 Time-of-Flight Spectrum 123
5.8 Long and Short Gate Charge Integration Over Signal Pulses 124
5.9 Short Gate Charge Integration vs. Long Gate Charge Integration . . 125
5.10 PSD Ratio vs. ADC Long Value 126
5.11 Fitting a Slice of the PSD Spectrum for Calibration 127
5.12 Fitting of PSD Parameter 128
5.13 Final Spectrum of Calibrated PSD Parameter 129
5.14 Spectrum of Time Difference Between Analyzer PMTs 131
5.15 Analyzer-Cell Coincidence Requirements 132
5.16 Time-of-Fight Spectrum from Neutron Detector 133
5.17 Light Output vs PSD 135

5.18 Time-of-Flight Spectrum After PSD Cut 136
5.19 Light Output vs PSD with Shifted Pedestals 137
5.20 Light Output vs PSD with Shifted Pedestals 138
5.21 PSD Spectrum in Low Light Output Region 139
5.22 Time-of-Fight Spectrum After PSD and Light Output Cuts 140
5.23 Application of Random Signal Subtraction to PSD Spectrum 142
5.24 Determining Shifted Pedestal Correction Factors 143
5.25 Fitting of PSD Spectrum to Determine PSD Cut Correction 145
5.26 Comparison of Normalized Neutron Yields Between Simulated and Experimental Data 146
5.27 Data-to-Simulation Neutron Yield Ratios to Determine Efficiency Calculations 147
5.28 Geometric Spread in Neutron Trajectories 148
5.29 Light Output Spectrum of Analyzing Events from a Counting Detector 150

6.1 Measurements from Each Day of Experimental Run Compared to the Weighted Average 154
6.2 Results for P_y^n at $E_\gamma = 16$ MeV with Circular Polarization 155
6.3 Exploratory Consideration of the Measurement at $\theta_n = 45°$ 157

List of Tables

1.1 Properties of the Deuteron 3
1.2 GDH Sum Rule for Select Targets 7

2.1 Properties of Mesons Involved in One-Boson-Exchange[28] 25
2.2 Notation Table for Calculating Observables in $d(\gamma, n)p$ 43
2.3 Properties of the Δ Baryons, Isobars of the Nucleons[28] 47

5.1 Variable Definitions for Analysis 149

A.1 Coefficients for Legendre Polynomial Expansion of Photodisintegration Cross Section 172
A.2 Gamma-ray Beam Parameters Applied to Event Generator 172

B.1 Effective Analyzing Powers for $E_\gamma = 16$ MeV 173
B.2 Analyzing Powers in n-^{4}He Scattering ($E_{n,lab} = 1.0 - 9.0$ MeV) 174

C.1 Results at $\theta_n = 45°$ by Day 175
C.2 Results at $\theta_n = 90°$ by Day 175
C.3 Results at $\theta_n = 135°$ by Day 175
C.4 Preliminary Results 175
C.5 Exploratory Results 175

Chapter 1

Introduction

Or

How I Learned to Stop Worrying and Love the Deuteron

1.1 Background

Nuclear physics pursues an understanding of the strong nuclear force and the strongly interacting matter prevalent throughout the physical universe. The field investigates a wide range of topics, from the fundamental interactions of quarks and gluons at the heart of all nuclear matter to astrophysical phenomena, such as Big Bang nucleosynthesis and neutron stars. The combined efforts of experimental and theoretical research have unlocked many mysteries about the universe, but they have also continuously raised more questions to be answered.

One of the oldest questions in nuclear physics is, *what is the nature of the force that holds the atomic nucleus together?* For almost a century, nuclei have been understood to be composed of protons and neutrons, often generalized as *nucleons*. Physicists have devoted decades of research to develop an understanding of the force that binds nucleons together and governs the interactions between them. To this day, these efforts remain a work in progress, which benefits greatly from the study of the two-nucleon bound state, the deuteron.

1.2 The Deuteron

The deuteron is a unique testing ground for studying the interaction between nucleons. *Deuteron* refers to the nucleus of deuterium, an isotope of hydrogen, which is a bound state of a proton and a neutron. In fact, it is the only known stable bound state of

two nucleons, making it the most direct tool for investigating nucleon-nucleon (NN) interactions.

The deuteron is considered a loosely bound nucleus, with a binding energy of $E_B = 2.2245$ MeV, much lower than the binding energy per nucleon of most other nuclei. The binding energy is calculated from the mass difference between the sum of the two nucleon masses ($m_p = 938.7833$ MeV, $m_n = 939.5656$ MeV) and the mass of the bound state ($m_d = 1876.1244$ MeV).

The quantum mechanical properties of the deuteron have been experimentally determined and offer insight into its nature. The deuteron has total angular momentum $J = 1$ and positive parity, $\pi = +1$. *Parity* refers to the behavior of the deuteron's wave function under a reflection of its spatial coordinates about the origin. Positive parity indicates a symmetric wave function about the origin, meaning interactions of the deuteron behave the same in either a right-handed or left-handed coordinate system.

The spin-parity of the deuteron, $J^\pi = 1^+$, implies the existence of two possible angular momentum states: a ${}^3S_1$ state ($l = 0, s = 1$) and a ${}^3D_1$ state ($l = 2, s = 1$). It is tempting to assume the deuteron ground state to be in the lower energy ${}^3S_1$ state. However, experimental measurements of the deuteron's magnetic dipole moment and a non-vanishing electric quadrupole moment indicate a small contribution to the ground state from the ${}^3D_1$ state. Therefore, the deuteron is treated as a superposition of the ${}^3S_1$ state (with about 96% contribution) and the ${}^3D_1$ state (with about 4% contribution). The admixture of the ${}^3D_1$ state means that the orbital angular momentum of the deuteron is not necessarily conserved, indicating that the interaction between the nucleons cannot be described solely by a central force. There must exist a tensor component to the nuclear force as well.

Isospin is a quantum number that indicates the up and down quark contributions of a system. The concept was originally intended to denote a symmetry of the strong interaction. Due to their similar masses, the proton and neutron were considered two projections of a single particle, with the proton having isospin $I_3 = +\frac{1}{2}$ and the neutron, $I_3 = -\frac{1}{2}$. The strong interaction was treated as invariant under transformations between these two isospin states. With the emergence of the quark model and the discovery of a mass splitting between the proton and neutron, isospin was realized to not be an exact symmetry, and it was adapted to quantify the quark nature of hadronic matter. Isospin still offers an approximate symmetry in strong interactions

and is a crucial contribution to models of the nuclear force between nucleons.

A two-nucleon system of $I = \frac{1}{2}$ nucleons can have total isospin of either $I = 0$ or $I = 1$. In determining the isospin of the deuteron, it is useful to consider the contributions to its wave function. As a bound state of two "identical" fermions, the total wave function of the deuteron must be antisymmetric, by the Pauli exclusion principle. Decomposing the deuteron wave function into components dependent on space, spin, and isospin yields

$$\psi_d = \phi(\vec{r})\chi(S)\xi(I) \tag{1.1}$$

As previously discussed, the spatial wave function of the deuteron is symmetric. For $S = 1$ states such as those of the deuteron, $\chi(S)$ is also a symmetric function. This leaves the isospin part $\xi(I)$ to contribute the antisymmetric behavior of the deuteron's wave function. This can only be the case for the $I = 0$ state, thus ruling out $I = 1$ states for the deuteron.

The properties of the deuteron outlined in this section are consolidated into Table 1.1.

Property	Value
m_d	1876.1244 MeV
E_B	2.2245 MeV
J^π	1^+
I	0
Q	2.875×10^{-27} cm^2

Table 1.1: Properties of the Deuteron. Collection of numerical values for several of the physical properties of the deuteron. As noted in the text, included are its mass (m_d), binding energy (E_B), total angular momentum (J), parity (π), and isospin (I). Also included is its electric quadrupole moment (Q) indicative of the admixture composition of the deuteron's ground state.

1.3 Photodisintegration of the Deuteron

Photodisintegration of the deuteron is the reaction in which an incident gamma-ray photon breaks apart the deuteron into its constituent particles, the proton and the

neutron. The reaction has the form

$$d + \gamma \rightarrow p + n, \tag{1.2}$$

or in compact notation, $d(\gamma, n)p$.[1] Probing the deuteron with a photon is the "cleanest" approach to studying the NN interaction inside because the photon does not contribute any additional nuclear forces in the reaction and the electromagnetic interaction is well understood.

Deuteron photodisintegration is often discussed in regards to energy thresholds for different channels of the reaction. The *photodisintegration threshold energy*[2] is the minimum photon energy required to break up the deuteron, equivalent to its binding energy $E_{Th} = E_B = 2.2245$ MeV. A high enough energy photon can also produce a new particle in the final state, as long as the energy is greater than the mass of the generated particle. The lightest of these particles is the pion which has a *pion photoproduction threshold* of $E_{\pi\text{-Th}} \approx 146 MeV$. The type of pion produced determines the final state of the photodisintegration reaction.

1.3.1 History

Deuterium (^{2}H) was discovered in 1931 by H.C. Urey, F.G. Brickwedde, and G.M. Murphy through spectroscopic analysis of hydrogen gas. [1] Operating under the hypothesis that water (^1H_2O) contains a small fraction of deuterated or heavy water (^2H_2O or D_2O), they evaporated samples of water to produce hydrogen gas and analyzed a small amount of the final cubic centimeter to evaporate. The stronger hydrogen bonding of heavy water causes it to evaporate slower than normal water. So, through this method, Urey et al. were able to produce higher concentrations of heavy water that could be detected through spectroscopy. They estimated a natural concentration of deuterium of 1 part per 4000 of hydrogen, in comparison with the modern accepted value of about 1 part ^2H_2O in 6400 of H_2O.

Investigations into the nature of the deuteron began shortly after its discovery. In 1934, Chadwick and Goldhaber published the results of the first experimental

[1] Compact notation uses the form $a(b, c)d$, notating an initial state with target a and projectile b and a final state with ejectile c and recoil particle d. Conventionally, the ejectile is the particle that is measured from the reaction.

[2] The photodisintegration threshold energy is also known as the breakup threshold, and is the threshold referenced by the title of this work.

measurements from photodisintegration of the deuteron. [2] They emphasized their motivation for the experiment, explaining "[the deuteron] is the simplest of all nuclear systems and its properties are as important in nuclear theory as the hydrogen atom is in atomic theory." [2] They inferred that a γ-ray of energy greater than the binding energy of the nucleus could separate the nucleons and provide insight into the properties and behavior of the deuteron and its constituents. Using γ-rays from the decay of thallium, they used the photodisintegration process to perform a measurement of the neutron mass. They were able to calculate a neutron mass of 1.0080 ± 0.0005 Da[3], rather close to today's accepted value of 1.0087 Da, making their measurement one of the most precise at the time. Their experiment had proven the usefulness of the $d(\gamma, n)p$ process and would inspire decades of experimental research of nuclear interactions.

Around the same time, physicists were working on developing a theoretical description of the nuclear interaction that binds nuclei together. In 1935, Yukawa published a model of the nuclear force, in which he proposed that the interaction was the result of the exchange of a mediating boson with finite mass. [3] The details of Yukawa's model are discussed further in Section 2.2.1, but the key historical mark here is the introduction of the meson exchange theory of the nuclear force. Yukawa's mediating meson, the pion, was eventually discovered in 1947 [4, 5], giving credence to his theory. Over time, more mesons were discovered as candidates for boson exchange in nuclear interactions. Theorists developed more complex nuclear potentials based on meson exchange models that were used to calculate observables in nucleon-nucleon interactions. Tests of these potentials became more precise as experimental techniques advanced, providing a wealth of data for comparison.

Chadwick and Goldhaber's first experiment of deuteron photodisintegration utilized 2.6 MeV γ radiation from the decay of thallium-208. At the time, radioactive decay of naturally occurring isotopes was the only source of sufficiently high-energy photons to break apart the deuteron. Eventually, advancements in accelerator technology provided new sources of particle beams for nuclear and particle physics experiments. Researchers utilized electron accelerators as a source of gamma-rays via bremsstrahlung radiation. An electron beam was accelerated into a radiating material that would slow the electron momentum and release the energy as photons. This technique was used by groups at the Yale Electron Linear Accelerator and the

[3]The Dalton (Da) is a mass unit equal to $\frac{1}{12}$ the mass of a carbon-12 atom.

Argonne High-Current Electron Linac for studies of deuteron photodisintegration, measuring cross sections and polarization observables of the reaction. The increased statistics provided by these accelerators facilitated more precise measurements to compare to calculations emerging from nucleon-nucleon potential models. However, bremsstrahlung beams produce a broad spectrum of photon energies, introducing uncertainty in the initial energy of an incident photon. These *untagged* beams introduced systematic errors into measurements as the energy and flux of the photon beam must be calculated from theory, rather than defined as an experimental input parameter. *Tagging* of photons was eventually incorporated into this accelerator technology, measuring the energy of recoil electrons for a more direct calculation of the photon energies. Despite the improvement offered by this method, it did not remove all of the uncertainty in the measurements, and required a trade-off in the flux of usable photons for experiments.

By the end of the 1970s, techniques in laser Compton scattering had progressed to meet the accelerator demands of nuclear physics experiments. At the National Laboratory of Frascati, the LADON facility came online as the first gamma-ray Compton light source. It provided polarized gamma-rays up to 80 MeV by colliding a laser photon source with an electron beam, opening up new observables for investigation in nuclear physics research. In 1987, the Laser Electron Gamma Source (LEGS) at Brookhaven National Laboratory (BNL) began operation with the capability to provide up to 500 MeV gamma-ray beams with either circular or linear polarization and a flux of $5 \times 10^6 \gamma/s$. Experiments at LEGS measured unpolarized and polarized cross sections for deuteron photodisintegration offering robust tests of theoretical predictions. In the late 1990s, the High Intensity Gamma-ray Source (HIγS) at the Triangle Universities Nuclear Laboratory (TUNL) came online as a highly polarized gamma-ray source driven by a Free-Electron Laser (FEL). Since then it has served as an important resource in the exploration of nuclear forces. HIγS provides the most intense monochromatic gamma-ray beams in the world with near 100% polarization (circular or linear). Experiments investigating the photodisintegration of light nuclei have been an integral part of the scientific program at HIγS for over twenty years.

1.3.2 Emergent Problems in Deuteron Photodisintegration

Modern capabilities in polarized gamma-ray sources have opened up new possibilities in measurements of polarization observables in photodisintegration, allowing for

rigorous tests of nuclear theory.

A fundamental measurement of particular interest is the Gerasimov-Drell-Hearn (GDH) Sum Rule. [6] The GDH Sum Rule relates the energy weighted integral of photonuclear cross sections for inelastic processes on a spin-polarized target with the anomalous magnetic moment of the target. It is derived from foundational principles such as Lorentz invariance, gauge invariance, causality, and unitarity, among others. For a target with spin S, anomalous magnetic moment κ, and mass m, which has photoabsorption cross sections σ^P and σ^A for target polarization parallel (P) and antiparallel (A) to the spin of the absorbed photon, the GDH Sum Rule is

$$I_{GDH} = \int_0^\infty \frac{d\omega}{\omega}\Big(\sigma_P(\omega) - \sigma_A(\omega)\Big) = -4S\pi^2\alpha\frac{\kappa^2}{m^2}. \tag{1.3}$$

The right hand side of Eq. 1.3 is calculable for different nuclear targets from definitive physical quantities, as demonstrated in Table 1.2.

Target	κ	m (MeV)	$I_{GDH}(\mu b)$
p	1.79	938.27	204.0
n	-1.91	939.57	232.0
d	-0.14	1875.61	0.6

Table 1.2: GDH Sum Rule for Select Targets. Theoretical calculations of the GDH Sum Rule quantities for light nuclear targets. The GDH integrand, I_{GDH}, is calculated from the anomalous magnetic moment, κ and mass, m, of each target.

The GDH Sum Rule provides a way to test the contributions of different inelastic reactions to the total GDH integral, I_{GDH}. These contributions can either be modeled with theoretical predictions of the nuclear and electromagnetic forces at play in each reaction, or they can be investigated with experimental measurements of reaction cross sections. In this way, the GDH Sum Rule informs the understanding of the role of certain reaction channels in photonuclear processes.

Experimentally measuring the GDH Sum Rule often involves separating the integral into energy regimes based on the reaction channels involved. For example, the GDH sum rule for a nucleon can be expressed as

$$I_{GDH} = \int_{\omega_\pi}^{\omega_{Max}} \frac{d\omega}{\omega}\Big(\sigma_P^N(\omega) - \sigma_A^N(\omega)\Big) + \int_{\omega_{Max}}^{\infty} \frac{d\omega}{\omega}\Big(\sigma_P^N(\omega) - \sigma_A^N(\omega)\Big), \tag{1.4}$$

and for the deuteron,

$$I_{GDH} = \int_{\omega_0}^{\omega_\pi} \frac{d\omega}{\omega}\Big(\sigma_P^d(\omega) - \sigma_A^d(\omega)\Big) + \int_{\omega_\pi}^{\omega_{Max}} \frac{d\omega}{\omega}\Big(\sigma_P^d(\omega) - \sigma_A^d(\omega)\Big) + \int_{\omega_{Max}}^{\infty} \frac{d\omega}{\omega}\Big(\sigma_P^d(\omega) - \sigma_A^d(\omega)\Big). \tag{1.5}$$

Here, ω_0 is the threshold energy for deuteron photodisintegration, ω_π is the pion production threshold, and ω_{Max} is the maximum photon energy achievable in an experimental setting. Other energy cutoffs can be incorporated based on the energies and reaction channels of interest.

The contribution from the energy regime above ω_{Max} must be calculated from theory. Below this threshold, cross sections are experimentally accessible through measurements with polarized beams and targets. The GDH integrand for the proton can be measured directly using a polarized proton target. However, the absence of a stable free-neutron target means the GDH integrand for the neutron must be measured indirectly through the use of a polarized deuteron target.

The GDH integrand above ω_π was measured in a series of experiments at the Mainz Microtron (MAMI) and the University of Bonn ELSA facility [7]. The measured contribution to the GDH integrand for the proton was found to be larger than predicted by theory. These results were later cross-checked at Brookhaven's LEGS facility [8]. With better precision in their measurement, the team at LEGS was able to verify a GDH Sum Rule for the proton that agreed with the theory, correcting the differences measured in prior experiments. However, when using a deuteron target to extract the neutron GDH integrand, the authors found a noticeably lower contribution than expected. This discrepancy for the neutron raised the question of how the GDH Sum Rule could work so well for one nucleon, but not another.

A theory that makes accurate predictions for the proton,but demonstrates discrepancies from experimental measurements with the neutron prompts renewed consideration of the efficacy of both measurement and theory. As the GDH Sum Rule is derived from foundational physical principles that have withstood rigorous experimental testing for decades, inaccuracy in the theory is unlikely. This implies the strong possibility of a flaw in the experimental method. With the crucial role of deuteron photodisintegration in the extraction of a measurement for the neutron, uncertainty emerges about the current understanding of the dynamics of this reaction.

Another long-standing problem in studies of deuteron photodisintegration is the "neutron polarization puzzle". [9] In 1972, Nath et al. [10] published the results of a measurement of the spin polarization of neutrons from $d(\gamma, n)p$ performed at the Yale Electron Accelerator Laboratory. They collected measurements at laboratory reaction angles of 45° and 90° for a series of photon energies below 30 MeV. Using an untagged bremsstrahlung beam produced by irradiating a tungsten foil with a 65 MeV electron beam, the group produced photoneutrons from both deuterated water and deuterated polyethylene targets. The neutron polarization was extracted from a measurement of the left-right asymmetry in elastic scattering from a helium polarization analyzer. The measurements are displayed in Figure 1.2 with a comparison to theoretical predictions.

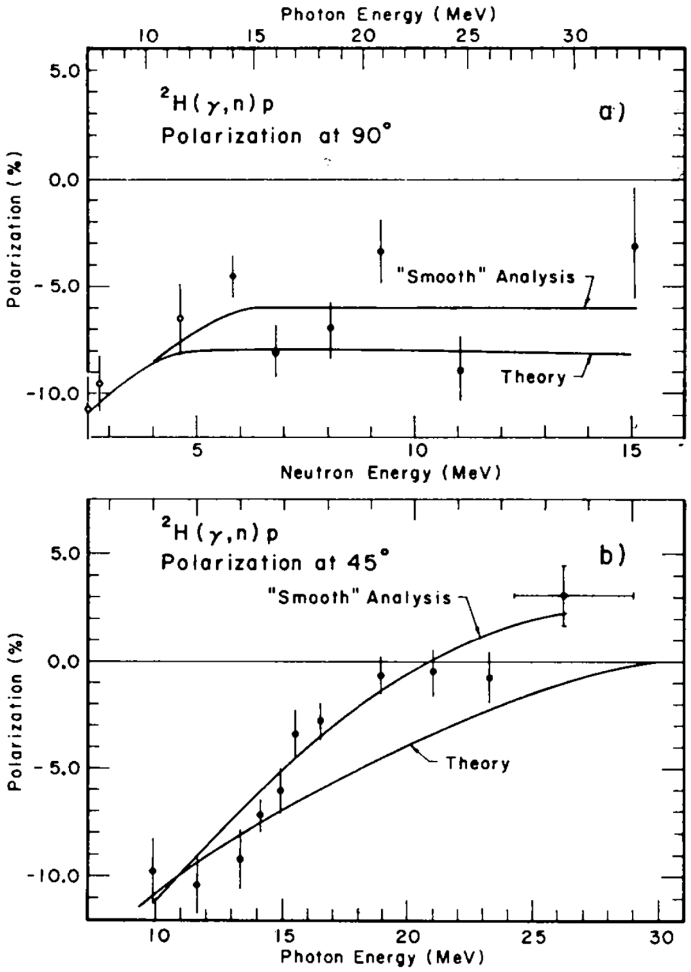

Figure 1.1: Experimental Results of R. Nath et al. Measurements of the neutron spin polarization from $d(\gamma, n)p$ published by Nath et al. in 1972, for laboratory reaction angles of 45° (Bottom) and 90° (Top). Image Credit: R. Nath et al. [10]

For $\theta_n = 45°$, the data demonstrated a stark departure from theoretical calculations starting at a photon energy of ∼12 MeV. The magnitude of the neutron polarization drops off to zero at much lower energies than predicted by theory. This discrepancy prompts consideration of whether mistakes were made in the theoretical formulation of the reaction, or in the experimental methodology of the measurement.

A few years later, the measurement was revisited at Yale as the subject of a Ph.D. dissertation. [13] Gamma-ray photons were again provided by bremsstrahlung radiation generated by an electron beam incident on tungsten and iron converters. For this measurement, the author used a liquid deuterium target, with the intent of removing any background photoneutrons produced from other nuclei in polyethylene or heavy water targets. The polarization was calculated by measuring the scattering asymmetry from a carbon target. Data was collected for photon energies of 6 to 15 MeV at lab reaction angles of $\theta_{Lab} = 60°, 90°,$ and $121.5°$.

The measurement demonstrated consistency with theoretical calculations this time, adding more ambiguity to the state of photoneutron polarization data. At that point, two experiments with very similar setups disagreed on the consistency between experimental data and nuclear theory. Slight differences in the experimental setups and analyses could have contributed to the divergent results, but there was no definitive answer to the nature of the observable.

In the 1980s, a group at Argonne National Laboratory took a crack at settling the issue. Holt et al. [14] measured neutron polarization in deuteron photodisintegration at a laboratory angle of $\theta_{Lab} = 90°$ for photon energies between 6 and 13 MeV. They produced a bremssstrahlung beam with 19 MeV electrons incident on a graphite block. The photoneutron source was a deuterated polyethylene target and the polarization was analyzed with a carbon target for measuring scattering asymmetries.

The Argonne group published results consistent with those of Nath et al., with a lower magnitude for the neutron polarization than predicted by theory. The measurement was only taken at one lab angle, and it did little to solve the problem at hand. The authors emphasized the importance of determining the nature of the discrepancies, stating "Clearly, a high-accuracy distribution of photoneutron polarization and cross section is necessary in order to unravel the multipole components of the reaction $^2H(\gamma, n)H$ at low energy." The data from the neutron polarization experiments are illustrated in Figure 1.2 alongside theoretical calculations performed by H. Arenhövel [11, 12] and S. I. Ando et al. [15, 16] for comparison.

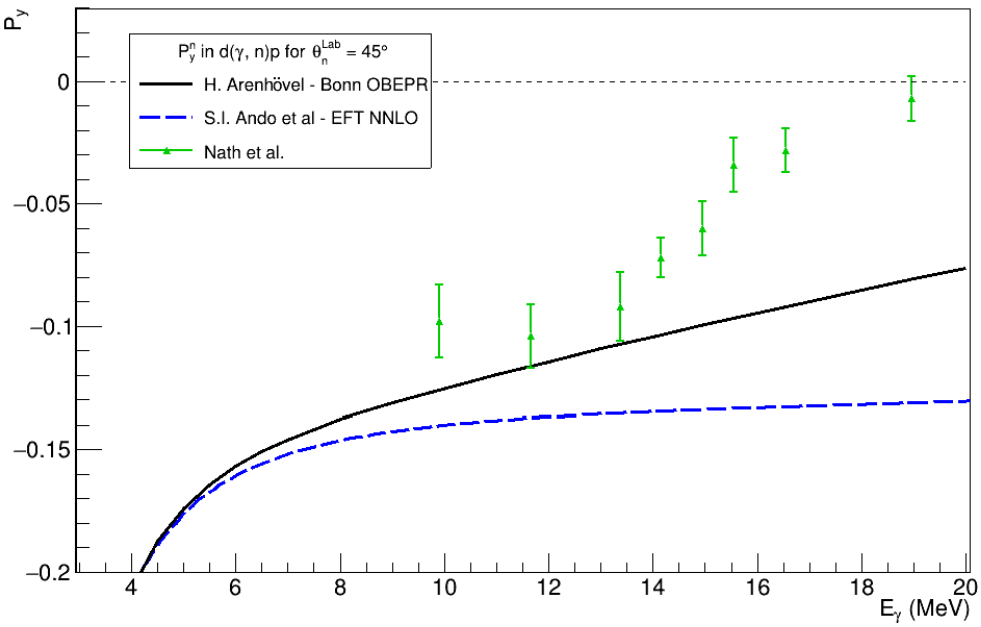

(a) Comparison of P_y experimental data with theoretical calculations at $\theta_{Lab} = 45°$

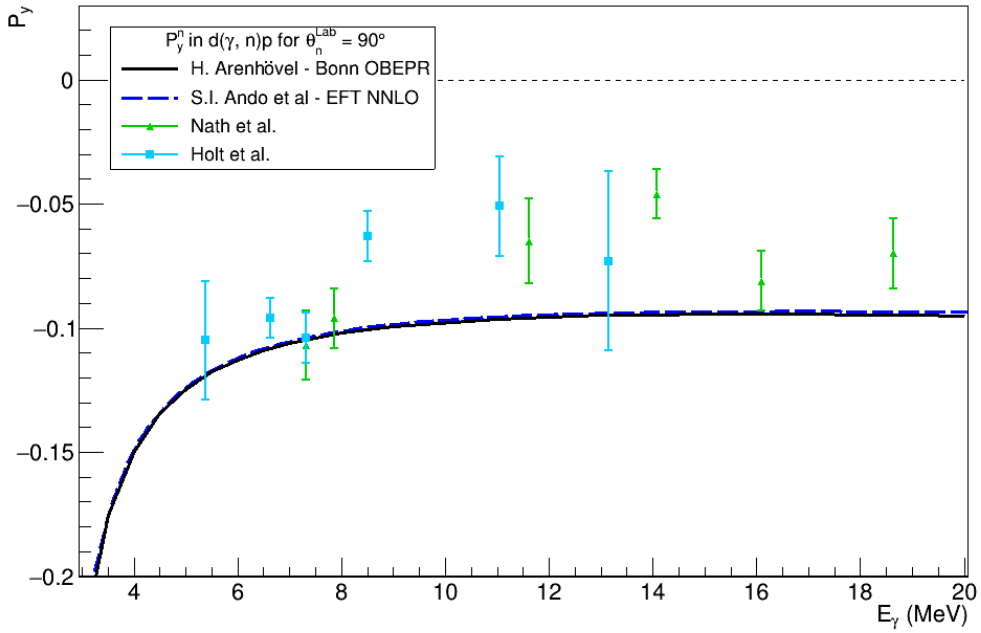

(b) Comparison of P_y experimental data with theoretical calculations at $\theta_{Lab} = 90°$

Figure 1.2: Historical P_y^n Measurements Compared to Theory. Experimental data of P_y^n in deuteron photodisintegration measured by Nath et al. [10] and Holt et al. [14] compared to theoretical calculations performed by H. Arenhövel [11, 12] and S. I. Ando et al. [15, 16]. It should be noted that at $\theta_n^{Lab} = 90°$, the theoretical calculations are nearly indistinguishable.

1.3.3 Deuteron Photodisintegration at HIγS

Studies of deuteron photodisintegration have been ongoing at HIγS to investigate the curiosities in the near threshold regime. A collaboration between groups from the University of Virginia, the University of Saskatchewan, and Duke University has contributed to this effort with the development and operation of a detector array known as the *Blowfish*, shown in Figure 1.3.

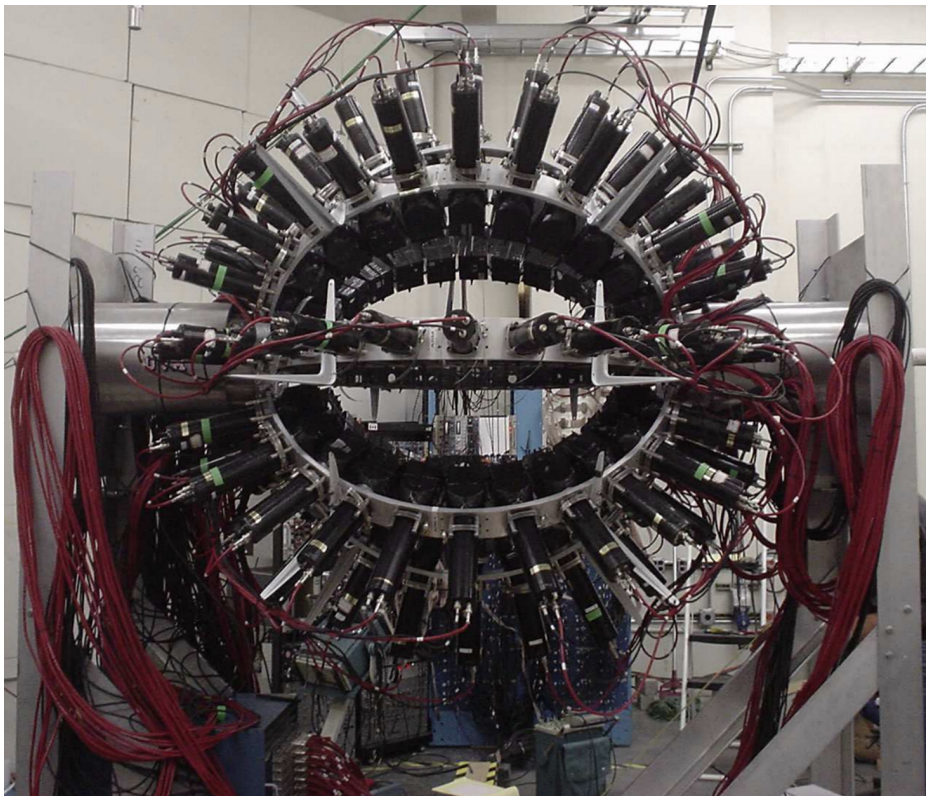

Figure 1.3: The Blowfish Detector Array. A detector array of 88 liquid organic scintillator neutron detectors assembled at HIγS to perform cross section and spin asymmetry measurements of deuteron photodisintegration. Image Credit: B. Sawatzky [17]

A segmented neutron detector array for low energy measurements, Blowfish consists of 88 liquid scintillating neutron detectors, evenly distributed along a sphere of radius 40.6 cm (16 in), covering a solid angle of π steradians. It was designed to take detailed cross section measurements of deuteron photodisintegration at low energies. In conjunction with Blowfish, a polarized target has been under development to enable double-polarization measurements, with a long term goal of measuring the GDH

integrand for the deuteron below the pion production threshold. Such data would complement previous measurements performed above the pion production threshold, and explore possible discrepancies observed in earlier experiments.

In the first experiment performed with Blowfish, B. Sawatzky et al. [17] measured neutron spin asymmetries and differential cross sections in $d(\vec{\gamma}, n)p$ using linearly polarized photons with energies of 3.5, 4, 6, and 10 MeV. Sawatzky found discrepancies between the measurements and theoretical predictions, noting a measurable forward-backward asymmetry in the differential cross section of photoneutron production for energies approaching threshold. Despite careful consideration of the uncertainties in the analysis, the origin of the asymmetry remained a mystery, leaving it unclear if it was due to an unaccounted for effect in the experimental methodology, or a missing reaction contribution in the theoretical framework.

A few years later, M. Blackston [18] extended the measurement performed by Sawatzky, using linearly polarized photons at 14 and 16 MeV. Repeating the methodology and analysis, Blackston observed a similar forward-backward asymmetry in the differential cross section of the reaction seen in Sawatzky's results. Despite validating this effect in the earlier data, there was still no explanation for this divergence of the measurements from the theoretical predictions. Complementing his analysis, Blackston also performed an indirect measurement of the GDH Integrand, extracting the contributions from both energies. Blackston calculated a small positive contribution to the GDH Integrand at these energies, in line with theoretical calculations.

Following up on the discrepancies demonstrated between theory and the results of Sawatzky and Blackston, S. Kucuker [19] performed cross section measurements of the reaction with circularly polarized photons at 18 MeV. To test different parameters of the experimental methodology, Kucuker used two heavy water targets of different lengths. Contrary to earlier measurements, Kucuker's data showed good agreement with theoretical calculations. However, when an analysis was done to evaluate the consistency between data from runs with the two different targets, a slight discrepancy was found between them. A forward-backward asymmetry (similar to that found by Sawatzky and Blackston) was found in the difference between the two sets of data. The longer target yielded a larger cross section in the backward angles than was seen in the shorter target. Further simulation and analysis was unable to identify the cause of the asymmetry, but this result provided an indication of some correlation with the finite target length.

1.4 Motivation

This experiment was performed at the High Intensity Gamma-ray Source (HIγS) at TUNL to measure the polarization of the neutron from deuteron photodisintegration at energies near threshold. Data was collected at laboratory reaction angles of $45°, 90°$, and $135°$ for photon energies of 8, 12, and 16 MeV with both circularly and linearly polarized photons. These parameters map the neutron polarization over a similar phase space as the earlier experiments described in Section 1.3.2. The goal of the experiment is to offer a contemporary measurement of the neutron polarization in $d(\gamma, \vec{n})p$ to address the so called "neutron polarization puzzle". The discrepancies between previous experimental data and theoretical calculations warrant investigation.

Previous measurements of the induced polarization of neutrons in deuteron photodisintegration used untagged bremsstrahlung beams as a photon source. An untagged beam of this nature lacks definitive verification of the energy spectrum and beam profile incident on the target. Analysis of the data required calculating the initial parameters of the photons from the final state kinematics of the measured neutrons. This introduced systematic uncertainties due to assumptions that must be made in the relevant reactions in the setup. Additionally, there was little control over the polarization parameters of the beam, limiting the scope of studying polarization observables in the reaction.

HIγS has the capability to provide a monochromatic gamma-ray photon beam with near perfect polarization (either circular or linear). It can accomplish this with the highest intensity photon beam in the world, providing sufficient statistics for precision measurements. These parameters remove the uncertainties associated with bremsstrahlung beams, enabling an unprecedented accuracy for the measurement. The facility offers a prime opportunity for this experiment to contribute to unraveling the ongoing mystery of this observable.

The underlying purpose of the measurement is a robust test of theoretical formulations of nucleon-nucleon interactions. The traditional approach in nuclear theory has been the development of meson exchange theories or phenomenological models to describe the nuclear force. More recently, the introduction of chiral effective field theory to nuclear physics has provided a model-independent method for calculating observables in nucleon interactions. The different theoretical approaches have been

tested against experimental data from two-nucleon systems to verify their efficacy. Contemporary theories and models have been tuned to NN scattering cross sections and bound state properties rather successfully, prompting further investigations to distinguish between theories. Polarization degrees of freedom offer stringent tests of nuclear theory to contribute to a deeper understanding of the NN interaction.

1.5 The Measurement

The measured quantity of this experiment is the directional asymmetry in the scattering of spin polarized neutrons. The asymmetry is calculated with the difference between the number of spin up neutrons (σ_+) and the number of spin down (σ_-) neutrons. For the purposes of this experiment,

$$A(\theta) = \frac{\sigma_+ - \sigma_-}{\sigma_+ + \sigma_-}. \tag{1.6}$$

This asymmetry manifests as a "left-right" asymmetry in the scattering of neutrons, the magnitude of which is proportional to their polarization. The neutrons scatter from an analyzing material with well-defined analyzing power, A_y, enabling a calculation of the measured neutron polarization, P_y, by

$$A(\theta) = P_y A_y(\theta) \rightarrow P_y = \frac{A(\theta)}{A_y(\theta)}. \tag{1.7}$$

P_y is dependent on polarization contributions from both unpolarized photons (P_y^u) and polarized photons P_y^l. As derived in Section 2.6, these quantities vary with the polar angle of photoneutrons, θ_n, as

$$P_y^m \frac{d\sigma(P_y^\gamma, \theta_n, \phi_n)}{d\Omega} = \frac{d\sigma(\theta_n)}{d\Omega}\bigg|_{P_y^\gamma=0} \Big[P_y^u(\theta_n) + P_y^\gamma P_y^l(\theta_n) \cos(2\phi_n) \Big] \tag{1.8}$$

These contributions are extracted from the measured polarization by changing the polarization of the incident photon beam. A circularly polarized beam ($P_y^\gamma = 0$) can isolate P_y^u, and then a linearly polarized beam ($P_y^\gamma = 1$) can offer a means to calculate P_y^l once P_y^u is known.

1.6 Document Overview

This dissertation describes the background, experimental work, and analysis necessary for the measurement of topic. Chapter 2 introduces the theoretical concepts in nuclear physics behind this experiment. It starts with a discussion of the theory and methods used to model the interactions between nucleons, building up their mathematical framework while explaining their physical significance. It then covers a treatment of the formulas used in the analysis, deriving them from foundational theorems and outlining their implications. Chapter 3 describes the simulation and computational efforts performed during both the preparation and analysis of the experiment. Chapter 4 details the experimental setup and methodology, including the HIγS accelerator facility, the development and operation of the detector technology, and the electronics and data acquisition system used to collect data. Chapter 5 outlines the data analysis process and techniques, motivating analysis decisions with physical interpretations. Chapter 6 presents the current status of the results and offers a window into their implications for the future.

Chapter 2

Theoretical Background

2.1 The Strong Nuclear Force

The proton and neutron within the deuteron are bound by a manifestation of the *strong interaction*[1], a fundamental force of the universe. The strong interaction is described by the quantum field theory (QFT) of quantum chromodynamics (QCD). The intricacies of the theory could fill up an entire chapter on their own, but for now, a quick outline of the physics included will be sufficient.

The theory is summarized by the QCD Lagrangian in Equation 2.1.

$$\begin{aligned}\mathcal{L}_{QCD} &= \bar{\psi}_i\Big(i\gamma^\mu(D_\mu)_{ij} - m\delta_{ij}\Big)\psi_j - \frac{1}{4}G^a_{\mu\nu}G^{\mu\nu}_a \\ &= \underbrace{\bar{\psi}_i\Big(i\gamma^\mu(\partial_\mu)_{ij} - m\delta_{ij}\Big)\psi_j}_{\text{quark propagator}} + \underbrace{\bar{\psi}_i\Big(g_s\gamma^\mu G^a_\mu\frac{\lambda_a}{2}\Big)\psi_j}_{\text{interaction term}} - \underbrace{\frac{1}{4}G^a_{\mu\nu}G^{\mu\nu}_a}_{\text{field tensor}}\end{aligned} \tag{2.1}$$

QCD describes the interactions between quarks, the fundamental particles of strongly interacting matter, and gluons, the mediating bosons of the strong force. $\mathcal{L}_{QCD}$ includes a term for the matter propagating field for quarks and a term for the quark-gluon coupling. These terms provide the foundation for quark interactions via gluon exchange. The field tensor, $G^a_{\mu\nu}G^{\mu\nu}_a$, describes the mechanism for gluon self-interactions. Thus, QCD allows for three types of fundamental interactions: quark-gluon, three-gluon, and four-gluon vertices. The possible combinations of these vertices that can emerge in strong interactions create rather complex dynamics for nuclear forces.

What differentiates quarks and gluons from other fundamental particles is an inherent property known as color charge. Similar to charges associated with other

[1] Also referred to as the *strong nuclear force.*

forces, such as the electromagnetic or weak charges, color is a conserved quantity in strong interactions. A color charge can exist as one of six possible states: red, blue, green, and their three corresponding anticolors. However, the strong force does not allow for the isolation of color-charged particles; only color-neutral states are stable enough to exist in nature. This concept of color *confinement* has been experimentally observed, but has yet to be analytically proven by theory. As a color-charged particle, the gluon is not stable enough at the scale of a nucleus to exist outside a nucleon. Therefore, to explain the interactions between nucleons, the nuclear force can no longer be considered as the exchange of gluons, but rather, must be due to the propagation of some colorless mediator.

The interaction term of $\mathcal{L}_{QCD}$ includes the coupling constant of the strong interaction, α_s (notated in Eq. 2.1 as $g_s = \sqrt{4\pi\alpha_s}$). A distinctive feature of α_s is the running of the coupling, referring to the dependence of the value of α_s on the energy scale of the interaction. At high energy scales (larger momentum transfers in strong interactions), α_s is small and quarks can be treated as free particles, a property known as asymptotic freedom. With a small coupling constant, calculations using $\mathcal{L}_{QCD}$ can be treated perturbatively. However, in the low energy regime, $\alpha_s \geq 1$, and perturbative expansions in strong interaction processes no longer converge. Calculations of observables in low energy nuclear interactions therefore require other theoretical methods to provide accurate predictions for nuclear physics.

The aspects of QCD outlined above reveal limitations in applying the theory in the low energy regime. Computation of interactions between nucleons or nuclei at this scale are prohibitively intense or impossible. Quark and gluon degrees of freedom are no longer appropriate in describing nuclear interactions. Instead, the nuclear force must be modeled with hadronic degrees of freedom.

For decades, the field of nuclear physics has pursued a theoretical description of nuclear structure and reactions, resulting in a variety of methods for modeling the nuclear force. The standard nuclear physics approach (SNPA) has been to develop nuclear potential models to describe the interactions between nucleons. These models take advantage of different approaches to understanding the nuclear force, including meson exchange theories and phenomenological methods. In more recent years, theorists have applied effective field theories to perform calculations of nucleon-nucleon interactions consistent with the underlying principles of QCD.

2.2 Meson Exchange Theory

This section outlines the development and details of *meson exchange theory*, in which the interaction between nucleons is treated as the exchange of a force-mediating meson. It approaches the topic through a historical lens, guided by the series of breakthroughs that led to contemporary meson exchange theory. The information covered in this section was compiled from a number of sources including Refs. [21–27] and other references directly cited in the text.

2.2.1 Yukawa Potential

As physicists first began to elucidate the properties of atomic nuclei, two seemingly contradictory principles emerged:

1. An atomic nucleus is composed of positively charged protons and neutrally charged neutrons.

2. A repulsive force manifests between protons due to the electromagnetic interaction.

Acting alone, the electromagnetic repulsion between protons should prevent the formation of any kind of bound state between them. Thus, some other interaction between the nucleons must generate a strong enough attraction between them to overcome the electromagnetic force. However, no such force had been observed outside of the nucleus with the strength to do so.[2] Thus began the search for some explanation for this "force of the nucleus", stronger than electromagnetism inside a nucleus, while inconspicuous at a longer range.

In 1935, H. Yukawa published his work on developing a model for the nuclear force. [3] He approached it with a treatment of classical field theory, drawing inspiration from the theory of the electromagnetic interaction. Yukawa derived a formula for this field by introducing the characteristic range of the nuclear force.

An electromagnetic field from a point particle with charge q has a scalar potential, $\varphi(r)$ with behavior described by Poisson's Equation, shown in Eq. 2.2.

$$\nabla^2\varphi(r) = -q\delta^3(\vec{r}) \tag{2.2}$$

[2] The other known force at the time, gravity, is not strong enough given the masses of the protons.

This differential equation can be solved to find a form for the potential. Placing a similar point charge, q, in the field yields the Coulomb Potential energy,

$$V(r) = \frac{q^2}{4\pi}\frac{1}{r}. \tag{2.3}$$

To formulate the nuclear force, Yukawa modified the wave equation for the field with an additional term dependent on the characteristic range of the nuclear force,

$$\Big(\nabla^2 - \lambda^2\Big)\varphi(r) = g\delta^3(\vec{r}). \tag{2.4}$$

where $\lambda = \frac{1}{R}$ (with units cm^{-1}) for a range of the nuclear force R, and g is the coupling constant of a nucleon to the field. The wave equation can then be solved for $\varphi(r)$ to find the scalar potential. A second nucleon in this field, also with coupling constant g, will experience the potential energy of the Yukawa potential,

$$V(r) = -g^2\frac{e^{-\lambda r}}{r}. \tag{2.5}$$

Eq. 2.5 includes a factor of $\frac{1}{r}$, indicating a force that decreases in magnitude with interaction distance. The force holding the nucleons together must be much stronger than the electromagnetic interaction within the radius of the nucleus, but also diminish much faster outside of the nucleus. This would explain a force that could overcome the electrostatic repulsion of the positive charges within the nucleus, but was immeasurable when compared to the electromagnetic force outside of the nucleus. The exponential factor in the Yukawa potential folds this behavior into the mathematical description, producing a large magnitude for $r \to 0$ that rapidly drops off with increasing r, resulting in a finite range for the potential. This formulation of the potential sets a restriction that $V(r) \leq 0$, implying an attractive force between the nucleons, as observed in nature.

The defining feature of the Yukawa potential is its handling of particle exchange as a mediator for the nuclear interaction. He inferred that the nuclear force could be modeled as the exchange of a boson between nucleons, similar to photon exchange in electromagnetic interactions. However, to explain the limited range of the nuclear force, he determined that the boson must have some finite mass. To demonstrate

this, Yukawa applied the wave equation for a field in vacuum to the potential.

$$\left(\nabla^2 - \frac{1}{c^2}\frac{\partial^2}{\partial t^2} - \frac{m_V c^2}{\hbar^2}\right)V = 0 \tag{2.6}$$

Evaluating with V(r) from Eq. 2.5 yields a quantum of mass $m_V = \frac{\lambda\hbar}{c}$. The range of the nuclear force had been experimentally measured, producing a value of $\lambda = 5 \times 10^{12} cm^{-1}$, corresponding to a mediator mass of $m_V = 98.66$ MeV $\approx 200 m_e$. This particle would later be deemed a "meson", from the Greek term *mesos* meaning *intermediate*, due to its intermediate mass between the electron and the proton. Yukawa's particle would not be experimentally verified until the discovery of the pion in 1947.[3] [4, 5] Yukawa's description of the interaction between nucleons became the earliest iteration of meson exchange that would take root in nuclear theory.

With the Yukawa potential, nuclear physics had its first mathematical model of the interaction between nucleons. Calculations could produce quantities for observables to test against experimental data. These comparisons would eventually reveal the limitations of the Yukawa potential, but the taste of the capabilities of such a model would fuel future endeavors into more precise potentials of nucleon interactions.

2.2.2 One Pion Exchange Potential

Despite the promise shown by Yukawa's phenomenological model in describing nucleon interactions, his original formulation would turn out to be incomplete. Turning to quantum field theory reveals a means for expanding upon Yukawa's original theory.

In Section 2.2.1, the Yukawa potential was found as a solution to the wave equation for a nuclear interaction field. This potential can also be described with quantum field theory. Yukawa's original formulation implied a scalar field coupling to the nucleons, described through pion exchange, represented by the scalar Yukawa Lagrangian,

$$\mathcal{L}_Y = -g\bar{\psi}\psi\phi. \tag{2.7}$$

To apply Eq. 2.7 to nuclear interactions, ψ is taken as the nucleon field and g is the coupling of the nucleon to the interaction field. Assigning the pion as the scalar

[3] Interestingly, Yukawa himself had doubts about the pragmatism of his own meson exchange model, claiming "As such a quantum of large mass and positive or negative charge has never been found by the [sic] experiment, the above theory seems to be on the wrong line." [3]

meson ($\phi = \pi$) assumes it to be a particle with total spin 0 and even intrinsic parity ($J^P = 0^+$). The form of the Yukawa potential given in Eq. 2.5 is derived from the Lagrangian through the scattering amplitude of the interaction:

$$f(\vec{p}) = ig^2\left(\frac{1}{(\vec{p}-\vec{p}')^2 + m_\pi^2}\right) \tag{2.8}$$

The scattering amplitude relates to the potential through the Born Approximation:

$$f(\vec{p}) = -i\frac{m}{2\pi}\int e^{i(\vec{p}-\vec{p}')\cdot\vec{r}}V(\vec{r})d^3\vec{r}. \tag{2.9}$$

Matching the right hand sides of these equations gives

$$\int e^{i(\vec{p}-\vec{p}')\cdot\vec{r}}V(\vec{r})d^3\vec{r} = -\frac{2\pi g^2}{m_\pi}\left(\frac{1}{(\vec{p}-\vec{p}') + m_\pi^2}\right) \tag{2.10}$$

$$V(\vec{r}) = -\frac{2\pi g^2}{m_\pi}\int \frac{e^{i\vec{q}\cdot\vec{r}}}{\vec{q}^2 + m_\pi^2}\frac{d\vec{q}}{(2\pi)^3} \tag{2.11}$$

$$V(\vec{r}) = \frac{-g^2}{4\pi}\frac{e^{-m_\pi r}}{r}. \tag{2.12}$$

The original Yukawa potential appears again from coupling the interacting nucleons to a scalar field. However, after the pion's discovery, further investigation revealed more about its nature which indicated the need for a modification to the Lagrangian. The pion actually refers to any of the isospin triplet $\pi^0, \pi^+,$ or π^- with $I = 1$ and $I_3 = 0, \pm 1$, respectively. Like a scalar meson, a pion has spin 0, but it was experimentally measured to have odd parity, qualifying it as a pseudoscalar meson ($J^P = 0^-$). This requires coupling the nucleons to a pseudoscalar pion field, $\vec{\pi}$, with a new notation for the coupling constant of g_π, to properly formulate an interaction due to pion exchange,

$$\mathcal{L}_Y = -ig_\pi\bar{\psi}\gamma^5\vec{\tau}\psi\cdot\vec{\pi}. \tag{2.13}$$

Here, γ^5 represents the product of the Dirac matrices and $\vec{\tau}$ denotes the Pauli matrices as applied to isospin space. The pion field used is a collection of orthogonal components of the three types of pions:

$$\vec{\pi} = \begin{pmatrix}\pi^1\\ \pi^2\\ \pi^3\end{pmatrix} = \begin{pmatrix}\frac{1}{\sqrt{2}}(\pi^+ + \pi^-)\\ \frac{i}{\sqrt{2}}(\pi^+ - \pi^-)\\ \pi^0\end{pmatrix} \tag{2.14}$$

Following the same derivation used for the scalar Yukawa coupling in Eq. 2.7, the potential due to a pseudoscalar pion exchange can be determined in momentum space as,

$$V_\pi(\vec{q}) = \frac{g_\pi^2}{3}(\vec{\tau}_1 \cdot \vec{\tau}_2)\left[\frac{-\vec{q}^2}{\vec{q}^2 + m_\pi^2}(\vec{\sigma}_1 \cdot \vec{\sigma}_2) - \frac{S_{12}(\vec{q})}{\vec{q}^2 + m_\pi^2}\right]. \tag{2.15}$$

Here, $S_{12}(\vec{q})$ is the tensor operator acting on the spin states of the nucleons, with the identity in Eq. 2.16,

$$S_{12}(\vec{q}) = 3(\vec{\sigma}_1 \cdot \hat{q})(\vec{\sigma}_2 \cdot \hat{q}) - (\vec{\sigma}_1 \cdot \vec{\sigma}_2). \tag{2.16}$$

A Fourier transform of $V_\pi(\vec{q})$ into position space reveals what is commonly referred to as the One-Pion-Exchange Potential (OPEP)

$$\begin{aligned} V_\pi(\vec{r}) &= \frac{g^2}{3}(\vec{\tau}_1 \cdot \vec{\tau}_2)\left[\left(\vec{\sigma}_1 \cdot \vec{\sigma}_2\right)\frac{e^{-m_\pi r}}{r} + S_{12}(\vec{r})\left(1 + \frac{3}{m_\pi r} + \frac{3}{(m_\pi r)^2}\right)\frac{e^{-m_\pi r}}{r}\right] \\ &= \frac{g^2}{3}(\vec{\tau}_1 \cdot \vec{\tau}_2)\left[\left(\vec{\sigma}_1 \cdot \vec{\sigma}_2\right)Y(m_\pi r) + S_{12}T(m_\pi r)\right] \end{aligned} \tag{2.17}$$

This formulation of V_π in Eq. 2.17 maps out the contributions to the nucleon-nucleon interaction from single pion exchange.

Isospin Dependence

The OPEP has a dependence on the total isospin of the two nucleon system $I_{NN} = I_{N1} + I_{N2}$ due to the factor,

$$\vec{\tau}_1 \cdot \vec{\tau}_2 = 2I_{NN}(I_{NN} + 1) - 3. \tag{2.18}$$

For two protons or two neutrons, $(\vec{\tau}_1 \cdot \vec{\tau}_2) = 1$. For np systems, the isospin factor can have values of 1 or -3, which correspond with the spin states of the nucleons. The change in sign between these two possibilities hints that the spin-isospin states of the nucleons determine whether the potential in Eq. 2.17 is attractive or repulsive.

Spin-Spin Interaction

The first term within the brackets of Eq. 2.17 is a spin-spin Yukawa interaction acting as a central force between nucleons. The alignment of the spins of the nucleons produces a contribution to the nuclear force, and the spin states of the nucleons

determine the nature of this contribution. Expanding the dot product of the Pauli spin matrices yields,

$$\sigma_1 \cdot \sigma_2 = 2S(S+1) - 3, \tag{2.19}$$

where S is the total spin of the two nucleon system. For two identical nucleons (pp or nn), the system must exist in the singlet spin state with a total spin of $S = 0$, in which case $\sigma_1 \cdot \sigma_2 = -3$, providing a negative contribution from the first term to the full potential.

For the np system, the contribution from the spin-spin interaction depends on both the total spin and total isospin. Maintaining the proper symmetries of the nucleon wavefunctions requires either $S = 0, I = 1$ (spin singlet state) or $S = 1, I = 0$ (spin triplet state). In either case, $(\vec{\tau}_1 \cdot \vec{\tau}_2)(\vec{\sigma}_1 \cdot \vec{\sigma}_2) = -3$, and the spin-spin interaction once again contributes a negative term to the OPEP.

The negative value of the spin-spin term for all two nucleon systems indicates an attractive contribution to the potential. It should be noted that the magnitude of this attractive force is a rather small contribution to the full nuclear interaction.

Spin-Spin Tensor Force

The final term in Eq. 2.17 contains the S_{12} tensor operator of Eq. 2.16 in position space, representative of a force that varies for different directions of $\vec{r}$. In the OPEP, the angular dependence comes from $S_{12}(\vec{r})$ due to the factors of $\sigma_N \cdot \hat{r}$. For the singlet spin state, $S_{12} = 0$, so this term vanishes for all pp and nn systems. For a np system such as the deuteron, the spin triplet state will generate a finite value for S_{12}. Coupled with the large magnitude of $T(m_\pi r)$ and $\vec{\tau}_1 \cdot \vec{\tau}_2 = -3$ for this state, the tensor force term adds a large negative contribution to the potential, again indicating an attractive force between the nucleons.

Putting It All Together

What becomes evident from the OPEP is the spin-isospin dependence of the nuclear force between nucleons. The central force of the spin-spin Yukawa term provides an attractive potential between nucleons, albeit one that is too small to bind nucleons together on its own. It is not until the large contribution from the tensor force is included can this behavior emerge. With $S_{12} = 0$ for two like nucleons, there are no bound states of two protons or two neutrons, as dictated by the OPEP. However,

for the spin triplet state of the np system, the addition of the large tensor force contribution generates a strong enough attraction to allow for the existence of a bound np state - the deuteron.

2.2.3 One Boson Exchange Potential

Despite improvement from the original Yukawa potential, the OPEP still demonstrates limitations in its ability to model the nuclear force. Pion exchange offers a successful model for long range NN interactions at distances greater than ∼2 fm. Inside this interaction radius, the OPEP fails to capture all of the features of the nuclear force. Other contributions must be considered for a more complete understanding.

To formulate a model for short range nucleon interactions, it is useful to reconsider an aspect of Yukawa's original formulation of pion exchange. Yukawa attributed the limited range of the nuclear force (as compared to the electromagnetic interaction) to the finite mass of the pion. From this idea, one could extrapolate that a mediator with a mass larger than the pion would result in a shorter characteristic range for its interaction.

It turns out, in the decades after the discovery of the pion, researchers were able to experimentally observe heavier mesons with different intrinsic properties, i.e. quantum numbers, from the pion. Table 2.1 contains a summary of the main mesons considered in nucleon interactions. Each meson contributes in its own way to the nuclear interaction, culminating in a summation of these contributions in the form of a one-boson-exchange-potential (OBEP).

Meson	Mass ($\frac{MeV}{c^2}$)	Quark Content	I	J^P (Spin-Parity)
$\pi^{\pm}$	139.6	$u\bar{d}$	1	0^- (Pseudoscalar)
π^0	135.0	$\frac{1}{\sqrt{2}}(u\bar{u} - d\bar{d})$	1	0^- (Pseudoscalar)
σ	500.0	–	1	0^+ (Scalar)
η	548.8	$\frac{1}{\sqrt{6}}(u\bar{u} + d\bar{d} - 2s\bar{s})$	0	0^- (Pseudoscalar)
ρ	775.1	$u\bar{d}$	1	1^- (Vector)
ω	782.7	$\frac{1}{\sqrt{2}}(u\bar{u} + d\bar{d})$	0	1^- (Vector)

Table 2.1: Properties of Mesons Involved in One-Boson-Exchange[28]. Collection of mesons that are most often incorporated into meson exchange theories. The properties of each meson drive how each one contributes to the nuclear force in a different.

Heavier Psuedoscalar Mesons: η

The pseudoscalar η meson couples to the nucleons in the same way as the pion, with Lagrangian,

$$\mathcal{L}_\eta = -ig_\eta \bar{\psi}\gamma^5 \vec{\tau}\psi \cdot \vec{\eta}. \tag{2.20}$$

The η-exchange potential is therefore similar to the OPEP, however, for the η meson, $I = 0$, so $\vec{\tau}_1 \cdot \vec{\tau}_2$ simplifies to a constant, giving

$$V_\eta(\vec{q}) = g_\eta^2 \left[\frac{-\vec{q}^2}{\vec{q}^2 + m_\eta^2} (\vec{\sigma}_1 \cdot \vec{\sigma}_2) - \frac{S_{12}(\vec{q})}{\vec{q}^2 + m_\eta^2} \right]. \tag{2.21}$$

With a similar formulation to the OPEP, V_η offers a similar contribution to the nuclear force at a shorter range than pions. However, the coupling of η to the nucleons, g_η, turns out to be rather small, and so its contribution to the potential is sometimes neglected in favor of the more dominant forces.

Scalar-Isoscalar Mesons: σ

The scalar-isoscalar σ has a scalar coupling to the nucleons governed by

$$\mathcal{L}_\sigma = -g_\sigma \bar{\psi}\psi\phi_\sigma, \tag{2.22}$$

which yields V_σ in momentum space,

$$V_\sigma(\vec{q}) = \frac{g_\sigma^2}{\vec{q}^2 + m_\sigma^2} \left(-1 + \frac{(\vec{p}^{\,'} + \vec{p})^2}{8M^2} - \frac{\vec{q}^2}{8M^2} - \frac{\vec{L} \cdot \vec{S}}{2M^2} \right). \tag{2.23}$$

The contributions from V_σ are an attractive central force and an attractive spin-orbit force from the $\vec{L} \cdot \vec{S}$ term with orbital angular momentum $\vec{L}$ and total spin $\vec{S}$. The inclusion of the σ exchange in OBEPs is unique due to the large mass width of the σ. [28] There is some debate over the role of the σ in meson exchange theory. Different masses are sometimes used to adjust the contribution of V_σ to better model the nuclear force at intermediate ranges, in some cases simulating the effects of multi-meson exchanges. More details are discussed in Section 2.2.3.

Vector Mesons: ρ, ω

Vector mesons can have both vector and tensor couplings to nucleons; however, these couplings have different strengths that determine which contributions must actually be included in the potential. The vector coupling of the ρ is negligible when compared to its tensor coupling, so the Lagrangian can be written as,

$$\mathcal{L}_\rho = -\frac{f_\rho}{4M}\bar{\psi}\sigma^{\mu\nu}\vec{\tau}\psi \cdot \Big(\partial_\mu(\vec{\phi}_\rho)_\nu - \partial_\nu(\vec{\phi}_\rho)_\mu\Big). \tag{2.24}$$

Deriving the potential in momentum space gives

$$V_\rho(\vec{q}) = \frac{f_\rho^2}{12M^2}(\tau_1 \cdot \tau_2)\left[2\left(\frac{m_\rho^2}{\vec{q}^2 + m_\rho^2} - 1\right)(\sigma_1 \cdot \sigma_2) + \frac{S_{12}(\vec{q})}{\vec{q}^2 + m_\rho^2}\right]. \tag{2.25}$$

Similar to the contributions in the OPEP in Eq. 2.17, there is a spin-spin interaction central force acting in the short range and adding to the same force from pion exchange. The spin tensor force is also present, but with an opposite sign from the respective force in the OPEP. This means that at intermediate and short ranges, where ρ exchange contributes, the spin tensor force is weaker than implied by the OPEP alone, an effect that has been experimentally verified.

The ω meson is also a vector meson, but now with a strong vector coupling to the nucleons and a negligible tensor coupling, yielding the potential

$$V_\omega(\vec{q}) = \frac{g_\omega^2}{\vec{q}^2 + m_\omega^2}\left(1 - 3\frac{\vec{L}\cdot\vec{S}}{2M^2}\right). \tag{2.26}$$

With its large mass, the ω produces short range contributions to the NN potential with a strong spin-orbit force due to the $\vec{L}\cdot\vec{S}$. What is especially notable about the ω OBEP is the first term, providing a short range repulsive central force. This contribution acts as a strong repulsive core growing exponentially as the NN interaction distance approaches the nucleon radius. This fits with the expected QCD behavior of nucleons at this scale, as the quark degrees of freedom begin to dominate and the Pauli Exclusion Principle prevents such close proximity between the nucleons.

Multi-Meson Exchange

It is prudent to consider that a "more massive mediator" of the strong interaction might actually be the result of the exchange of more than one boson. It turns out, multi-meson exchanges contribute considerably to the short and intermediate range behavior of the nuclear force. In particular, the two-pion and pion-rho exchanges provide crucial contributions to understand the intermediate-range attraction between nucleons. The introduction of multi-meson exchanges to the NN potential adds considerable complexity and an energy dependence[4] that complicates calculations of nuclear interactions.

To handle these multi-meson contributions, some models of the nucleon potential use the one-sigma-exchange potential to "simulate" their effect. These models take advantage of the wide range in the mass distribution of the σ to implement it as a tunable parameter to best approximate the effects of multi-meson exchanges. In this case, multiple masses of the σ are used for calculating different contributions to the potential. With this method, the NN potential can be maintained as a one-boson-exchange model and remain energy independent.

Putting It All Together...Again

With all the OBEPs derived, a typical NN potential model based on meson exchange is taken as the sum over all the possible single boson exchanges,

$$V = \sum_{\alpha=\pi,\eta,\sigma,\rho,\omega} V_\alpha \tag{2.27}$$

The original OPEP is then still an important contribution, often acting as the tail of the potential in the long range regime. As the interaction distance between nucleons decreases, heavier meson and multi-pion exchanges become more prominent, and have more influence over the nuclear interaction in the intermediate and short ranges. The ranges of these contributions, along with some example potential models that utilize different methods of applying OBEPs, are illustrated in Figure 2.1. With all the parameters to be adjusted in the collection of OBEPs, it is evident that they can produce variable results depending on how theorists fit them to experimental data in NN scattering and bound states. Additionally, the OBEPs themselves do not

[4] An energy dependence of the potential between nucleons presents problems in applications to nuclear structure and many-body systems.

fully account for all phenomena observed in NN interactions. They require further corrections to develop higher precision models. The following section outlines an example of a contemporary nuclear potential model that uses the OBEP to describe the NN interaction.

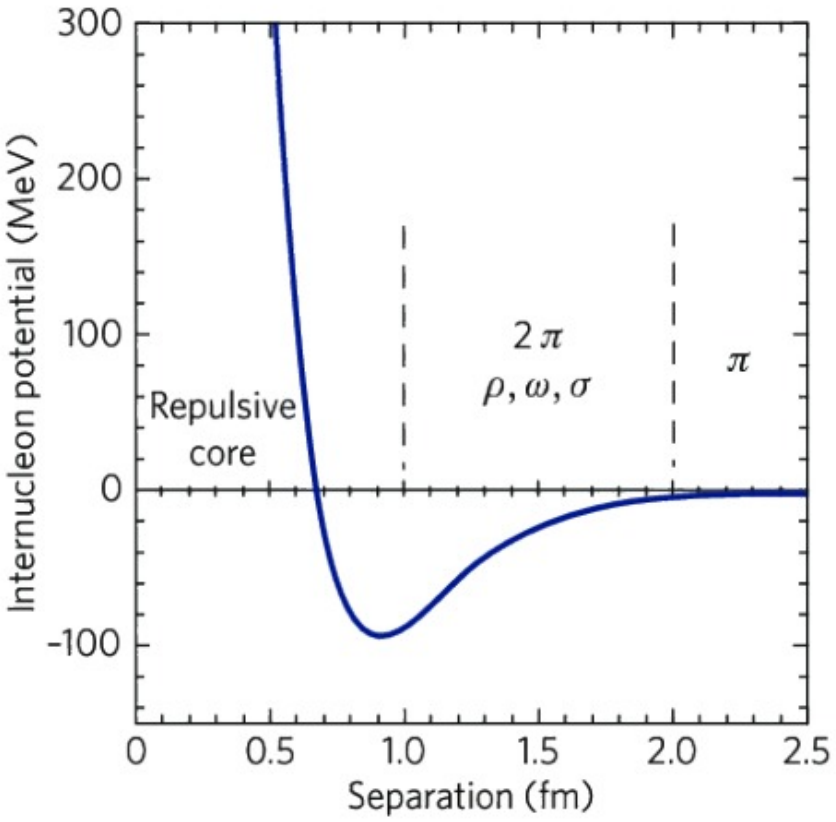

Figure 2.1: Ranges of Meson Contributions to Nuclear Potential. Sample form of nuclear potential demonstrating the ranges of contributions from the exchange of different mesons. Single pion exchange typically models long range forces, for internucleon distances above 2 fm. Heavier mesons contribute to shorter range contributions to the nuclear force. Image Credit: Adapted from F. Wilczek [29]

2.2.4 CD Bonn Potential

Meson exchange theory was instrumental in the development of the Bonn Potential, published by a nuclear theory group affiliated with the University of Bonn in 1987 [30]. It was a combination of OBEPs and multi-meson exchanges to describe NN

interactions with reasonable agreement to experimental data. However, the original formulation did not properly account for the charge dependence in nuclear interactions, prompting the release of the updated CD (Charge Dependent) Bonn Potential in 2001[31]. The CD Bonn model incorporates the charge-symmetry-breaking (CSB) caused by the nucleon mass difference ($m_n > m_p$). Multi-meson exchange contributions demonstrate a dependence on CSB. Additionally, the meson exchange itself exhibits charge-independence-breaking (CIB) in NN interactions, due to the pion mass splitting. The CD Bonn Potential is structured to account for these charge dependencies.

The model begins with the summation of OBEPs in Eq. 2.27 with the exception of the a_0 meson of mass 980 MeV, since it is heavier than the nucleons. In order to maintain a one-boson-exchange model, the Bonn potential uses the scalar-isoscalar σ to account for multi-meson exchange. Because of the mixing of mesons in multi-boson exchange, a single σ mass does not account for enough of this order of contribution. So, two masses for σ are included, σ_1 and σ_2. Finally, the model acknowledges experimental measurements demonstrating a small coupling of the η meson to the nucleon; therefore, it assumes a negligible contribution that can be dropped from the final model. With these considerations, the potential is given as,

$$V(NN) = \sum_{\alpha=\pi,\rho,\omega,\sigma_1,\sigma_2} V_\alpha\Big[M(NN)\Big]. \tag{2.28}$$

Here, the CSB due to the nucleon masses emerges with the dependence on $M(NN)$ such that,

$$M(NN) = \begin{cases} M_p, & \text{if } NN = pp \\ M_n, & \text{if } NN = nn \\ \sqrt{M_p M_n}, & \text{if } NN = np \end{cases}. \tag{2.29}$$

The CIB from the pion mass splitting becomes clear by decomposing the V_π contribution to the model as

$$\begin{aligned} V(NN) &= V_\pi(NN) + \sum_{\alpha=\rho,\omega,\sigma_1,\sigma_2} V_\alpha\Big[M(NN)\Big] \\ &= V_\pi\Big[g_\pi(NN), m_\pi(NN), M(NN)\Big] + \sum_{\alpha=\rho,\omega,\sigma_1,\sigma_2} V_\alpha\Big[M(NN)\Big], \end{aligned} \tag{2.30}$$

where V_π is of the form of the OPEP in Eq. 2.17 and the parameters are dependent on the nucleons as

$$V_\pi = \begin{cases} V_\pi\Big[g_\pi(M), m_{\pi^0}, M\Big], & \text{if } NN = pp \\ V_\pi\Big[g_\pi(M), m_{\pi^0}, M\Big], & \text{if } NN = nn \\ -V_\pi\Big[g_\pi(M), m_{\pi^0}, M\Big] + 2V_\pi\Big[g_\pi(M), m_{\pi^\pm}, M\Big], & \text{if } NN = np, T = 1 \\ -V_\pi\Big[g_\pi(M), m_{\pi^0}, M\Big] - 2V_\pi\Big[g_\pi(M), m_{\pi^\pm}, M\Big], & \text{if } NN = np, T = 0 \end{cases} . \quad (2.31)$$

For V_π, M is assigned as described in Eq. 2.29 and g_π becomes a function of the nucleon masses and a coupling constant.

In its full form, with appropriately charge dependent OBEPs, the Bonn Potential is capable of describing many of the contributions to the nuclear force between nucleons. It is standard to fit calculations performed with such potential models to the world collection of NN scattering data. Upon development of the model, the Bonn group found it to fit pp scattering data below 350 MeV with a χ^2/datum $= 1.01$ and np scattering data with χ^2/datum $= 1.02$. It offers some of the closest agreement to experimental data, opening it up to be tested against further measurements, such as polarization observables in NN interactions and nuclear forces in larger nucleon systems. As the model's authors describe, "the CD-Bonn potential represents a promising starting point for exact few-body calculations and microscopic nuclear many-body theory". [31]

2.3 Phenomenological Models

In parallel to the development of meson exchange theories, some theorists approached modeling the nuclear force through phenomenological means. They constructed nucleon-nucleon interaction potentials with a series of terms to represent different contributions to the nuclear force. These potentials contained tunable parameters to adjust the "strength" of each contribution. The models would then be fit to available experimental data of nucleon scattering in the hopes of producing precise interaction potentials to describe the nuclear force.

In 1958, Okubo and Marshak [32] used phenomenology to derive a "most general" expression for the nucleon-nucleon interaction potential. They observed that previous

static potential models struggled to fit two-nucleon scattering data below 300 MeV. They proposed the inclusion of more contributions due to the momenta and spins of two interacting nucleons. To obtain an expression for the potential, the authors required that it satisfied the following conditions:

1. Translational Invariance
2. Galilean Invariance
3. Particle Symmetry
4. Rotation Invariance
5. Space Reflection Invariance
6. Time Reversal Invariance
7. Hermiticity

Okubo and Marshak arrived at a potential they considered to be "the most general velocity-dependent nonrelativistic potential". It included dependence on the relative positions of two nucleons, $\vec{r}$ ($r^2 = \vec{r} \cdot \vec{r}$), the relative momentum of the nucleons, $\vec{p}$, the total orbital angular momentum of the nucleons, $\vec{L}$, the individual spins of the nucleons, $\vec{\sigma}_1$ and $\vec{\sigma}_2$, and the total spin of the system, $\vec{S}$. They arrived at the potential of the form

$$\begin{aligned} V = &\underbrace{V_0(r^2, p^2, L^2)}_{\text{central force}} + \underbrace{(\vec{L} \cdot \vec{S})V_1}_{\text{spin-orbit force}} + \underbrace{(\vec{\sigma}_1 \cdot \vec{\sigma}_2)V_2}_{\text{spin-spin force}} + \underbrace{(\vec{\sigma}_1 \cdot \vec{r})(\vec{\sigma}_2 \cdot \vec{r})V_3}_{\text{tensor force}} \\ &+ (\vec{\sigma}_1 \cdot \vec{p})(\vec{\sigma}_2 \cdot \vec{p})V_4 + \frac{1}{2}\Big[(\vec{\sigma}_1 \cdot \vec{L})(\vec{\sigma}_2 \cdot \vec{L}) + (\vec{\sigma}_2 \cdot \vec{L})(\vec{\sigma}_1 \cdot \vec{L})\Big]V_5, \end{aligned} \tag{2.32}$$

where V_i are all functions of r^2,p^2, and L^2. The terms of this potential exhibit familiar contributions to the nuclear force including the central force (V_0), the spin-orbit force (V_1), the spin-spin force (V_2), and the tensor force (V_3). This phenomenological derivation thus arrives at a similar description to the nuclear force that arises from meson exchange theories, modeling different aspects of the nuclear force that are observed empirically. Potentials of this form can be fit to nucleon-nucleon scattering data to adjust the V_i parameters, producing precise models of nucleon interactions.

2.3.1 Argonne v_{18} Potential

One of the more contemporary phenomenological NN potentials is the Argonne v_{18} Potential (Av_{18}). The model, published in 1995 [33], is an updated version of an original Argonne potential [34] that incorporates charge dependence of the NN interaction. The Av_{18} group observed that other potentials failed to precisely model experimental data of both *pp* and *np* scattering; they could handle one or the other fairly well, but not both. They proposed that other potentials (including the original Av_{14}) did not properly account for "charge-independence breaking in the strong interaction". The group hoped to more accurately model this phenomenon in their work. A look at how this potential is constructed offers insight into the physics that was considered in its development.

The Argonne v_{18} potential is composed of an electromagnetic (EM) contribution, a one-pion-exchange (π) contribution, and a phenomenological term (R) for intermediate- and short-range interactions.

$$V(NN) = V^{EM}(NN) + V^{\pi}(NN) + V^{R}(NN) \tag{2.33}$$

The electromagnetic term contains different contributions based on all potential electromagnetic interactions with the form,

$$V^{EM}(pp) = V_{C,1\gamma}(pp) + V_{C,2\gamma} + V_{DF} + V_{VP} + V_{MM}(pp). \tag{2.34}$$

For two protons (*pp*), the potential reflects the contributions to the interaction of two charged particles. $V_{C,1/2\gamma}$ represents the single and double photon Coulomb potentials. The Darwin-Foldy (DF) term is included as the correction to the charge radius of the proton. Vacuum polarization (VP) accounts for virtual particle pair contributions to the photon exchange. Finally, a term is added for the interaction of the magnetic moments (MM) of the protons.

For two neutron (*nn*) interactions, the contributions from nucleon charges (or in this case, charge distributions) can be neglected, leaving only a dependence on the magnetic moment term,

$$V^{EM}(nn) = V_{MM}(nn). \tag{2.35}$$

For the *np* system, V^{EM} includes the magnetic moment interaction, but also brings back a Coulombic potential term due to proton interaction with the charge

distribution of the neutron,

$$V^{EM}(np) = V_{C,1\gamma}(np) + V_{MM}(np). \tag{2.36}$$

The OPEP contribution in the second term of Eq. 2.33 also has a dependency on the type of nucleons in the interaction. For pp and nn interactions,

$$V^{\pi}(NN) = f_{NN}^2 v_\pi(m_{\pi^0}), \text{ for } NN = pp, nn, \tag{2.37}$$

with coupling constants f_{pp} and f_{nn}. With the benefit of simplicity, analysis of low energy ($< 350MeV$) NN scattering data has determined the coupling constants to be close enough to assume $f_{pp} = -f_{nn}$.

In the np system (such as the deuteron again),

$$\begin{aligned} V^{\pi}(np) &= f_{pp} f_{nn} v_\pi(m_{\pi^0}) + (-1)^{T+1} 2 f_c^2 v_\pi(m_{\pi^\pm}) \\ &= -f^2 v_\pi(m_{\pi^0}) + (-1)^{T+1} 2 f^2 v_\pi(m_{\pi^\pm}) \end{aligned} \tag{2.38}$$

for isospin T. Once again, experimental scattering data has demonstrated that the coupling constants in Eq. 2.38 can be chosen as $f_{pp} = -f_{nn} = f_c = f$. This form of V^π becomes familiar as a OPEP when substituting v_π as,

$$\begin{aligned} v_\pi(m_x) = \left(\frac{m_x}{m_{\pi^\pm}}\right)^2 \frac{m_x c^2}{3} \Big[&(\vec{\sigma}_1 \cdot \vec{\sigma}_2) Y(\mu r) \left(1 - e^{-cr^2}\right) \\ &+ S_{12} T(\mu r) \left(1 - e^{-cr^2}\right)^2 \Big], \text{ for } x = \pi^0, \pi^\pm \end{aligned} \tag{2.39}$$

into Eq. 2.38.

Both the spin-spin central force and the tensor force in Eq. 2.39 have additional exponential cutoffs dependent on a parameter, c, that is extracted from fitting of experimental data. Interestingly, the cutoff on the tensor term, $\left(1 - e^{-cr^2}\right)^2$, can be physically interpreted as the exchange of a ρ meson, as described in [35].

The final term in the Av_{18} Potential is the phenomenological term V^R, which describes the intermediate and short range behavior of the NN potential. It uses phenomenology to construct the contributions to the nuclear force and includes terms for central (c), angular momentum ($l2$), tensor(t), spin-orbit(ls), and quadratic spin-

orbit ($ls2$) forces.

$$V^R(NN) = v_c(r) + v_{l2}(r)L^2 + v_t(r)S_{12} + v_{ls}(r)\vec{L}\cdot\vec{S} + v_{ls2}(r)(\vec{L}\cdot\vec{S})^2 \tag{2.40}$$

Each of these contributions incorporates a factor that greatly increases in magnitude as $r \to 0$, generating a highly repulsive "hard core" of the potential. The range and strength of this core are driven by fit parameters that can be adjusted with fits to NN scattering data.

The Av_{18} Potential is also projected into operator format, with 18 operators (hence the name), which incorporate the types of force contributions to the nuclear force.

$$V^R(NN) = \sum_{i=1}^{n=18} V^i O_i \tag{2.41}$$

The first 14 operators are the original charge independent terms of the Argonne potential. The final four terms incorporate the charge symmetry breaking and charge independence breaking of the nuclear force due to the different nucleon masses. These charge dependent terms include the isotensor (T_{12}) and spin tensor (S_{12}) operators.

The Argonne v_{18} Potential offers another method of modeling the nuclear force between nucleons. The potential is built up through a phenomenological approach, describing and modeling the types of force contributions, rather than deriving them all through meson exchange. Through the standard fitting comparisons to NN scattering data, the Argonne group found the model to fit *pp* scattering data below 350 MeV with a χ^2/datum = 1.10 and *np* scattering data with a χ^2/datum = 1.06, demonstrating another potential with reasonable agreement to experimental data. Once again, the authors succinctly express their confidence in the success of their approach with a familiar "the Argonne v_{18} potential has a promising future for use in microscopic nuclear many-body theory".

2.4 Chiral Effective Field Theory

With the advent of QCD in the 1970s, the meson exchange and phenomenological approaches to nuclear forces were relegated to "models" rather than true theories. QCD became widely accepted as the most fundamental description of the nuclear force, treating strong interactions in terms of the dynamics of quarks and gluons.

However, as outlined in Section 2.1, the nonperturbative nature of QCD at low energies still prevented its use in calculations of low energy nucleon interactions. Theorists set out to find a means for applying QCD in this regime, perhaps in a way that could reconcile it with the decades of work that had been performed to model the nuclear force.

A breakthrough arrived in the early 1990s, in a series of works published by Steven Weinberg [36, 37], in which he applied an effective field theory formulism to low-energy QCD. This section outlines the use of effective field theory (EFT) in nucleon-nucleon interactions, with information compiled from Refs. [21, 38–40]. These sources provide more detailed reviews of the mathematics and historical context of EFTs in QCD.

An effective field theory (EFT) provides a model for describing a physical phenomenon on a dimensional scale[5] that may not be sensitive to the more fundamental degrees of freedom of the underlying theory. In doing so, the EFT must maintain consistency with the foundational principles of the underlying theory. In an EFT designed to handle low-energy QCD, the interactions between nucleons would not be sensitive to the constituent quarks and gluons of each nucleon, and must instead be treated in terms of hadronic degrees of freedom (nucleons and mesons). This must be done while respecting the properties and symmetries of QCD.

Weinberg [36] identified the important symmetry for low-energy QCD as *chiral symmetry*. Chirality, or "handedness", describes the alignment of a particle's spin and momentum. A right-handed particle has parallel spin and momentum, while a left-handed particle has antiparallel spin and momentum. Chiral symmetry is an approximate symmetry of QCD, emerging when the quarks of the QCD Lagrangian are treated as massless. This approximation can be made in low energy nucleon interactions where the hadrons involved are much more massive than the quarks. In this case, the QCD Lagrangian is invariant under transformations of the right- and left-handed quarks, thus, the chiral symmetry.

The dynamics of an effective field theory emerge when the underlying symmetries of the theory are broken. In chiral EFT, two types of symmetry breaking contribute to the emergence of the strong interaction between nucleons.

Explicit symmetry breaking is when a symmetry is broken by the underlying Lagrangian of the theory. In chiral EFT, chiral symmetry emerges as a consequence of treating the quarks as massless. In the actual QCD Lagrangian, the quarks do have

[5] such as energy or length

a finite mass, albeit much smaller than the mass of the nucleons and mesons that are normally handled in low-energy QCD. Thus, the quark masses explicitly break chiral symmetry.

Spontaneous symmetry breaking occurs if the symmetry is broken in the ground state of the system. Spontaneous breaking of chiral symmetry is evidenced by the array of mesons of light-quark mesons. Chiral symmetry would imply the pairing of hadrons into "parity doublets", with equivalent quantum numbers except for opposite parity. However, the mass splittings between mesons of opposite parity indicate the broken symmetry.

From spontaneous symmetry breaking, a massless Goldstone boson emerges from the ground state of a system, generating a psuedoscalar field that couples to the ground and excited states. In low-energy QCD, these states represent a vacuum state and the fermion fields (hadrons) that can occupy it. The Goldstone boson in this case is the pion, which can now mediate an interaction between other hadrons, such as the nucleons. In this way, chiral effective field theory remarkably recovers meson exchange in nucleon interactions, all while maintaining consistency with QCD.

It should be noted that the pion is not actually a massless particle, having a mass of 135.0 MeV for the π^0 and 139.6 MeV for the $\pi^{\pm}$. The finite mass of the pion is due to the explicit symmetry breaking of chiral symmetry with the introduction of the quark masses in the QCD Lagrangian. Because of this, the pion is considered a pseudo-Goldstone boson, existing as a uniquely light particle (when compared to other hadrons[6]) that mediates low-energy hadronic interactions.

2.4.1 Chiral Perturbation Theory

In chiral EFT, nucleon interactions can be treated perturbatively, and are done so using *chiral perturbation theory* (ChPT). ChPT provides the framework to perform calculations using an effective Lagrangian for low-energy QCD through a low-momentum expansion.

Generating a low-momentum expansion requires defining what constitutes "low-momentum". This is done by defining the "hard scale", Λ_χ, the resolution scale with which the interaction is compared. Often in ChPT, a value of $\Lambda_\chi \sim 1$ GeV is chosen, being much larger than the typical momenta of particles in nonperturbative QCD.

[6]The next lightest particle is the kaon with a mass of 493.7 MeV ($K^{\pm}$), over three times the mass of the pion!

Since most hadron masses tend to be above 1 GeV, this is generally accepted as the scale at which nonperturbative QCD begins to dominate. For external momentum of an interaction, Q, the effective Lagrangian can be expanded in powers of $\frac{Q}{\Lambda_\chi}$. With these assumptions, calculations with ChPT are carried out with the steps outlined below.

1. Determine the appropriate degrees of freedom of the resolution scale (Λ_χ) considered for the interaction (such as nucleons and pions).

2. Identify the relevant symmetries from low-energy QCD and determine if and how they are broken.

3. Formulate the most general Lagrangian that obeys the relevant symmetries and symmetry breaking.

4. Organize contributions based on their importance, determined through a low-momentum expansion.

5. Using the low-momentum expansion, calculate the relevant Feynman diagrams to a desired accuracy.

As with other particle interactions, the force between two nucleons is calculated with a series of Feynman diagrams, each one representing a possible contribution to the interaction. Each diagram contributes some order of $\frac{Q}{\Lambda_\chi}$ with power ν resulting in a hierarchy of contributions depending on ν. This provides a way to organize the most important contributions based on their order, illustrated by the hierarchy of diagrams in Figure 2.2.

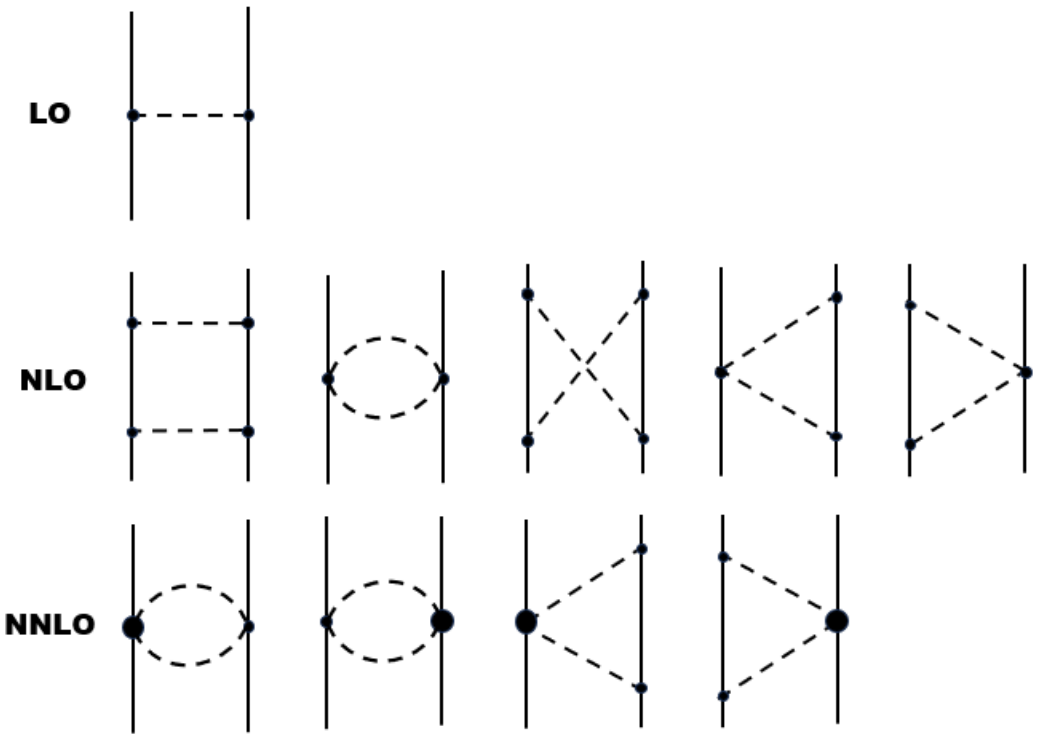

Figure 2.2: Hierarchy of Feynman Diagrams for Calculating Internucleon Forces. Sample collection of Feynman diagrams, organized by the order of their contribution to nucleon interactions. Solid lines represent nucleon propagators, dashed lines represent virtual pions, and small and large circles represent different types of interaction vertices. Leading Order (LO) terms, such as single pion exchange, contain no momentum dependence, $\left(\frac{Q}{\Lambda_\chi}\right)^0$. Next-to-Leading Order (NLO) terms invoke two-pion-exchange and introduce momentum dependence as $\left(\frac{Q}{\Lambda_\chi}\right)^2$. The order of the momentum dependence increments with each additional set of contributing terms.

Calculations with the Feynman diagrams can be performed to a desired precision by incorporating higher order contributions. The application of the most general effective Lagrangian to do so provides a model-independent method for performing calculations in low-energy QCD, removing possible uncertainties introduced by phenomenological methods. In doing so, ChPT has become a rather powerful tool for calculating observables in two-nucleon systems.

2.5 Deuteron Photodisintegration

With a variety of theories available to model the interaction between nucleons, each are thoroughly tested against experimental measurements As mentioned throughout Section 2.2, nuclear potential models are tested against experimental NN scattering data to determine their validity. The benchmark is often the ability to produce calculations in line with the plethora of pp and np scattering data available. These models can also be used to make predictions of the bound state of the deuteron. After calculations of the properties of the deuteron, further checks need to dig a little deeper for more robust tests of different models.

An electromagnetic probe offers a clean method for investigating the NN interaction within the deuteron. Analysis of the NN interactions is more straightforward if no additional nuclear forces are injected into the system. Photodisintegration of the deuteron provides a versatile means of measuring nuclear interactions.

2.5.1 Kinematics of $d(\gamma, n)p$

To provide a treatment of the kinematics of $d(\gamma, n)p$ relevant to the measurement of this work, a few assumptions are made:

1. A photon of energy E_γ traveling along the z-axis is incident on a deuterium nucleus of mass m_d at rest in the laboratory frame (S frame).

2. The center-of-momentum (CoM) frame (or S' frame) is considered the inertial reference frame in which $\vec{p}_\gamma = -\vec{p}_d$.

3. Natural units are used such that $c = \hbar = 1$. A consequence of these units is matching of the dimensions of mass, energy, and momentum: $[m] = [E] = [p]$. Factors of c (or c^2) will not appear in the derivations that follow since they are set to unity.

The four-momenta of the reaction are expressed as:

$$p_\gamma = \begin{pmatrix} E_\gamma \\ \vec{p}_\gamma \end{pmatrix} = \begin{pmatrix} E_\gamma \\ 0 \\ 0 \\ E_\gamma \end{pmatrix} \qquad p_d = \begin{pmatrix} E_d \\ \vec{p}_d \end{pmatrix} = \begin{pmatrix} m_d \\ 0 \\ 0 \\ 0 \end{pmatrix}$$
$$p_p = \begin{pmatrix} E_p \\ \vec{p}_p \end{pmatrix} = \begin{pmatrix} \sqrt{m_p^2 + p_p^2} \\ \vec{p}_p \end{pmatrix} \qquad p_n = \begin{pmatrix} E_n \\ \vec{p}_n \end{pmatrix} = \begin{pmatrix} \sqrt{m_n^2 + p_n^2} \\ \vec{p}_n \end{pmatrix} \tag{2.42}$$

The final state kinematics are calculated by transforming the system from the lab frame into the center-of-momentum (CoM) frame. To do so, the relative velocity between the two reference frames is calculated as,

$$\beta = \frac{|\vec{p}_{Lab}|}{E_{Lab}} = \frac{E_\gamma}{E_\gamma + m_d}, \tag{2.43}$$

which also provides the Lorentz factor,

$$\gamma = \frac{1}{\sqrt{1-\beta^2}}. \tag{2.44}$$

With these relativistic quantities, the four momenta of the initial particles are Lorentz boosted into the CoM frame:

$$p'_\gamma = \begin{pmatrix} E'_\gamma \\ \vec{p'}_\gamma \end{pmatrix} = \begin{pmatrix} \gamma E_\gamma(1-\beta) \\ 0 \\ 0 \\ \gamma E_\gamma(1-\beta) \end{pmatrix} \qquad p'_d = \begin{pmatrix} E'_d \\ \vec{p'}_d \end{pmatrix} = \begin{pmatrix} \gamma m_d \\ 0 \\ 0 \\ -\gamma\beta m_d \end{pmatrix} \tag{2.45}$$

The momenta of the outgoing particles are calculated in the CoM frame using conservation laws. Conversation of Momentum implies

$$\vec{p'}_\gamma + \vec{p'}_d = \vec{p'}_p + \vec{p'}_n = 0 \rightarrow \vec{p'}_n = -\vec{p'}_p \rightarrow |\vec{p'}_n| = |\vec{p'}_p|, \tag{2.46}$$

and Conservation of Energy gives

$$E'_p + E'_n = E' = E'_\gamma + E'_d = \gamma E_\gamma(1-\beta) + \gamma m_d \tag{2.47}$$

Simplifying this in terms of the initial state parameters provides

$$E'_p + E'_n = E' = \sqrt{m_d^2 + 2m_d E_\gamma}. \tag{2.48}$$

The final momentum of the neutron can then be calculated:

$$\begin{aligned} E'_n = E' - E'_p &\implies (E'_n)^2 = (E' - E'_p)^2 \\ &\implies m_n^2 + (p'_n)^2 = E'^2 - 2E'E'_p + m_p^2 + (p'_p)^2 \\ &\implies m_n^2 = m_d^2 + 2m_d E_\gamma - 2E'\sqrt{m_p^2 + (p'_p)^2} + m_p^2 \\ &\implies |\vec{p'}_n| = |\vec{p'}_p| = \sqrt{\frac{(m_d^2 + 2m_d E_\gamma + m_p^2 - m_n^2)^2}{4m_d^2 + 8m_d E_\gamma} - m_p^2}. \end{aligned} \tag{2.49}$$

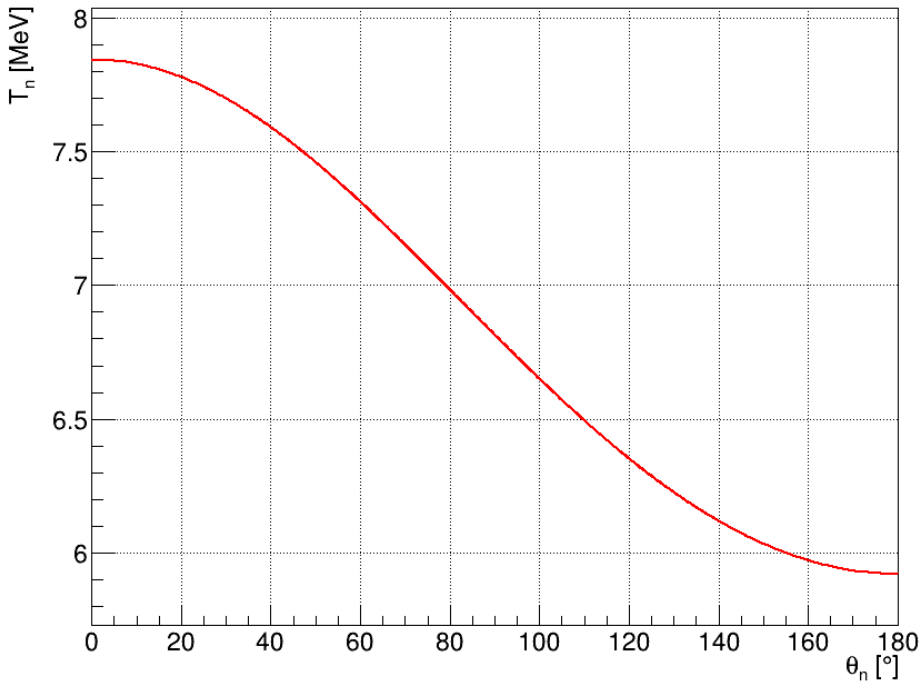

Figure 2.3: Kinetic Energy of Photoneutron as a Function of Lab Reaction Angle. Illustrated is the dependence of the neutron kinetic energy in $d(\gamma, n)p$ as a function of the neutron's ejection angle in the laboratory frame for a 16 MeV incident photon. The angle of the neutron's momentum is with respect to the incident photon momentum. The neutron's kinetic energy decreases for increasing reaction angle.

2.5.2 Polarization Observables in Deuteron Photodisintegration

Arenhövel [11] offers a thorough treatment of calculating observables in $d(\gamma, n)p$. To provide an overview of the material, it is prudent to outline some useful notation. The reaction is treated in the center of momentum frame, with an incoming photon momentum of $\vec{p}_\gamma$ and final state momenta of the nucleons $\vec{p}_n = -\vec{p}_p = \vec{k}$. When treating polarization observables, the Madison Convention then recommends a reference frame in which $\hat{z} \parallel \vec{p}_\gamma$ and $\hat{y} \parallel (\vec{p}_\gamma \times \vec{k})$. Relevant quantities can then be defined as in Table 2.2 [11].

Variable	Definition
θ, ϕ	Spherical Coordinates of $\vec{k}$
λ	Incident Photon Polarization
m_d	Deuteron Spin Projection on $\hat{z}$
s	Total Spin of Final State
m_s	Projection of s on $\vec{k}$

Table 2.2: Notation Table for Calculating Observables in $d(\gamma, n)p$. Key variable definitions used by H. Arenhövel [11] for calculating observables in $d(\gamma, n)p$.

Arenhövel formulates the reaction matrix for $d(\gamma, n)p$,

$$T_{s,m_s,\lambda,m_d} = exp\{i(\lambda + m_d)\phi\} t_{s,m_s,\lambda,m_d}(\theta), \tag{2.50}$$

where t_{s,m_s,λ,m_d} is the t-matrix with elements $t_{fi} = \langle f|V|i\rangle$. The kinematics are treated in the center of momentum frame such that Arenhövel calculates observables, $\mathcal{O}$, in $d(\gamma, n)p$ through the reaction matrix T:

$$\mathcal{O} = tr(T^\dagger \Omega T \rho) \tag{2.51}$$

where

$$\mathcal{O} = \begin{cases} \frac{d\sigma}{d\Omega}, & \text{if } \Omega = \mathbb{1} \\ P_\alpha(j)\frac{d\sigma}{d\Omega}, & \text{if } \Omega = \sigma_\alpha(j) \end{cases} \tag{2.52}$$

Applying the Pauli matrices, σ_α and carrying out the matrix algebra, full formulas can be derived for the j-th nucleon polarization, $P_\alpha(j)$. Again using the Madison Convention, the case will be consider for the neutron polarization projected along the

axis $\hat{y} \parallel (\vec{p}_\gamma \times \vec{k})$.

$$\begin{aligned} P_y(j)\frac{d\sigma}{d\Omega} =& \frac{d\sigma_0}{d\Omega}\sum_{I=0}^{2}\Bigg[\sum_{M=0}^{I}\Bigg(P_y^{0,IM}(j,\theta)\cos(M(\phi_d-\phi)-\delta_{I1}\frac{\pi}{2}) \\ &+ P_c^\gamma P_y^{c,IM}(j,\theta)\sin(M(\phi_d-\phi)+\delta_{I1}\frac{\pi}{2})\Bigg)d^I_{M0}(\theta_d) \\ &+ P_l^\gamma \sum_{M=-I}^{I} P_y^{l,IM}(j,\theta)\cos(-\delta_{I1}\frac{\pi}{2})d^I_{M0}(\theta_d)\Bigg] \end{aligned} \tag{2.53}$$

For an unpolarized deuteron target, I = 0, and therefore, M = 0, simplifying the summations.

$$\begin{aligned} P_y(j)\frac{d\sigma}{d\Omega} =& \frac{d\sigma_0}{d\Omega}\Bigg[\Bigg(P_y^{0,00}(j,\theta)\cos((0)(\phi_d-\phi)-\delta_{01}\frac{\pi}{2}) \\ &+ P_c^\gamma P_y^{c,00}(j,\theta)\sin((0)(\phi_d-\phi)+\delta_{01}\frac{\pi}{2})\Bigg)d^0_{00}(\theta_d) \\ &+ P_l^\gamma P_y^{l,00}(j,\theta)\cos(-\delta_{01}\frac{\pi}{2})d^0_{00}(\theta_d)\Bigg] \end{aligned} \tag{2.54}$$

Evaluating the factors $\delta_{01} = 0$, $\cos(0) = 1$ and $\sin(0) = 0$ yields:

$$P_y(j)\frac{d\sigma}{d\Omega} = \frac{d\sigma_0}{d\Omega}\Bigg[P_y^{0,00}(j,\theta)d^0_{00}(\theta_d) + P_l^\gamma P_y^{l,00}(j,\theta)\cos(2\phi)d^0_{00}(\theta_d)\Bigg] \tag{2.55}$$

Finally, recognizing the d-functions $d^K_{M0}(\theta)$ of the rotation matrices being related to the associated Legendre polynomials,

$$\begin{aligned} d^K_{M0}(\theta) &= \sqrt{\frac{(K-M)!}{(K+M)!}}P_K^M(\cos\theta) \\ \Longrightarrow d^0_{00}(\theta) &= \sqrt{\frac{0!}{0!}}P_0^0(\cos\theta) = 1 \end{aligned} \tag{2.56}$$

Reducing the equation to its final form of

$$P_y(j)\frac{d\sigma}{d\Omega} = \frac{d\sigma}{d\Omega}\Bigg[P_y^0(j,\theta) + P_l^\gamma P_y^l(j,\theta)\cos(2\phi)\Bigg] \tag{2.57}$$

Observing this quantity for the neutron ($j = n$):

$$P_y(n)\frac{d\sigma(\theta_n,\phi_n)}{d\Omega} = \frac{d\sigma(\theta_n)}{d\Omega}\bigg|_{P_y^\gamma=0}\left[P_y^0(\theta_n) + P_y^\gamma P_y^l(\theta_n)cos(2\phi_n)\right] \tag{2.58}$$

Evidently, the measured polarization of a recoil neutron is dependent on contributions due to unpolarized photons (P_y^0) and linearly polarized photons (P_y^l). Following through the derivation above, it can be seen that these coefficients emerge from calculations with the t-matrix, and therefore, the nuclear potential used to construct the t-matrix.

2.5.3 Additional Techniques in Photodisintegration Calculations

With a collection of formulae available for calculating observables in deuteron photodisintegration, calculations are performed using the theories and models discussed earlier in this chapter as a foundation. Additional considerations and techniques are applied in different combinations to try to best capture the physical phenomena that contribute to the reaction.

Impulse Approximation

In classical scattering theory, the *impulse approximation* (IA) treats the effect on a particle scattered in a field as an instantaneous occurrence. It assumes the particle continues along its original trajectory and calculates the transverse momentum transfer to the particle as an impulse by integrating the transverse projection of the force over time. The change in the particle's trajectory is then calculated using the impulse.

A similar treatment can be applied to calculations of the NN interaction in deuteron photodisintegration. The interaction time of the photon with one of the bound nucleons is short enough with respect to the period of the deuteron wave function that the interaction can be approximated as instantaneous. The impulse approximation offers advantages in the spatial treatment of the interaction as well. The deuteron is considered loosely bound with a diffuse structure, enough that scattering waves from each nucleon can be approximated to not affect each other. The scattered wave would still be treated as a combination of the final state wave functions from

each nucleon, but the interaction with each nucleon can be treated individually. Essentially, in this approximation, each bound nucleon in the deuteron can be treated as a free particle.

Meson Exchange Currents

Despite the virtuality of meson exchange between nucleons, the mediator still plays a role in the NN system as it pertains to external interactions. As a charged particle (or a neutral particle with a charge distribution), the exchanged meson affects electromagnetic interactions with the nucleons. In photodisintegration of the deuteron, there is a possibility for the incident photon to interact with the virtual meson. Feynman diagrams representative of the interaction are shown in Figure 2.4. This phenomenon is known as a *meson exchange current*, and must be considered as a contribution in calculations of deuteron photodisintegration.

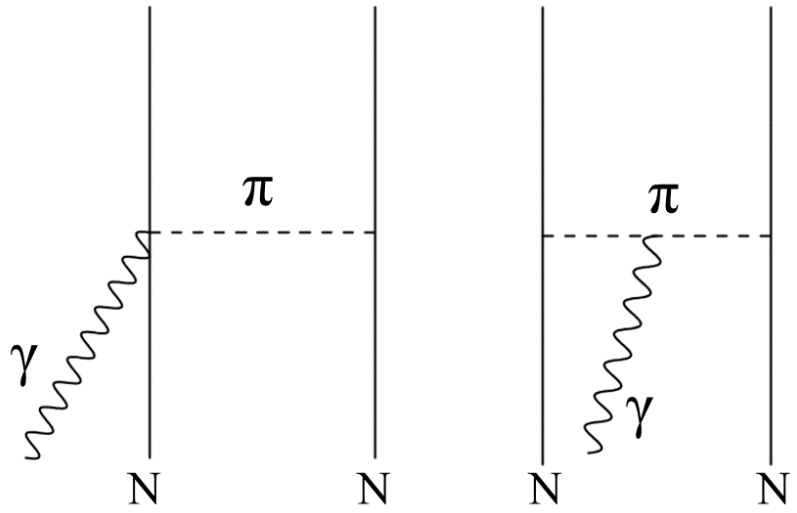

Figure 2.4: Feynman Diagrams for Meson Exchange Currents. An incident photon can interact with the virtual meson exchanged between two nucleons. This effect, known as a meson exchange current, contributes to the calculations of deuteron photodisintegration. The Feynman diagrams illustrated here demonstrate this effect acting on the virtual pion exchanged between two nucleons.

Isobar Configurations

Another phenomenon that contributes in NN interactions is the excitation of the nucleons to resonant states. The exchange of mesons opens up the possibility of

exciting the nucleons to virtual isobars. An *isobar* is a heavier spin-excitation of a nucleon, which is part of a larger group of resonant states known as Δ baryons.

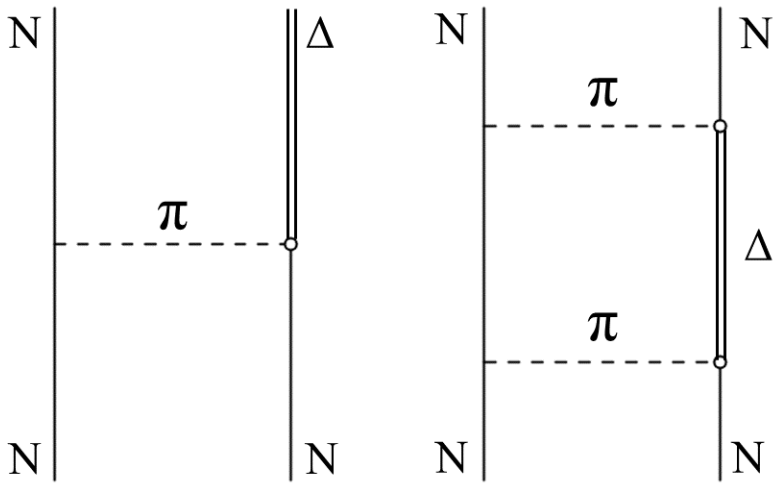

Figure 2.5: Feynman Diagrams for Isobar Configurations. Interactions between nucleons can excite one or both of the nucleons into resonant states known as *isobars*, impacting the dynamics of the interaction. The isobars for the nucleons are the Δ baryons identified in Table 2.3.

The relevant Δ baryons are the Δ^+ and Δ^0 whose properties are listed in Table 2.3. The new intrinsic properties of the interacting baryons will modify the contributing

Baryon	Mass (MeV)	I_3	J^P	Ground State
p	938.27	$\frac{1}{2}$	$\frac{1}{2}^+$	-
n	939.57	$-\frac{1}{2}$	$\frac{1}{2}^-$	-
Δ^+	1232	$\frac{1}{2}$	$\frac{3}{2}^+$	p
Δ^0	1232	$-\frac{1}{2}$	$\frac{3}{2}^+$	n

Table 2.3: Properties of the Δ Baryons, Isobars of the Nucleons[28]. The Δ baryons are excited states of the nucleons that can play a role in the NN interaction. Notably these baryons have higher mass and spin than the ground state nucleons. The difference in quantum numbers between nucleons and their isobars contribute to their effects on the nucleon interaction.

forces in the NN potentials. Considering the example of a Δ excitation in one pion exchange, the Lagrangian of Eq. 2.13 is modified to a Lagrangian with the pion

coupling to a N-Δ transition. [42]

$$\mathcal{L}_{\pi}^{\Delta} = g_{\pi}^{\Delta} \bar{\psi}^{N} \vec{T} \psi^{\Delta} \cdot \vec{\pi} \tag{2.59}$$

Here, $\vec{T}$ is the isospin transition operator acting between N and Δ. A spin transition operator $\vec{S}$ is also introduced generating a new tensor operator $S_{12}^{N\Delta} = 3(\vec{\sigma}_1 \cdot \hat{r})(\vec{S}_2 \cdot \hat{r}) - \vec{\sigma}_1 \cdot \vec{S}_2$. The OPEP then becomes the transition potential as shown in Eq. 2.60.

$$V_{\pi}(NN \leftrightarrow N\Delta) = \frac{g_{\pi} g_{\pi}^{\Delta}}{12} m_{\pi} (\vec{\tau}_1 \cdot \vec{T}_2) \left[\left(\vec{\sigma}_1 \cdot \vec{S}_2 \right) \frac{e^{-m_{\pi} r}}{m_{\pi} r} + S_{12}^{N\Delta} \left(1 + \frac{3}{m_{\pi} r} + \frac{3}{m_{\pi} r} \right) \frac{e^{-m_{\pi} r}}{m_{\pi} r} \right] \tag{2.60}$$

It is then evident that the transition operators and the $\pi - \Delta$ coupling g_{π}^{Δ} contribute to the nucleon potential, motivating the inclusion of corrections due to isobar configurations.

Relativistic Effects

Early nuclear theories were developed using non-relativistic techniques as the energy scale associated with studying nucleon-nucleon interactions did not prompt the inclusion of relativistic effects. Later studies demonstrated that relativistic corrections must be included to reproduce measurements of the nuclear force. Arenhövel [11] outlines the three main types of relativistic effects that play a role in NN interactions as:

1. Relativistic effects in the internal dynamics of an interacting system, i.e. a system's wave function in its rest frame
2. Lorentz boosts of these systems into a moving frame, affecting the spin parameters and internal structure of the system
3. Relativistic treatment of the current operators in electromagnetic interactions within the nucleon potential

In particular, Arenhövel details how these types of corrections are applied to formulations of deuteron photodisintegration. Even for photon energies down to about 20 MeV, relativistic effects must be accounted for in the NN potential.

2.6 Spin Polarization in Nuclear Reactions

This section outlines the mathematical formulation for polarization observables in nuclear reactions. This overview was developed from information provided by Refs. [43, 44].

2.6.1 Spin Polarization

The polarization of an ensemble of particles describes the average spin state over all the particles. For a spin-$\frac{1}{2}$ particle, the polarization is represented by a vector, $\vec{P}$, the direction of which points along an axis defined by the spin states of the particles. "Spin-up" particles are polarized pointing in the direction of $\vec{P}$, while "spin-down" particles are polarized in the opposite direction. The magnitude of the polarization, P, is then equal to the normalized difference in the quantities of spin-up vs. spin-down particles:

$$P = \frac{N_+ - N_-}{N_+ + N_-}. \tag{2.61}$$

This can also be represented as the expectation value of the spin, $\vec{S}$, such that

$$\vec{P} = \left\langle \vec{S} \right\rangle = \frac{1}{2}\langle \vec{\sigma} \rangle \tag{2.62}$$

for the Pauli spin operator, $\vec{\sigma}$, with components,

$$\sigma_x = \begin{pmatrix} 0 & 1 \\ 1 & 0 \end{pmatrix}, \qquad \sigma_y = \begin{pmatrix} 0 & -i \\ i & 0 \end{pmatrix}, \qquad \sigma_z = \begin{pmatrix} 1 & 0 \\ 0 & -1 \end{pmatrix}. \tag{2.63}$$

For a spin-1 particle, the polarization is described in terms of a vector polarization and a tensor polarization due to the incorporation of a second rank tensor. The Cartesian spin tensor moments are

$$P_{ij} = \frac{3}{2}\Big\langle S_i S_j + S_j S_i \Big\rangle - 2\delta_{ij} \text{ for } i, j = x, y, z. \tag{2.64}$$

The polarization can also be expressed in terms of the spherical spin tensor moments, τ_q^k, where, for a particle with spin s, $0 \leq k \leq 2s$ and $-k \leq q \leq k$. The

polarization is then calculated as

$$t_{kq} = \langle \tau_q^k \rangle. \tag{2.65}$$

The spherical tensor moments are related to the Cartesian moments as

$$\tau_0^0 = 1 \qquad \tau_0^2 = \frac{\sqrt{3}}{2} S_z \tag{2.66}$$

$$\tau_0^1 = \sqrt{\frac{3}{2}} S_z \qquad \tau_{\pm 1}^2 = \mp \frac{\sqrt{3}}{2} \Big[\Big(S_x + i S_y \Big) S_z \pm S_z \Big(S_x + i S_y \Big) \Big] \tag{2.67}$$

$$\tau_{\pm 1}^1 = \mp \frac{\sqrt{3}}{2} \Big(S_x \pm i S_y \Big) \qquad \tau_{\pm 2}^2 = \frac{\sqrt{(3)}}{2} \Big(S_x \pm i S_y \Big)^2 \tag{2.68}$$

Calculating the polarization uses the spin density matrix ρ, where for a set of spin states ψ_j each with probability p_j,

$$\rho = \sum_j p_j |\psi_j\rangle\langle\psi_j|. \tag{2.69}$$

Then the expectation value of the spin tensor moment is calculated as

$$\langle \tau_q^k \rangle = Tr\Big(\rho \tau_q^k \Big) = t_{kq}, \tag{2.70}$$

providing the polarization. If ρ is not normalized, then a normalization constant is included:

$$t_{kq} = \frac{1}{Tr(\rho)} Tr\Big(\rho \tau_q^k \Big) \tag{2.71}$$

2.6.2 Polarization in Nuclear Reactions

For a nuclear reaction $a(b,c)d$, the spin density matrix ρ of the system transitions with the T-matrix as

$$\rho_{cd} = T \rho_{ab} T^\dagger. \tag{2.72}$$

The differential cross section of the reaction is then found from the trace of the final state density matrix,

$$\frac{d\sigma}{d\Omega} = \frac{\mu_{ab}\mu_{cd}}{(2\pi)^2} \frac{k_f}{k_i} Tr(\rho_{cd}) = \frac{\mu_{ab}\mu_{cd}}{(2\pi)^2} \frac{k_f}{k_i} Tr\Big(T \rho_{ab} T^\dagger \Big), \tag{2.73}$$

where μ_{ab},μ_{cd} are the reduced masses of the initial and final states. The polarization of the ejectile, c, is also calculable as in Eq. 2.71:

$$t_{k_c q_c} = \frac{1}{Tr(\rho_{cd})} Tr\left(\rho_{cd} \tau_{q_c}^{k_c}\right) \tag{2.74}$$

In the case of an unpolarized projectile (with spin s_b) incident on an unpolarized target (with spin s_a), the spin density matrix is then a constant equal to

$$\rho_{ab} = \frac{1}{(2s_a+1)(2s_b+1)}. \tag{2.75}$$

So, by Eq. 2.72, the final state spin density is

$$\rho_{cd} = \frac{1}{(2s_a+1)(2s_b+1)} TT^\dagger \tag{2.76}$$

The differential cross section in this case is

$$\left.\frac{d\sigma}{d\Omega}\right|_0 = \frac{\mu_{ab}\mu_{cd}}{(2\pi)^2}\frac{k_f}{k_i}\frac{1}{(2s_a+1)(2s_b+1)} Tr\left(TT^\dagger\right), \tag{2.77}$$

and the polarization of the emitted particle is then

$$t_{k_c q_c} = \frac{1}{Tr\left(TT^\dagger\right)} Tr\left(TT^\dagger \tau_{q_c}^{k_c}\right) \tag{2.78}$$

For a polarized projectile on an unpolarized target, the initial state density matrix is

$$\rho_{ab} = \frac{1}{(2s_a+1)}\frac{1}{(2s_b+1)} \sum_{k_b q_b} (-1)^{q_b} t_{k_b q_b} \tau_{-q_b}^{k_b}. \tag{2.79}$$

This gives a cross section of

$$\frac{d\sigma}{d\Omega} = \frac{\mu_{ab}\mu_{cd}}{(2\pi)^2}\frac{k_f}{k_i}\frac{1}{(2s_a+1)(2s_b+1)} Tr\left(T \sum_{k_b q_b} (-1)^{q_b} t_{k_b,-q_b} \tau_{q_b}^{k_b} T^\dagger\right). \tag{2.80}$$

This simplifies by introducing the analyzing power, T_{kq}, a quantity that indicates the asymmetry in a reaction due to the spins of the particles. The analyzing power is equivalent to

$$T_{kq} = \frac{1}{Tr\left(TT^\dagger\right)} Tr\left(T \tau_{q_c}^{k_c} T^\dagger\right), \tag{2.81}$$

or, in Cartesian notation,

$$A_i = \frac{1}{Tr\left(TT^\dagger\right)} Tr\left(TS_iT^\dagger\right) \tag{2.82}$$

$$A_{ij} = \frac{1}{Tr\left(TT^\dagger\right)} Tr\left(TS_{ij}T^\dagger\right) \tag{2.83}$$

The similarity between the analyzing power formula and Eq. 2.78 should be noted, indicating a close relationship between the analyzing power, T_{kq}, of a reaction and the polarization, t'_{kq}, of the emitted particle in the inverse reaction. Time reversal invariance results in

$$T_{kq} = (-1)^{k+q} t'_{kq}. \tag{2.84}$$

Substituting the analyzing power into Eq. 2.80 relates the cross section in the polarized case to the unpolarized cross section as

$$\frac{d\sigma}{d\Omega} = \frac{d\sigma}{d\Omega}\bigg|_0 \left[1 + \sum_{k\neq 0} \sum_q (-1)^q t_{k,-q} T_{kq}\right] \tag{2.85}$$

A spin-$\frac{1}{2}$ projectile only the vector polarization is nonzero. The summation in Eq. 2.85 in this case is often expressed in Cartesian notation, in which it is expressed as a vector dot product:

$$\begin{aligned} \frac{d\sigma}{d\Omega}(\theta,\phi) &= \frac{d\sigma}{d\Omega}\bigg|_0 \left[1 + \vec{P}\cdot\vec{A}\right] \\ &= \frac{d\sigma}{d\Omega}\bigg|_0 \left[1 + P_y A_y cos(\phi)\right] \end{aligned} \tag{2.86}$$

where ϕ is the azimuthal angle between the polarization of the projectile and the normal vector to the reaction plane. This factor dependent on the analyzing power quantifies the asymmetry in the reaction discussed earlier. It manifests as a left-right asymmetry in the reaction; a measurbale quantity that provides insight into the polarization states of particles in the reaction.

Chapter 3

Monte Carlo Simulation

A Monte Carlo simulation of the experimental setup was developed to assist in preparation of the experiment and to complement analysis. The simulation was instrumental in understanding how to extract the desired measurement from the collected data. This chapter outlines the tools and techniques used to develop this simulation with the goal of providing realistic and precise modeling of the experiment.

3.1 Monte Carlo Methods

Monte Carlo simulation is a common technique for statistical analysis of a variety of physics processes. It is a powerful tool in nuclear and particle physics where particle interactions are often defined by cross sections and stochastic processes. This section offers insight into the Monte Carlo techniques used in the simulation developed for this experiment, with information compiled from Refs. [28, 45, 46].

Monte Carlo methods utilize random sampling to obtain a numerical result when the outcome of a process cannot be analytically determined. With some defined probability distribution function (PDF) describing the behavior of a physical system, an *event* can be randomly generated to sample one possible final state of the system. Repeating this for a large number of events allows for an effective estimation of the distribution function. Each generated event will have a set of deterministic parameters, and the collection of events can be aggregated to produce a numerical result with some corresponding statistical uncertainty. The uncertainty in the result can be reduced by increasing the number of sampled events. A number of Monte Carlo techniques exist that follow this general procedure to model different types of distribution functions.

Acceptance-rejection sampling is a Monte Carlo method used to sample from a

PDF that is too complex to work with analytically. To perform rejection sampling of a function $f(x)$, a simpler proposal function, $g(x)$ is defined such that $f(x) < cg(x)$, with a known constant c, for all x. The procedure for rejection sampling is as follows:

1. Randomly select $x \in [x_{min}, x_{max}]$ for sampling.
2. Evaluate $cg(x)$.
3. Randomly generate y from a uniform distribution over $[0, cg(x)]$.
4. Compare y and $f(x)$. If $y > f(x)$, reject the sample and return to the first step to start over. If $y < f(x)$, keep the sample and continue to the next event.

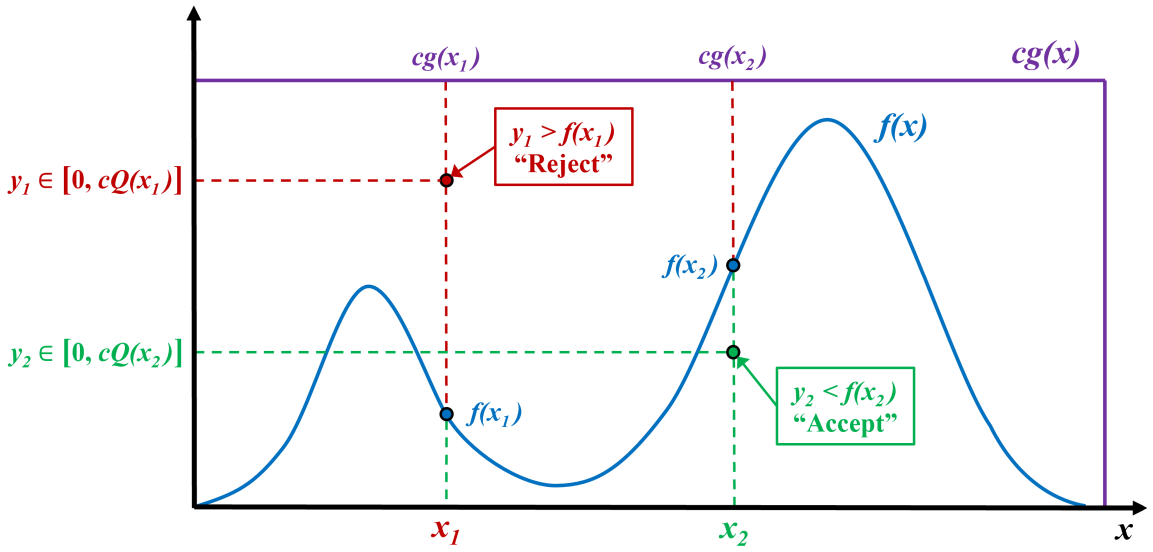

Figure 3.1: Visualization of Acceptance-Rejection Sampling. In this example, x_1 and x_2 serve as two sampled values of the PDF $f(x)$ (Blue). With some proposal function $g(x)$ scaled by c (Violet), y_1 and y_2 are then randomly selected over the range $cg(x_1)$ and $cg(x_2)$ respectively. Points above $f(x)$, such as y_1 are rejected (Red) and points below $f(x)$, such as y_2 are accepted (Green). This process is continued to obtain a collection of accepted sample values of x.

These steps are carried out until the desired number of sampling events is attained. The final collection of samples should be representative of the modeled function and provide a means for calculating quantities generated by the function.

3.2 GEANT4: A Simulation Toolkit

GEANT4[1] is a software toolkit for simulating how particles interact with matter. [47–49] It is widely used for particle detector simulation and analysis in nuclear and particle physics. This section aims to outline some of the basics of how GEANT4 works. An understanding of these introductory concepts provides insight into a user's methodology in developing a simulation and how to analyze its output.

3.2.1 Particle Tracking in GEANT4

GEANT4 handles particle transport through matter as a step-by-step process. It follows the *track* of a particle as it passes through a user-defined geometry. This track begins when a particle is created either by the user or some physics process during the simulation. GEANT4 then continues computations for this track until the particle is "destroyed"[2]. A particle track is made up of a collection of steps. A *step* is a segment of the particle's path that is bounded on both ends by either a boundary between volumes or the occurrence of a physics process. Figure 3.2 offers a visual representation of the stepping process in GEANT4.

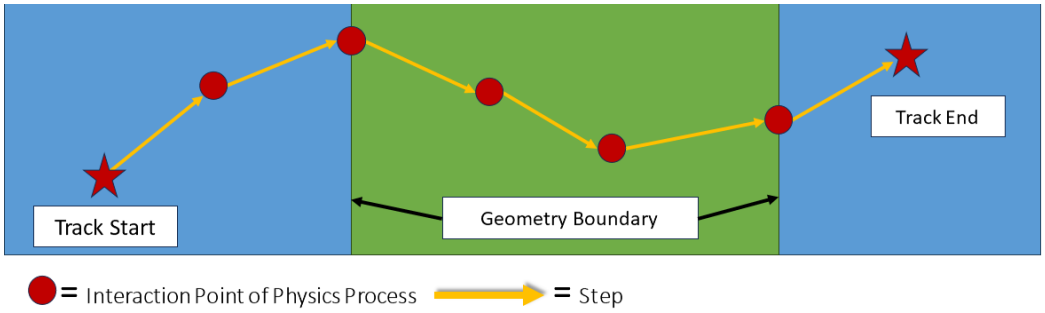

Figure 3.2: Diagram Demonstrating Tracking in GEANT4. Particle trajectories are traced out in steps which can be bounded by different occurrences: interaction points of physics process, geometric boundaries between simulated volumes, or total loss of kinetic energy of the particle. Figure reproduced from Ref. [50].

A particle track begins with the generation of a particle with definite momentum and energy at a specific location within the simulation volume. The particle is then

[1] An acronym for "GEometry ANd Tracking software, version 4".

[2] A particle track ends due to any of the following criteria: running out of kinetic energy, conversion to other particles through an interaction, exiting the world volume of the simulation, or reaching some stopping parameter defined by the user.

transported step-by-step through the volume, each step calculated as some interval in distance or time. A step can also be terminated by the crossing of a material boundary or the occurrence of a physics process. At each step, GEANT4 computes the probabilities of the possible interactions a particle can undergo and then selects an interaction (or no interaction) through a Monte Carlo method. The final state parameters of the interaction are calculated, and the next step of the particle track is initiated with these parameters. This continues until the end of the track.

Tracking particles in this way enables powerful control over the simulation and provides access to detailed information regarding the physics of particles interacting with detectors. These features make GEANT4 a valuable resource for users in nuclear and particle physics. To make the program accessible for users, it is built on a modular software framework that makes it flexible and thorough. Users can build simulations by assembling different classes defined in GEANT4. The following sections outline some of the standard modules that are included when developing a full simulation.

3.2.2 Physics Lists

In order to model the interactions of particles with matter, the possible physics processes must be defined. GEANT4 includes a series of classes that model these different processes for implementation into a simulation. As with much of the GEANT4 framework, the physics classes are modular in nature and can be pieced together into a physics list. The *physics list* is thus an object that handles all the particles and their corresponding physics interactions in a simulation.

One might wonder: *why should it be up to the user to select and implement a set of physics processes?* Why not just have GEANT4 automatically set up with a complete set of physics to define every interaction? Well, the simple answer is efficiency. Very rarely will a simulation require detailed modeling of every single physics process across all regions of phase space. Additionally, some simulations may not require high precision models of every process, and can get by with approximations that speed up computation. Therefore, the ability to select which processes to include can significantly streamline the development and performance of a simulation.

Almost any physics process a user might want to implement in a simulation is included in the standard GEANT4 software package. A "standard" set of electromagnetic processes is available, including models for ionization, bremsstrahlung, optical photon interactions, and more. This standard list covers physics for particles with

energies from a few keV up to PeV. Models are also included for low energy electromagnetic process to cover energies below the keV range all the way down to about 100 eV. Weak interactions are included as weak decays of fundamental particles and radioactive decay of nuclei. For hadronic physics, the fundamental strong interactions are modeled up to the TeV range. Electro- and gamma- nuclear physics are treated from 10 MeV to a few TeV. For energies below 20 MeV, particle transport is handled by a high precision particle model (labeled ParticleHP).

Any number of these physics classes can be assembled together into a user defined physics list. Alternatively, the GEANT4 collaboration has developed several standard physics list for convenient implementation into simulations. A fairly standard example is the QGSP_BERT_HP physics list. [51] It is a widely used physics list preferred by many groups such as the CMS and ATLAS collaborations of CERN. The name of a GEANT4 physics list identifies the models incorporated into the physics. In the case of the QGSP_BERT_HP list, "QGSP" represents the Quark-Gluon String Precompounded library used for high energy ($\sim$12 GeV to 50 TeV) interactions between hadrons and nuclei. "BERT" refers to the Bertini-type cascade model used for medium energy (200 MeV - 10 GeV) treatment of hadron-nucleus interactions in which nuclei are treated with a shell model. Finally, "HP", meaning High Precision, uses the ParticleHP model for low energy (< 20 MeV) particle transport.

Whether selecting a pre-built physics list library provided by GEANT4, or developing a custom physics list, defining the physics processes used in a simulation is important for complete understanding of its results.

3.2.3 Detector Construction

The "Geometry" of GEANT4's full moniker, "GEometry ANd Tracking", encapsulates one of the fundamental aspects of its strength in simulation capability. It provides the user complete control to design and develop the geometry of a simulation specific to their needs. As a resource tailored to simulation of nuclear and particle physics experiments, definition of the geometry is often referred to as *detector construction*. With such a wide variety of detector concepts and designs, the freedom offered by GEANT4 on this front has contributed to its pervasiveness in the field.

Detector construction in GEANT4 usually begins with definition of the materials to be used in the simulation. Materials are built up from basic elements and isotopes, all of which have properties that can be explicitly defined by a user. Alternatively,

GEANT4 maintains a database (through NIST[3]) of elements and a number of standard materials that can be implemented instead. An example of material definition implementation is provided in Figure 3.3.

```
void DetectorConstruction::DefineMaterials()
{

  //Instantiate NIST Database
  G4NistManager* nist = G4NistManager::Instance();

  //Declare material property variables
  G4int Z, N;
  G4double A, density;
  G4String name, symbol;
  G4int ncomp, natom;
  G4double abundance, fractionmass;

  // Define Isotopes
  G4Isotope* isoD = new G4Isotope(name="H2", Z=1, N=2, A=2.014*g/mole);

  // Define Elements
  G4Element* elH = nist->FindOrBuildElement("H");
  G4Element* elD = new G4Element(name="Deuterium", symbol="D", ncomp=1);
  elD->AddIsotope(isoD, abundance=100*perCent);
  G4Element* elO = nist->FindOrBuildElement("O");

  //Define Materials

  //Water
  G4Material* H2O = new G4Material(name="Water", density=1.000*g/cm3, ncomp=2);
  H2O->AddElement(elH, natom=2);
  H2O->AddElement(elO, natom=1);
  // Heavy Water (D2O)
  G4Material* D2O = new G4Material(name="HeavyWater", density=1.1115*g/cm3, ncomp=2);
  D2O->AddElement(elD, natom=2);
  D2O->AddElement(elO, natom=1);
}
```

Figure 3.3: Example of Material Definition in GEANT4. Material definitions in simulations can either be selected from the NIST materials library included with GEANT4 or constructed by a user. User-defined materials are built up from the base isotopes and elements of material, with physical properties assigned by the user.

The next step in detector construction is building the actual geometry of the simulation. This is done in three "conceptual layers": the solid, the logical volume, and the physical volume. The *solid* refers to the actual basic shapes of the simulated components. GEANT4 provides a set of classes for defining a sundry of three-dimensional shapes to build up complex geometries. Some examples of the shapes that are available in GEANT4 are illustrated in Figure 3.4

[3]National Institute of Standards and Technology

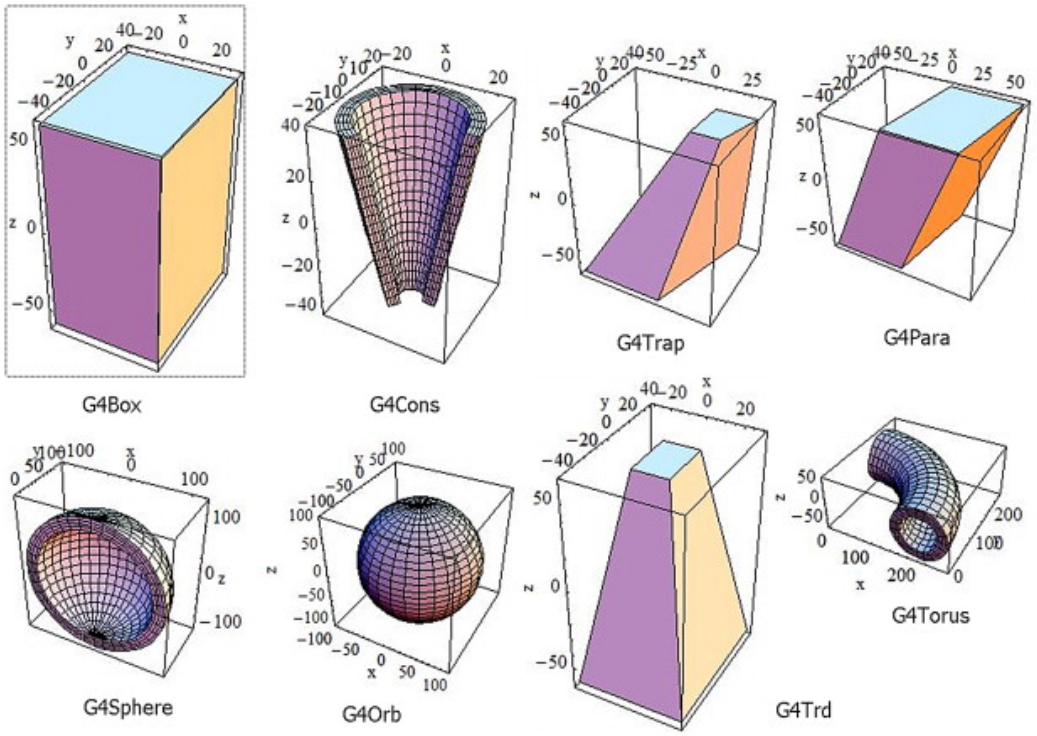

Figure 3.4: Sample Geometry Classes Available in GEANT4. A variety of foundational geometric volumes are available in the GEANT4 software package. Users can assemble combinations of these volumes to develop unique and precise detector geometries. Image Credit: J. Apostolakis *et al.* [52]

Once the solid is defined, it is implemented in the next layer, the *logical volume*. The logical volume defines the detector properties including the geometry (from the solid), the material, and the object's name. The final layer is the *physical volume* which is used to manage the spatial positioning of the detector components and their relations to each other. Through this layered framework within GEANT4, geometries of entire experimental setups can be developed and simulated.

3.2.4 Primary Generation

Simulating particle transport in GEANT4 requires an input of the initial state of the particles to be tracked. *Primary generation* (or event generation) is the modeling of the input parameters for these particles based on the processes by which the particles are initiated. These processes can range from a "simple" incident beam with defined particle type, energy, and direction to a more complex nuclear or particle reaction where the kinematics of outgoing particles can vary from event to event. With a set

of initial parameters, events in GEANT4 can be instantiated with a GEANT4 object known as a *G4ParticleGun*. The event generation can then be defined by the user as input into the *G4ParticleGun* object. A closer look at how this process works is given in Section 3.3 which outlines the event generation methods used for this experiment.

3.2.5 User Actions

A GEANT4 simulation requires different levels of management to coordinate the order of computation. At each of these levels, a user can dictate the simulation parameters and extract information relevant at that scale.

The *Run Action* of a simulation defines the parameters for an entire run of a simulation. The geometry and physics are fixed throughout an entire run. At this level, the user can also manage the data handling and storage for the output of the simulation. Each run normally consists of a large number of events.

The *Event Action* controls the operation of a simulation on an event-by-event basis. For each event, the primary generation is reset to start the simulation over from the initial reaction. At this level, the user can extract all of the final state information of the particles generated during the event.

Within each event, the user management layers continue down to smaller segments of the simulation. A user can input controls and extract information from each of the *Stacking Action*, the *Tracking Action*, and the *Stepping Action*. Each layer provides a different level of control of the simulation and different available parameters for data output.

3.3 Event Generation

As mentioned in Section 3.2.4, any GEANT4 simulation begins with generation of the primary particles. The event generation requires careful consideration of the input parameters for the simulation. For this experiment, an event generator was developed to model the photodisintegration reaction, specifically to provide the initial conditions of the outgoing neutrons. This section details the features incorporated into this event generator for the experimental simulation.

3.3.1 Angular Distribution of Neutrons

The first step in the event generation was selection of the initial momenta directions of neutrons. Differential cross sections for photodisintegration provided the angular distribution of neutrons necessary for the simulation.

The differential cross section for photodisintegration can be parameterized as an expansion in terms of the associated Legendre polynomials, P_k^q, such that for linearly polarized photons incident on an unpolarized target, the cross section is

$$\frac{d\sigma}{d\Omega} = \frac{\sigma}{4\pi}\left[1 + \sum_{k=1}^{\infty} a_k P_k^0(\cos\theta) + \sum_{k=2}^{\infty} e_k P_k^2(\cos\theta)\cos 2\phi\right], \tag{3.1}$$

where σ is total cross section, and a_k and e_k are fitting coefficients. In the case of circularly polarized photons, $e_k = 0$ for all k, so the differential cross section is

$$\frac{d\sigma}{d\Omega} = \frac{\sigma}{4\pi}\left[1 + \sum_{k=1}^{\infty} a_k P_k^0(\cos\theta)\right]. \tag{3.2}$$

With properly normalized coefficients, this expansion served as a probability distribution function for sampling the angular distribution of photoneutrons. A (θ, ϕ) coordinate was randomly generated for an outgoing neutron and used to evaluate the Legendre expansion of the differential cross section, yielding a value between 0 and 1. Rejection sampling was then used to determine if the (θ, ϕ) pair should be kept. Using this method to simulate many events resulted in an angular distribution of neutrons that is representative of the Legendre polynomial expansion. The momentum and energy of each neutron were then calculated with the kinematics detailed earlier.

3.3.2 Photodisintegration Kinematics

With (θ, ϕ) coordinates generated for the photoneutrons, the rest of the kinematic variables could be calculated with the formulas derived in Section 2.5.1. These equations demonstrate the relationship between the energies and momenta of neutrons with their outgoing reaction angle, θ, in the laboratory frame.

3.3.3 Geometric Effects

Positional placement of the primary particles in an event generator depends on the type of experiment being simulated. For instance, in collider experiments, primaries will be generated at a singular interaction point, often at the center of the simulated volume. For an experiment generating particles from a reaction with a target of finite size, the initial positions of particles are more spread out based on the parameters of the setup. Simulating neutron production from photodisintegration within a heavy water target requires consideration of these effects.

Beam Attenuation

To start, in a target of finite length, photodisintegration events can occur anywhere along the length of the target. Thus the event generator was set up to produce neutrons along the z-axis within the target. However, not every position within the target demonstrates the same probability for neutron production. As the photon beam travels through the target, photons are either absorbed or Compton scattered out of the target. Thus, only a fraction of the original intensity of the photon beam is incident on the downstream end of the target. This *beam attenuation* results in a lower neutron production yield from the downstream end. The attenuation of the beam results in an exponential decay of the beam intensity through the target expressed as

$$I(z) = I_0 e^{-\mu z}. \tag{3.3}$$

μ is the beam attenuation coefficient, a property of the target material based on the incident beam particles.[4] The beam attenuation is modeled in the event generator with a rejection sampling algorithm. A z position within the target is chosen with a random number generator. This position is used to calculate the fraction of beam attenuation, $e^{-\mu z}$. Another random number is generated between 0 and 1 and compared to the beam attenuation factor. For any event in which the random number is greater than the attenuation coefficient, the z position is rejected and a new one is selected. Otherwise, the z position is kept and used as the starting point of a photoneutron. As the beam attenuation function decreases further into the target, this method weights the distribution of neutrons towards the upstream end of the target, realistically modeling the physical effect.

[4] For γ-rays in heavy water, $\mu = 0.0226$ cm^{-1}.

Beam Profile

A particle beam provided by an accelerator is never point-like. The beam has some width and shape known as the transverse beam profile. Because of this, there will be some spread around the beam axis in which photodisintegration can occur. This effect was also incorporated into the event generator.

A beam profile typically resembles a Gaussian distribution, or at least a similar shape. However, with collimation, the gamma-ray beam provided at HIγS exhibits a fairly steep peak in its distribution and can be reasonably approximated to be uniform over a finite width. To model this in the event generator, an initial position in the $x-y$ plane around the beam axis (z-axis) is randomly generated within a radius defined by the beam width. For a uniform distribution, no rejection sampling method is needed, as typical pseudo-random number generation already samples uniformly.

3.3.4 Polarization of Neutrons

The event generator was also written to set the initial polarization of neutrons from photodisintegration. A measurement of the neutron polarization benefits from simulating how this polarization might propagate through the setup and affect the neutron's trajectory. The significance of this is made more clear in the next section, but for now, a brief comment on including polarization in the event generator is sufficient.

Despite the ambiguity in the neutron polarization being investigated by this measurement, theoretical models can be used as a starting point for simulations of the experiment. Values for the polarization were obtained from calculations performed by Arenhövel [11, 12]. The theoretical "data" was tabulated for a set of photon energies below 20 MeV and for reaction angles from 0° to 180° in increments of 10°.

The neutron polarization was interpolated from the theoretical table using the incident photon energy and outgoing angle θ of the neutron. This calculation provided a value for P_y, the projection of the neutron's polarization on the normal vector to the reaction plane ($\hat{n}_y = \vec{k}_\gamma \times \vec{k}_n$). The polarization vector of the neutron was then defined as a vector along the reaction plane normal with magnitude equal to the neutron polarization. Although not physically representative of the spin polarization of an ensemble of particles, this method becomes statistically equivalent after simulation of many events.

3.4 Polarized Neutron Scattering in GEANT4

As discussed in Section 2.6, spin polarization contributes to the cross sections and observables of nuclear reactions. It can demonstrate a considerable effect that should be accounted for in experimental measurements. Simulations should also be able to model this to provide complementary information to the experimental setup.

Despite its extensive capabilities in physics modeling, GEANT4 is only as good as the physics that is provided by developers. Development of physics lists in GEANT4 is an ongoing process as models and methods are improved or added. Until now, the effects of spin polarization on low energy nuclear reactions had not been included in physics models in GEANT4. As part of the work performed for this dissertation, an improved physics model was developed to account for spin polarization in low energy elastic neutron scattering. This model proved to be a critical addition to the Monte Carlo simulation of the experiment. This section details the development and use of this physics model in support of the experimental analysis.

3.4.1 ParticleHP Model

In GEANT4 , the recommended model for lower energy (< 20 MeV) particle transport is the *ParticleHP* model (HP for High Precision). Originally a library for handling low energy neutron interactions (formerly NeutronHP), it was eventually generalized to include charged particles. For particle energies below 100 MeV, theoretical models of particle transport struggle to accurately reproduce experimental data. The ParticleHP model addresses this issue with a data-driven approach. It uses evaluated nuclear cross section databases of low energy interactions, including inelastic processes, to perform Monte Carlo computations for very precise particle tracking.

Because of its origins in modeling neutron physics, the ParticleHP library is an excellent model for simulating neutron scattering for kinetic energies below 20 MeV. This positions it as an optimal choice for performing simulations of this experiment. As discussed, GEANT4 does not offer a treatment of polarization in nuclear reactions and therefore, modifications were made to the ParticleHP model to incorporate the effects of spin polarization.

3.4.2 Polarization in ParticleHP

The most relevant process for implementing spin polarization in the simulation of this experiment was elastic scattering of neutrons. As the main technique for measuring the polarization of the neutrons was analyzing the asymmetry in their scattering, properly modeling this process with the effects of spin polarization was crucial to an accurate simulation of the experiment. To do so, the ParticleHP physics model provided by GEANT4 was adapted to incorporate the contribution of spin polarization to differential cross sections of elastic scattering and handle the tracking of a particle's spin during its transport.

Recall that a spin-$\frac{1}{2}$ particle, such as the neutron, with polarization, $\vec{P}$, has a differential cross section for scattering defined by

$$\frac{d\sigma}{d\Omega}(\theta,\phi) = \frac{d\sigma}{d\Omega}\bigg|_0 \Big[1 + |\vec{P}| A_y cos(\phi)\Big]. \tag{3.4}$$

Here, A_y is the analyzing power of the scattering target and ϕ is the azimuthal angle of the reaction in the center-of-mass frame. The polarized differential cross section can be treated as a weighting in ϕ of the unpolarized cross section.

This "weighting factor" for the polarized cross section was applied to the angular distribution provided by the standard GEANT4 libraries. A Monte Carlo algorithm was incorporated into the ParticleHP model to implement the new angular distribution. This modified version of ParticleHP was referred to as *PolarizedParticleHP* to distinguish it from the original model.

Assume a neutron with polarization $\vec{P}$ and initial momentum $\vec{k}$, incident on a target nucleus. After scattering, the neutron has a final momentum of $\vec{k'}$. The direction of the outgoing neutron was determined with the following steps:

1. Obtain the reaction plane normal vector with:

$$\hat{n}_y = \frac{\vec{k} \times \vec{k'}}{|\vec{k}||\vec{k'}|}. \tag{3.5}$$

2. Calculate the projection of the neutron's polarization onto the reaction plane normal:

$$P_y = |\vec{P}| \cos(\phi) = \vec{P} \cdot \hat{n}_y. \tag{3.6}$$

3. Determine the analyzing power A_y of the reaction. As mentioned, the analyzing power is a property of the reaction, dependent on the incident neutron's energy and the final polar scattering angle, θ. Values are extracted from a database of experimental data[5] and interpolation is used to find appropriate quantities.

4. Calculate the scattering asymmetry:

$$A = 1 + P_y A_y. \tag{3.7}$$

5. The asymmetry is used as a sampling "function" in a Monte Carlo algorithm for sampling the azimuthal scattering angle, ϕ, of the outgoing neutron. This angle effectively indicates the rotation of the scattering plane through the reaction. By definition of the polarization, P_y and analyzing power, A_y, the asymmetry must be such that $A \in [0, 2]$, and so a random number is generated within this range to compare to the asymmetry.

6. If the randomly generated number is below A, the neutron's generated direction is kept. If the random number is above A, the neutron's direction is rotated by π radians in ϕ. This rotation applies a flip to the neutron's momentum in the "left-right" plane in the center-of-momentum reference frame. From there, the event is processed with the standard GEANT4 computations.

This Monte Carlo method is rather similar to rejection sampling except no events are "thrown away", but instead adapted to properly weight the angular distribution. Full rejection sampling was not used for more than one reason. First, the algorithm had to be implemented in a way that did not affect the total cross section for neutron scattering. Rejecting scattering events due to the asymmetry would lower the total cross section in an unphysical way. By choosing to rotate the final direction of the neutron instead, the weighting in the angular distribution still emerges properly without sacrificing real cross sections. Additionally, from a pragmatic standpoint, the rejection method increases the computation time of a simulation as events need to be regenerated and sampling values recalculated. With quite a few calculations added in as part of this algorithm, ensuring they only had to be performed once saved valuable time and computational resources.

[5]Data was obtained from the National Nuclear Data Center (NNDC).

3.5 Implementation of *nvec* Simulation

A full simulation of the experimental setup was developed using GEANT4. Identified as the *nvec* simulation, it was built to model the materials, geometry, and physics of the experiment as accurately as possible, using the techniques outlined in this chapter. A screenshot of the GEANT4 model is shown in Figure 3.5.

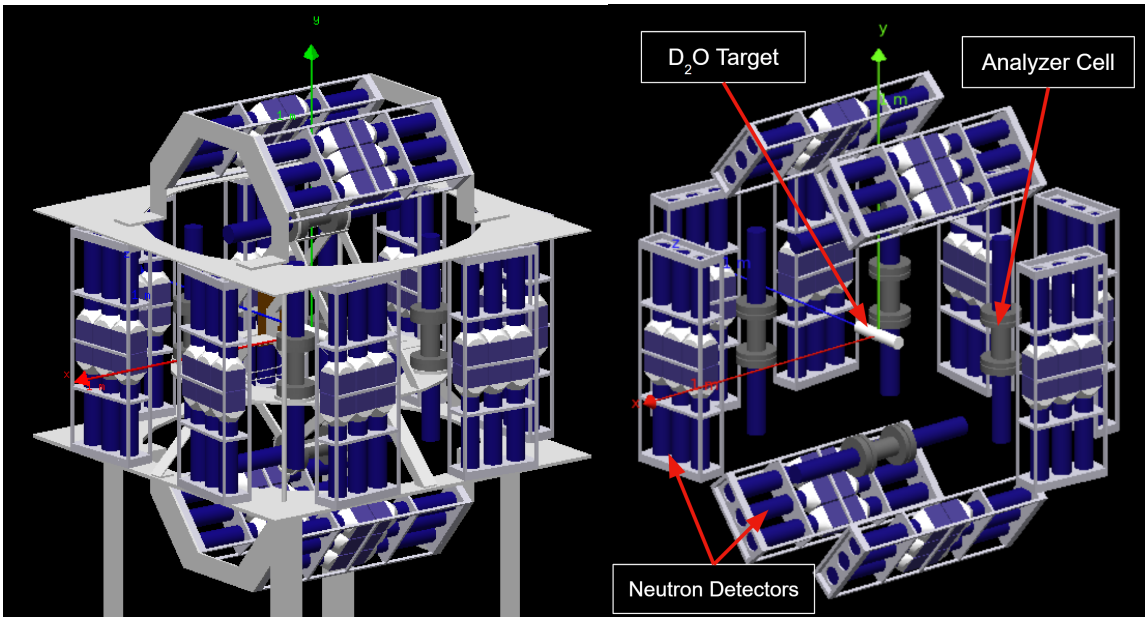

(a) Full *nvec* GEANT4 model for simulation of experiment

(b) Cutaway of *nvec* GEANT4 model without frame for inside view

Figure 3.5: Simulated Detector Geometry from GEANT4. A full simulation of the experiment was implemented in GEANT4 to model systematic corrections and background effects. The simulation incorporated accurate detector geometries and physics models for precise comparisons to real data. The full simulated geometry is displayed above. Image Credit: T. Polischuk [53]

The simulation operated in two main modes: photon source and neutron source. The photon source simulated a gamma-ray beam provided by the accelerator incident on the target. This gave estimations of the background gamma-rays that Compton scattered from the target into the detectors. The neutron source simulated the photoneutrons from photodisintegration generated with the methods described in Section 3.3. The simulation provided information regarding several aspects of the experiment to inform correction factors that could not be measured experimentally.

3.5.1 Light Output Scaling

Due to imperfections in the assembly and electronics of detectors, the signals produced by particles did not always convert 100% of the light output to signal. Lower measured light output caused by energy loss somewhere in the system meant inaccurate readings of the parameters used to perform the analysis. Therefore, the light output of each detector had to be calibrated to its expected amount to properly scale the signals being received from the detectors.

The *nvec* simulation incorporated detailed light output tables for BC-505 in order to calculate accurate data of the expected output due to neutron or photon detection. Running the simulation provided a light output spectrum for each detector that was used to calibrate the data from the experimental run through the method discussed in Section 5.2.1.

3.5.2 Simulating Geometric Asymmetries

The polarization of neutrons was not the only source of asymmetries that the experimental setup was sensitive to. The geometry of the setup and attenuation of the photon beam in the target resulted in an additional asymmetry in the trajectories of neutrons, which is detailed further in Section 5.4.6. Without adding polarization effects into the GEANT4 simulation, it could provide an accurate measurement of the geometric asymmetry that was not possible experimentally. This asymmetry was then applied as a correction factor in the analysis to calculate the true asymmetry due to polarization.

3.5.3 Calculation of Effective Analyzing Powers

The geometry of the experimental setup also introduced consequences to the use of analyzing powers in the extraction of the neutron polarization. The intent of the experiment was to extract the polarization of a neutron, P_y, from its scattering asymmetry A, through a proportional relationship defined as

$$A = P_y A_y(E_n, \theta_n). \tag{3.8}$$

The analyzing power, A_y, of n-^{4}He elastic scattering is a function of the incident neutron energy, E_n, and the scattering angle θ_n. A simple application of Equation 3.8

implies a known, single-valued analyzing power for a neutron scattered in an analyzer and detected by a certain counting detector. Analyzing powers relevant to this measurement were obtained from theoretical calculations published by Stammbach and Walter [54], and can be found in Appendix B. However, the actual detector geometry complicated this methodology.

Due to the finite length of the target, neutrons incident on an analyzer would vary in energy depending on their starting location in the target.[6] Additionally, neutrons traveling along different trajectories from the target to the analyzer could scatter in the analyzer at different angles, but be collected by the same detector. A geometric demonstration of these concepts is illustrated in Figure 3.6. The spread in the energy and scattering angle of neutrons collected by each detector meant that the analyzing powers that were needed to calculate the polarization were no longer single-valued. Because of this, the polarization could not be calculated using the "nominal" values for the analyzing powers.

The Monte Carlo simulation was used to develop a method for extracting the neutron polarization from the measured asymmetries. The ParticleHP physics model discussed in Section 3.4 with polarized scattering modifications was implemented into the simulation to properly model the transport of polarized neutrons in the experimental setup. The simulation was first run with unpolarized neutrons to obtain quantities for the geometric asymmetries. Next, the simulation was run with a sample set of values for the polarization, based on theoretical predictions. Using the mean polarization of neutrons incident on an analyzer and the corrected scattering asymmetries[7], a set of *effective analyzing powers* were calculated, each one corresponding to a certain detector in a station.

The effective analyzing powers were verified with a follow-up set of test polarizations. Measured asymmetries were obtained again, and the effective analyzing powers were successfully applied to extract the original mean neutron polarization. With proper verification in place, these effective analyzing powers facilitated a more accurate calculation between the observed scattering asymmetries and the neutron polarization. Effective analyzing powers for neutrons produced with a 16 MeV photon beam are listed in Appendix B.

[6] The neutron energy depends on its outgoing angle from photodisintegration. Different interaction points within the target correspond to different angles for neutron trajectories to an analyzer.

[7] The corrected scattering asymmetries were found by subtracting the geometric asymmetries from the measured asymmetries.

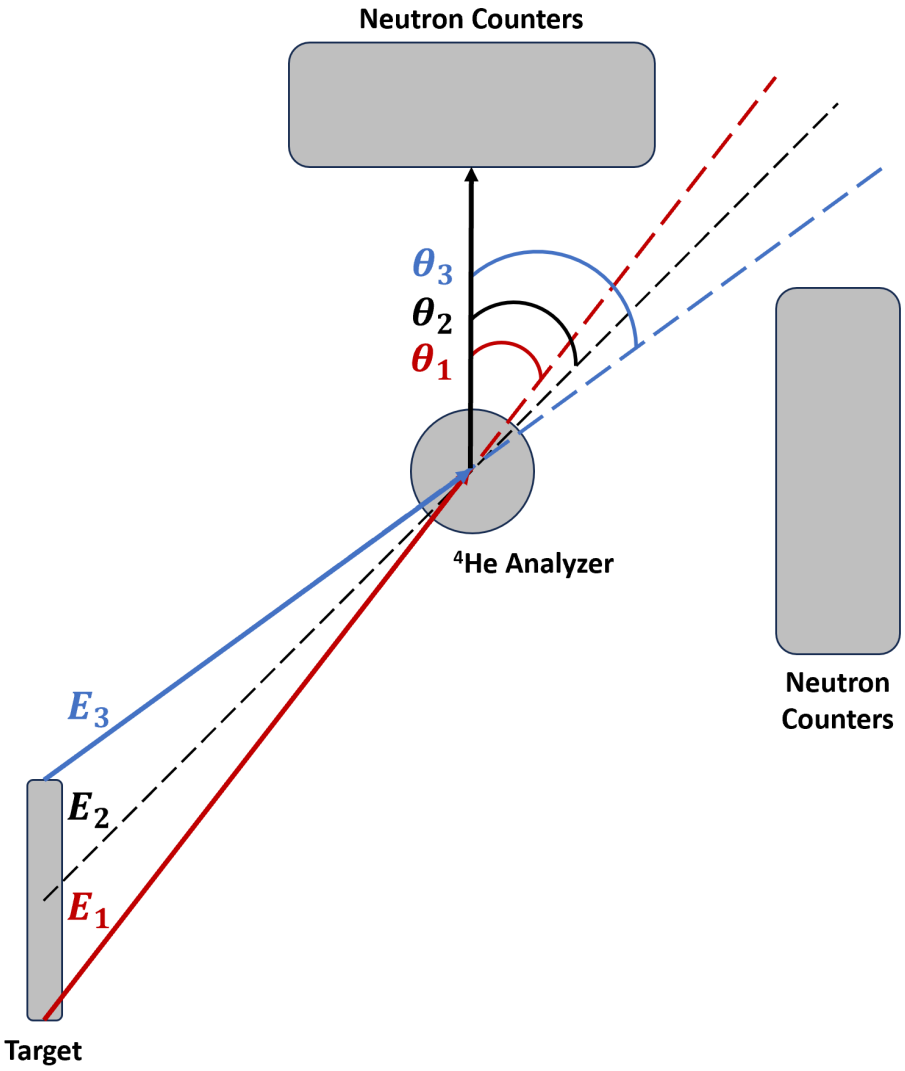

Figure 3.6: Geometric Effects on Analyzing Power Uncertainties. The finite length of the target produced a spread in the energy and scattering angles of neutrons collected by each detector, resulting in a large uncertainty in the analyzing powers. The analyzing powers obtained from theoretical calculations only applied to the nominal trajectory of neutrons through an analyzer, labeled as (E_2, θ_2). A set of effective analyzing powers were calculated using simulated data for more accurate extraction of the neutron polarization from measured asymmetries, with lower uncertainty.

Chapter 4

Experimental Overview

In order to measure the spin polarization of neutrons through observation of the directional asymmetry in their scattering, the experiment was designed in such a way as to compare neutron yields between two sides of a scattering event on an *analyzing* nucleus. The setup was centered around the use of a set of scattering volumes known as *polarization analyzers*[1].

The target was a cylindrical volume of heavy water (^2H_2O or D_2O), 20 cm in length and 4 cm in diameter, fixed along the beam axis at the center of the experimental setup. Heavy water serves as a safe and logistically convenient supply of deuterium. The beam energies used (8, 12, and 16 MeV) were all low enough to avoid neutron production from the oxygen nuclei in the compound, ensuring all photoneutrons originated from deuterium nuclei.

Surrounding the target, the experimental frame held six "stations" of detectors. Each station was composed of an analyzer surrounded by two groups of six liquid organic scintillating neutron detectors borrowed from the *Blowfish* detector array from Section 1.3.3. The neutron detectors acted as counting detectors to determine the number of neutrons that scattered left vs right in the analyzer.

Two stations were placed at each of the three laboratory polar angles $\theta_{Lab} = 45°, 90°$, and $135°$. The $45°$ and $135°$ stations were in the horizontal plane of the experimental setup at $\phi = 0°$ and $\phi = 180°$. The $90°$ stations were in the vertical plane, at $\phi = 90°$ and $\phi = 270°$. The layouts within the two planes of the experiment are detailed in Figure 4.1.

[1] Also referred to as polarimeters

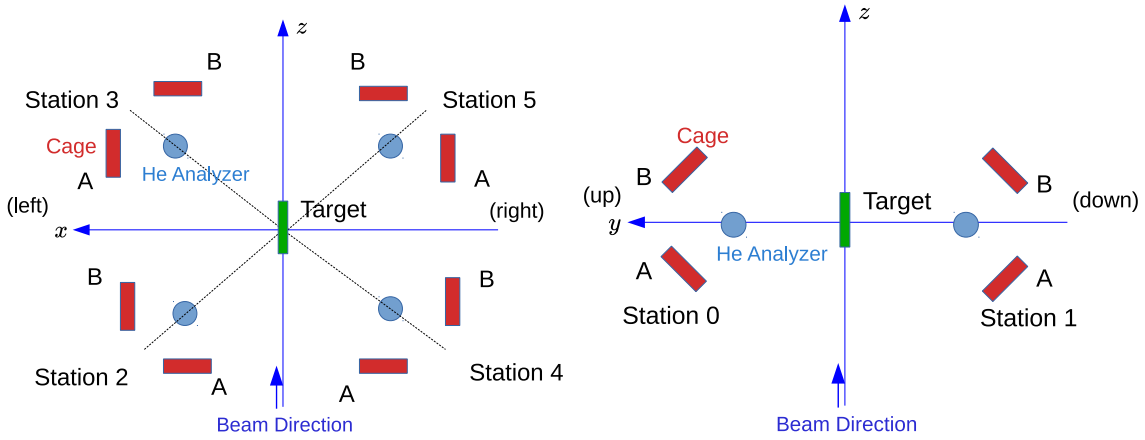

(a) Horizontal plane containing the 45° and 135° stations

(b) Vertical plane containing the 90° stations

Figure 4.1: Experimental Layout Diagrams. Geometry of the experimental layout of detector stations. A 20 cm cylindrical heavy water target is surrounded by six stations of detectors, (a) two each at 45° and 135° in the horizontal plane and (b) two at 90° in the vertical plane. Each station contains a polarization analyzer with a "cage" of neutron counting detectors on either side. Image Credit: T. Polischuk [53]

This orientation of stations mapped the desired polar angles of photoneutrons and simplified the extraction of contributions to the neutron polarization in Equation 1.8. For the azimuthal angles covered in the setup, $\cos(2\phi) = \pm 1$, making calculations with Equation 1.8 more straightforward.

4.1 High Intensity Gamma Source

The experiment was hosted at the High Intensity Gamma Source (HIγS or, HIGS) at the Triangle Universities Nuclear Laboratory (TUNL) in Durham, North Carolina. HIγS produces high intensity gamma rays via Compton backscattering, in which photons from a Free Electron Laser (FEL) are scattered off an accelerated electron beam producing high energy photons. Through this process, HIγS has the capability to precisely tune the energy and polarization of these photons for use in a variety of nuclear physics experiments. HIγS holds the status as the highest intensity gamma ray source in the world, able to provide up to 1000 photons per second per eV.

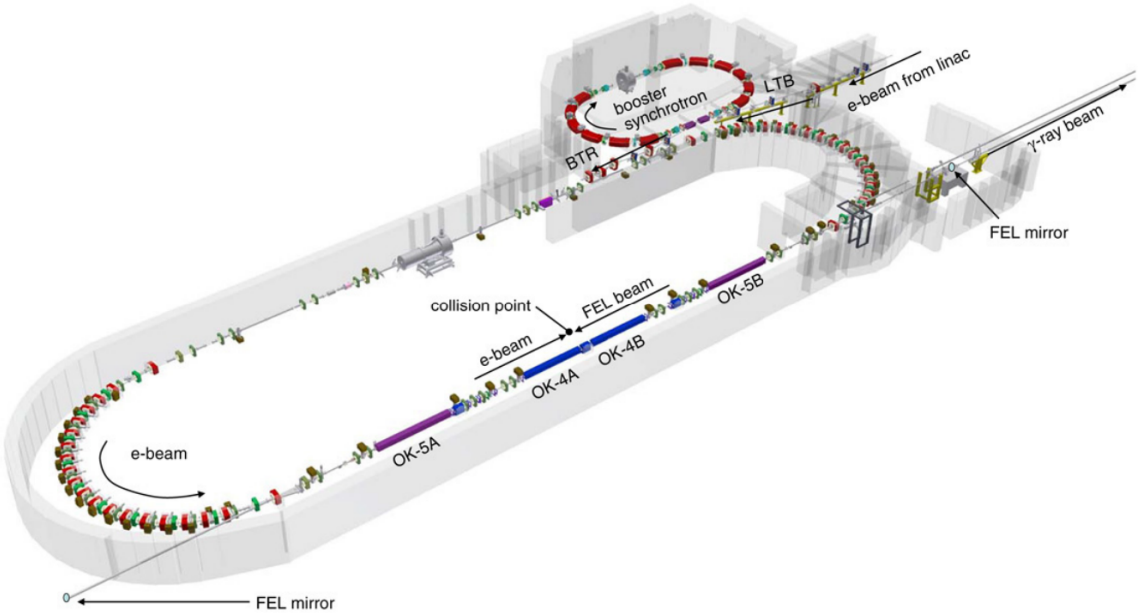

Figure 4.2: HIγS Facility. Illustration of the High Intensity Gamma Source.[55] The northeast corner contains the linac and booster ring for injection into the storage ring. The closest straight side in the diagram contains the FEL, which produces UV photons by wiggling electron with the OK-4 and OK-5 magnets. These photons are reflected within an optical cavity along this straight side by the FEL mirrors. At the collision point, the photons will collide with a second bunch of electron, prompting Compton backscattering to boost the photons up to γ-ray energies. The γ-rays travel down the beamline to one of two target rooms: the Upstream Target Room (UTR) or the Gamma Vault (GV).

4.1.1 Electron Beam Acceleration

Beam production at HIγS begins with the acceleration of groups, or *bunches*, of electrons in a linear accelerator (*linac*) to energies of 0.18-0.28 GeV. The linac feeds electrons into a booster synchrotron for timed injection into a larger storage ring.

A synchrotron generates oscillating electric and magnetic fields to control the energy of charged particles traveling in a cyclic trajectory. A magnetic field bends the particles along the trajectory, increasing in time *synchronized* to the increasing energy of the particles. Precise control of the energy of particles is achieved by oscillating the strength of the electromagnetic potential in time, creating periodic potential energy minima known as *buckets* occupied by accelerated particles. The oscillating fields are generated in a radio-frequency (RF) cavity where particles can

either be stored at a tuned energy, or accelerated to other energies.

The booster ring accelerates electrons to energies of 0.18-1.2 GeV, at which point they can be injected into the electron storage ring. The storage ring has a "racetrack" shape with two long straight sides. One side accepts injection from the booster ring and contains the RF cavity system for electron acceleration. The other straight section houses the FEL.

4.1.2 Free Electron Laser

In "FEL only mode", the storage ring is operated with a single-bunch electron beam. The straight section of the ring contains two sets of electromagnetic "wigglers", more formally known as *Optical Klystron* (OK) magnets. The wigglers use magnetic fields to "wiggle" the electrons, producing UV photons from synchrotron radiation. The orientation of the wiggling of the electrons imparts a polarization in the emitted photons. For its early years of operation, HIγS only used planar electromagnetic wigglers, the OK-4 magnets, to produce linearly polarized photons. Later, four helical electromagnetic wigglers (OK-5s) were added to provide circular polarization capability. These additions enable HIγS to provide either mode of polarization.

4.1.3 Gamma Ray Production

For gamma ray production, the HIγS storage ring is operated with a two-bunch beam. The second bunch of electrons added to the storage ring is stored half a cycle behind the first bunch. Meanwhile, the UV photons produced by the FEL travel along an optical cavity that reflects them back towards their point of origin. The timing is aligned so that the second electron bunch collides with the UV photons at the center of the optical cavity.

At the interaction point, the UV photons will Compton scatter from the electrons. For an initial photon energy E_γ and electron beam energy E_e, the final energy of the photon is expressed as

$$E_\gamma^{'} = \frac{E_\gamma(1-\beta\cos(\theta_i))}{1-\beta\cos(\theta_f)+\frac{E_\gamma}{E_e}(1-\cos(\theta_f)-\cos(\theta_i))}. \tag{4.1}$$

Here, $\beta = \frac{v}{c}$ is the relativistic velocity of the electrons and θ_i and θ_f are the angles between the electron beam momentum and the initial and final photon momenta,

respectively.

At HIγS, the relativistic electrons collide head-on with the comparatively low energy photons, and the photons that scatter directly back along their incident trajectory will have the maximum energy. This is referred to as *Compton backscattering*, and implies $\theta_i = \pi$ and $\theta_f = 0$, resulting in a final state energy of

$$E_\gamma^{'} = E_\gamma \frac{\gamma^2(1+\beta)^2}{1 + 2\gamma^2 \frac{E_\gamma}{E_e}(1+\beta)}. \tag{4.2}$$

With electron energies much larger than the initial photon energy,

$$E_\gamma^{'} \approx \gamma^2(1+\beta^2)E_\gamma, \tag{4.3}$$

and for ultra-relativistic electrons, $\gamma \gg 1 \rightarrow \beta \approx 1$, so

$$E_\gamma^{'} \approx 4\gamma^2 E_\gamma. \tag{4.4}$$

It is evident from Eq. 4.4 that Compton backscattering can significantly boost the energies of photons into the gamma-ray regime. After scattering, the photons are collimated about 60 m away from the collision point and travel to a number of downstream target rooms. Since the energy of the Compton-scattered photons has a strong dependence on the scattering angle, collimating the beam within a narrow solid angle provides a nearly monochromatic photon beam. Additionally, polarization of the photon undergoes very little reduction during Compton backscattering, and the small solid angle of the collimator prevents much reduction as well. All in all, HIγS is able to preserve most of the almost complete polarization of the original FEL beam, achieving $> 95\%$ polarization for both linear and circular polarization.

4.1.4 Background Effect of HIγS Bunching Mode

A note should be made about a secondary effect of the bunching mode operation of the HIγS accelerator. Typically, the accelerator operates in a two-bunch mode, where two RF buckets contain bunches of electrons separated by half the circumference of the electron storage ring. [55] The electrons in the "second" bunch are used to boost synchrotron photons produced by the "first" bunch through Compton backscattering.

Over time, electrons from either of these RF buckets can "slip" into neighbor-

ing buckets and occupy these as operation continues. In these instances, these new additional bunches of electrons will also generate gamma-ray photons, but now at a slightly different point within the cycle of the storage ring. The Compton scattering interaction thus occurs at a different time than is anticipated and provided by the accelerator bunch pick-off signal, creating a periodic series of *out-of-time photons* that travel to the experimental hall. Depending on the nature of an experimental setup, this effect can produce measurable background events during an experimental run.

4.2 Methods in Particle Detection

A successful measurement of neutron polarization in this experiment required detection of the photoneutrons produced in $d(\gamma, n)p$ and identification to discern them from other particles. There are a number of particle detection techniques in nuclear and particle physics that enable a wide range of experimental measurements. The detector subsystems of this experiment were scintillation-based detectors that utilized different scintillating materials depending on the role of the detector in the measurement. The light output produced by each of these detectors was collected by photomultiplier tubes for conversion into electronic signals that could be interpreted by data acquisition electronics.

This section aims to introduce the particle detection techniques used in this experiment. The hope is that these fundamentals principles will provide insight into the design and operation of each of the detector subsystems discussed in subsequent sections.

4.2.1 Scintillation

Scintillation is one of the most commonly applied methods used in particle and radiation detection. Ionizing radiation passing through a medium will transfer energy to atoms of the medium, transitioning them into an excited state. After some amount of time, these atoms will de-excite back to their ground state, emitting the absorbed energy as photons. This emission is known as *fluorescence*, and it is typically a prompt response that produces visible light. The photons released in the process can be collected with some form of light sensor, enabling measurements of the interaction that provide insight into the nature of the initial ionizing radiation.

There are a variety of materials that act as scintillators, each with unique capabilities that make them useful for different purposes in detection. Knoll [56] identifies a set of ideal properties of an effective scintillation material, outlined below:

1. A scintillator should efficiently convert kinetic energy from charged particles into light emission.

2. The light output produced by the material should be proportional to the amount of energy deposited by the particle; a property known as *linearity*.

3. The medium should be transparent to the light output from the scintillation process so this light can be measured outside of its volume.

4. Fluorescence should occur quickly to produce fast signal pulses upon detection.

5. The scintillator's index of refraction should be similar to that of glass for efficient optical coupling to light sensors.

6. The logistics of developing the material for the specific need of the particle detector should be practical.

There is no "perfect" scintillator for all uses in radiation detection. Each type has different strengths among the properties listed above, while falling short in other aspects. Choosing a scintillating material for a specific use requires balancing the capabilities that best meet the desired detection requirements.

4.2.2 Noble Gas Scintillators

Noble gases used for scintillation detection were employed for the polarization analyzers in this experiment because of their effectiveness in neutron detection due to their scintillation properties. In a typical noble gas scintillator, ionizing radiation passing through the medium will excite atoms of the gas into their lowest molecular excited states. Upon de-excitation, the atoms will emit ultraviolet photons due to the energy differences of the transitions. As most photon detection instrumentation is tuned to visible light, additional measures must be taken to enable detection of the scintillation light output. Often, some form of wavelength shifter is incorporated to convert photons, either in the form of an additional gas in the medium or as a filter between the scintillation volume and the light detectors.

Typically, noble gas scintillators respond to interactions with charged particles. Detecting neutral particles such as the neutron requires additional consideration in the selection of gas. Historically, fast neutron detection with gas scintillators has used a combination of gases with a mixture of helium and xenon as a common option. Fast neutrons predominantly interact with matter via the strong interaction.[2] Detection of neutrons relies on them to scatter from light nuclei in the scintillator, such as helium. The recoiling helium nucleus (i.e. an alpha particle) passes through the gas scintillator as ionizing radiation. This initiates the excitation of the scintillating material, in this case, xenon, resulting in the final light output, thus enabling neutron detection.

As discussed, any type of scintillating material comes with a balance of strengths and weaknesses. The energy state transitions of gas molecules occur within a few nanoseconds, giving them one of the fastest response times of any type of particle detector. The ease of control of the geometry of a gas volume makes them logistically convenient for detector development. The main drawback of a gas scintillator is low light output. With a number of means of de-excitation within the volume, the energy is dissipated rather quickly, with a comparatively low amount of conversion to light.

4.2.3 Organic Scintillators

As mentioned earlier, the neutron detectors used in this experiment were liquid organic scintillators. Organic scintillators fluoresce due to the transition in the energy level structure of individual molecules. This process is a behavior of the molecule itself, independent of its physical state.

Scintillation in these types of organic materials occurs when ionizing radiation generates excited states in the π-electron structure of the molecule.[3] The π-electron structure of a molecule is a property of some organic molecules due to certain symmetries and is illustrated by the diagram in Figure 4.3.

[2]The electromagnetic, gravitational, and weak interactions can all be ruled out when considering fast neutrons. As neutral particles, neutrons do not interact electromagnetically. The gravitational force has a negligible strength on the length scales associated with particle interactions. The weak interaction takes too much time for fast neutrons to interact in a medium. Thus, the strong interaction is left as the dominating force.

[3]π-electron structure refers to the electrons in π bonds between covalently bonded atoms.

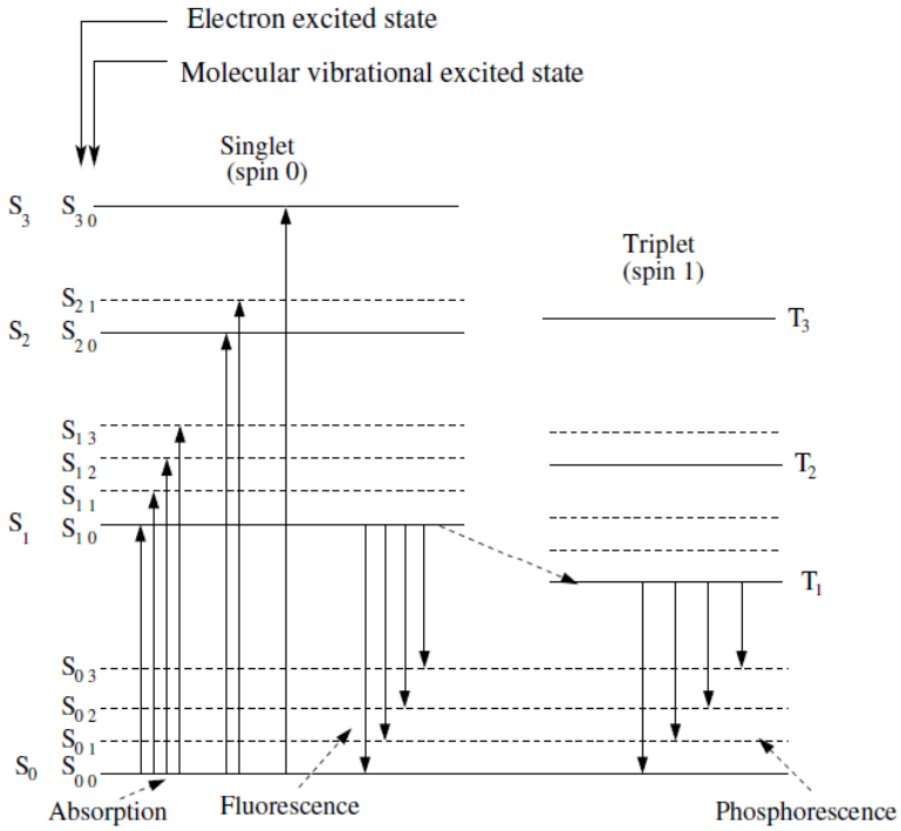

Figure 4.3: π-Electron Structure of Organic Molecules. Scintillation of organic scintillators is a result of energy level transitions of electrons in the covalent bonds of the organic molecules (π-electrons). Most scintillation light output is generated in de-excitation from the lowest excited singlet state, S_{10}, to the ground state as prompt fluorescence. Some light output is more delayed due to conversions to the triplet states, known as phosphorescence. Image Credit: G. Pridham [57]

Ionizing radiation transfers some of its kinetic energy to a molecule, exciting its electron configuration into any of its possible excited states. The energy levels are split based on the different singlet and triplet spin states of the electrons and the vibrational states of the molecule. Singlet states above the S_{10} state will quickly lose energy through radiationless conversions, until a population of molecules exist in the S_{10} state. From this state, the molecules can take two paths towards de-excitation.

One possibility is prompt fluorescence, in which molecules transition directly back to the ground state, emitting scintillation light. The intensity of this light output is modeled as

$$I = I_0 e^{-\frac{t}{\tau}}, \tag{4.5}$$

where τ is the fluorescence decay time of the molecule. A typical decay time is on the order of a few nanoseconds, resulting in a rather quick emission of light.

Alternatively, molecules in the S_{10} state can convert into a T_1 triplet state of slightly lower energy. These states have a much longer lifetime than the S_{10} state, and so they exhibit a delayed emission of light, called *phosphorescence*. Due to the lower energy level of the T_1 state, light output from phosphorescence will have longer wavelength than that of fluorescence; a noticeable shift in the scintillation spectrum.

It should be noted that the energy level transitions in fluorescence and phosphorescence are smaller than most transitions that occur during absorption. Most of the emitted light from scintillation will not have enough energy for subsequent excitations. This allows the organic scintillator to be "transparent" to its own scintillation light, ensuring that it can escape the medium to be detected and measured.

As discussed earlier, scintillation is a response from interactions with charged particles. Scintillation due to neutral particles requires an additional interaction step to initiate charged particle movement. The significant hydrogen content of organic scintillators provides a prime environment for interactions with incident neutrons in particular. Due to the relatively large cross section of neutron-proton elastic scattering, an incident neutron will deposit a significant portion of its kinetic energy within the scintillator. The transfer of energy sends protons traveling through the volume, exciting electrons along the way.

Photons will also induce scintillation due to their strong coupling to the electrons. In fact, photons are more likely to interact with the electrons directly, rather than with nuclei in the scintillator. This creates a rather quick response, leading to most of the light output coming from prompt fluorescence. Meanwhile, the additional $n-p$ scattering requirement for neutron detection causes a slower energy transfer to the electrons, resulting in more delayed fluorescence. This behavior is observable in the properties of the light output from each of these particles.

4.2.4 Pulse Shape Discrimination

Experiments in nuclear and particle physics rely on the ability to distinguish between the particles that are being measured; this experiment is no exception. This requirement motivated the inclusion of liquid organic scintillators for the measurement. The value of these organic scintillators lies in their excellent capabilities in neutral particle identification through a procedure known as *pulse shape discrimination*.

The scintillation process in organic scintillators does not behave identically for all particles. The majority of light output from scintillation is emitted in prompt fluorescence, but there will be a fraction of the light produced during delayed fluorescence. The combination of these phenomena manifests in the shape of the pulse produced by a light sensor collecting the light output. The prompt fluorescence generates a waveform with a sharp peak and the delayed fluorescence adds in a slow exponential decay in the form of a "tail" of the pulse. The characteristic of this tail depends on the species of particle causing the scintillation and can therefore act as an identifier for different types of particles.

As discussed in the previous section, neutrons generate scintillation light output with a higher fraction of delayed fluorescence than photons. This is evident in Figure 4.4, which plots the intensity of scintillation light output over time for different particles.

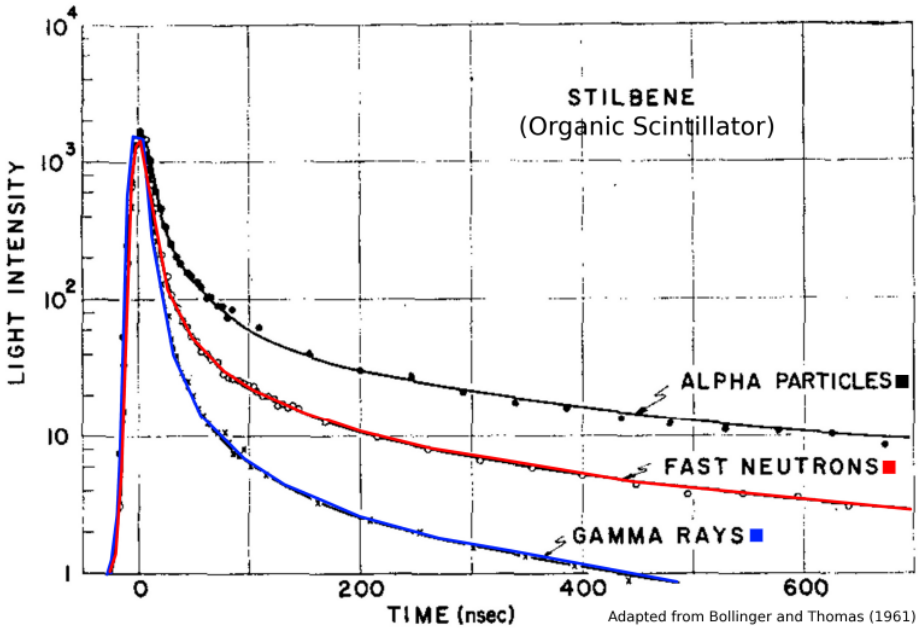

Figure 4.4: Intensity of Light Output Over Time in Organic Scintillator. Intensity of the light output over time from different particles in an organic scintillator (stilbene). Image Credit: Adapted from Bollinger and Thomas by Pridham [57].

The shape of each light intensity curve translates fairly proportionally to the pulse shape of the electronic signal produced by a light sensor. The higher amount of delayed fluorescence due to neutrons produces a larger tail than that from photons. This illustrates how a distinction can be made between these two types of particles

based on the size of these tails. This provides a crucial technique in particle identification that was implemented for this experiment, which is discussed in further detail in Section 5.2.3.

4.3 Polarization Analyzers

A polarization analyzer is used for the measurement of the spin polarization of neutrons. It contains an analyzing material with well-understood properties in elastic scattering of neutrons. For this experiment, the analyzers used were high pressure ^4He-Xe gas scintillators. This type of device has a history as an effective neutron detector and polarimeter because of the well-documented behavior of the $^4He(\vec{n},n)^4He$ process. [58–60]

The analyzers contained a gas mixture of 90% partial pressure of helium-4 and 10% partial pressure of xenon at a total pressure of 2500 pounds per square inch (PSI). This high of a pressure provided a volume of high density ^4He to increase the probability of neutrons scattering from helium nuclei in the analyzer. The $^4He(\vec{n},n)^4He$ reaction serves as the polarization analyzing process. It exhibits an asymmetry in the scattering angle, θ, of the neutron proportional to its spin polarization. A polarized neutron incident on an analyzer will scatter off a helium nucleus, transferring some of its kinetic energy to the helium. The recoiling helium will collide with xenon, initiating another transfer of energy that will excite xenon atoms in the mixture. When a xenon atom transitions back to its ground state, it scintillates, releasing energy as photons. The light output from this process can be measured with photomultiplier tubes (PMTs) to detect neutron scattering events within the analyzer.

4.3.1 Analyzer Design and Assembly

A proper design was critical to the success of the analyzers requiring certain parameters to be effective in detection of neutron scattering. To start, the analyzers had to contain an internal gas pressure of 2500 PSI, requiring a strong material and a geometry with structural integrity. This had to be balanced with the ability for scintillation light to reach PMTs outside of the analyzer. Holding the high pressure gas while having an optically transparent path for light output adds to the challenge of designing the analyzers. Internal treatment of the analyzer to prepare it for effective

detection capabilities requires the design to also allow access to the inside of each analyzer.

An engineering firm was commissioned to develop the design shown in Figure 4.5. The analyzer is a 17-4 stainless steel tube with a length of 15 cm, an inner diameter of 6 cm, and 250 mm thick walls. On the ends of the analyzer are glass windows held onto the cylinder by steel flanges. The windows have 3 in. diameter and 0.75 in. thickness. The flanges holding the windows in place have 2 in. openings where PMTs can be attached to measure the light passing through the windows.

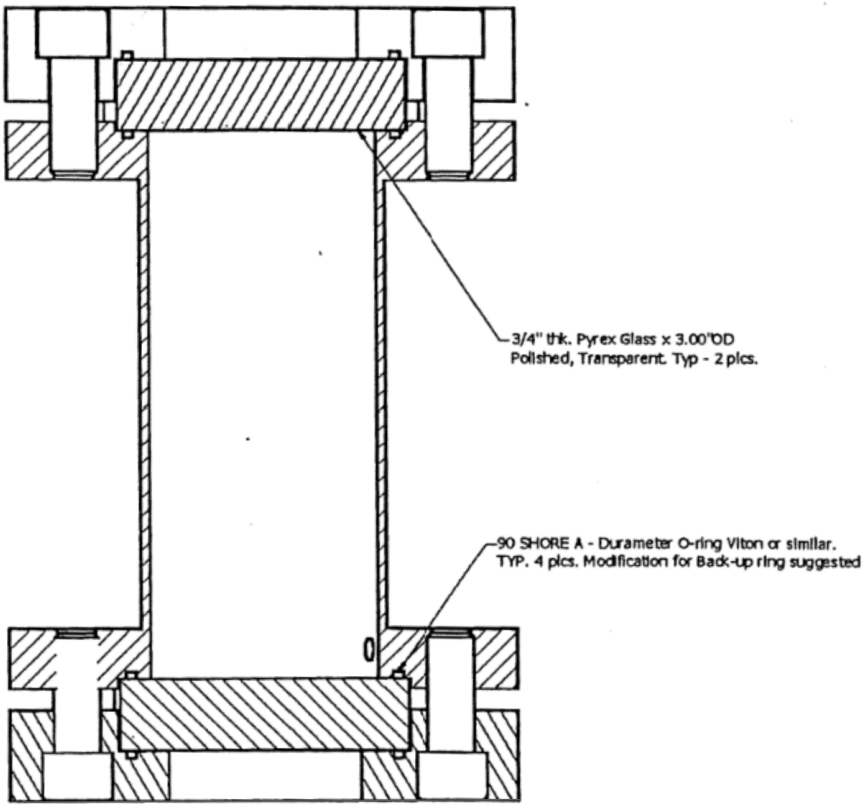

Figure 4.5: Original Analyzer Cell Design. Original design for the polarization analyzers made of stainless steel. The geometry consisted of a cylindrical tube with Pyrex glass windows on the ends. The windows were clamped in by steel flanges that were bolted into the body of the analyzer.

This original design would prove to be insufficient. In preparation of the experiment, the analyzers would be filled to 2500 PSI and stored at this pressure until needed. While being stored, a window in one of the analyzers shattered under the in-

ternal pressure, discharging high pressure gas and glass fragments in a burst of energy. No impetus for the failure could be discerned, indicating some gradual decline in the structural integrity of the glass window without any ability to predict or prevent a final failure. This was an unacceptable problem with potential consequences for the success of the experiment and personnel safety.

The exact cause of the failure remained unknown, but a number of factors could have contributed. To start, the design placed the window under a bending force, exerting dangerous tensile forces on the material. Glass has a much lower tensile strength (about 7 MPa or 10^3 psi) [61] than compressive strength (1000 MPa or 1.45 $\times 10^5$ psi) [62]. With the edges of each window clamped between the steel analyzer and flange, the internal pressure from the gas would exert force on the center of the window, creating a predominantly tensile stress on the glass.

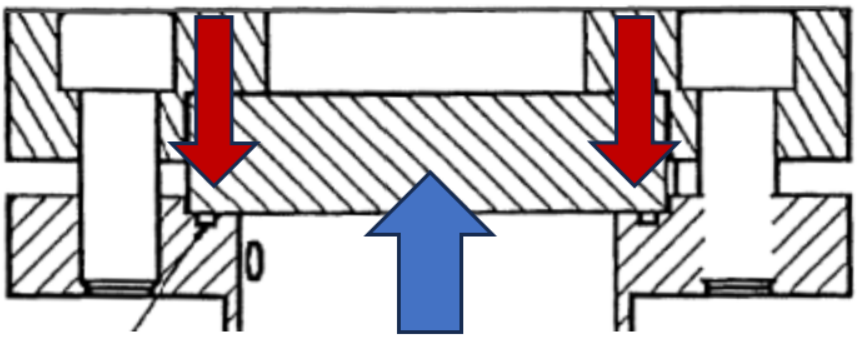

Figure 4.6: Free Body Diagram of Analyzer Windows. Direction of forces acting on analyzer window. When an internal pressure of gas is applied to the system, an outward force (blue) pushes on the center of the window. Meanwhile, the steel flange holding the window in place applies an inward force (red) along the outer edge of the window. The combination of these forces results in a shear stress on the glass window that threatens its structural integrity.

Another issue with the original design was the glass-on-steel contact holding the windows in place. With the glass held between two pieces of steel, the integrity of this contact relied on the surface purity of the glass and the steel. Any irregularity in either piece would create a point load that could cause the glass to fracture and fail. Attempts to mitigate this issue were made by placing gaskets between the glass and steel. Both rubber and kapton gaskets were tested in this capacity. Neither type of gasket was able to maintain a strong enough seal to hold the internal pressure. As the operating pressure was approached, the gaskets would warp, allowing gas to

escape. The gaskets had to be removed to keep an air tight seal on the cell, but the problems causing the glass to break persisted, leading to another failure of a window.

After two failures, the analyzer design was reconsidered. Potential correction methods and adjustments were discussed to enable the analyzers to hold the operating pressure required for the experiment. After careful consideration, a decision was made to retire the original design, in favor of a design suggested by W. Tornow [63] based on a similar ^{4}He-Xe scintillator used by Wilburn et al. [59]. The modified design is shown in Figure 4.7.

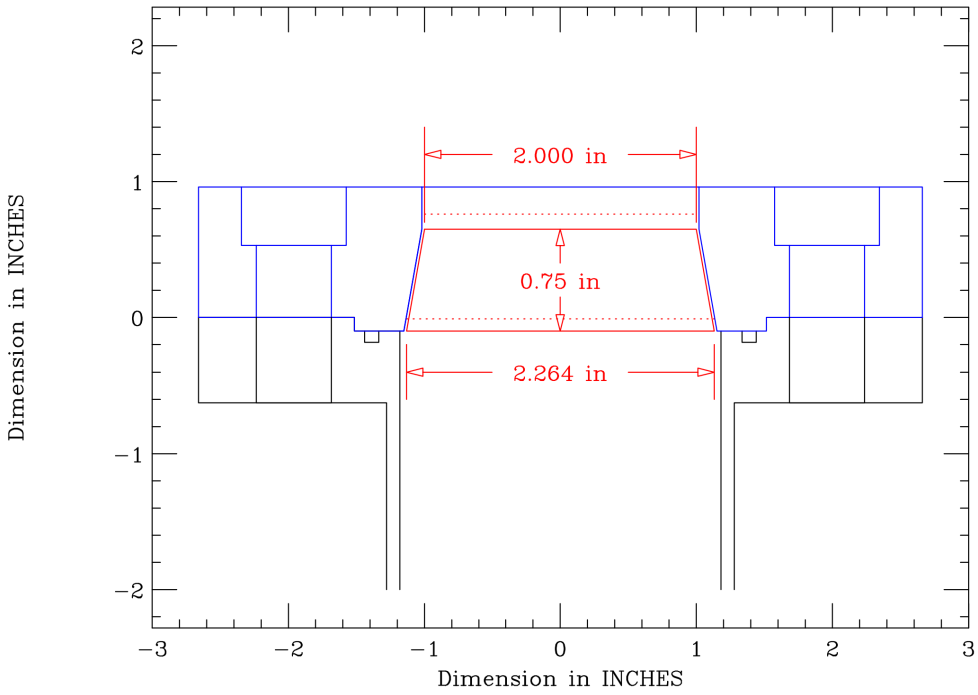

Figure 4.7: Modified Analyzer Cell Design. Modified geometry of the analyzer cell window and flange. The glass window is shaped with a beveled edge to fit into a corresponding angle in the flange. The window is held in place by a layer of epoxy, providing a protective buffer between the glass and steel surfaces.

The updated design kept the original body of the analyzer, only requiring manufacturing of new flanges for the ends of the cell. The main new feature of the design was a ten degree angled opening in the flange to hold a correspondingly beveled glass window instead of clamping one inside of a straight inset.

The glass was held into place in the flange with epoxy. Epoxy was spread evenly around the edge of the glass window. The window was lowered into the opening in the flange, and slowly rotated while being pressed into place. Rotating the window

ensured an even coat of epoxy between the glass and steel, removing any air bubbles that may have formed as the window entered the opening. The face of the window aligned with the inner face of the flange, and the epoxy layer was pressed to about 1 mm thickness. A 1 kg weight was then left on top of the window to hold it in place in the flange while the epoxy cured overnight.

The new design avoided the flaws in the original design believed to be contributing to its failure. The geometry of the flange meant that internal pressure would push the window into the walls of the flange, creating compressive forces on all edges of the glass. The glass could withstand much higher compressive forces than the previous bending forces, making it a more secure design for holding 2500 PSI of gas. Additionally, the epoxy layer between the glass and steel created a buffer layer to smooth out impurities on the surfaces, avoiding point loads that could fracture the glass.

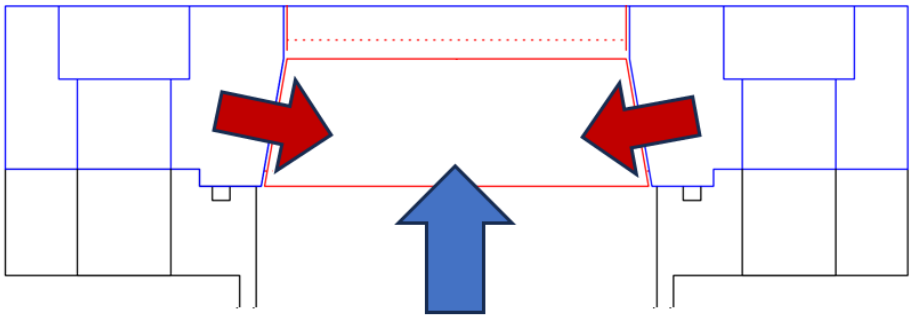

Figure 4.8: Free Body Diagram of Analyzer Windows. Direction of forces acting on new design of the analyzer window. Internal gas pressure applies an outward force (blue) on the inner surface of the window. A reactionary force (red) is applied by the flange pressing inwards along the beveled edges. All of these forces act as compressive forces on the glass, under which it is much more resilient than under shear or tensile stresses.

4.3.2 Pressure Tests

With a new design manufactured and assembled, the analyzer then had to be tested to verify its capability to contain the operating pressure of gas for the experiment. The gas handling system in Figure 4.9 was developed to perform a pressure test of the new analyzer design alongside the original design.

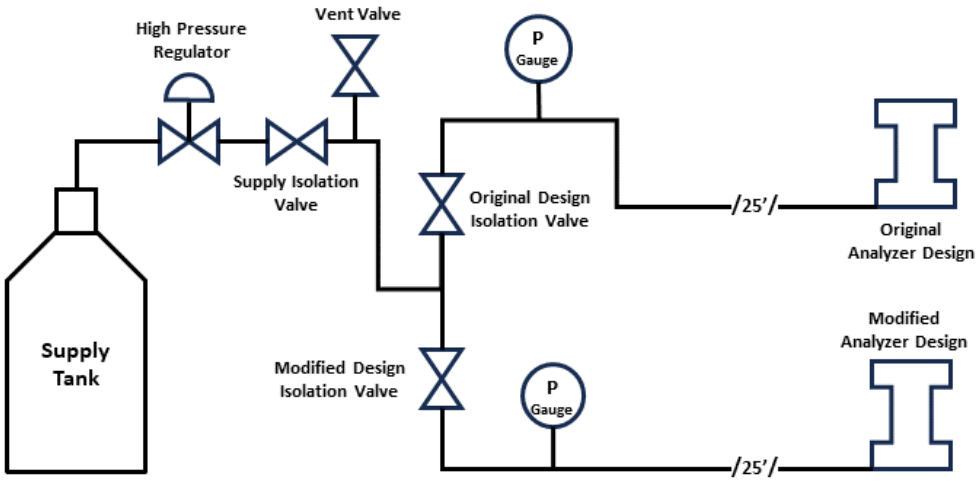

Figure 4.9: Analyzer Pressure Test Setup. Diagram of the gas handling system used for initial pressure testing of the new analyzer design. The system was designed to test two cells at once for a comparison test between the old and new designs, as well as faster quality assurance testing of each analyzer after manufacturing.

The analyzers were isolated from each other during tests to avoid ambiguity about sources of leaks or failures. In the interest of personnel safety, each cell was placed 25 ft. away from the operating station, in a tub of water to act as a blast chamber.

Instruction from the laboratory safety at TUNL requested a pressure test of at least 10% over operating pressure for approval of the design. The initial goal was thus set to about 25% over operating pressure, or 3200 PSI. Additionally, the analyzers had to maintain this high pressure for an extended period of time.

The analyzers were filled slowly to prevent injecting too much energy into the internal systems. Each cell was filled in increments of 400 PSI and left at a constant pressure for one hour. This continued until both cells reached 3200 PSI, and they were left at this pressure for 12 hours. After this time, the gas was vented to repeat the process. This procedure was repeated three times to test each cell's ability to withstand multiple cycles of filling and venting. On the final run, the cells were left at pressure for five days to verify they could hold pressure for a longer period of time.

By the end of the test, both analyzer designs had proven to hold pressure without leaks or failure of their structural integrity. Upon inspection, there were no cracks, deformities, or other signs of damage to the glass windows, providing further verification. Despite this apparent success of the original design, the previous failures still indicated unreliability, and the modified design was implemented going forward.

After selection of the new design, 8 analyzers were constructed in total, to provide 6 cells for the experimental setup, with 2 backups as a precaution. The analyzers were pressure tested (two at a time) on the system in Figure 4.9 to verify each was assembled properly. For this next wave of tests, the analyzers were tested up to 4000 PSI, for over a week each, to investigate the capability of the design. No signs of failure ever appeared during any of these tests, validating the earlier results. During one run, one analyzer was tested up to 4500 PSI. Inspection of the windows after this run did reveal some deformities in the glass, the first signs of a pressure limit for the new analyzer design. 4000 PSI was accepted as the safe limit for further tests.

By the end of the pressure tests, all 8 analyzers had been tested at 4000 PSI for over a week at a time. Each one also proved to withstand multiple filling and venting cycles. With confidence in the pressure capabilities of the analyzers, the next steps in their preparation for the experiment could proceed.

4.3.3 Surface Treatment

Each analyzer required certain preparation techniques inside to maximize the scintillation light output measured by the PMTs.

Reflective Surface

Light produced by the scintillation process is released isotropically within the cell. Ideally, all of the light eventually reaches one of the PMTs on either end of the cell. For this to happen, the light will likely reflect off the inner walls multiple times before finding its way to either end of the cell. With a reflectivity of 50% - 65% [64] the steel walls of the cell cause a significant drop in light output, and therefore efficiency, of the analyzer. To avoid this, a reflective layer of magnesium oxide (MgO) is applied to the walls. MgO reflects light with only about 5% light loss [65], greatly enhancing the analyzer's ability to preserve light output.

The method for coating the walls of the cell with MgO was combustion chemical vapor deposition, shown in Figure 4.10. A vacuum environment is not required for this type of deposition, making it a convenient and efficient method for covering the inner walls of the cell with MgO. Magnesium ribbon is ignited and burned below one of the openings of the analyzer. As the magnesium burns, the smoke released contains particulates of the oxidized form of magnesium (MgO). A cover placed over

the top opening of the cell traps the smoke inside. The smoke cools and the MgO particles collect and deposit on the inner walls of the cell. The goal in this procedure was to deposit a layer about 1 mm thick (roughly 200 $\frac{\mu g}{cm^2}$). The analyzer was flipped halfway through the process to evenly coat the entire cell.

(a) Burning of magnesium to produce MgO for coating the analyzer

(b) Close-up image of final layer of MgO to demonstrate desired thickness

Figure 4.10: Reflective Layer Coating Procedure. Coating the inner walls of an analyzer with MgO through vapor deposition. A magnesium strip is burned below the analyzer, releasing a vapor of MgO that cools and settles on the inner walls.

Wavelength Shifter

Scintillation inside the analyzer produces light in the very ultra violet region, but conventional PMTs are sensitive to visible light. The light output of the analyzer had to be converted with a material known as a wavelength shifter (WLS) to be detectable with PMTs. Diphenylstilbene (DPS) was used in this capacity due to its appropriate emission spectrum and short luminescence time. [66]

To optimize the wavelength shifting effect, the inner surfaces of the analyzer windows and the inner wall of the analyzer body were coated in thin layers of DPS.

The DPS layer on the wall was applied on top of the reflective MgO coating, with a thickness of about 200 $\frac{\mu g}{cm^2}$. Each window was coated with about 50 $\frac{\mu g}{cm^2}$ of DPS. This ensured conversion of the light output to visible light before reaching the PMTs.

Layers of DPS were applied to the analyzer through evaporative deposition, a method of physical vapor deposition for thin-film coating of surfaces. This procedure was performed with a vacuum evaporator available at TUNL. The evaporator consisted of a bell jar chamber that was evacuated to vacuum pressure by a diffusion pump. Inside the chamber was a pair of electrodes to supply an electric current that would evaporate substances through resistive heating. The evaporator setup is pictured in Figure 4.11.

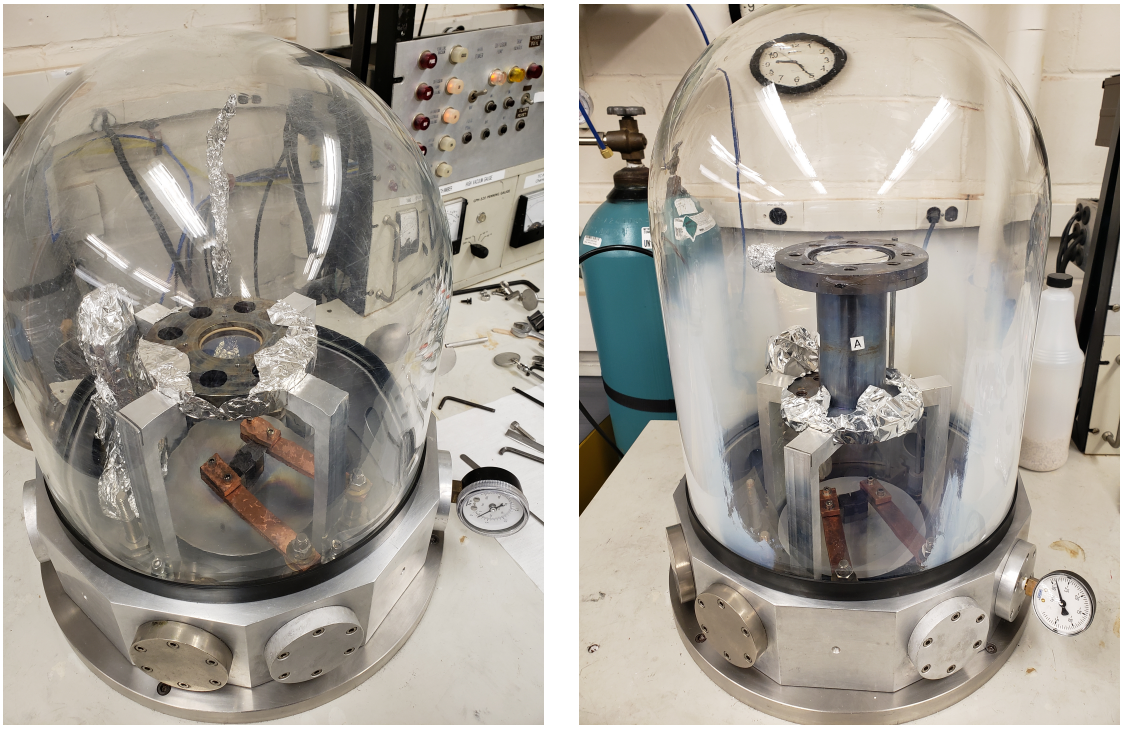

(a) Coating an analyzer window with DPS

(b) Coating the inner walls of the analyzer body with DPS

Figure 4.11: Evaporative Deposition of Wavelength Shifter on Analyzer. Shown are images of the bell jar chamber of the vacuum evaporator used for deposition of the wavelength shifter (DPS) on the inner surfaces of each analyzer.

A precise amount of DPS was carefully measured into an evaporative container known as a "boat", pictured in Figure 4.12. The mass of the DPS was measured using a high precision (0.01 mg) scale. The required mass to coat a surface was

determined with a calibration run, in which a layer was evaporated on the surface of an aluminum foil sheet. The thickness of the layer on the foil was calculated from precise measurements of the mass and area of deposition of the foil.

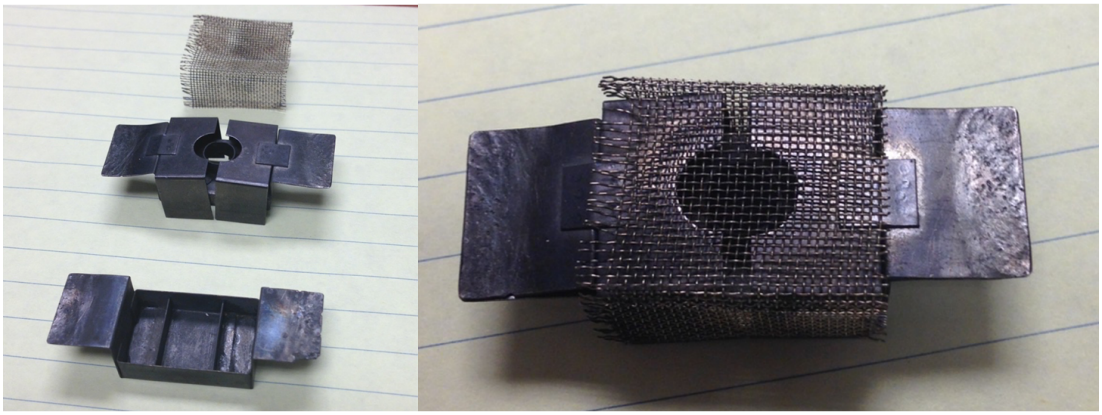

(a) Separated into pieces **(b)** Fully assembled

Figure 4.12: Boat for Evaporation Deposition. Boat used for evaporation deposition of diphenylstilbene (DPS) was a wavelength shifter (WLS) on inner surfaces of the analyzer. DPS powder was measured into the boat and enclosed with the lid. The hole in the lid provides a path for DPS vapor to expand directly towards surface for coating. The wire mesh was wrapped around the boat to prevent large crystals of the DPS from escaping during evaporation, ensuring all material was properly evaporated. The "wings" of the boat connected to the electrodes within the evaporator chamber to close the electrical circuit and induce resistive heating in the boat.

The boat containing DPS was secured between the two electrodes in the bell jar chamber. A wire mesh was wrapped around the boat to prevent large crystals of DPS from escaping during evaporation. The target surface was positioned several inches above the boat. With the bell jar chamber sealed, the diffusion pump evacuated the volume below 10^{-5} torr, to provide a clean environment for deposition.

With the chamber at high vacuum, a voltage difference was applied between the two electrodes, inducing a current through the boat. The resistance of the boat generated heat that slowly melted and evaporated the DPS crystals. The DPS vapor would expand to fill the volume of the bell jar, until it made contact with a surface where it would cool and deposit as a fine layer. For even coating across the entire body of the analyzer, this procedure was repeated after rotating the analyzer between runs. With both the DPS and reflective MgO layers in place, the analyzers were prepared for optimal light output collection from neutron detection.

4.3.4 Gas Handling Techniques

Each analyzer required a 90:10 mixture of He-Xe gas at 2500 PSI with as little contamination as possible. Pollutants in the gas such as water vapor would interfere with the scintillation process inside and decrease the efficiency of the analyzers. Gas handling techniques were implemented to achieve a "clean", high-pressure gas mixture.

Two different gas handling systems were used to fill analyzers: one for a xenon fill to 250 PSI (10% of the operating pressure) and one for the helium fill up to the final pressure of 2500 PSI. The xenon fill was done using a filling station in the Laboratory for Experimental Nuclear Astrophysics (LENA) at TUNL, shown in Figure 4.13.

Figure 4.13: LENA Gas Handling System. Gas handling system in the Laboratory for Experimental Nuclear Astrophysics at TUNL used for evacuating analyzer cells and filling with xenon. The system used a combination of a scroll pump and turbo pump to achieve high vacuum in the desired volume. The set of valve controls were then used to carefully fill the analyzer to a desired pressure.

The system was designed to evacuate a target volume to vacuum pressure and then refill it with a desired mixture of gases. A schematic of the gas handling system is displayed in Figure 4.14 to offer a more detailed look at the components of the setup to understand its operation.

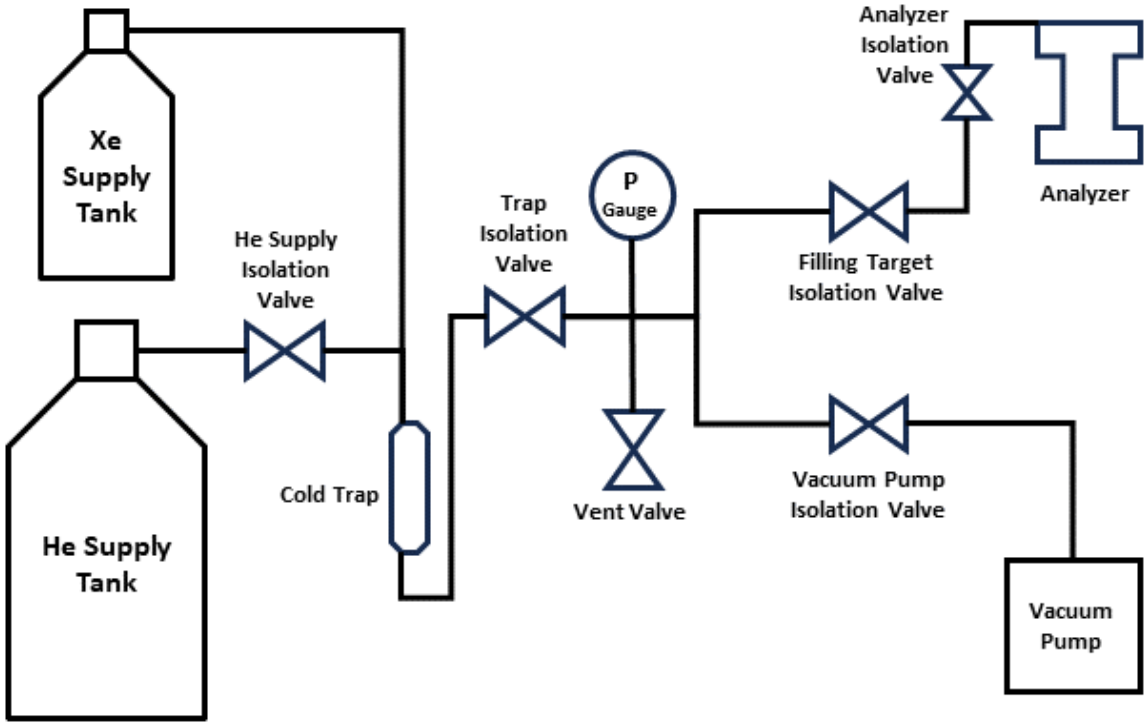

Figure 4.14: LENA Gas Filling Station Schematic. Analyzers were filled with xenon up to 250 PSI using the LENA filling station. The station was connected to two supply tanks of xenon and helium. The helium supply isolation valve provided the option to fill solely with xenon or with a xenon-helium mixture. The system included a cold trap that could solidify any contaminants (such as water vapor), when submerged in a liquid nitrogen bath. The cold trap could also be used for recovering xenon from volumes as xenon would solidify in the cold trap as well. A high precision pressure gauge allowed for careful filling of detectors to desired pressures. Two isolation valves leading to the analyzer helped to protect the coatings on its inner surfaces. A rush of gas due to exposure to high pressure could disrupt the powdered layers deposited inside of the analyzer. Two types of vacuum pumps were included to evacuate the volume of the filling station to remove any contaminating gases from the system before filling. A scroll pump decreased the system pressure from atmospheric pressure down to $\approx 10^{-2}$ mbar, the safe starting pressure for the turbo pump. The high vacuum turbo pump could then evacuate the system down to pressures below 10^{-6} mbar, to ensure the removal of any contaminants from the gas lines.

High vacuum was achieved within the system with a dual pump setup. A scroll pump was used to lower the pressure from atmosphere to about 10^{-2} mbar, an acceptable starting pressure for a turbo pump to avoid causing damage. A Varian Turbo-V 70 pump would then evacuate the system down to high vacuum. A digital high vacuum pressure gauge monitored the pressure just above the inlet of the turbo pump. Each analyzer was left to pump down to vacuum for about a week, achieving a pressure in the range of 3×10^{-7} mbar to 7×10^{-7} mbar. The finite length of tubing between the pressure gauge and the analyzer meant the pressure in the analyzer would be higher than the reading on the gauge. Later tests of the efficiencies of the analyzers would demonstrate these parameters would produce a clean enough gas mixture for neutron detection.

With the system pumped down to vacuum, an analyzer could be filled with a sufficiently pure volume of xenon. Filling the analyzer was done in small, gradual increments of increasing pressure in order to protect the coatings on the inner surfaces. A rush of air into the cell could disturb the deposited layers, decreasing the efficiency of an analyzer. The analog pressure gauge on the gas handling system was used to monitor the pressure during filling.

The helium supply and vacuum pump isolation valves were kept closed as those lines were not needed for a xenon fill. Then to start, the analyzer isolation valve was closed to limit the amount of xenon entering the system. Xenon was slowly released from the supply into the lines up to about 50 PSI. The analyzer isolation valve was then slowly opened to fill the analyzer with xenon. As the filling volume increased, the pressure would decrease back below 50 PSI. Once at equilibrium, the analyzer would be isolated again to fill the lines with more xenon. This process was repeated, gradually increasing the filling pressure in the lines, until the entire system reached a pressure of 250 PSI, the 10% partial pressure intended for the experimental run.

The helium fill of the analyzers was performed with a gas handling system developed for the experiment in the target room (known as the "Gamma Vault"). The system is broken into multiple sections with an overall setup designed for safe and effective handling of the high pressures needed for operation. There are three main work areas: an interior gas manifold, an exterior gas manifold, and a shielded gas recovery system. A schematic of the system separated into these sections is provided in Figure 4.15.

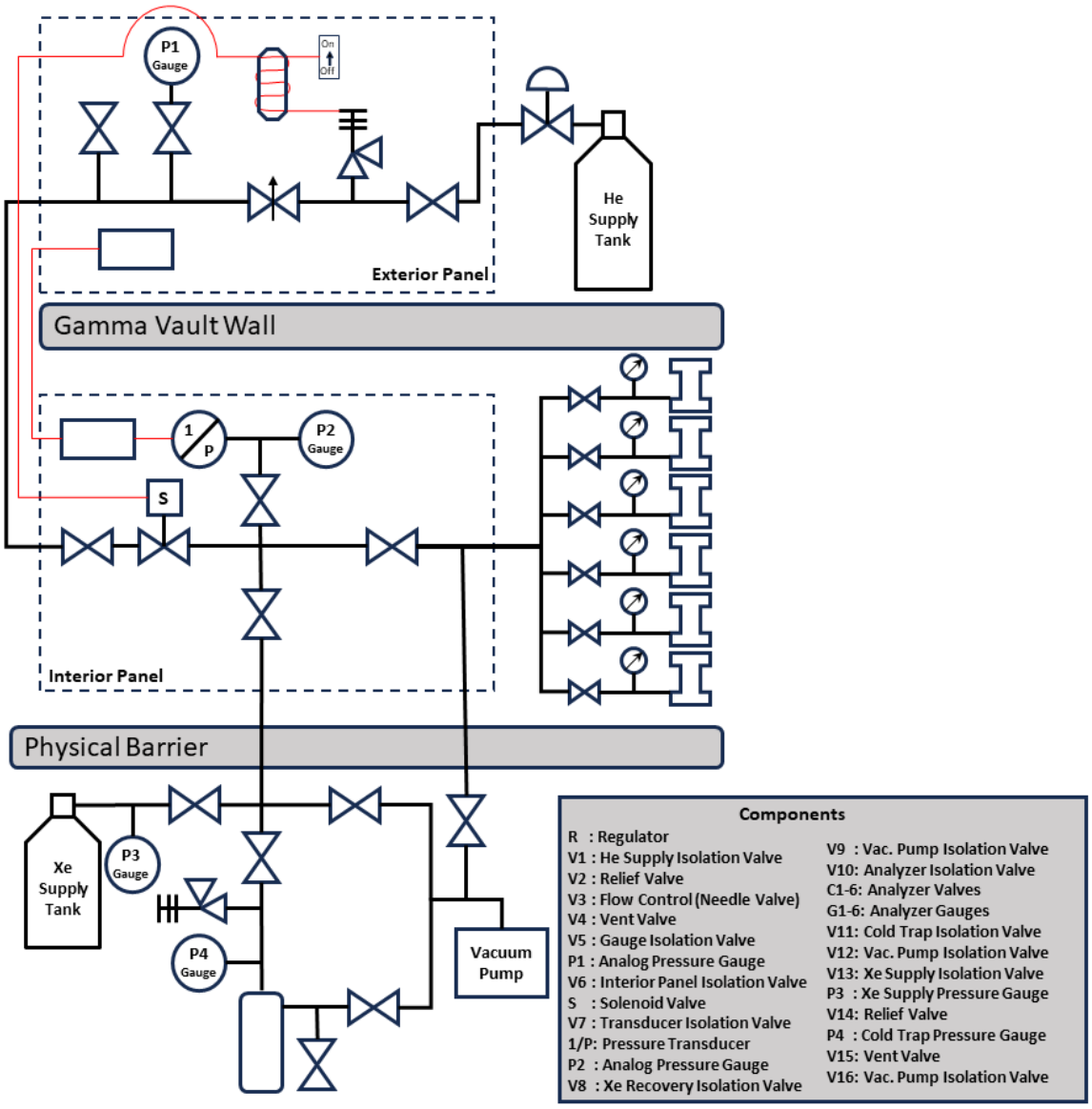

Figure 4.15: Gamma Vault Gas Handling System. Gas handling system used during the experimental run for filling of the analyzers at high pressure. The system could be controlled from outside the Gamma Vault for safe operation during beam time. A gas recovery section was included to recover as much xenon from the mixture as possible using cryogenic cooling of a cold trap.

The interior manifold diverted gas flow between the different parts of the setup. It connected the analyzers, the exterior manifold, and the gas recovery area with the ability to isolate any of these sections from the rest. As the closest operating area to the analyzers, it was only used when the analyzers were at low pressure.

This manifold also contained a pressure transducer and an analog pressure gauge. The transducer relayed pressure readings to digital readouts on both the interior and exterior panels, while the analog gauge provided a backup reading for verification. The interior manifold also included a solenoid valve that could be controlled from the exterior manifold. The solenoid valve would trigger closed if a flow switch on the exterior panel registered too high of a flow rate (concerning behavior when dealing with high pressure systems).

The exterior gas manifold was the main operation station when handling high pressure in the system. This area was the location of the helium supply tank, fitted with a high pressure regulator. The regulator controlled the output of the helium supply to provide a specific pressure, lower than the internal pressure of the tank. A needle valve was then included to offer flow control to the rest of the system. This enabled slow helium filling of the system and analyzers, preventing excessive forces on the different parts of the setup. The digital readout connected to the pressure transducer inside the gamma vault allowed precise monitoring of the internal pressure. An overpressure relief valve connected to a flow switch ensured pressures remained at safe levels for the capability of the analyzers. The relief valve was set to open at 2750 PSI. An excessive flow of air through the relief valve would trigger the flow switch to close the solenoid valve on the interior panel, protecting the user and the analyzers from a rapid increase in pressure in the system. Finally, a vent valve on the manifold provided the ability to release gas from the system in a controlled manner.

The final area of the gas handling system was the gas recovery station. The main objective of this station was a safe and efficient means for recovering as much xenon gas from the system as possible. As a safety precaution, any work performed on the experimental frame or detectors could only be done when the analyzers were at a pressure below 250 PSI. Being a rather valuable resource, conservation of the xenon was prioritized however possible in the experimental design. Instead of releasing the entire gas mixture from the system into the atmosphere, the recovery station was used to temporarily store the xenon while the helium was released.

The recovery station exploited the drastic difference between the temperatures for phase changes of helium and xenon. Xenon condenses to a liquid at 165 K and then solidifies at 161 K, but helium remains a gas down to a temperature of 4.2 K. When a mixture of the two gases is cooled by a liquid nitrogen bath (at a temperature of 77 K, the xenon will solidify and separate out from the helium. The volume can then be

vented out to release the helium while the xenon remains in the liquid nitrogen trap. The xenon can be stored as a solid until the time arrives to refill the system.

This procedure was used during the run whenever work was performed on the experimental frame. It was also implemented at the end of the run to recover as much xenon as possible back into the supply tank.

4.3.5 TUNL Tandem van de Graaff Beam Test

After preparation of the analyzers was completed, their capabilities in neutron detection were tested with the TUNL Tandem van de Graaff accelerator. This accelerator has the ability to provide beams of hydrogen, helium, and other light ions. Additionally, it is capable of producing nearly monoenergetic neutron beams, making it a valuable resource for characterizing neutron detectors.

The floor plan of the TUNL Tandem van de Graaff Laboratory is provided in Figure 4.16.

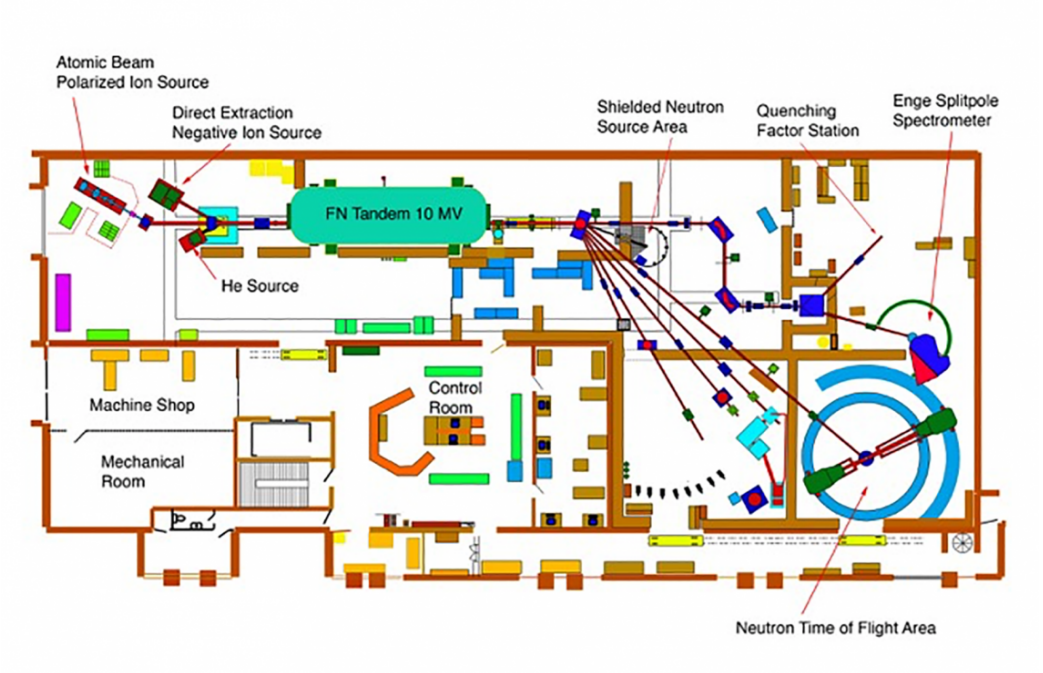

Figure 4.16: TUNL Tandem van de Graaff Accelerator Floor Plan. The TUNL tandem van de Graaff accelerator can provide neutron, proton, and light ion beams to a number of target rooms. Neutron detector tests are often performed in the Shielded Neutron Source Area (Top, Center) or the Neutron Time-of-Flight Area (Bottom, Right). Image Credit: TUNL Website

To verify the analyzers were ready for an experimental run, this beam test had to demonstrate their ability to produce light output as a result of neutron scattering events. Five analyzers were prepared with a gas mixture of 500 PSI partial pressure of helium and 100 PSI partial pressure of xenon. They were all tested in the "Shielded Neutron Source Area" where the tandem accelerator provided an 8 MeV neutron beam. The setup used is shown in Figure 4.17.

Figure 4.17: Setup for Tandem Beam Test of Analyzers. An analyzer cell was placed in the beam line at the center of a ring of liquid scintillators. The accelerator provided an 8 MeV neutron beam. Three of the liquid scintillators were used to detect neutrons that had scattered inside the analyzer. The coincident signals between the analyzer and a neutron detector enabled analysis of the kinematics of the scattering.

Each analyzer was centered on the beam axis at the center of a ring of liquid scintillator neutron detectors. The neutron detectors would collect neutrons that had scattered at different angles in the analyzer to provide kinematic information about the scattering. Although several detectors are shown in Figure 4.17, only three of them were used to collect data, placed at 52°, 85°, and 150° from the beam axis.

Data acquisition was performed with electronics available in the tandem accelerator control room. An analog-to-digital converter (ADC) was used to measure and quantify the light output of the detectors. The details of ADCs are covered in Section 4.5.2, but the important note for now is that an ADC provides a spectrum of the light output from scintillation events within a detector. Since the light output of a scintillator is linear with respect to the energy deposited by a particle, the ADC spectrum effectively measures this energy deposition.

All of the analyzers demonstrated strong capabilities in producing light output as a result of scintillation from the neutron beam. An (uncalibrated) ADC spectrum is provided in Figure 4.18.

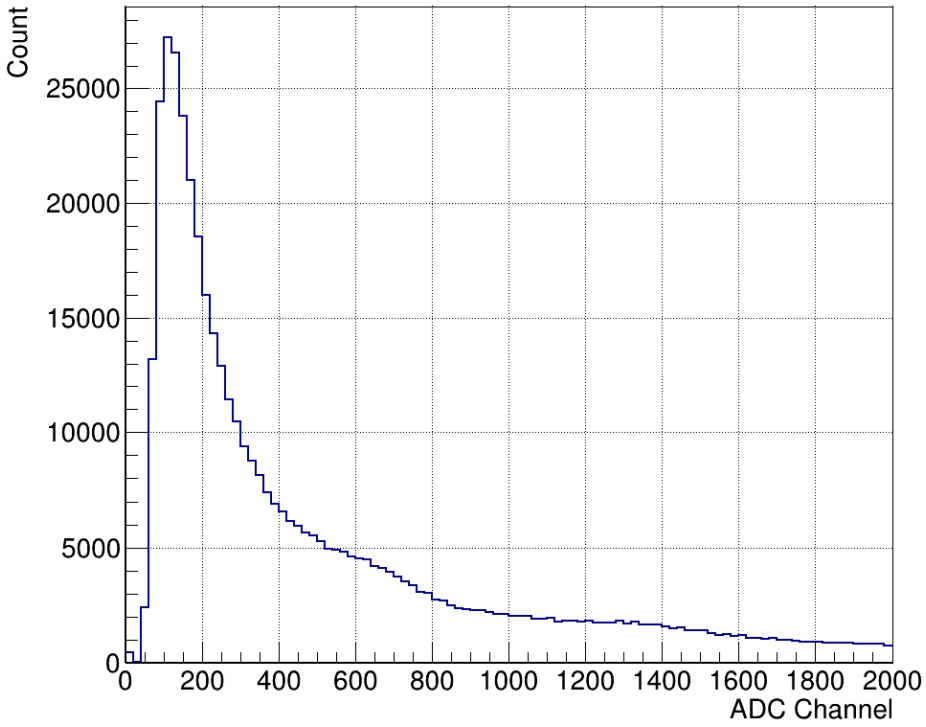

Figure 4.18: ADC Spectrum of Pulse Integration from Analyzer Signals. Uncalibrated ADC spectrum measured within an analyzer. This spectrum does not distinguish between neutrons and photons and thus includes both types of events.

This spectrum is useful for observing the light output from the analyzer, but it does not discern between scintillation events caused by neutrons vs photons. Neutron events were isolated from this spectrum using a pulse shape discrimination (PSD) analysis made possible by the liquid scintillators surrounding the analyzer. The background and methodology of PSD are covered in Sections 4.2.4 and 5.2.3, respectively.

Using this technique, an ADC spectrum can be generated for neutron scattering events inside an analyzer that coincide with detection at a scattering angle based on the location of the liquid scintillator. In this way, an energy spectrum can be produced for each of the measured scattering angles. A sample histogram is shown in Figure 4.19.

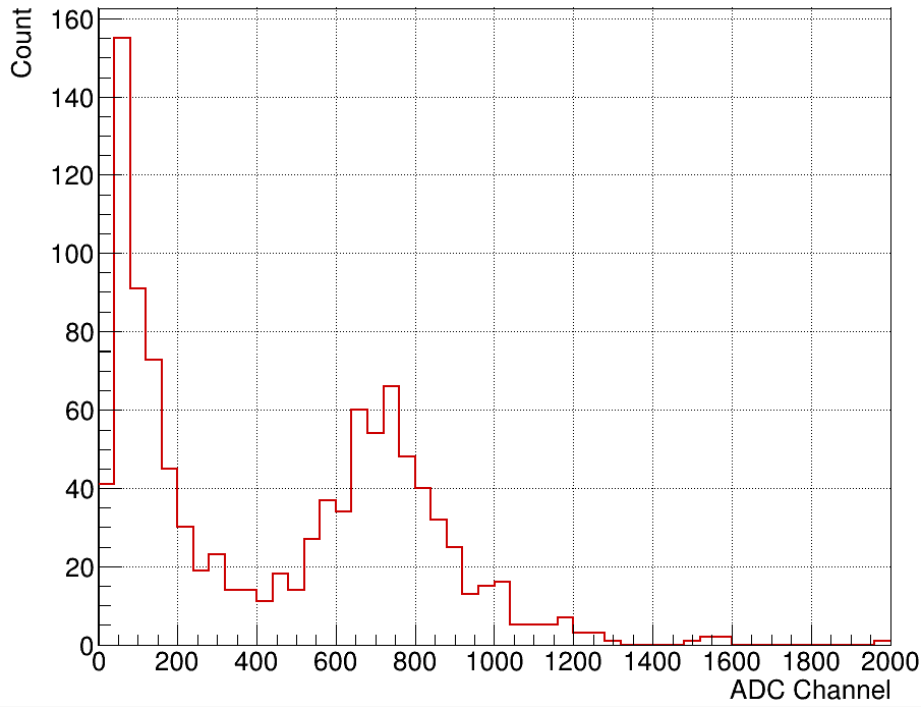

Figure 4.19: ADC Spectrum of Neutron Events in Analyzer. PSD analysis of the data can filter out signals produced by photons in the analyzer, resulting in a spectrum produced by neutron scattering events. In this case, the recoil energy curve of the neutron scattering becomes apparent in the spectrum. This curve is peaked at an ADC channel corresponding to the energy deposited by the neutron based on its scattering angle.

The defining feature of this spectrum is the *recoil energy curve* of the neutron scattering. The peak of this curve represents the mean energy deposited by the neutron which has a direct kinematic relationship to the scattering angle.

This spectrum can be generated for each of the three scattering angles covered by neutron detectors to demonstrate how the energy deposition increases for more backward scattering. Normalizing each spectrum, they can be compared side-by-side in the histogram shown in Figure 4.20.

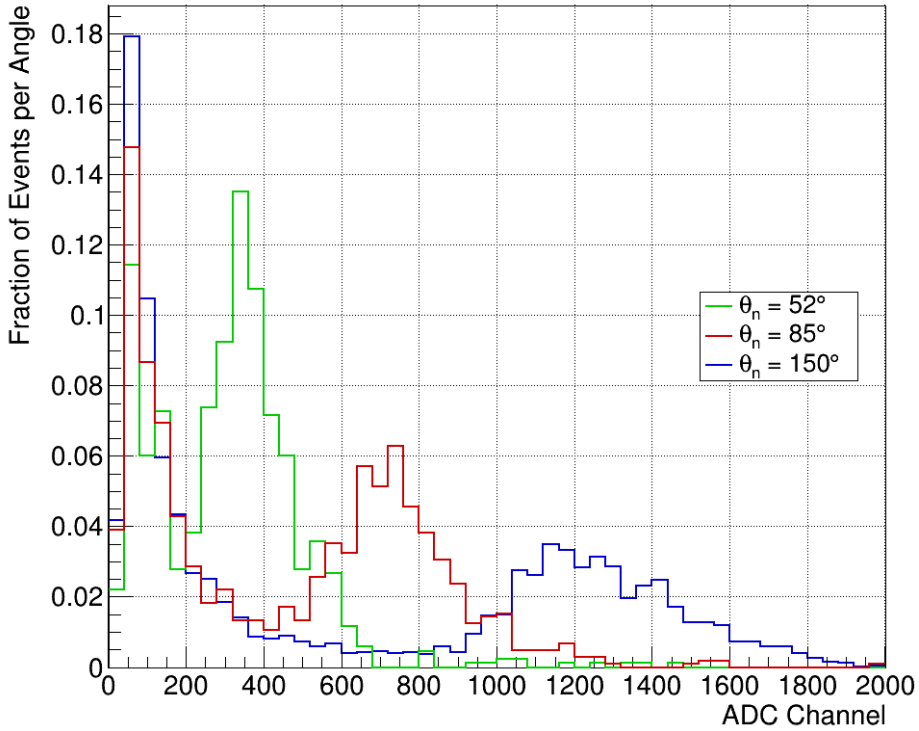

Figure 4.20: ADC Spectra of Neutrons Scattering at Three Different Angles. Comparison of the recoil curves of neutrons scattering in the analyzer for three different angles. The deposited energy increases with increasing angle, as would be expected kinematically.

Thus, this beam test verified the capabilities of the analyzers as neutron detectors, providing confirmation that they were prepared for use in the experimental run.

4.3.6 TUNL Tandem van de Graaff Timing Test

During analysis after the experimental run, a curious feature in the data from the analyzers emerged. As discussed in Section 5.3.1, part of the analysis includes a coincidence requirement between signals from the two PMTs on the ends of each analyzer. Any neutron scattering within the active volume of an analyzer would generate enough light output to be measured by both PMTs. Thus, events were identified within the analyzer when two signals were received from the PMTs within a short time window. For an analyzer with a height of about 6 in., there was not much expectation for the light to take much longer than a few nanoseconds to reach either PMT. Therefore, the time difference between signals from the PMTs should only ever be a few nanoseconds, and so a preliminary cut was applied at ±10 ns.

However, inspection of the data after the run demonstrated time differences on the order of 20 or 30 nanoseconds, as demonstrated in Figure 4.21.

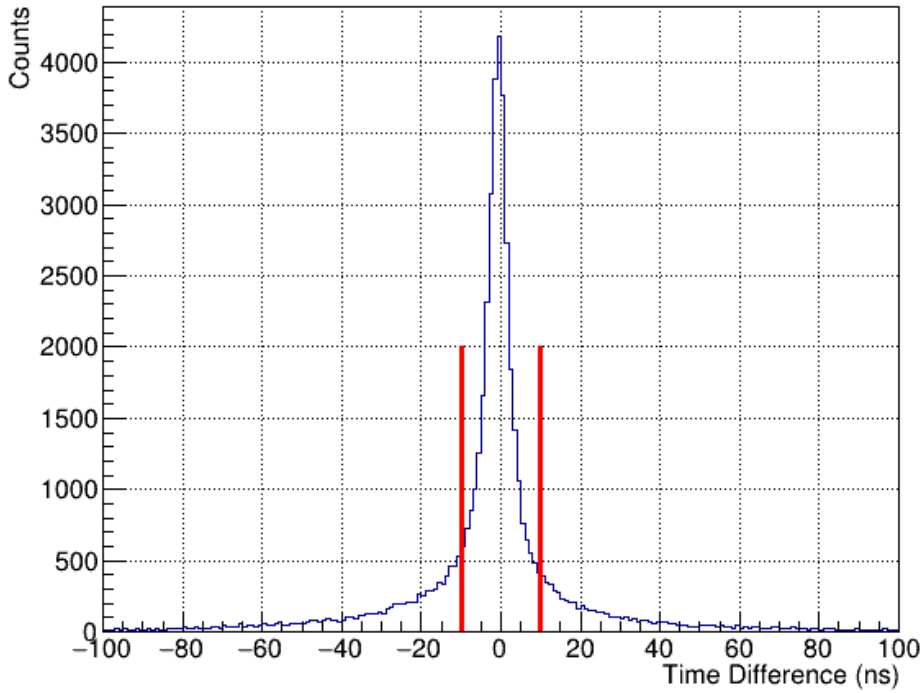

Figure 4.21: Time Difference Between Signals in Analyzer. Sample histogram of the signal time differences between two PMTs on an analyzer. A ± 10 ns cut is shown in red to invoke a coincidence requirement within the analyzer. With a number of events exhibiting time differences of 20 or more nanoseconds, it is evident that a finite amount of these are removed from the analysis. The amount turns out to be about 25% of total recorded events.

With a wider peak in this time difference spectrum than expected, selection of this cut parameter played an important role in the analysis. Too narrow of a timing window would remove too many neutron events, lowering statistics and skewing the measurement. Too wide of a cut would include too many background events, which would also be a problem for the integrity of the measurement. Furthermore, it was unclear whether the shape of this histogram truly reflected the nature of the analyzer or it was a manifestation of an error in the electronics or analysis software.

Another beam test was scheduled at the TUNL Tandem van de Graaff Accelerator to investigate the timing behavior within the analyzer. A secondary goal of the test was to determine if the larger than expected time difference was related in any way to the pressure of gas inside the analyzer. Three analyzers were prepared with internal

pressures of 300, 500, and 700 PSI, all with the standard 90:10 He-Xe gas mixture.

The analyzers were tested in the "Neutron Time of Flight Area" of the Tandem Lab which is visible in the lower right corner of Figure 4.16. The accelerator was tuned to provide a 3 MeV neutron beam in order to match the typical energies of neutrons detected during the experimental run. Each analyzer was centered on the beam axis 193 cm away from the neutron source. A liquid organic scintillator detector was placed directly behind the analyzer at 462 cm from the neutron source. This "zero degree" detector was included to monitor beam timing.

A sample histogram of the time difference spectrum for an analyzer during the beam test is provided in Figure 4.22.

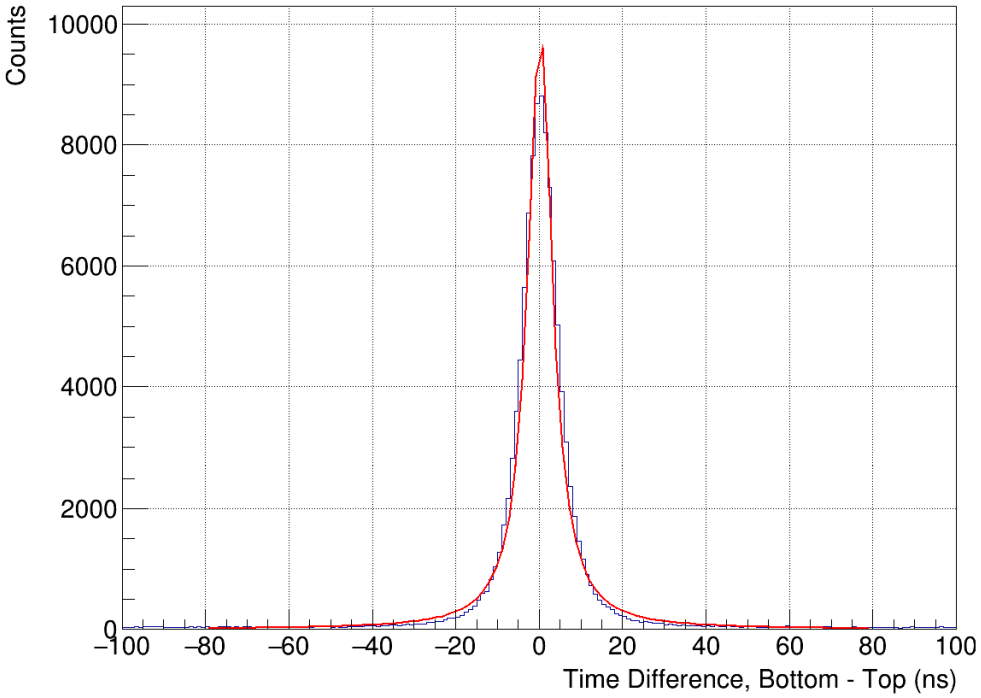

Figure 4.22: Time Difference Between Signals in Analyzer from Beam Test. Spectrum of time difference between signals within an analyzer. "Bottom" and "Top" refer to each of the PMTs on the ends of the analyzer based on their geometric orientation with respect to the analyzer. The data was fit to a Lorentzian distribution (shown in red) to characterize the width of the peak.

The timing spectrum was fit to a Lorentzian-like distribution to characterize the

width of the peak. A Lorentzian distribution has the functional form

$$f(x) = \frac{1}{\pi} \frac{\frac{1}{2}\Gamma}{(x - x_0)^2 + (\frac{1}{2}\Gamma)^2}, \tag{4.6}$$

where x_0 is the mean of the distribution and Γ is the width of the peak. This fit was performed for each of the three analyzers implemented in the beam test, as well as all six analyzers used during the experimental run. The width of each distribution was extracted from the fit to plot as a function of the internal pressure of the analyzer. This plot is shown in Figure 4.23.

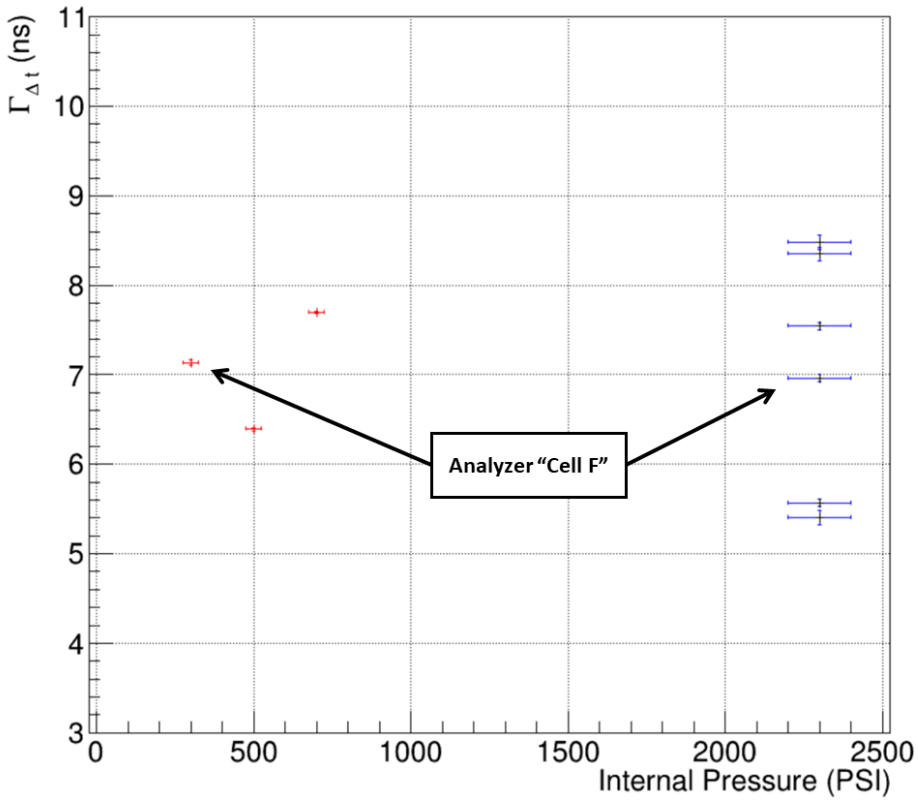

Figure 4.23: Signal Timing Difference in Analyzer vs Gas Pressure. The time difference spectra for signals coming from the two PMTs on each analyzer were fitted to a Lorentzian distribution. The characteristic widths of these fits were then plotted against the internal gas pressures of the analyzers, shown here. It is clear there is no strong dependence on the pressure. However, a notable feature is the rather similar value for the same analyzer (Cell F, labeled in the plot) in both runs, offering evidence that the timing difference is an internal property of each analyzer.

It is evident from Figure 4.23 that the time differences within the analyzers demonstrated no dependence on the internal pressure. Every analyzer had rather similar peak widths in their spectra. The reproduction of this behavior during both the experimental run and the beam test verified that the timing difference inside an analyzer was a feature of its neutron detection ability.

The confirmation of the timing behavior within an analyzer provided confidence that a wider cut on the time difference could be implemented and still be including "real" neutron events. To determine where to apply a cut, different timing windows were tested to determine the fraction of total events included as the window was expanded.

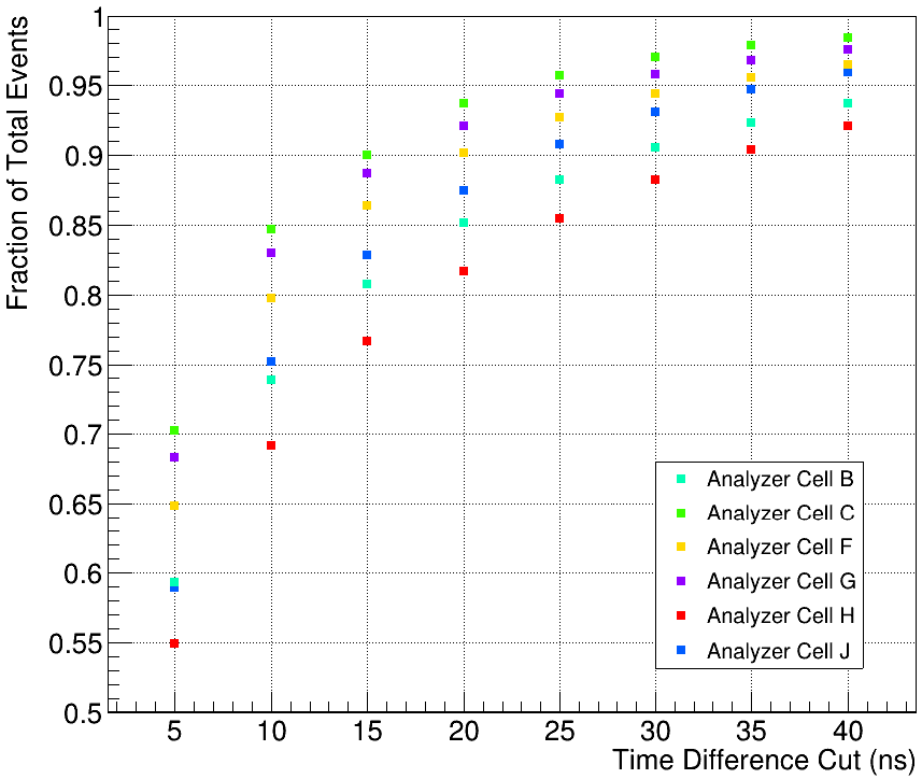

Figure 4.24: Fraction of Events Included in Analysis as a Function of the Cut Applied to the Time Difference. To determine where to apply a cut on the time difference between analyzer signals, the fraction of events included in the analysis was calculated for a series of possible cut values. Widening the cut above ±10 ns can increase the number of events included by up to 20%.

Figure 4.24 illustrates how extending the allowed time difference from 10 ns to 25 or 30 ns adds up to 20% of the total events back into the analysis. This provides a

noticeable improvement to the statistics, and therefore uncertainties, in the analysis; a valuable addition for a precision measurement.

4.4 Organic Scintillator Neutron Counters

On each side of an analyzer were six neutron detectors obtained from the *Blowfish* array. These detectors used BC-505 liquid organic scintillator for neutral particle detection. As discussed in Section 4.2.4, this type of detector provides excellent capability in distinguishing between neutrons and photons through pulse shape discrimination. A diagram of a Blowfish cell is shown in Figure 4.25.

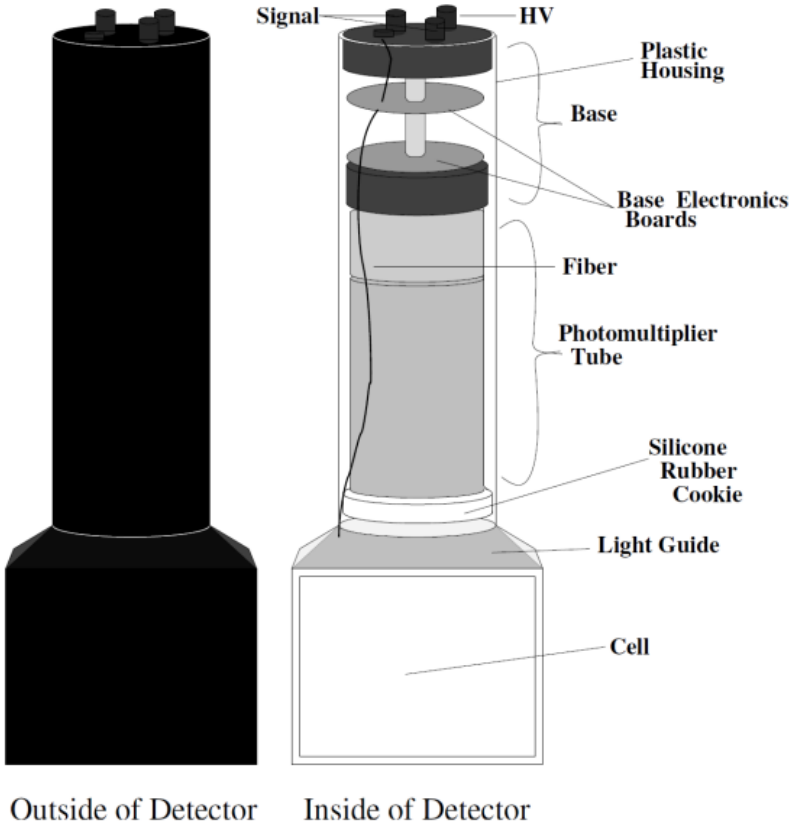

Figure 4.25: Diagram of Neutron Detector from Blowfish Array. Diagram of the components of a neutron detector from the Blowfish array. The "cell" of the detector is a volume of BC-505 liquid organic scintillator, offering excellent neutral particle ID capabilities. The PMTs used were Phillips 2262B models.
Image Credit: B. Bewer [67]

The active volume of each detector is 7.6 cm × 7.6 cm × 6.4 cm of BC-505 contained in a 0.32 cm thick Lucite cell. The scintillator cell is then connected to a Phillips 2262B PMT, optically coupled through a 4.5 cm light guide.

Preventing light loss was imperative in the assembly of these detectors, so steps were taken to mitigate light leaks from the scintillating cell. A reflective coating was painted on the outside of the Lucite cell which was then wrapped in aluminum foil. These two layers reflected light back within the cell until it reached the lens of the PMT. These detectors could also be rather sensitive to light leaks into the cell from ambient light, so this had to be mitigated as well. The cell was thoroughly wrapped in black tape which blocked light from entering the active volume and triggering the PMT.

The neutron counters were assembled into "cages" of six detectors, as shown in Figure 4.26.

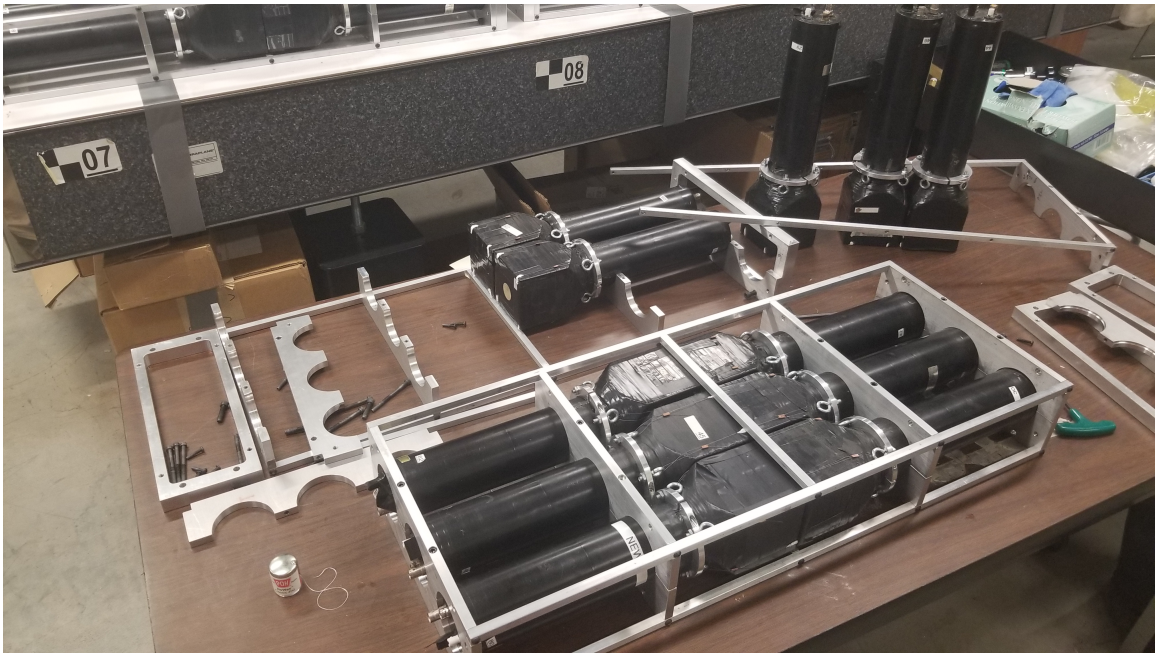

Figure 4.26: Neutron Detector Cage Assembly. Liquid scintillating neutron counters were assembled into groups of six in "cages" to be placed on either side of a polarization analyzer. This assembly provided sufficient solid angle coverage on either side of an analyzer to measure a scattering asymmetry of polarized neutrons.

The detectors were held together, face-to-face to create a detection area of 22.5 cm × 13 cm on each side of an analyzer. Arranging the detectors in these cages provided easy access to groups of detectors during orientation swaps for testing instrumental

asymmetries between detectors. Figure 4.27 provides a view of a fully assembled station within the experimental setup.

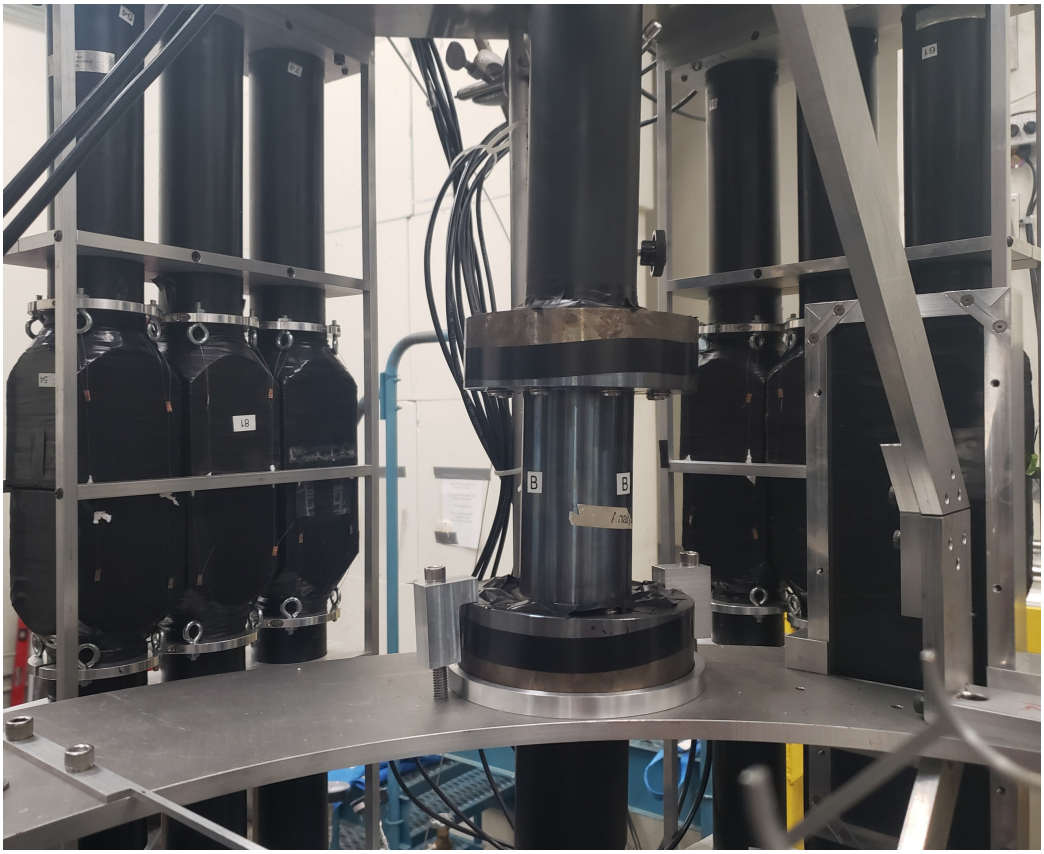

Figure 4.27: View of Detector Station from Target. From the perspective of the target, the counting detectors sit to the left and right of the polarization analyzer, positioned to measure the neutron scattering asymmetry in the analyzer.

4.5 Electronics and Data Acquisition

As the analyzers and the neutron counters detected particles, they produced electronic signals that contained quite a bit of useful information about the detected particles. Access to this information required interpretation into understandable data for users. Conversion of these signals into digital data was performed by a series of electronic modules. This section outlines the electronics and data acquisition (DAQ) systems used to record experimental data.

4.5.1 Discriminators

As signals passed from the detectors to the electronics, there was a level of background electronic noise that had to be removed to isolate the physically meaningful signals. Filtering of this noise was done with CF8000 constant fraction discriminators. The discriminators allowed signals to pass only when they exceeded a user-set voltage threshold. Most, if not all, noise consisted of much lower amplitudes than the actual signals from detectors. The discriminators would allow the analog signals to pass while simultaneously producing a digital logic pulse acting as an indicator of an event in one of the detectors. Each detector was assigned to its own discriminator channel to preserve the identity of the relevant detector.

4.5.2 Analog-to-Digital Converters (ADCs)

After passing through the discriminator, the analog signal traveled to a charge integrating analog-to-digital converter (ADC), which integrated the signal over time. An ADC can integrate the waveform from a detector over two different time windows. The *long-gate* ADC integrated the signal over a long time window, aiming to integrate over the entire signal. This provided a measure of the total charge in the electronic signal, which could be calibrated to determine the light output from a detector. The *short-gate* ADC integrated the signal over a shorter time scale, only including a part of the entire waveform. The combination of the long-gate and short-gate ADC integration helped to discern the properties of the received signal. This information was crucial in pulse-shape discrimination, and thus, particle identification of the neutrons.

4.5.3 Time-to-Digital Converters (TDCs)

The logic signal emitted by the discriminator continued on to a number of other modules in the electronics. One destination of this signal was a *time-to-digital converter* (TDC). A TDC effectively acts as a stop watch for particle travel. The logic pulse from a discriminator indicates to the TDC to stop counting, which might prompt the question, *when did it start counting?*

The HIγS accelerator provided a "bunch pick-off" signal that acted as a trigger for the TDC. However, if a photon bunch did not end up producing hits in any of the detectors, there was no trigger to stop the TDC. Therefore, it was preferred to

confirm an event within any detector in the setup before starting the TDC. This may seem to be a counterintuitive requirement, to confirm an event in the future before accepting a trigger in the present. Yet, incorporating precisely timed delays in the bunch signal can accomplish this. The bunch signal can be delayed to arrive in coincidence with a detector signal that passed the discriminator. The TDC then started tracking time after this coincidence. The logic pulse that directed the TDC to stop counting was then delayed similarly to preserve the time difference between the bunch signal and a detector signal. Scattered beam photons would generate a detector signal with a regular arrival time, which could be used to calibrate the TDC timing spectrum, providing a time-of-flight spectrum of any detected particles.

4.5.4 Scalers

The data acquisition also included a series of signal counting modules known as *scalers*. Not only did the scalers count events in each detector, but they also monitored points before and after sub-circuits within the electronics to identify anomalies or inconsistencies within the modules. Signals were ported into two types of scalers: inhibited and uninhibited scalers. The uninhibited scalers counted all logic pulses received. The inhibited scalers only counted signals if the DAQ was "live" and therefore available to read in new data. The difference in counts between the two scalers provided the dead time of the system.

4.5.5 Data Acquisition Windows

With the role of each of the electronics understood, the circuit logic that controlled the data acquisition can be outlined. This begins with a consideration of when data was accepted by the electronics. This is defined by *data acquisition windows*, the logic of which is mapped out in Figure 4.28.

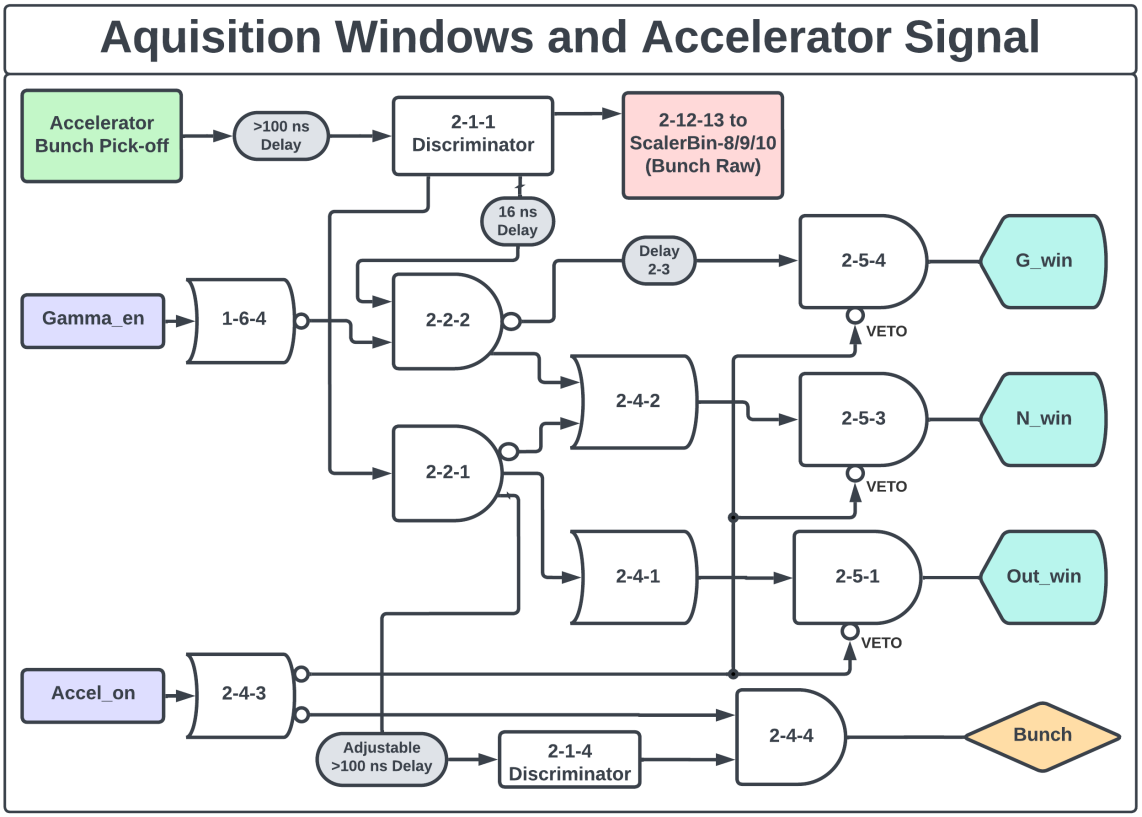

Figure 4.28: Circuit Logic for Data Acquisition Windows. Logic diagram for the data acquisition windows: Out_win, N_win, and G_win (outlined in the main text). Data is accepted when these veto windows are closed i.e. have a value of 0. A delay is added to the bunch pick-off signal to verify events are detected in the system before starting data acquisition. The circuit encodes other capabilities that can be operated by the user. *Gamma_en*, meaning "gamma enabled" allows periodic trigger of G_win to provide data for time-of-flight calibrations. *Accel_on* can be disabled to remove the veto windows and accept all data.
Image Credit: T. Polischuk [53].

The data acquisition windows acted as veto windows, time frames in which data was not accepted.[4] They enabled control over when data was collected to better conserve resources for neutron detection as opposed to "empty" data from background effects. The logic circuit would be initiated by the "bunch pick-off" signal provided by the HIγS accelerator indicating when a gamma ray bunch had been produced. With an appropriate delay to allow for confirmation of events in the detector array,

[4] A veto window acts in the opposite sense of a gate which provides a window in which information is accepted.

this signal would tell the data acquisition when to begin accepting data. At this start time, the TDCs would start counting time and the aforementioned data acquisition windows would be established.

There were four veto windows for data collection. A gamma ray bunch would interact with the target, sending neutrons and photons traveling to the detectors. The difference in velocity between the two types of particles would create a separation that could be timed for efficient data collection. A neutron-gamma window (N+G_win) was set to accept signals after the expected arrival time of photons at the target. During this window, data was collected from detection of photoneutrons and Compton scattered photons from the target. An "out" window was established outside of the N+G_win, to collect data from background events in the detectors. The gamma window (G_win) provided a very short time frame to accept signals arriving based on the expected time of photons at the target. From N+G_win and G_win, a neutron window (N_win) could be determined, accepting signals during the time frame when neutrons produced in the target were expected to arrive at the detectors.

4.5.6 Trigger Logic

A series of triggers were established in the electronics to control when the data acquisition system was accepting data. The trigger circuit was shared across all electronic modules, and its circuit logic is outlined in Figure 4.29. Any one of the triggers generated a logic pulse that would inhibit the DAQ, initiating a readout of the ADCs and TDCs. While the DAQ was busy, all other trigger signals were inhibited, preventing readout of new events that would interrupt the currently processing event. After readout was complete, the inhibit was reset by the DAQ and data can be recorded again. The neutron trigger (N_trig) started the ADCs associated with the detector, providing the trigger signal. The pedestal trigger (P_trig) started all ADCs for a pedestal measurement from every module.

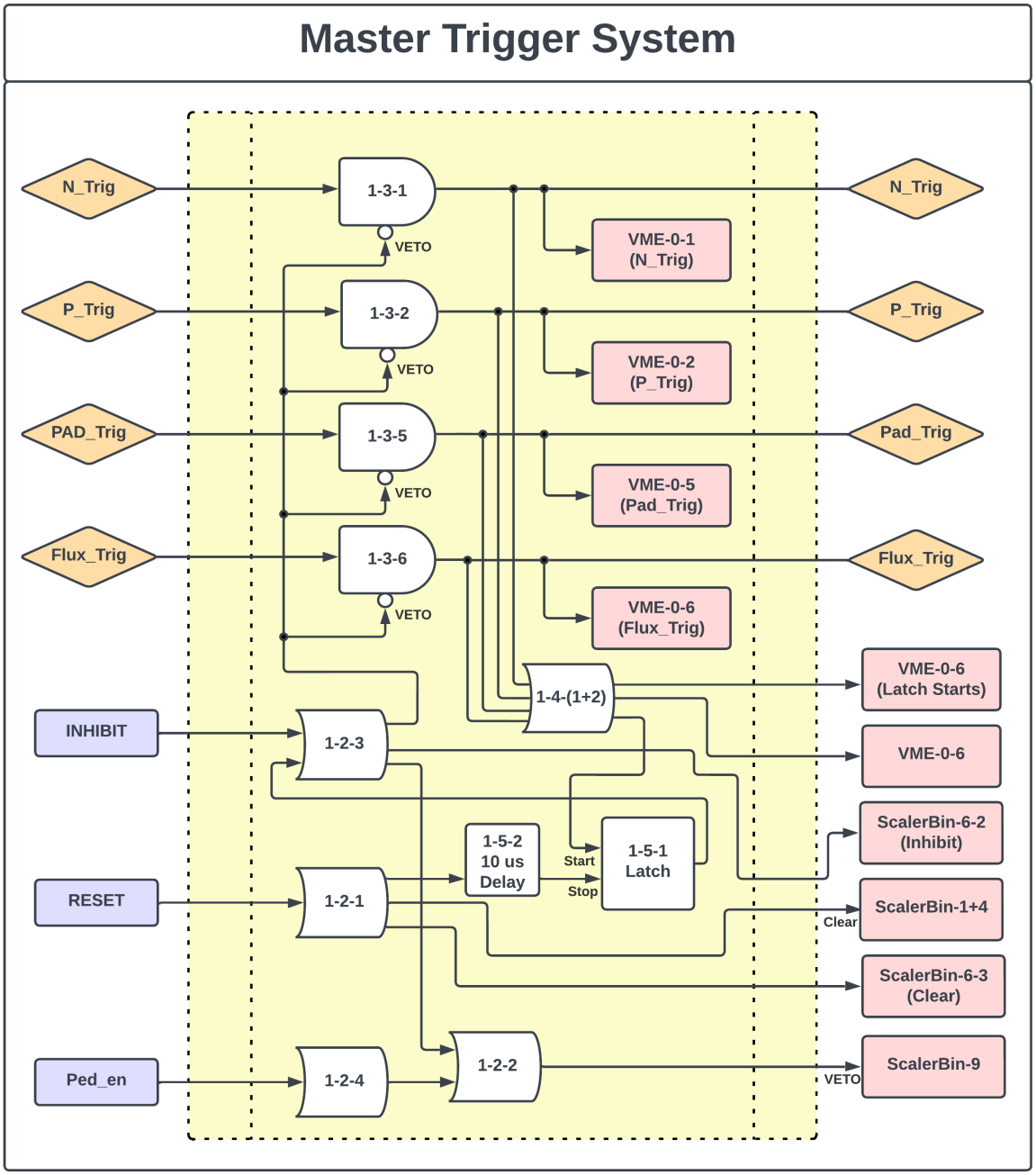

Figure 4.29: Master Trigger Logic. Logic diagram for the trigger system of the data acquisition system. A series of triggers indicate to the DAQ when to accept data by reading out the ADCs and TDCs. The trigger system ensures complete processing of events without interruption from new events during the DAQ live-time.
Image Credit: T. Polischuk [53].

4.5.7 Data Acquisition Software

For the data acquisition (DAQ) software, this experiment used a software package known as LUCID. Originally developed for the Saskatchewan Accelerator Laboratory, LUCID was designed to be "experimenter-friendly", providing flexible capabilities in setting up a DAQ system for variable experimental apparatus.

Lucid provides three main programs for data collection and management referred to as the *reader*, the *looker*, and the *writer*. The *reader* accepts data from the electronics and stores it in user defined variables. The reader can perform a few basic cuts and calculations for better data handling. The *looker* offers a more user-friendly means of viewing the data. It provides convenient visualization of data and enables more complex analysis of the incoming data. For a thorough analysis of this experiment, the data was ported into other software packages with better capabilities, but the Lucid looker was helpful for data quality monitoring during the run. Finally, the *writer* receives data from the reader and saves it to disk for data storage.

After data collection was performed with Lucid, further analysis continued with a number of other software packages that are outlined in Section 5.1.

Chapter 5

Data Analysis

5.1 Software Packages

Analysis of the data from this experiment was performed with a number of software packages.

As discussed in the last chapter, data was collected and stored with the LUCID software package. [68] LUCID provides the ability to replay data event-by-event for preliminary checks during running. Preliminary analysis can be done within the LUCID framework, however a more robust analysis was performed by implementing the ROOT framework.

ROOT is a C++ based software package for analysis and visualization of large sets of data. [69] It was developed at CERN, incorporating analysis methods that are useful in nuclear and particle physics experiments. ROOT organizes data in a format known as "trees", in which a set of quantities are stored per event. It then offers a variety of classes tailored for statistical analysis and visualization of the data. The analysis for this experiment was performed with a collaboration-developed package built around the ROOT framework.

The data collected by LUCID was converted into the ROOT format with a software package called RLucid. RLucid is a code developed within the University of Saskatchewan Experimental Subatomic Physics Group by W. A. Wurtz [70] for convenient data format conversion. It takes data stored in LUCID files and uses it to fill ROOT trees that can be accessed within the ROOT framework. RLucid also fills sets of standard histograms for visualizing the raw data collected during the experimental run. All of these are stored in the ROOT file format for further analysis.

BFROOT (shorthand for Blowfish ROOT) is a ROOT GUI developed for analysis of data collected with the Blowfish detector array. Initially developed by W.

Wurtz [71], it provides a user-friendly interface for utilizing ROOT analysis methods when handling experimental data. The original intent of the software was to determine particle yield within each detector of an experiment for cross section measurements. It was modified for this analysis as the "NVEC Version". [72] The modifications provided capability to require timing coincidences between detectors and to perform final calculations of the neutron scattering asymmetries and the neutron polarization.

5.2 Calibrations

5.2.1 ADC Calibrations

When properly calibrated, an ADC measures the light output from the scintillating detectors. Calibration of the ADC requires two steps: identifying the zero offset in the ADC spectrum (the pedestal) and determining the amount of light output represented by each ADC bin (the gain).

Pedestal Calibrations

A charge-integrating ADC draws a constant DC current as part of its operation, in order to maintain ADC linearity. As the ADC performs the charge integration, the DC bias is also integrated over, creating an offset in the final ADC values known as a *pedestal*. Before performing any analysis on the signals collected by the ADC, the pedestals from each ADC channel must be measured and subtracted.

A pedestal is found by measuring the total integrated charge in each ADC channel (ADC short and long) when the corresponding detector is empty. The default setting in Lucid is to ignore any signals that are measured with a charge less than some preset threshold. When a detector event is accepted by a discriminator, Lucid is triggered to receive a pedestal readout, bypassing the charge threshold requirement. This signal is received before the event signal, saving the charge provided by an empty detector, thus providing the offset value in the ADC caused by the DC bias. The collection of ADC offset values from all events in a run are stored in pedestal spectra for each ADC channel, as shown in Figure 5.1.

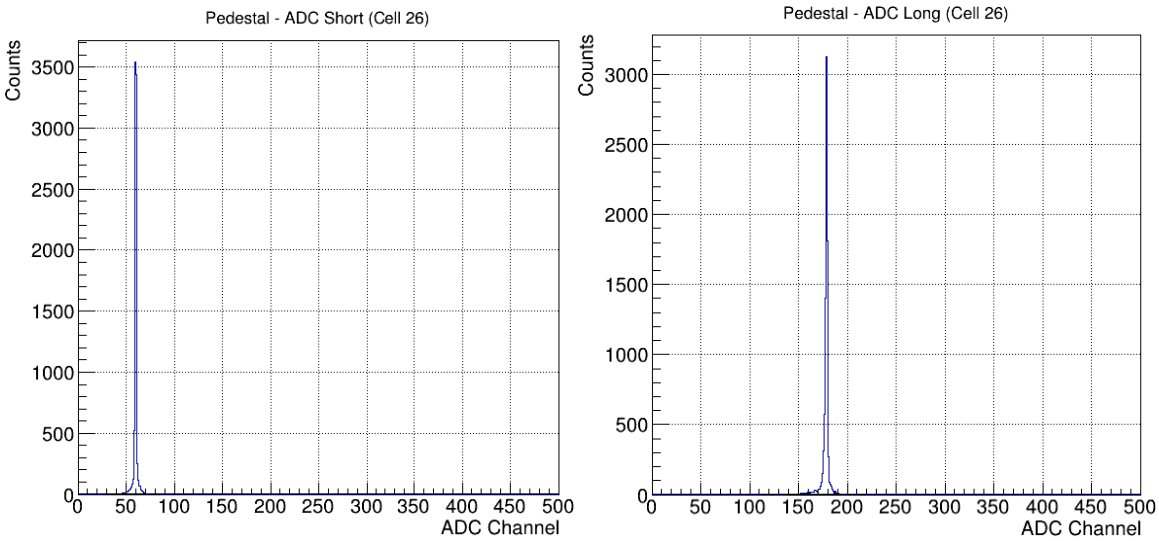

(a) Pedestal Spectrum for ADC Short **(b)** Pedestal Spectrum for ADC Long

Figure 5.1: Sample Pedestal Spectra for ADC Channels. ADC pedestals are measured by the charge in a signal provided by an empty detector (no particle hit). When the ADC spectrum is plotted for each channel, the bin number of the peak in the spectrum indicates the value of the pedestal to be subtracted for proper calibration of each ADC channel, **(a)** short and **(b)** long.

Under normal operation, the bias on each ADC channel remains consistent over an extended period of time. So ideally, when all events from a run are collected in a single pedestal spectrum, a distinct, narrow peak will manifest at the value of the ADC offset. A peak finding algorithm was used to identify the ADC bin associated with this peak for each detector. The bin value provided the pedestal for each ADC channel that was then subtracted from the ADC values to properly calibrate the ADC spectrum of each detector.

Shifted Pedestal Events

Analysis after the experimental run demonstrated anomalies in calculations of cut parameters based on data provided by the ADCs. For some events, calculated values, such as the PSD parameter, exhibited behavior that did not make physical sense. Upon deeper inspection, the problems appeared to be caused by untended fluctuations in the pedestals.

Some phenomena during the experimental run periodically caused a shift in the DC bias on the ADCs, smearing the pedestals to different values across different

events. Examples of this are shown in Figure 5.2.

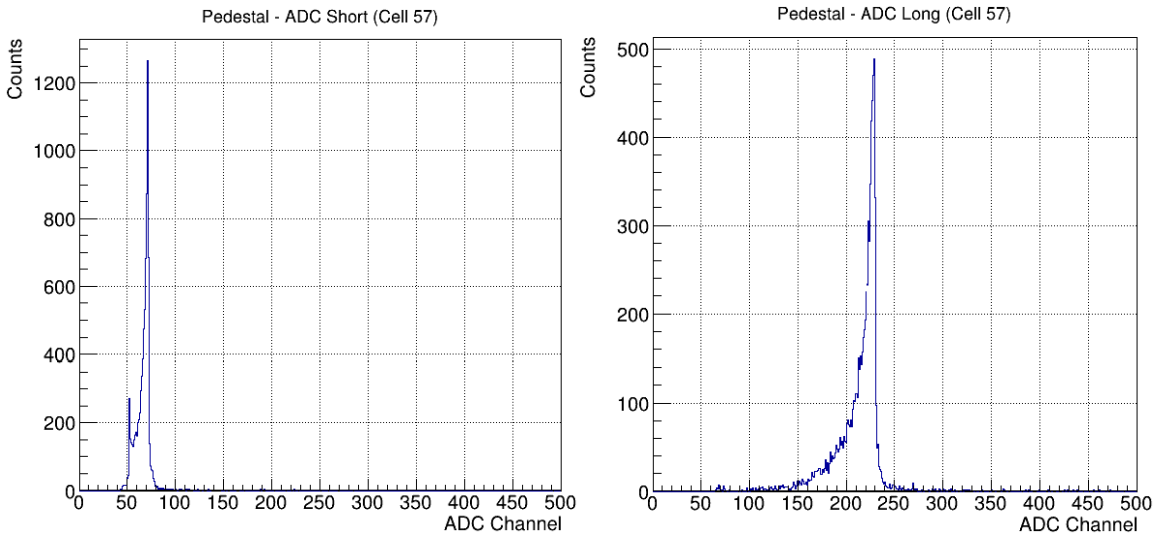

(a) Pedestal Spectrum for ADC Short **(b)** Pedestal Spectrum for ADC Long

Figure 5.2: Sample Pedestal Spectra for ADC Channels with Shifted Pedestals. Detectors close to the beamline experienced some phenomenon that shifted their ADC pedestals. The pedestal spectra for these ADC channels demonstrated a tail or additional smaller peaks offset from the main pedestal peak of the spectrum. These shifted pedestals created problems in the ADC calibrations needed to calculate analysis parameters.

This behavior was observed as most prevalent in detectors positioned closest to the beamline, suggesting some kind of high intensity beam effect.

The shift in the ADC calibration due to the shifted pedestals would propagate through calculations of event selection parameters creating errors in these values. Often, the error generated in these parameters removed them from event selection windows, causing false decreases in the neutron yields of certain detectors. These "shifted pedestal events" had to be corrected for to try to improve the accuracy of the neutron counts. A correction factor was calculated to account for the shifted pedestal events through a procedure outlined in Section 5.4.3.

Detector Gains

The gain of a detector calibrates the ADC channel number to the light output of the scintillator. Gains were found by analyzing the ADC spectrum produced by a radioactive source with a known energy spectrum.

Two radioactive sources were used for gain calibration: Cs-137 and AmBe. Each of these sources emits gamma-rays of known energy as they decay. The gamma-rays will enter the detectors and Compton scatter from electrons in the organic scintillator, initiating scintillation. A recoiling electron will have some maximum energy value imparted by the photon when it is Compton backscattered. This will manifest in the energy spectrum measured by the detector as a feature known as a Compton edge. For a photon of known energy E_γ, the energy of the Compton edge, E_{CE} can be calculated as

$$E_{CE} = \frac{2E_\gamma^2}{m_e c^2 + 2E_\gamma} \tag{5.1}$$

Although this edge represents the maximum energy of a single recoiling electron, subsequent scatters by a photon can deposit more energy in the scintillator, producing a tail in the energy spectrum beyond the Compton edge. Thus, the inflection point in the tail is used to identify the Compton edge in an ADC spectrum.

A sample ADC spectrum produced by a Cs-137 source is shown in Figure 5.3.

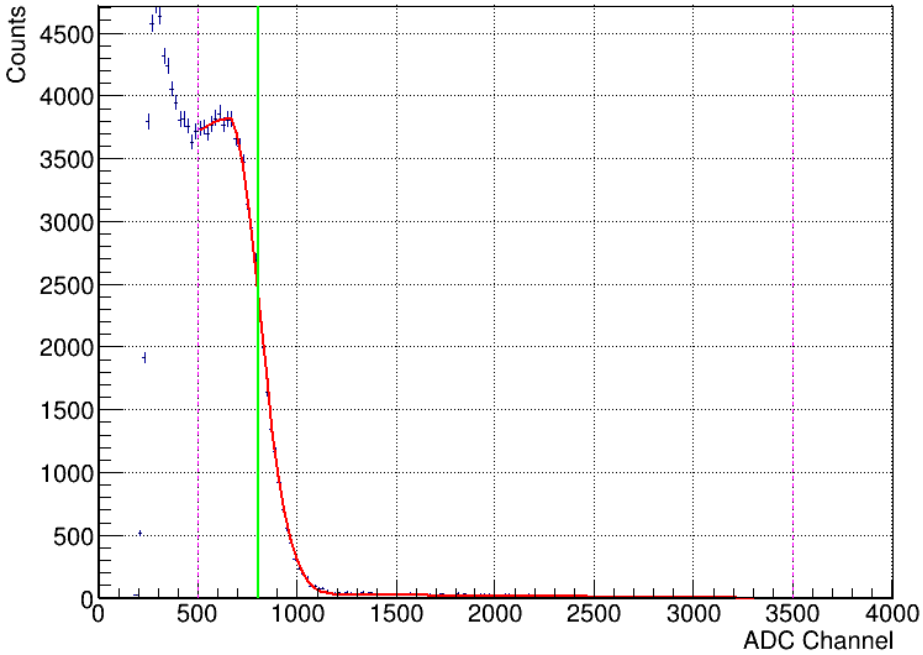

Figure 5.3: ADC Spectrum from Cs-137 Source for Gain Finding. The gain of a detector was found by relating the Compton edge of the energy spectrum from a radioactive source to the inflection point on the ADC spectrum produced in a detector by the source.

The tail of the spectrum is fit with a function defined as

$$f(x) = p_0 \exp\left\{ -\frac{(x-p_1)^2}{2p_2^2} \right\} + p_3 x + p_4, \tag{5.2}$$

with fitting parameters p_i. This fit function includes a contribution from a Gaussian distribution, which provides parameters for defining the infection point in terms of the ADC channel number. The inflection point is then identified as $p_1 + p_2$.

The inflection point of the spectrum does not align exactly with the Compton edge of the spectrum, but rather, was offset by some correction factor. A GEANT4 simulation was used to determine the correction factor.

Dividing the energy of the Compton edge by the corresponding ADC bin number in the spectrum, an energy-per-bin scaling factor can be calculated to properly calibrate the light output of a detector.

Gain Scaling Factors

As discussed in 4.4, the detectors used as neutron counters in this experiment were borrowed from the Blowfish detector array. In commissioning these detectors for previous experiments, Pywell *et al.* [73] tested the light output parameters for BC-505, the organic compound used as a liquid scintillator in the detectors. They found that the these parameters were accurately reproduced by simulation with GEANT4, providing valuable insight into the efficiency of the detectors.

However, later experiments [18, 19, 57, 74] found that the actual light output efficiency of the Blowfish detectors for neutrons was worse than predicted by simulation. Even with careful calibration using different gamma-ray sources, the gains of the detectors were lower for neutron events than they should have been. A reason for the lower detector response was not confirmed, but several potential contributing factors were proposed [57] including signal quenching caused by pollution of the detection volume with oxygen. Whatever the reason, a decrease in the light output efficiency of the detectors jeopardizes the validity of analysis cuts made to data collected by the ADCs.

To correct for the drop in efficiency, the gains of the detectors were compared to the expected gains determined by simulation to calculate gain scaling factors. This process is demonstrated in Figure 5.4.

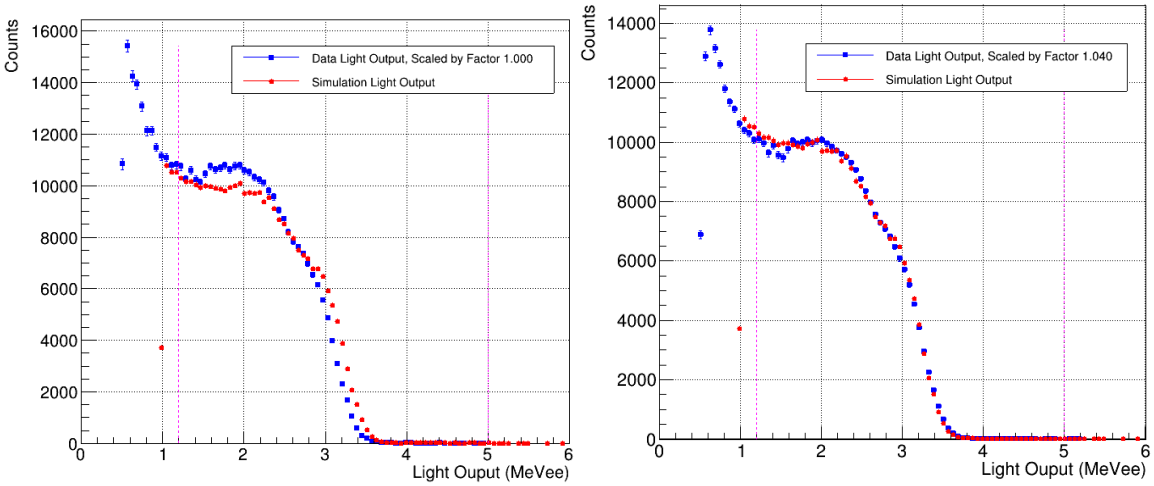

(a) Light Output Spectra before Gain Scaling

(b) Light Output Spectra with Gain Scaling Factor of 1.040

Figure 5.4: Gain Scaling of Light Output Spectrum. The light output physics model in the Monte Carlo simulation of the experiment produced accurate light output spectra from organic scintillator detectors based on incident particle energies. Comparing the spectra of individual detectors to the expected results produced by the simulation indicated changes in the efficiency of detectors. These light output efficiencies were converted into gain scaling factors to calibrate experimental data.

A calibrated ADC spectrum from a detector was fitted against its simulated gain spectrum with a χ^2-fitting. Figure 5.4a shows this comparison without any gain scaling. The measured spectrum was scaled iteratively until the reduced χ^2 was minimized. Figure 5.4b shows how well the two spectra align after gain scaling. The scaling factor was then stored for each detector. Before any parameter cuts were applied to the data, the light output spectrum of a detector was multiplied by its scaling factor. With this corrective factor applied, the ADC spectrum accurately represented the light output (and therefore energy spectrum) of neutrons that were detected.

5.2.2 TDC Calibrations

As discussed in 4.5.3, the TDCs kept time for the arrival of signals to provide time-of-flight (ToF) information about the detected particles. TDCs were started by the bunch signal provided by the accelerator and were stopped by signals arriving from detectors. The TDC produces a timing spectrum across its 4096 channels (or bins)

resulting in a raw TDC spectrum such as the one in Figure 5.5.

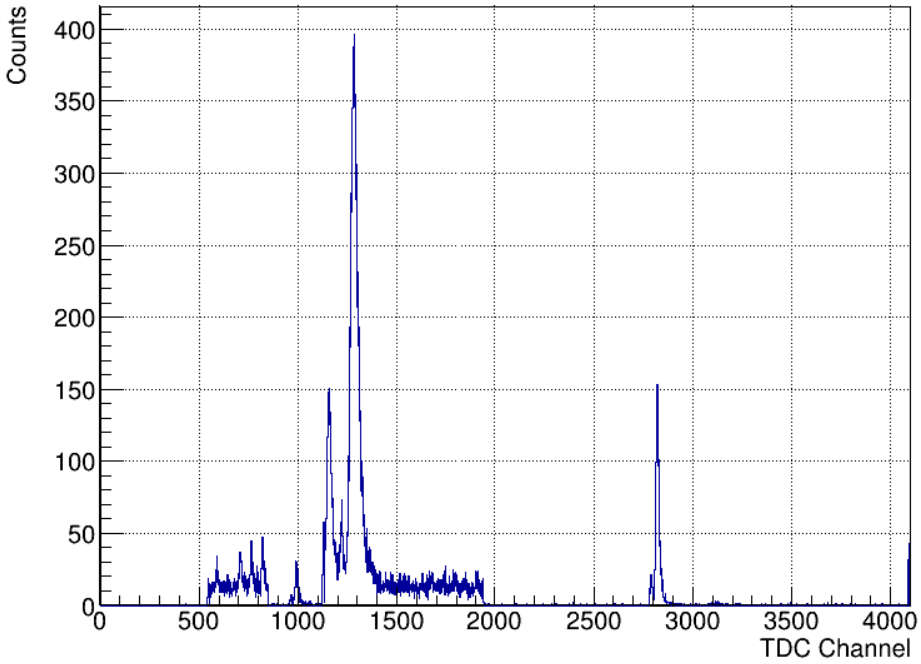

Figure 5.5: Raw TDC Spectrum. A TDC measured the arrival times of signals in each detector and digitally stored the information by binning the time values into channels, generating a raw TDC spectrum as illustrated above. The raw data from the TDC then had to be calibrated properly to produce a time-of-flight spectrum for each detector.

Due to the travel time of a photon and the delays caused by electronics and cabling, there is a constant offset in the TDC spectrum specific to each detector. The exact distance traveled by the photons after gamma-ray production is not known, so a zero point for the TDC spectrum cannot be properly aligned with this event. Instead, a TDC offset is found from the zero point of the interaction of a photon with the target. The distance from the target to a detector and the speed of light are both fixed quantities that can be used to calibrate the TDC spectrum.

The TDC offset was found by examining the timing peak of Compton scattered photons from the target. The DAQ was switched to gamma_enabled mode in which the *gamma-prescale factor* was set to 1. This means the photon acceptance window (G_win from 4.5.5) would only be active once for every 1000 events. Data collection in this mode would yield a spectrum with a sharp peak due to Compton scattered gamma-rays from the target as shown in Figure 5.6.

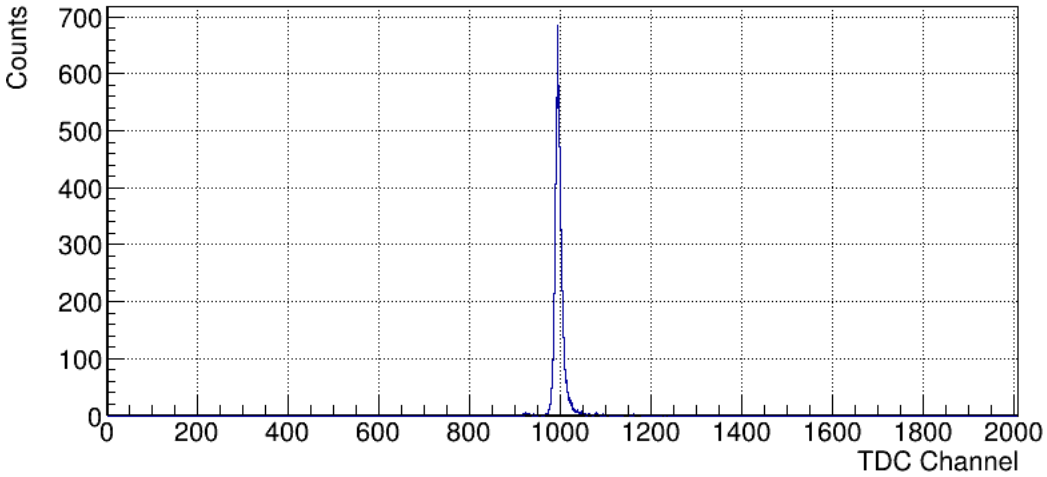

Figure 5.6: TDC Offset. The offset of a TDC provides the baseline channel around which the TDC spectrum is "zeroed". Using kinematics, the TDC offset is calculated as the TDC channel corresponding to the interaction time of a photon within the target, assigning this as time $t = 0$. This allows all time-of-flight spectra in the analysis to represent the time-of-flight of particles from the target to a detector.

A peak-finding algorithm was used to identify the TDC channel corresponding to the TDC offset. Using the target-to-cell distance, the speed of light, and the TDC offset, a ToF spectrum was obtained for each detector as displayed in Figure 5.7. Having properly calibrated ToF spectra for detectors was crucial for later analysis when neutron events were identified with the help of kinematically based timing cuts.

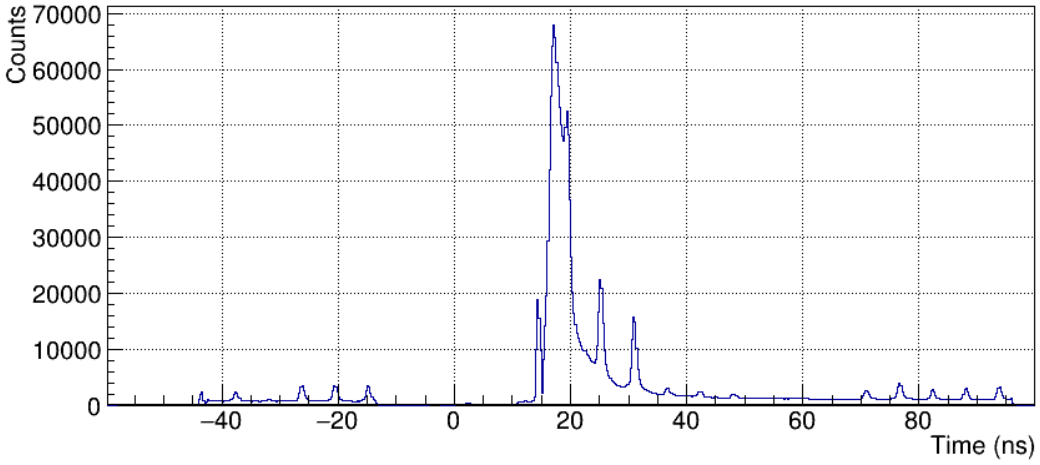

Figure 5.7: Time-of-Flight Spectrum. A time-of-flight spectrum is generated for each detector from the properly calibrated TDC data. This spectrum is key to particle identification methods in the analysis.

5.2.3 PSD Parameters

As mentioned in Section 4.4, the strength in the use of BC-505 liquid scintillators as neutron detectors lies in their excellent capability to distinguish between photons and neutrons through pulse shape discrimination (PSD). The difference in fluorescence behavior between these types of particles results in differently shaped pulses generated by their scintillation light output. This difference can be digitized by charge-integrating the pulses over two time windows: a long time gate to integrate over the whole pulse and a short gate meant to integrate over just the peak of the pulse. These integration gates are demonstrated by the diagram in Figure 5.8.

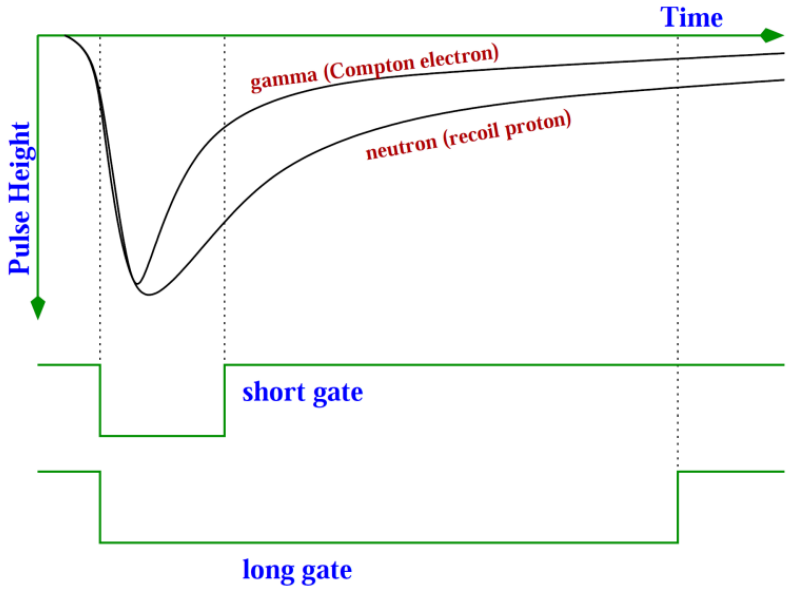

Figure 5.8: Long and Short Gate Charge Integration Over Signal Pulses. Liquid organic scintillators provide neutral particle identification through pulse shape discrimination (PSD). Photons are detected through Compton scattering on electrons in the organic molecules. The direct interaction induces the scintillation process immediately, producing an electronic signal with a sharp narrow peak and a small tail. Neutrons are detected by interacting with protons which recoil in volume, which act as ionizing radiation that will induce scintillation. This creates a delayed fluorescence that manifests as an electronic pulse with a broader peak and large tail. Photons and neutrons can be distinguished by quantifying the difference in sizes of the pulse tails. Charge integrating each pulse over a long time gate provides a total charge of the entire pulse. Charge integrating over a short time gate provides the charge within the peak of the pulse. The different between these charges yields a quantitative value for describing the shape of the tails of each pulse. Image Credit: B. Sawatzky [17]

There is a clear distinction between the tail sizes for pulses of different particles. This can be observed by plotting the two time gate integrals against each other as in Figure 5.9. Two distinct bands emerge, corresponding to the diverging behavior of signals from neutrons and photons.

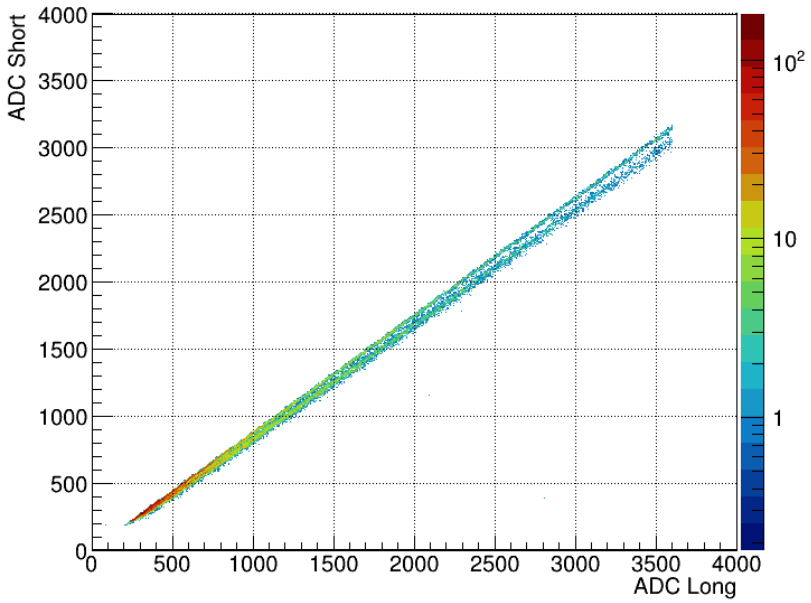

Figure 5.9: Short Gate Charge Integration vs. Long Gate Charge Integration. The distinction between neutron and photon signals begins to emerge when inspecting the ADC spectra of the short gate charge integrating channels vs the long gate charge integrating channels. Two "bands" appear as the events separate between the two types of signals. This separation becomes more apparent and easier to analyze with a properly calibrated PSD parameter.

The separation of the two bands becomes more evident when plotting the standard PSD ratio: the normalized difference between the long gate and short gate integrals $(\frac{Q_{long}-Q_{short}}{Q_{long}})$.

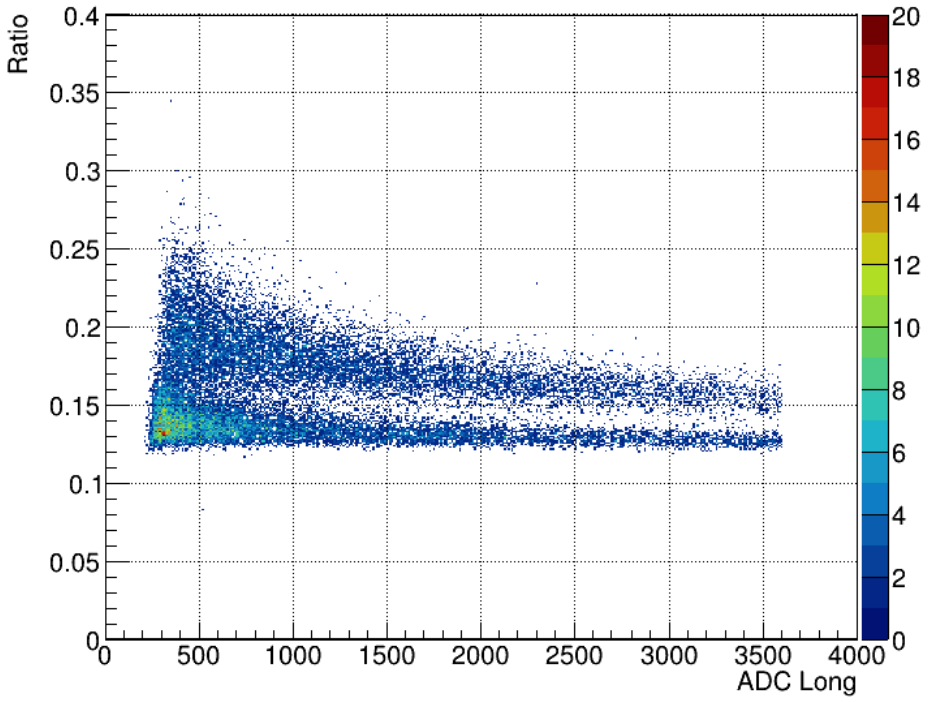

Figure 5.10: PSD Ratio vs. ADC Long Value. The PSD ratio is plotted vs the charge integration value from the ADC long channel to facilitate the identification of neutron and photon events. This spectrum exhibits the separation between these two types of events. Proper calibration of these spectra from all detectors provided a method for uniformly filtering out photon events across all detectors with the same acceptance cuts.

Although this PSD parameter exhibits separation between neutrons and photons, there is still some mixing between events that can be improved by modifying the PSD parameter with some additional degrees of freedom. This starts by recognizing that the a profile at a certain value along the x-axis in Figure 5.10 generates a projection along the y-axis that resembles a double Gaussian distribution; one peak for photon-like events, one peak for neutron-like events. To analyze these peaks, slices were taken to generate PSD ratio projections and fitted to double Gaussian distributions. Figure 5.11 shows what one of these slices looks like during fitting.

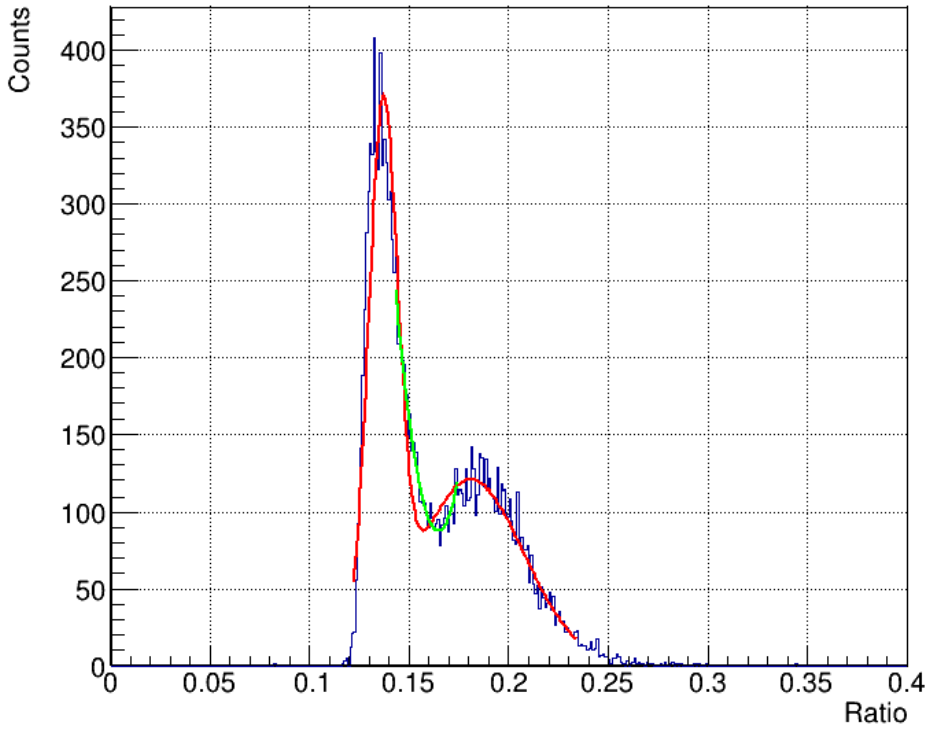

Figure 5.11: Fitting a Slice of the PSD Spectrum for Calibration. Calibrating the PSD parameter of each detector required transforming the separation of the neutron and photon peaks to correspond with PSD = 0. The axis of separation was found by producing "slices" of the PSD spectrum at certain light output values and fitting them to find the "valley" between peaks. The minimum of the fit function applied to this valley was used in conjunction with a series of other PSD slices to find a function for transforming the PSD parameter, as demonstrated in Figure 5.12.

This fit was used to carry on with calibration of the final PSD parameter. However, it served an additional benefit of providing statistics of the full neutron peaks in the PSD spectrum. As the PSD parameters are calibrated and cuts are applied, some neutron events are inadvertently removed in the regions of PSD mixing between neutrons and photons. Fitting the neutron peak enabled a calculation of a PSD cut correction factor to scale the final neutron yield in a detector.

For each slice that is fitted, a point is generated at the center of the slice along the x-axis and at a value along the y-axis that is 2 standard deviations away from the mean of the neutron peak. The interpretation of this plot is difficult to visualize in words, so Figure 5.12 illustrates how these points appear in relation to the PSD ratio histogram.

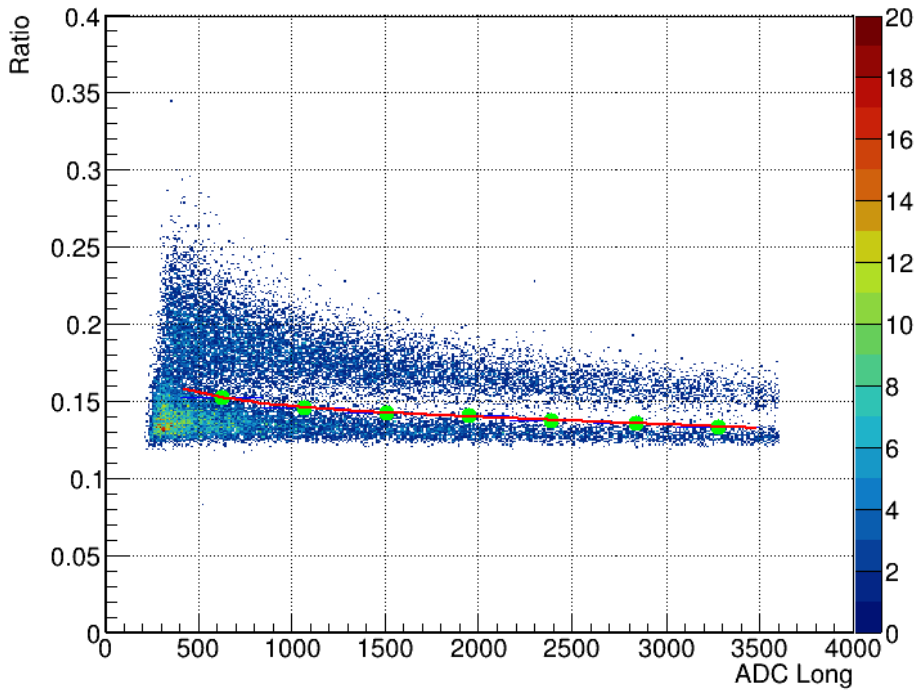

Figure 5.12: Fitting of PSD Parameter. A collection of slices in the PSD spectrum were fit to find the minimum point in each slice between the neutron and photon peaks. The results of these fits were fit to an exponential function to identify the a functional form for the "valley" separating the neutron and photon peaks. With the fitting parameters calibrated in this way for each detector, the PSD parameters were transformed with this function so that the separation of the two peaks corresponded to a value of PSD =0. This facilitated a consistent method for applying PSD cuts to the data from each detector during event selection.

This collection of points extracted from the PSD spectrum was fit to a modified PSD function. Using L and S in place of Q_{long} and Q_{short}, the formula for the new PSD parameter is

$$PSD = 1000\Big(\frac{L-S}{L} + p_0 e^{p_1 L} + p_2 + p_3 L\Big). \tag{5.3}$$

The fitting parameters were extracted to define a calibration for each detector to generate a PSD spectrum with good separation between neutron and photon events. The calibration included an adjustment to the PSD parameter such that all photon-like events had a negative value while all neutron-like events were positive. This made for a well calibrated PSD spectrum as illustrated in Figure 5.13.

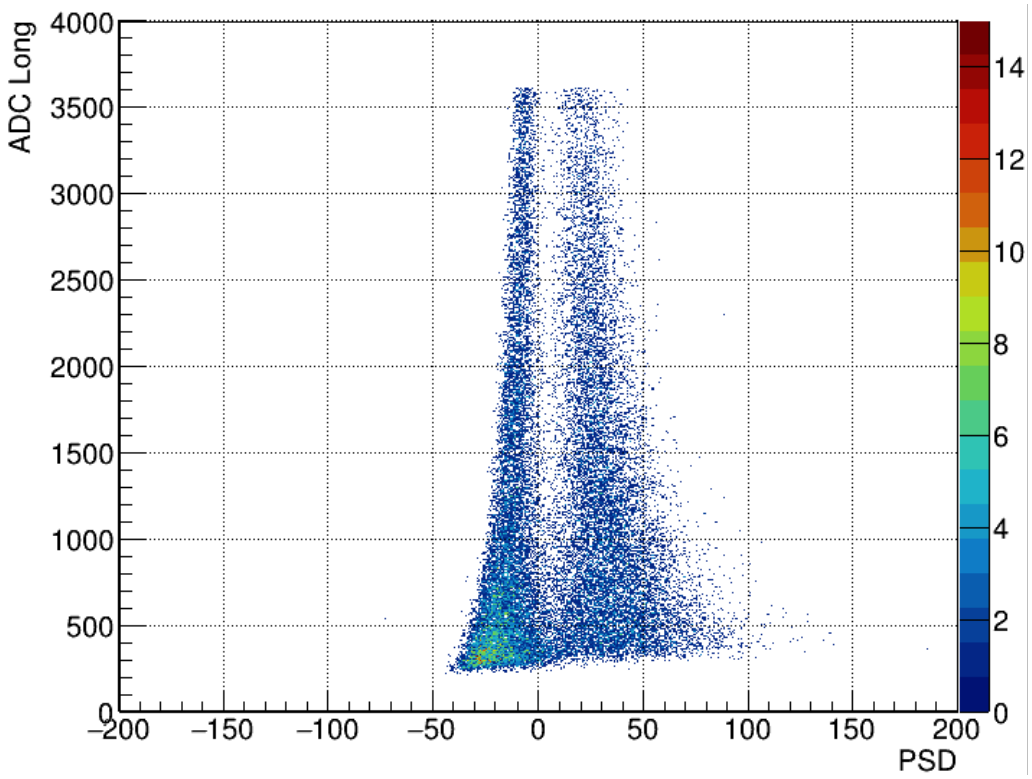

Figure 5.13: Final Spectrum of Calibrated PSD Parameter. A fully calibrated PSD spectrum demonstrates clear separation between the neutron event peak and the photon event peak. The calibrations align these peaks such that they can be separated at PSD = 0, providing a method for filtering photon events out of the analysis.

Calibration of the PSD parameter for each detector was done with data collected from an AmBe source run. Source runs were performed at the beginning and end of each day to check for PSD drift in the detectors. The PSD parameters did not vary much (if at all) throughout a day, and could therefore be reliably computed from the source runs for a full day.

5.3 Analyzing Event Selection

The measurement required identification of events in which neutrons scattered on a helium nucleus within a polarization analyzer and were detected by one of the counting detectors on either side of the analyzer. These *analyzing events* provided the means for calculating the scattering asymmetry, and therefore, the neutron polarization.

These events had to be distinguished from possible background processes that would also be picked up by the detectors including:

1. *Direct neutrons* which traveled directly from the target to the counting detectors, without passing through an analyzer

2. Neutrons that scattered from other parts of the setup or experimental hall before reaching the counting detectors

3. Background photons that Compton scattered within the target and were detected by either an analyzer or counting detector, including the out-of-time photons discussed in Section 4.1.4

This section outlines the parameter cuts made within the analysis to select analyzing events and remove background.

5.3.1 Analyzer Hit Identification

The first step to distinguishing an analyzing event was identifying events in which a hit was registered within a polarization analyzer. Measuring the scattering asymmetry of neutrons required assurance that the detected neutrons scattered from a helium nucleus within an analyzer. This was accomplished by requiring *coincident* signals between the PMTs on the two ends of an analyzer. Any neutrons that scattered in the analyzer should have produced enough light output to be measured by both PMTs. The signals from the PMTs should subsequently be collected within a certain amount of time from each other to ensure the signals were generated by the same event. Therefore, a coincidence requirement was set by applying a cut on the difference in time between signals from the two PMTs, as demonstrated in Figure. 5.14.

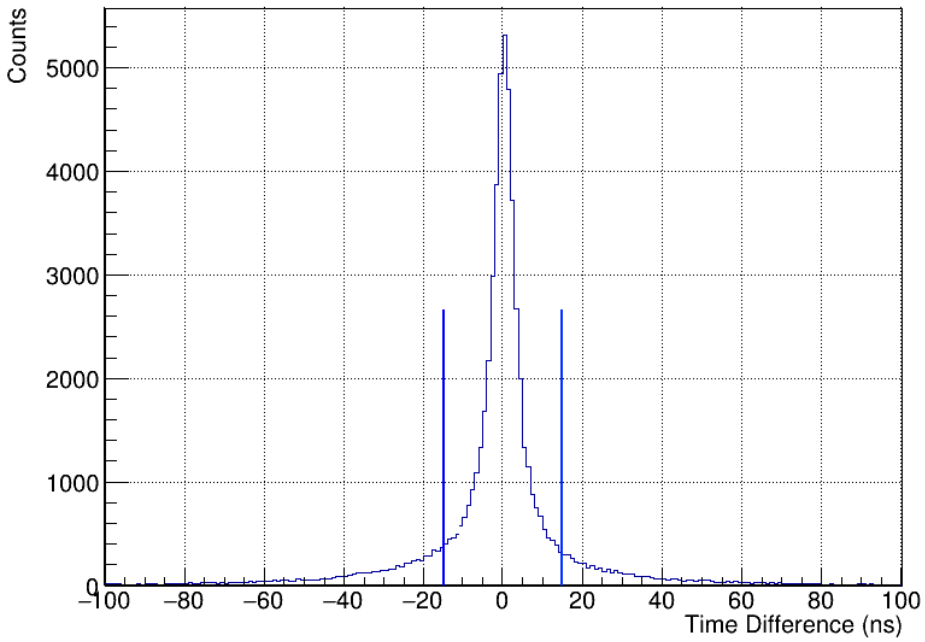

Figure 5.14: Spectrum of Time Difference Between Analyzer PMTs. The difference between the arrival times of signals from the analyzer PMTs is calculated to identify events in which neutrons pass through the analyzer. Many background particles would not deposit enough energy in the analyzer to produce signals in both PMTs. Restricting this time difference ensures the acceptance of single-particle events, rather than signals from two independent events.

The beam test discussed in Section 4.3.6 informed the timing cut to be made, set at ± 15 ns to maximize the statistics of analyzer hits, without risking the addition of too many accidental coincidences.

5.3.2 Analyzer-Cell Coincidences

After confirming a neutron scattered within an analyzer, coincident signals were also required between the analyzer and a counting detector (cell). This restricted the accepted trajectories of particles to those that provide an analyzing event. The coincidence requirement was set by applying a cut on the relative time difference between signals arriving from the analyzer and a counting detector, shown in Figure 5.15b.

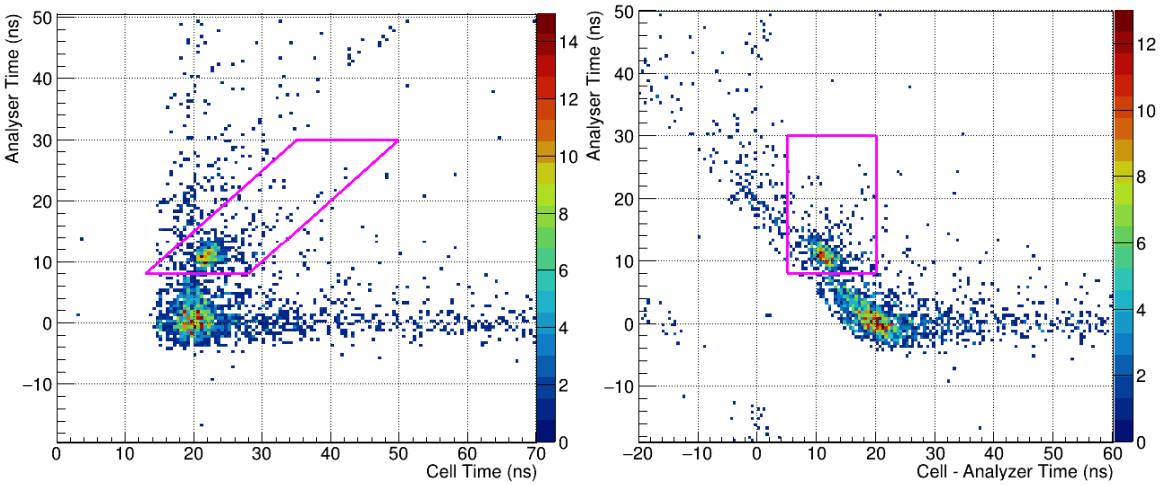

(a) Timing Cuts on Analyzer and Counting Detector

(b) Relative Time Difference Between Analyzer and Counting Detector

Figure 5.15: Analyzer-Cell Coincidence Requirements. The expected travel times of neutrons from the target to the analyzer and from the analyzer to a counting detector (labeled as "cell") were calculated using kinematics. Using these calculations, time-of-flight cuts were applied to require coincident signals between an analyzer and a counting detector. Signals arriving outside of these coincidence requirements were excluded as events that could not have physically possible for neutrons. Almost all of these excluded events arrived at detectors too early, most likely being caused by photons traveling much faster than neutrons.

Acceptable arrival times of signals were calculated from kinematics using the expected energies of neutrons ejected from the target (as calculated in Section 2.5.1) and then scattered in the analyzer. Signals arriving in either the analyzer or the cell too early or (much less likely) too late were filtered out by this method. Many of these events could be attributed to the detection of photons that had traveled much faster than neutrons to either of the two detectors. Additionally, some of these events were caused by out-of-time photons or neutrons produced by out-of-time photons arriving outside of the expected time window.

With the analyzer hit requirement and the analyzer-cell coincidence in place, many background events that could not have been analyzing events were properly filtered out. However, with the combination of direct neutrons, out-of-time photons, out-of-time neutrons, and other potential background signals, these methods could not guarantee the exclusion of *accidental coincidences* that would produce similarly timed signals to analyzing events. As an example, an accidental coincidence could

be generated by two out-of-time photons detected in each of the detectors (analyzer and counter). Particle identification techniques were implemented to filter out more of these background events.

5.3.3 Time-of-Flight Analysis

Complementary to the timing restrictions used to require coincidence between detectors, analysis of the arrival time of signals from detectors provided information for particle identification and background estimation. The possible neutron energies in this experiment resulted in neutron velocities much lower than the speed of light. The finite distance between the target and the detectors meant a measurable separation between the arrival times of neutrons vs. photons. A time-of-flight spectrum was constructed for each detector as exhibited in Figure 5.16.

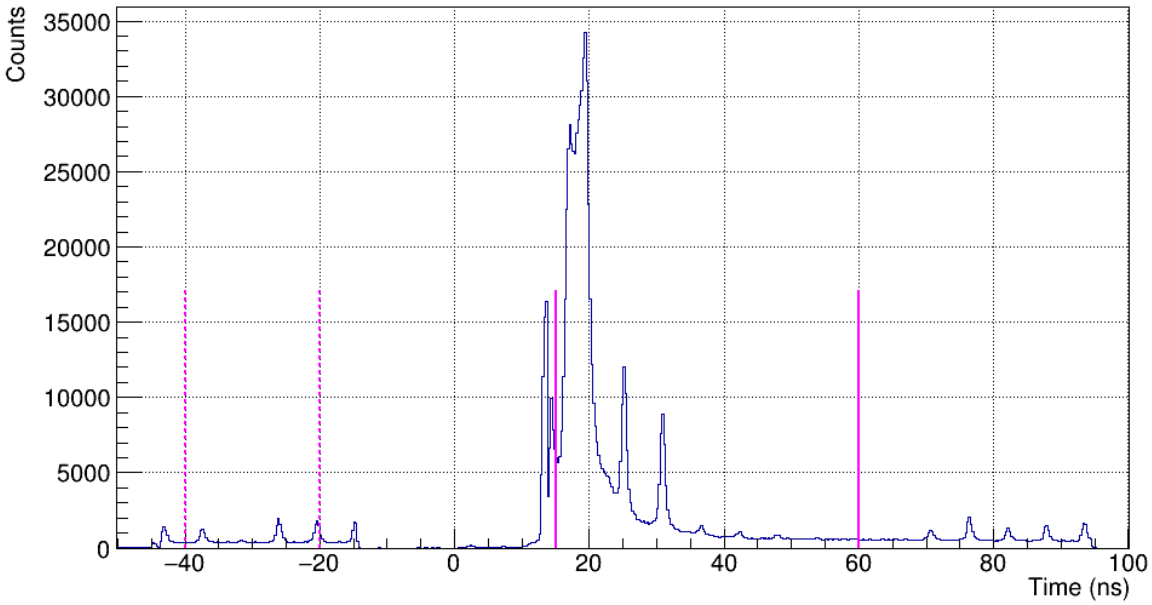

Figure 5.16: Time-of-Fight Spectrum from Neutron Detector. A time-of-flight analysis helped with particle identification and background subtraction by establishing two acceptance windows. The prompt window accepted events that arrived at detectors when neutrons were expected based on kinematics. The prompt window inadvertently included a number of background events due to out-of-time photons and other effects. An earlier window, the random window, was applied to measure the level of background picked up by a detector. Events within the random window were used to produce a background subtraction from the prompt window after all other parameter cuts had been applied.

As previously discussed, the expected time-of-flight of a neutron to each detector was calculated with the kinematic analysis of Section 2.5.1. This set a physical limit on the minimum time it could take a neutron to be detected, which was to used create a signal window on the time-of-flight spectrum. This region of the spectrum was referred to as the "prompt window". It encapsulated the entire neutron peak within the spectrum while excluding any events that had occurred at a physically unreasonable time for neutrons traveling through the experimental setup. Most of the events outside the prompt window were caused by Compton scattered photons from the target.

It is clear from Figure 5.16 that a number of additional peaks appear within the prompt window, indicative of some other type of event producing signals during this time. A clue to their nature comes from consideration of the entire spectrum, in which a series of small, periodic peaks appears. These additional peaks were attributed to the out-of-time photons, mimicking the periodicity of the buckets in the accelerator RF cavity. Because of this effect, the prompt window inadvertently included a number of these out-of-time photons, that needed to be filtered out through further analysis.

The time-of-flight spectrum was also used to generate a background subtraction, in the case of background events that managed to pass through the coincidence and particle identification analyses. A "random window" was established within a region on the time-of-flight spectrum that was too early to contain the neutrons being measured, and must have been occupied by "random" events due to out-of-time photons or other background. This window can be seen in Figure 5.16 between -40 and -20 ns. After finalizing the rest of the analysis, the remaining event yield within the random window was subtracted from the neutron yield of each detector with proper scaling to compare between the two timing windows.

5.3.4 Pulse Shape Discrimination Analysis

As discussed in Section 4.2.4, pulse shape discrimination (PSD) is an efficient technique used with liquid organic scintillators for neutral particle identification. The stark PSD separation between neutrons and photons meant that this method could be applied to exclude photons from the analysis with fairly low uncertainty. With the calibration procedure outlined in Section 5.2.3, the PSD parameters were aligned such that signals produced by neutrons generated a positive value while photons generated a negative value. This is demonstrated in the sample light output vs. PSD spectrum

displayed in Figure 5.17.

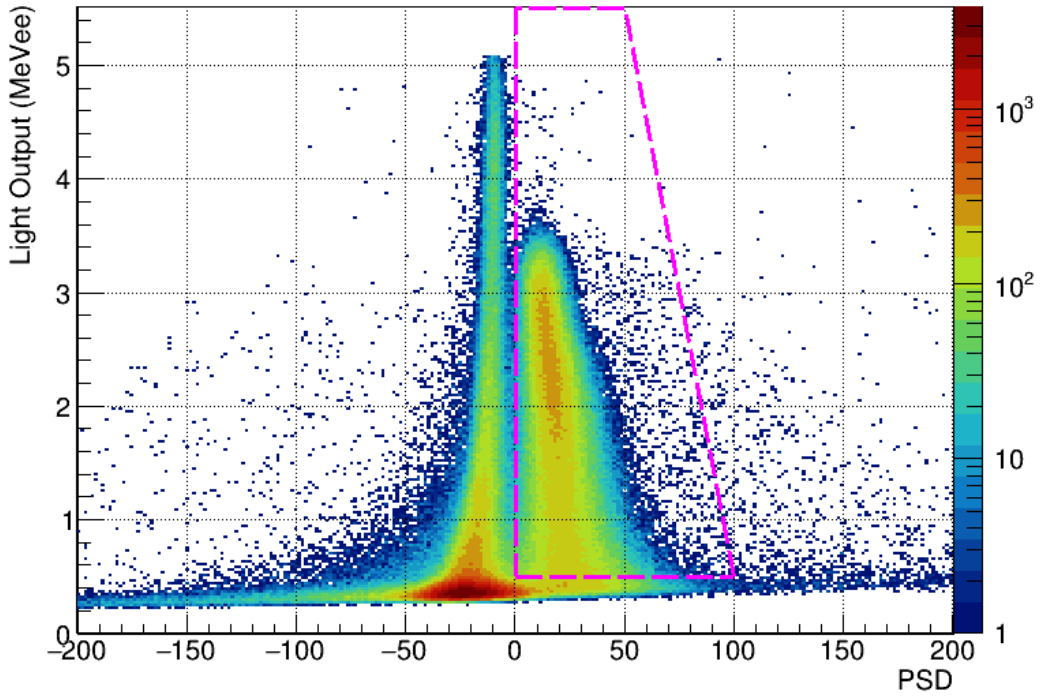

Figure 5.17: Light Output vs PSD. Neutron events are identified through pulse shape discrimination (PSD), a method that facilitates the exclusion of photon events from the analysis. When the PSD spectrum of a detector is generated, two distinct peaks appear demonstrating the separation of neutron and photon events. At this point in the analysis, the PSD spectra have been calibrated such that neutron events correspond to PSD > 0, and photon events correspond to PSD < 0. An acceptance window was applied with a minimum cut at PSD $= 0$ to include neutron events in further analysis, and filter out photon events. This cut was applied in conjunction with a light output cut described in Section 5.3.5, to maintain optimal PSD separation between neutrons and photons. The spectrum displayed above demonstrates the cuts applied to all events (rather than only analyzing events) for a clear illustration of the efficacy of the PSD analysis.

Two peaks are clearly visible in the PSD spectrum separated at zero. A cut was placed to exclude photon events starting at zero and extending out to encapsulate the neutron peak. Events within this window (formed in conjunction with light output cuts detailed in Section 5.3.5) were kept in the analysis to calculate detector yields. Events outside of these cuts were filtered out of the analysis, removing the vast majority of random photons that could not be removed by timing cuts. This is illustrated by a noticeable decrease in background events in the time-of-flight spectrum after the

PSD cut, as shown in Figure 5.18, when compared to Figure 5.16.

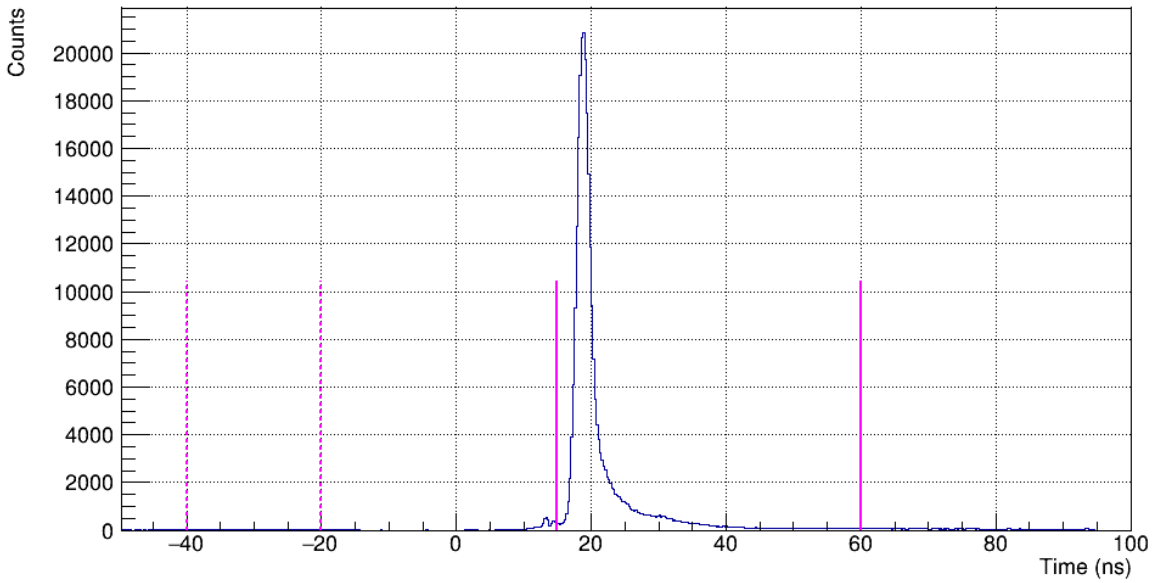

Figure 5.18: Time-of-Flight Spectrum After PSD Cut. Applying a PSD cut to the data from each detector removed a large majority of background photon events from the analysis. This illustrated above by the removal of many of the smaller background peaks from the time-of-flight spectrum as compared to Figure 5.16.

Effects of Shifted Pedestals

The shifted pedestal events discussed in Section 5.2.1 affected the calibration of the ADCs, which propagated through to the calculation of the PSD parameters. As mentioned, a number of detectors, especially those closest to the beamline, experienced some phenomenon that caused a systematic offset in the ADC pedestal, and, in turn, the ADC spectrum for some events. An improperly calibrated ADC due to this problem skewed the measured values from the ADC charge integration, leading to shifts in the values of the PSD parameters for these events. This effect is shown in Figure 5.19.

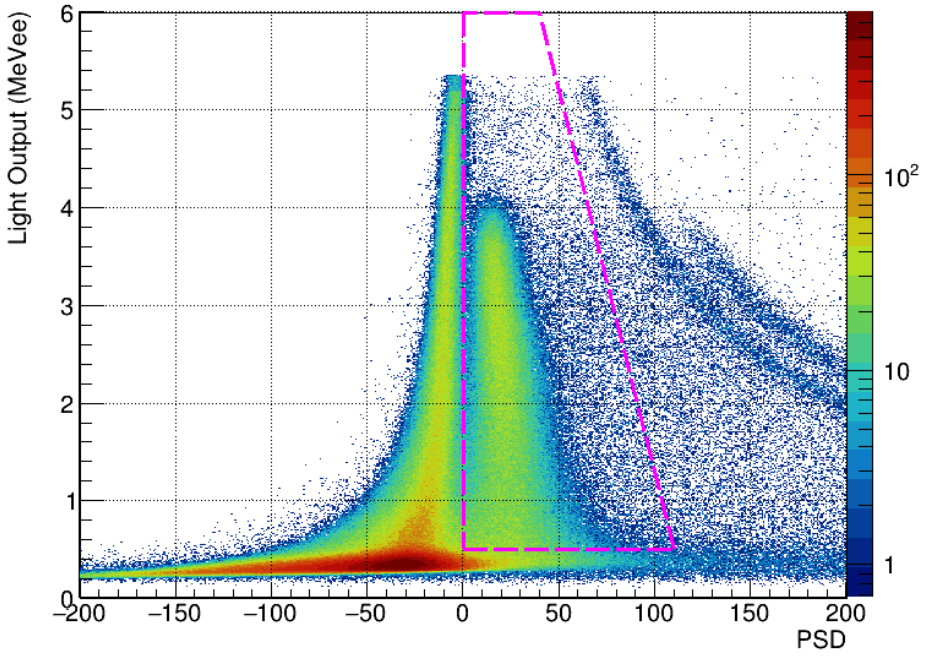

Figure 5.19: Light Output vs PSD with Shifted Pedestals. The PSD spectra of some detectors demonstrated noticeable effects due to shifted ADC pedestals. The main effect was a systematic shift in events from the neutron and photon peaks, manifesting as two additional bands of events outside the main peaks of the spectrum. Additionally, there was a lower level "smearing" effect where events were inaccurately scattered across the PSD spectrum. The combination of these effects removed neutron events from the acceptance window and introduced false events that should not have passed the PSD cuts.

Figure 5.19 exhibits a smearing in the PSD parameter beyond the neutron peak, culminating in two distinct bands representative of large amounts of neutron and photon events shifted by a systematic offset. These shifts caused many otherwise acceptable neutron events to be excluded from the PSD acceptance window. With little confidence in the separation between neutrons and photons in this shifted region of the PSD spectrum, these events were not included by additional acceptance windows. Instead, a shifted pedestal correction factor was implemented through the method outline in Section 5.2.1.

Detectors closest to the beamline demonstrated the most extreme cases of the shifted pedestal effects. The smearing of the PSD parameters was so severe that there could be little confidence in the separation of neutron and photon events to define an acceptance window, as shown in Figure 5.20.

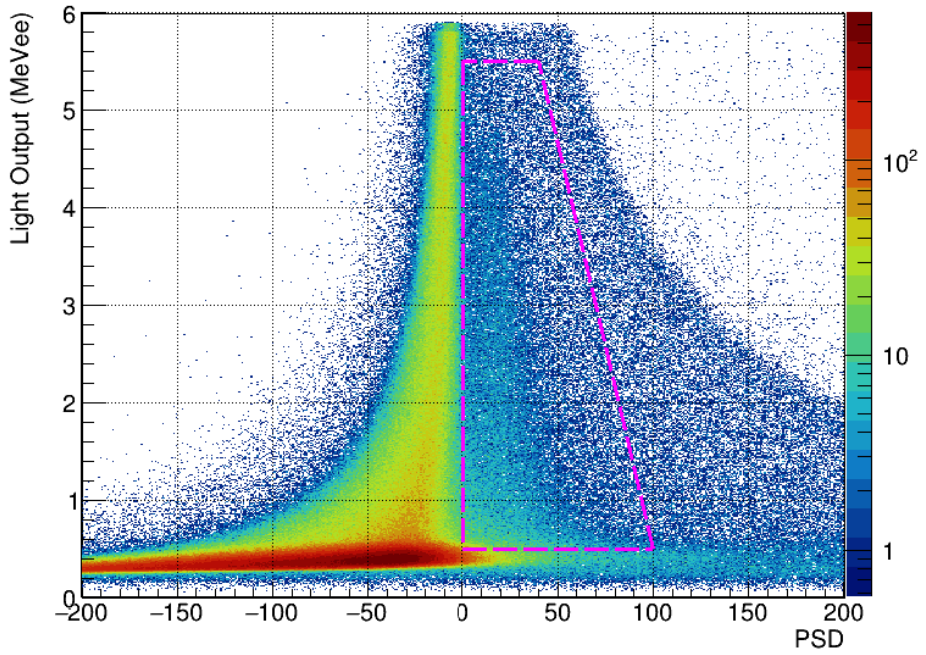

Figure 5.20: Light Output vs PSD with Shifted Pedestals. The most extreme cases of detectors with shifted ADC pedestals exhibited strong smearing effects that introduced contamination into the PSD acceptance window and removed otherwise useful neutron events. Detectors with this level of corruption to the PSD spectra has to be excluded from the final analysis.

In such cases, the level of shifted PSD parameters polluting the PSD spectrum could not be corrected for. To preserve the integrity of the measurement, these detectors with such extreme problems had to be excluded from the final analysis.

5.3.5 Light Output Cuts

The light output of a scintillator is proportional to the energy deposited by incident particles. Low energy neutrons can produce signals that are indistinguishable from background signals. A light output cut must be applied to exclude these background events, at the expense of some of the low energy neutrons.

The discriminators offered a first cut on the light output with their acceptance threshold. However, some low level events still got through, and had to be removed in the analysis. A light output cut of 0.5 MeVee provided this exclusion. An upper limit was also placed based on the energies of neutrons that were kinematically possible from each beam energy. Sample cuts are shown in the light output vs PDF spectrum

in Figure 5.17.

The main difficulty in distinguishing low energy neutrons from background events is the efficacy of the PSD analysis for low energy particles. Figure 5.8 is helpful to visualize why this is the case. Signals from both neutrons and photons would have a smaller amplitude from low light output events. The smaller the amplitudes of these signals, the more difficult it would be to separate the two types of signals based on the pulse shape. This is evident when inspecting the low light output regime of the PSD spectrum, shown in Figure 5.21.

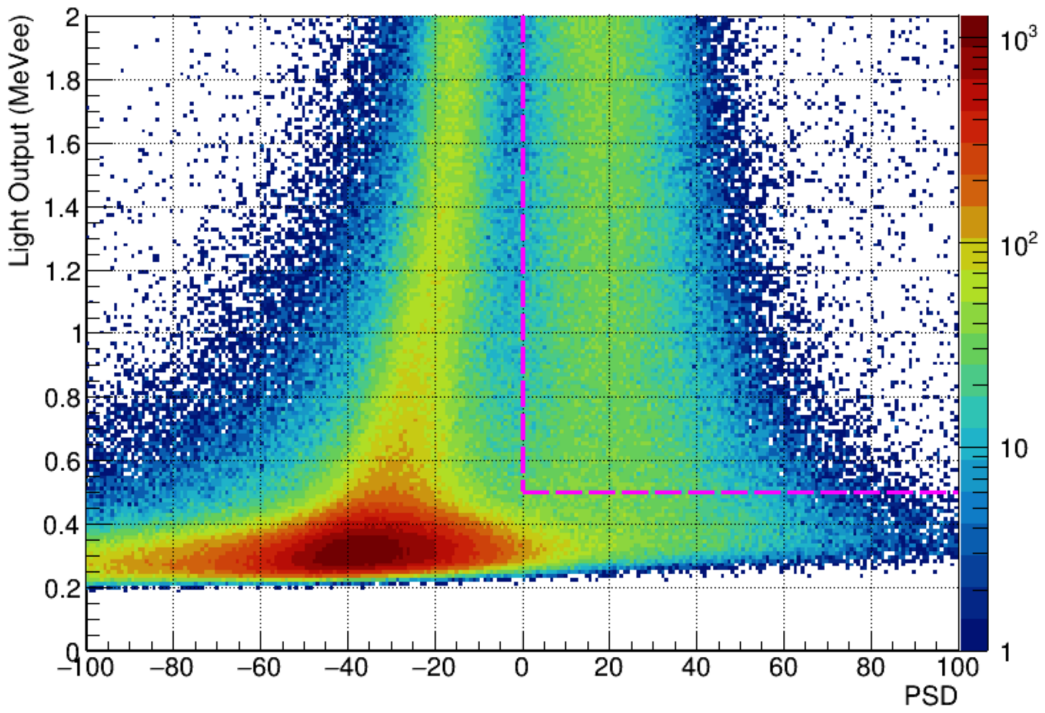

Figure 5.21: PSD Spectrum in Low Light Output Region. The PSD spectrum above offers a closer look at the features of low light output events. The PSD parameter acceptance cuts are displayed as magenta dashed lines, set at PSD = 0 and at minimum light output of 0.5 MeVee. The minimum light output cut is applied to exclude events where the PSD separation between neutron and photon signals loses distinction. This plot demonstrates how below 0.5 MeVee, the neutron and photon event peaks begin to blend together.

Below a light output of about 0.5 MeVee, the separation of the neutron and photons peaks disappears as the PSD parameters of the two events begin to mix together. Restricting accepted events to have a light output above 0.5 MeVee ensured a successful PSD analysis to isolate neutron events.

After both the PSD and light output cuts are applied, there is excellent reduction of background photon events, which can be observed in the time-of-flight-spectrum in Figure 5.22.

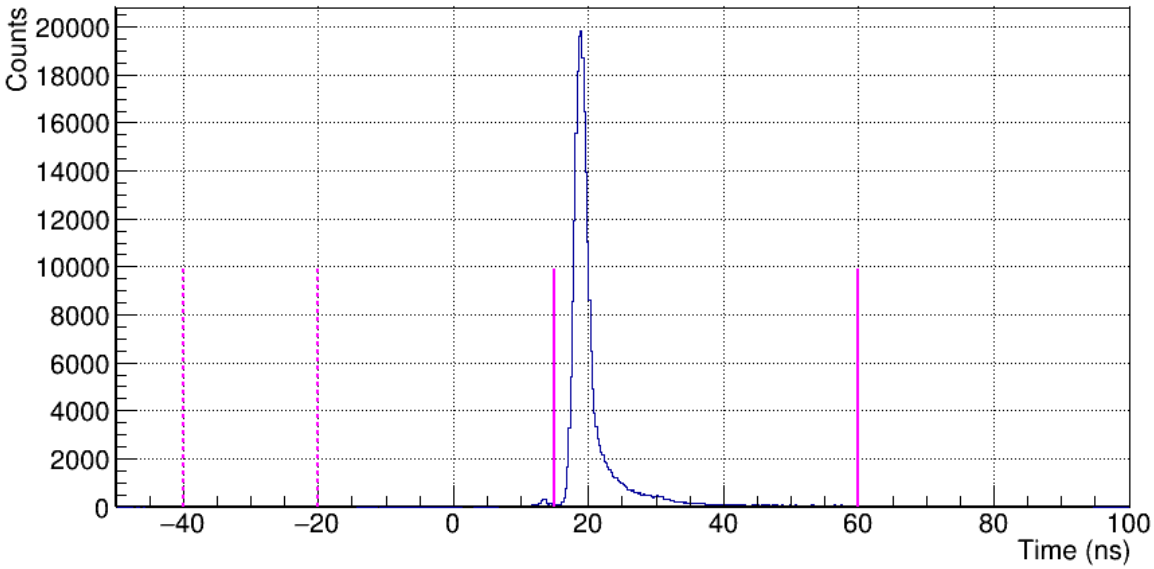

Figure 5.22: Time-of-Fight Spectrum After PSD and Light Output Cuts. The combination of the PSD and light output cuts on the data filtered out the background events, leaving only neutron events to be analyzed for extraction of the neutron polarization. The time-of-flight spectrum exhibits a "clean", distinct neutron peak with negligible background, as compared to the only spectrum in Figure 5.16.

With the coincidence requirements and particle identification techniques outlined in this section, neutron analyzing events were identified and selected, from which the measurement of the neutron polarization could be extracted.

5.4 Systematic Corrections

Several corrections to the statistics were implemented to account for systematic effects on the neutron yield of each detector. Background events, instrumentation efficiencies, and artifacts of some of the analytic methods all produced effects on the final yields which required correction for an accurate measurement.

5.4.1 Multiplicity Correction

Due to the limitations of the electronics, consideration had to be made for the possibility of multiple detectors registering different events within a short time window. When a discriminator accepted a signal from one detector, it would initiate a data readout from the ADCs of every detector over a consistent time gate. Keeping this time gate consistent across every detector ensured properly calibrated PSD parameters for the entire detector array. This time gate would be aligned in such a way as to integrate over the entire signal of the triggering event. If subsequent events were registered from other detectors in rapid succession, these would also be read out by the ADCs while they were processing the initial signal. These additional events were considered to have *multiplicity* equal to the number of detectors that recorded events.

The problem with a multiplicity event was the alignment of the integration time gate. Any event recorded after the first one was not guaranteed to have its entire signal received within the integration time window. Therefore, it must be assumed that these were registered as partial events which were not fully integrated by the ADCs. These events were excluded by a restriction on the multiplicity, as they would more than likely produce inaccurate measurements of the PSD parameter.

Multiplicity was calculated as the number of detectors that recorded an event during readout. All events with multiplicity greater than 1 were excluded from analysis, before PSD and light output cuts were applied. This ensured accurate PSD analysis for all included events. The number of removed events was stored as a multiplicity correction factor for each detector. When neutron yields were calculated for each detector, they were scaled by the correction factor to provide a *multiplicity corrected yield*.

5.4.2 Random Signal Subtraction

Section 5.3.3 discussed the setup of the "random" and "prompt" timing windows for the subtraction of background. Events collected during the prompt window consisted of a mix of neutrons and background photons. Events collected during the random window provided a measurement of the statistics of background photons over a certain time frame. The PSD spectra were plotted for each of these acceptance windows, as demonstrated in Figures 5.23a and 5.23b.

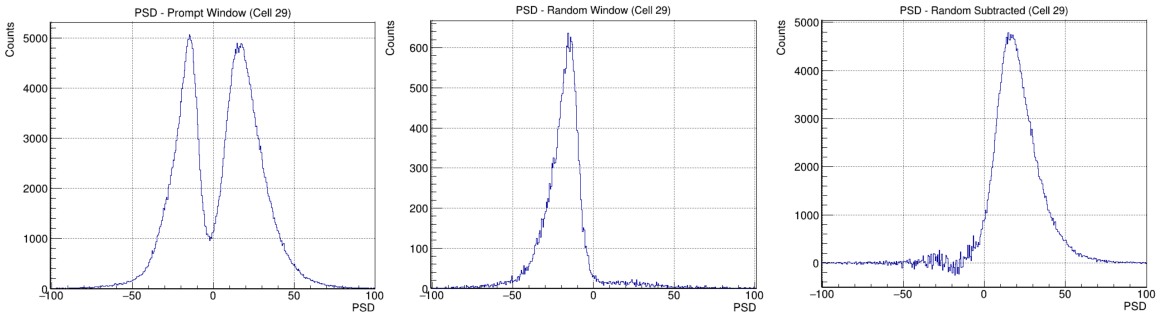

(a) Prompt Events **(b)** Random Events **(c)** Random Subtracted

Figure 5.23: Application of Random Signal Subtraction to PSD Spectrum. The random window applied to the time-of-flight spectrum identified background events that were subtracted from the prompt events. The statistics were normalized to the prompt window based on the total yield of the detector. The same normalization was applied to background events subtracted from analyzing events. Shown above is an illustration of the random subtraction procedure applied to all events, as the background statistics were often too low to clearly demonstrate the effects. The low number or even lack of background statistics in the random subtraction of analyzing events demonstrated the power of the analysis process in isolating neutrons in analyzing events.

The PSD spectrum in Figure 5.23a demonstrates the two distinct peaks of neutron events (PSD > 0) and photon events (PSD < 0). Meanwhile, Figure 5.23b contains a clear photon peak with a small number of events where a neutron peak would exist. Since these events were collected much earlier than the expected arrival time of neutrons, they must be signals produced by photons. This provides a measurement of the background that accidentally passes through the rest of the analysis.

The count of random events are scaled appropriately based on the length of time of the two acceptance windows. The photon peak in the random PSD spectrum is normalized to the photon peak of the prompt PSD spectrum to again properly scale the statistics of the background. The random events can then be subtracted from the prompt events to provide a true count of the neutrons detected during the prompt window, as illustrated in Figure 5.23c. It is evident from the "random subtracted" PSD spectrum, that the main photon peak has been properly subtracted out, indicating that the background photons in the PSD > 0 region have also been removed.

5.4.3 Shifted Pedestal Correction

The shifted pedestal problem in Section 5.2.1 also had to be accounted for to obtain more accurate neutron yields. Events with these shifted pedestals registered offset ADC measurements, which skewed the calculations of crucial analysis parameters such as the PSD values. This would remove otherwise useful counts from analyzing events on a per detector basis. Without proper correction, asymmetry measurements would be inaccurate as the shift in each detector was an independent phenomenon.

Since shifted pedestals appeared in both ADC long and short channels, a spectrum of their ratio provided a method for determining a correction factor. Plotting this ratio generates two "bands" of events, due to the different signal behaviors between neutrons and photons, similar to the PSD parameter, as demonstrated in Figure 5.24.

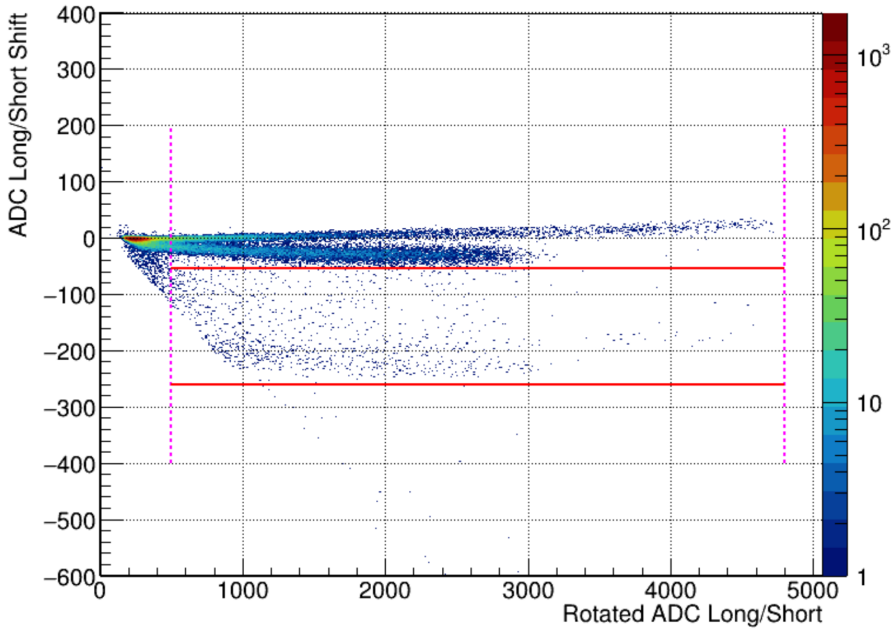

Figure 5.24: Determining Shifted Pedestal Correction Factors. A correction factor was implemented to account for neutron events that had been falsely removed from the PSD acceptance window due to shifted ADC pedestals. Producing a spectrum of the shift in the ratio of the ADC long and short channels provided clear visualization of events affected by the shifted pedestals. Events outside of the two primary bands (corresponding to the neutron and photon events) were counted to determine the number of shifted pedestal events. Comparing this to the total yield of events (within an equivalent ADC/light output acceptance), provided a fraction of shifted pedestal events that used to determine a correction factor to apply to the final neutron yield of each detector.

Shifted pedestal events are identifiable in this spectrum as events that fall outside either of the two main bands. A correction factor for the shifted pedestals was determined from the fraction of these events compared to the total number of events. An integration window was established encompassing the shifted pedestal events, as demonstrated in Figure 5.24. The number of events within the window was compared to the number of events outside the window to calculate the event fraction. These fractions were calculated for each detector, and the neutron yield of each was scaled appropriately to account for shifted pedestal events that had not passed the proper analysis cuts.

5.4.4 PSD Cut Correction

The PSD analysis outlined in Section 5.3.4 isolated neutron events from photons events with an acceptance window on the PSD spectrum. These events were separated by applying an exclusion cut at PSD = 0 to remove the photon events from the analysis. However, applying a straight cut at zero did not exactly capture the behavior of the neutron peak. As a distribution of statistical events, the collection of neutron events had tails on both sides that decreased more gradually than a straight cutoff. Often, a fraction of neutron events extended down into the negative region of the PSD spectrum, which would be excluded by the PSD cut. A PSD cut correction was implemented to account for the these events that were inadvertently removed.

The PSD cut correction factor was generated using the PSD spectrum of proper analyzing events. Within the acceptance window on this spectrum, the neutron events were fit to a Gaussian distribution as demonstrated in Figure 5.25.

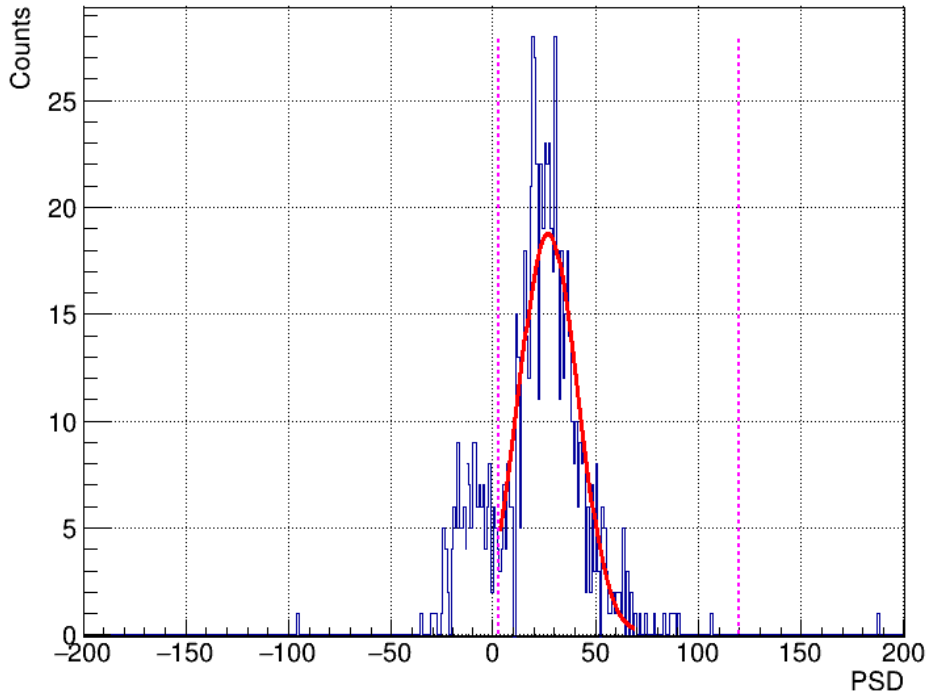

Figure 5.25: Fitting of PSD Spectrum to Determine PSD Cut Correction. The PSD spectrum of analyzing events in each detector was fit to a Gaussian distribution to determine the fraction of neutron events improperly excluded by a straight PSD cut at PSD = 0. This fraction was used as a correction factor applied to final neutron yield of each detector.

The fit was used to determine the fraction of neutron events that fell below the PSD cut. The neutron yield of each detector was scaled accordingly with this fraction to account for the removed events.

5.4.5 Relative Detector Efficiencies

Understanding the relative efficiencies of the counting detectors was crucial to an accurate measurement of the scattering asymmetry of the neutrons. If detectors were measuring lower neutron yields at different rates due to different efficiencies, this would cause systematic errors in the measured asymmetries. Relative efficiencies were investigated to determine any necessary corrections.

Relative detector efficiencies were investigated by examining the direct neutron yields per detector. Direct neutrons did not pass through an analyzer, traveling straight from the target to a counting detector. The differential cross section for direct

neutrons is well defined and understood, and was accurately modeled by the Monte Carlo simulation discussed in Section 3.5. The measured yield of each detector was normalized and compared to the corresponding detector in the simulation, as shown in Figure 5.26.

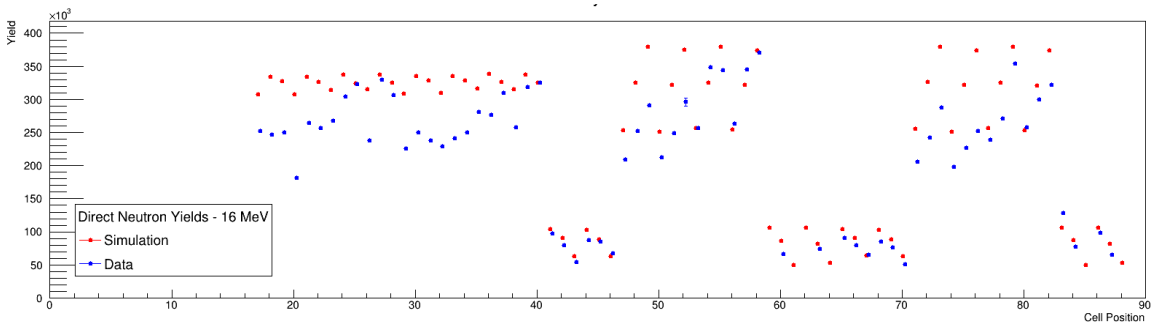

Figure 5.26: Comparison of Normalized Neutron Yields Between Simulated and Experimental Data. The total neutron yield of each detector was normalized to the expected yields from simulated data. Without requiring coincidences with the analyzers, the vast majority of these yields were direct neutron counts, which were accurately modeled by the simulation. A single detector was normalized to the simulation with all the other detectors scaled by the same normalization factor. Comparing these normalized yields to the simulation demonstrated that detectors were measuring neutrons at different rates than each other. This difference in relative efficiency between the detectors introduces asymmetries that skew measurements of the true polarization asymmetries.

The direct neutron yield of one detector was normalized to the simulated yield to provide a normalization for all detectors. For matching detector efficiencies, the measured yields would all match the simulated yields when normalized in this way. However, Figure 5.26 illustrates that the yields did not match the simulated data, indicating different relative efficiencies for all detectors.

To quantify the relative efficiency of each detector, a data-to-simulation yield ratio was calculated, plotted in Figure 5.27.

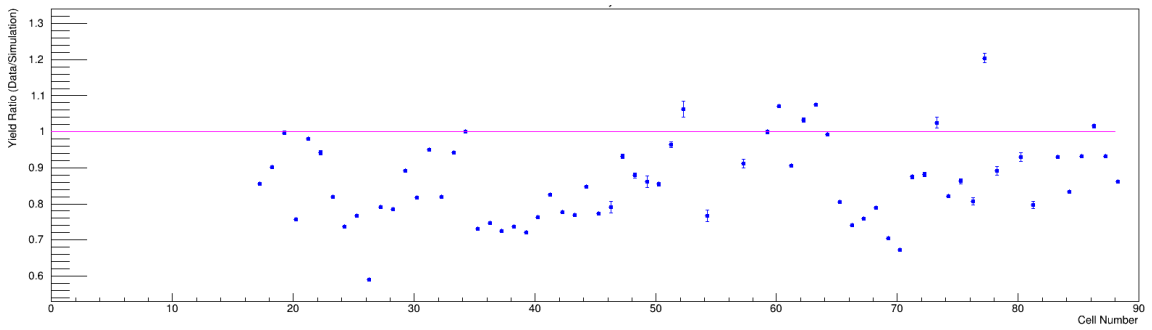

Figure 5.27: Data-to-Simulation Neutron Yield Ratios to Determine Efficiency Calculations. After normalizing the neutron yields of each detector to the simulated results, the data-to-simulation yield ratios were calculated to identify the fraction of events that were missing from detector yields due to a decrease in efficiencies relative to other detectors. These ratio calculations were used to produce relative efficiency correction factors to apply to the neutron yields of analyzing events in each detector.

The ratio calculated for each detector provided an efficiency fraction that was used as a correction factor to properly scale the neutron yields. This efficiency correction was applied to the analyzing event neutrons mitigate this systematic error in the measurement.

5.4.6 Instrumental Asymmetries

The geometry of the experimental setup introduced an additional asymmetry in the scattering of neutrons that had to be determined and removed from the observed asymmetry. The finite length of the target produced a spread in the possible trajectories of neutrons traveling to an analyzer. Due to the higher probability of low angle scattering in the elastic scattering within the analyzers, the variable trajectories would propagate through their scattering process. They would exhibit a preference to be detected on different sides of the analyzer. This spread in the paths of neutrons is illustrated in Figure 5.28.

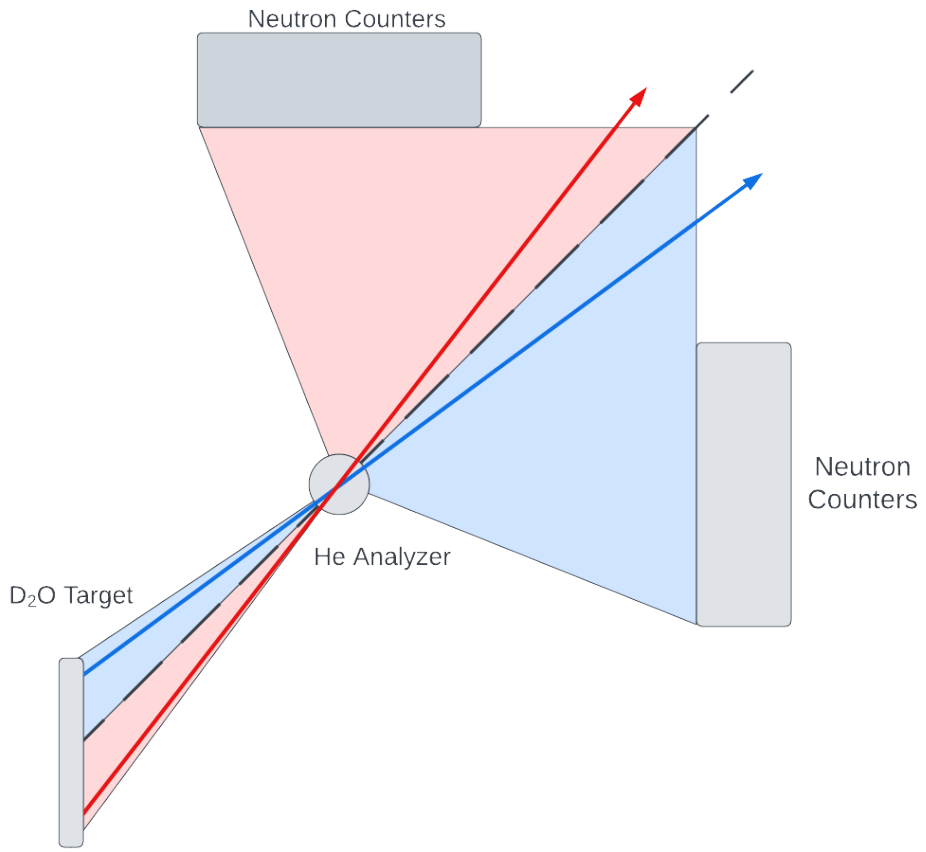

Figure 5.28: Geometric Spread in Neutron Trajectories. The finite length of the target produced a spread in the trajectories of neutrons traveling from the target to the analyzer. The differential cross section for neutron-helium elastic scattering increases for smaller angles of scattering. This resulted in an asymmetry in the final detected position of neutrons depending on their production location within the target and independent of their polarization. Neutrons generated in the upstream half of the target were more likely to scatter into the downstream counting detectors (Red). Those produced in the downstream half of the target were more likely to end up in the upstream detectors (Blue). For equal production of neutrons throughout the target, this geometric asymmetry would cancel out. However, the attenuation of the gamma-ray beam through the target prompted a higher count of neutrons produced in the upstream end of the target. The combination of the beam attenuation and the geometric asymmetry resulted in an instrumental asymmetry contributing to the final measured asymmetry. This instrumental asymmetry was calculated using simulation results and subtracted from the measured asymmetry.

This spread by itself did not inherently create an asymmetry in the neutron yields between detectors. The asymmetry arose from other properties of neutron production within the target, including the differential cross section of photodisintegration and

beam attenuation in the target. The number of neutrons ejected in the direction of each analyzer changed as a function of the interaction point within the target. With different amounts of neutrons traveling along different trajectories in each station, an asymmetry emerged that contributed to the total measured asymmetry in neutron yields.

Determination of the geometric asymmetry was performed with the Geant4 simulation of the experiment. The standard simulation does not model polarized neutron scattering inside the analyzer. Thus, when analysis is performed on simulation data, any asymmetry calculated within a station is due to the contribution from the geometric asymmetry. The simulation was run to calculate asymmetries for each station at each of the beam energies (8, 12, and 16 MeV). During the final calculation of neutron polarization, the simulated values were subtracted from the observed asymmetries to provide the actual asymmetry due to spin polarization.

5.5 Neutron Polarization Extraction

Calculating asymmetries to extract the neutron polarization required totaling the number of neutrons scattering in each direction through an analyzer. The analysis cuts made to the data isolated the neutron events in each detector to determine the total neutron yields on either side of an analyzer.

Reviewing the key variables used in the geometry of the setup is useful in understanding the process of extracting the neutron polarization.

Variable	Description	Values
θ_n	Lab reaction angle of n from $d(\gamma, n)p$	$45°, 90°, 135°$
θ'	Scattering angle of n in analyzer	$30°, 45°, 60°$
ϕ	Azimuthal angle of experimental setup	$0°, 90°, 180°, 270°$
A	Asymmetry	Measured Quantity
A_y	Analyzing power	Interpolated from Data
P_y^m	Measured neutron polarization	Measured Quantity
P_y^u	Unpolarized γ contribution to P_y^m	Measured Quantity
P_y^l	Unpolarized γ contribution to P_y^m	Measured Quantity

Table 5.1: Variable Definitions for Analysis. Identifying the key kinematic and polarization variables used in the analysis facilitates the necessary calculations.

5.5.1 Integrating Neutron Yields

With analyzing events selected, asymmetries were calculated using the yields of neutrons detected by counting detectors. The total yield of each detector was determined by integrating over all analyzing events in the light output spectrum, illustrated in Figure 5.29.

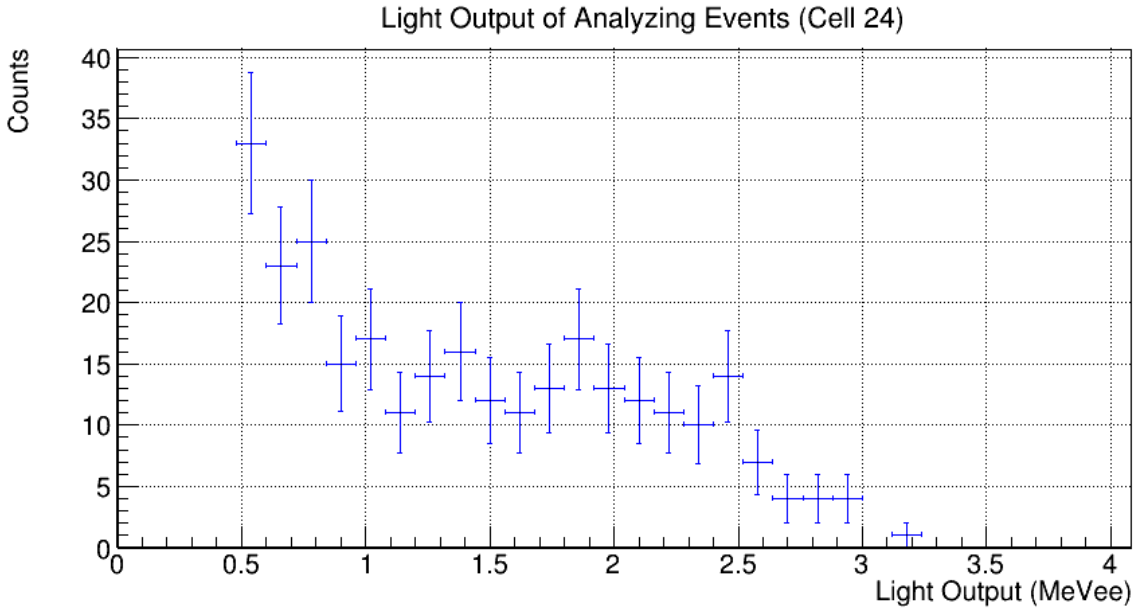

Figure 5.29: Light Output Spectrum of Analyzing Events from a Counting Detector. The raw neutron yield of each detector was extracted from the light output spectrum of analyzing events. Integrating over this spectrum provided the number of neutrons that were directly measured by the analysis. Systematic correction factors were applied to the raw yields to obtain the true count of neutrons at each detector position.

The correction factors outlined in Section 5.4 were applied to the raw neutron yield extracted from the light output spectrum to obtain a true count of neutrons scattering to each side of the analyzer.

5.5.2 Calculating Asymmetries

With a final, corrected neutron yield for each detector, the weighted average of yields was calculated between two detectors paired at the same scattering angle, θ', on the same side of the analyzer. The asymmetry was then found from the difference between the yields on each side of the analyzer (calculated for the same scattering angle).

The asymmetry quantifies the difference between the number of spin up vs spin down particles:

$$A = \frac{N_+ - N_-}{N_+ + N_-}. \tag{5.4}$$

For the directional asymmetry in the scattering of neutrons measured in this experiment, this asymmetry is angle dependent:

$$A(\theta') = \frac{\sigma(\theta'_+) - \sigma(\theta'_-)}{\sigma(\theta'_+) + \sigma(\theta'_-)}. \tag{5.5}$$

In other words, the asymmetry is determined by the difference between neutrons scattering left vs right:

$$A = \frac{N_L - N_R}{N_L + N_R}. \tag{5.6}$$

Through this method, an asymmetry was calculated for each θ'.

5.5.3 Extraction of Polarization Contributions

From the neutron yields of the detectors, asymmetries were calculated for each of the three scattering angles, $\theta' = 30°, 45°, 60°$, at each reaction angle θ_n. For each of these asymmetries, the neutron polarization was calculated as

$$P_y(\theta_n) = \frac{A(\theta')}{A_y(E_n, \theta')}. \tag{5.7}$$

The analyzing powers, A_y, were obtained from a database, interpolated as a function of the energy of the neutron incident on the analyzer and the neutron's scattering angle. This provided three values of the neutron polarization for each θ_n, each with different statistics. The weighted average was calculated over all three scattering angles to obtain the final value for the neutron polarization at each reaction angle, θ_n.

This calculation provided values for the measured polarization at each reaction angle. This measured polarization was used to find the contributions to the neutron polarization from different photon polarization orientations. These contributions relate to the measured polarization as

$$P_y^m \frac{d\sigma(P_y^\gamma, \theta_n, \phi_n)}{d\Omega} = \frac{d\sigma(\theta_n)}{d\Omega}\bigg|_{P_y^\gamma = 0} \Big[P_y^u(\theta_n) + P_y^\gamma P_y^l(\theta_n) \cos(2\phi_n) \Big]. \tag{5.8}$$

For data collected during runs with a circularly polarized photon beam, $P_y^\gamma = 0$, and so

$$P_y^m = P_y^u. \tag{5.9}$$

For data collected with a linearly polarized photon beam, $P_y^\gamma = 1$. The geometry of the experimental setup was such that $\cos(2\phi_n) = 1$, reducing Eq. 5.8 to a simple summation:

$$P_y^m = P_y^u + P_y^l. \tag{5.10}$$

Thus, after the unpolarized photon contribution was extracted from the circular polarization data set, the linearly polarized photon contributions could easily be calculated.

Chapter 6

Results and Discussion

6.1 Results

The results presented here cover the measurements taken with a 16 MeV circularly polarized photon beam. Chapter 5 outlined the methods used to calibrate and analyze the experimental data to extract the measurement of the neutron polarization. Experimental runs were grouped on a per day basis during analysis, as the detector and electronic calibrations remained consistent over the course of a day. Examining measurements day-by-day provided insight into the consistency of the results over multiple days of running. The daily results for the neutron polarization are displayed in Figure 6.1, along with the weighted average of all the days. The final results of the measurement at $E_\gamma = 16$ MeV with a circularly polarized photon beam are presented in Figure 6.2.

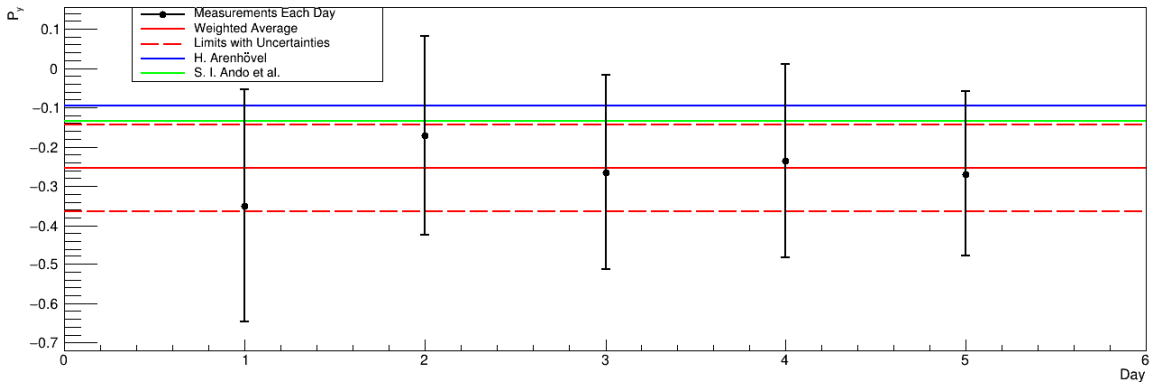

(a) Daily Measurements at $\theta_n = 45°$

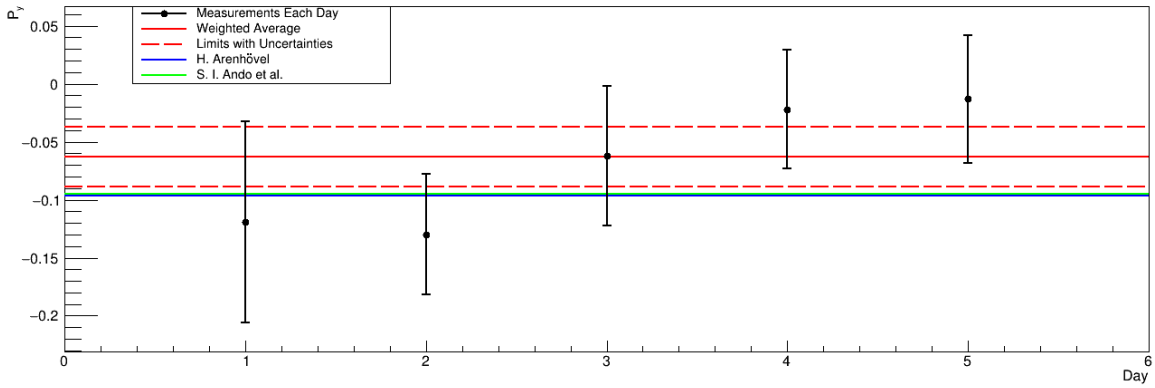

(b) Daily Measurements at $\theta_n = 90°$

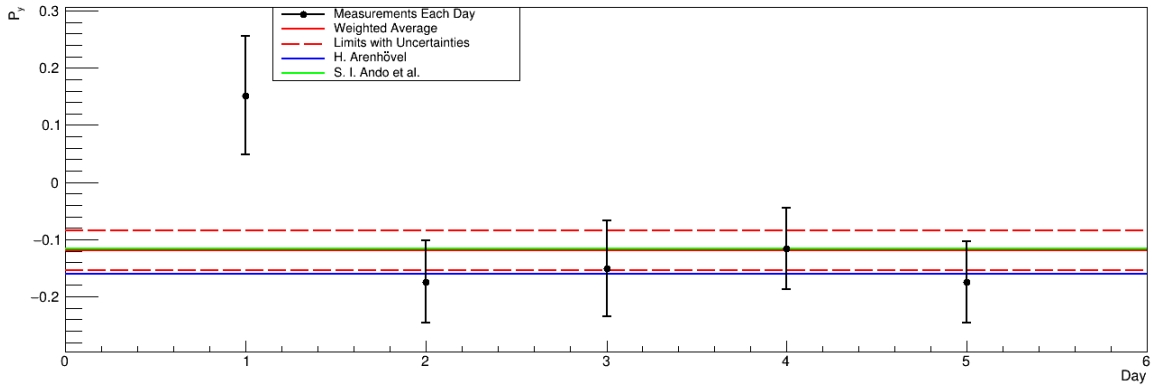

(c) Daily Measurements at $\theta_n = 135°$

Figure 6.1: Measurements from Each Day of Experimental Run Compared to the Weighted Average. Displayed are the collection of measurements for each day (Black) at each of the laboratory angles of interest, (a) 45°, (b) 90°, and (c) 135°. The final result for each angle is calculated as a weighted average of all five days (Red Solid Line) and includes the uncertainties on this result (Red Dashed Lines). Two theoretical calculations are included at each angle for comparison from H. Arenhövel [11, 12] (Blue) and S. I. Ando et al. [15, 16] (Green).

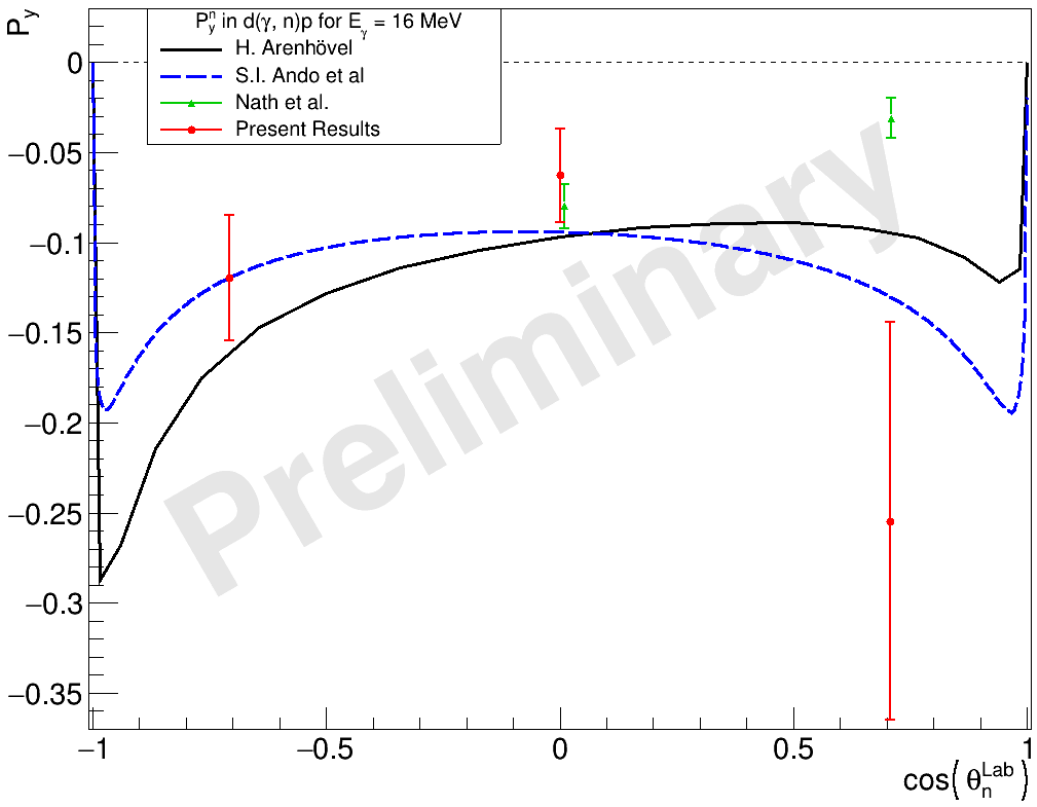

Figure 6.2: Results for P_y^n at $E_\gamma = 16$ MeV with Circular Polarization. The results of this work (Red) compared to two theoretical calculations. The calculation performed by H. Arenhövel [12] (Black, Solid) was performed using the Bonn-OBEPR nuclear potential model. The calculation by S.I. Ando *et. al* [15, 16] (Blue, Dashed) was performed using Pionless Effective Field Theory. The results are also compared to interpolations at 16 MeV from the measurements performed by Nath *et al.* [10] (Green). The measurements by Nath *et al.* are shifted slightly off the exact reaction angles (45° and 90°) for clear distinction from the present results.

The results in Figure 6.2 are compared to two theoretical calculations, each obtained using a different approach. The calculation from H. Arenhövel [11, 12] uses the Bonn-OBEPR (One-Boson-Exchange Potential in R-space, or Position-Space), introduced in Section 2.2.4. It incorporates the corrections outlined in 2.5.3, including meson exchange currents, isobar configurations, and relativistic corrections. The calculation by S. I. Ando et al. [15, 16] uses Pionless Effective Field Theory, a variation of the Chiral Perturbation Theory discussed in Section 2.4.1, up to Next-to-Next-Leading Order (NNLO). Interpolations were also made from the experimental data of Nath et al. 1.2 to compare at $E_\gamma = 16$ MeV.

The results at $\theta_n = 90°$ and $135°$ demonstrate agreement with both theoretical calculations, though aligning more closely with the EFT calculation of S. I. Ando et al. Additionally, the result at $\theta_n = 90°$ demonstrates excellent agreement with the measurement from Nath et al., both consistent with theoretical predictions. The measurement at $\theta_n = 45°$ presents a much more ambiguous result, that prompts further discussion of its details.

6.2 Discussion of the Results at $\theta_n = 45°$

One thing that is evident in Figure 6.2 is the much larger uncertainty on the result at $\theta_n = 45°$, which is due to certain analysis decisions in obtaining a result. The shifted pedestal problems discussed in Section 5.2.1 produced the most contamination in signals from detectors close to the beamline, on the downstream end of the experimental setup ie. the $45°$ stations. Corrections for this effect were implemented as outlined in Section 5.4.3, however, they seemed unable to properly correct for the most extreme cases. The PSD spectra of these detectors were unreliable as a means of particle identification, offering very little, if any, distinction between neutron and photon events. Analyzing the results from all detectors in these stations often produced unphysical measurements (such as a neutron spin polarization with a magnitude greater than 1), with little consistency across geometry or days of data collection.

To overcome these challenges, the decision was made to only consider the detectors most protected from the beam effects that seemed to cause the shifted pedestals. This meant only including the detectors placed at the smallest scattering angle from the analyzers in each station. These detectors provided the most confidence in the accuracy of the measurement. However, excluding two-thirds of the detectors from the analysis produces much lower statistics available for the measurement, resulting in the large uncertainties on the final result.

As an exploratory exercise, some of the contaminated detectors were added back into the analysis of the data at $\theta_n = 45°$, to investigate their impact on the result. The added detectors were considered to be "the next most reliable" detectors, but still with some concerns about their integrity. In this case, the main detectors still excluded from the analysis were those closest to the beamline, along with a couple other detectors that failed to demonstrate enough reliability. The result of this "exploratory" analysis is shown in Figure 6.3.

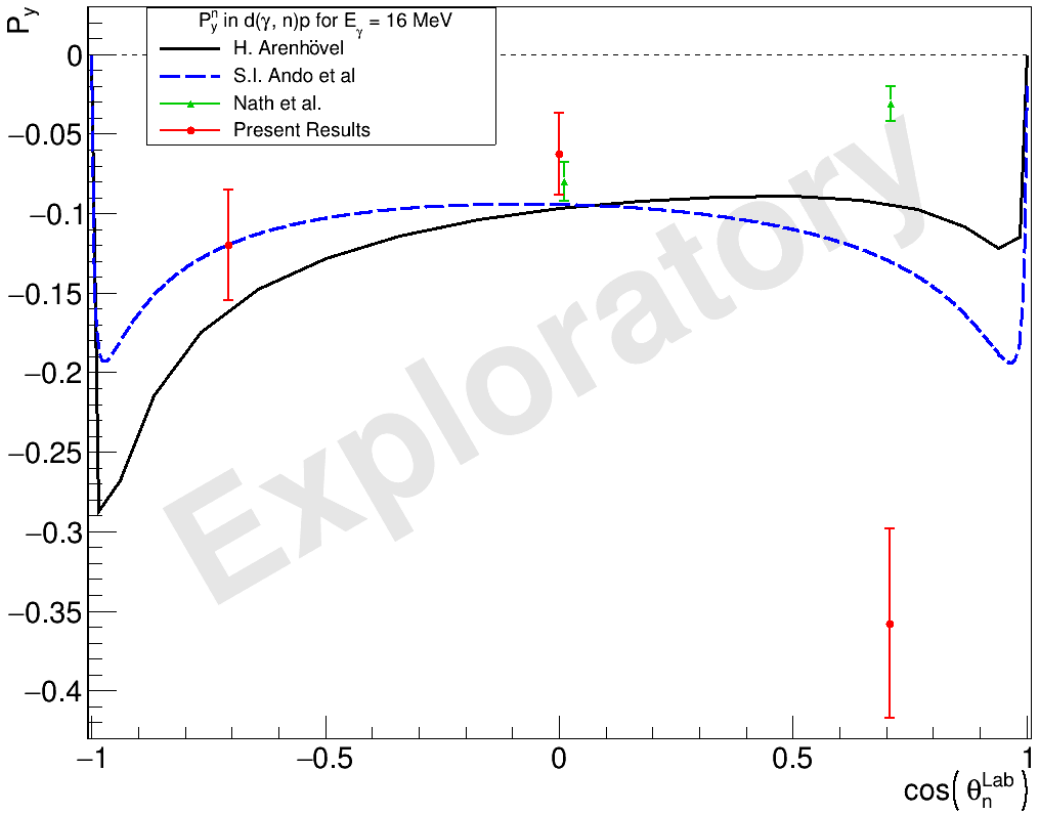

Figure 6.3: Exploratory Consideration of the Measurement at $\theta_n = 45°$. Exploratory analysis of the results when reintroducing some detectors in the 45° stations with contaminated data demonstrates an increase in the magnitude of the measured polarization with a decrease in nominal uncertainties. However, the unreliability of the data from these detectors prevents confidence in this analysis as a final result.

The increase in statistics from the addition of more detectors noticeably decreases the nominal uncertainties on the measurement. The result in this case exhibits a larger magnitude in polarization than the result in Figure 6.2. However, the persisting concerns about the integrity of the data from these detectors prevents confidence in the reliability of this result.

Though no definitive claims can be made due to the large uncertainties in the final result presented in Figure 6.2, the measurement at $\theta_n = 45°$ does offer promising features in the search for an answer to the "neutron polarization puzzle". The finite value of the neutron polarization hints at a behavior more in line with theoretical calculations than the previous measurement by Nath et al. in which the polarization approached zero. Being almost in agreement with the EFT calculations performed by S I. Ando et al., the result offers at least some support of the validity of the theory over

the Nath et al. result. However, a more conclusive resolution to this study would require further investigation, most likely with a modification to the experimental methods to prevent similar data contamination.

6.3 Future Prospects

As is often the case in experimental research, the results of this work prompt consideration of the future of the "neutron polarization puzzle" in deuteron photodisintegration. For one, the ambiguity that still exists for the measurement at $\theta_n = 45°$ provides motivation to return to this experiment with potential modifications to methodology for a more precise result. Combine this with the promising results at 90° and 135°, a strong case exists for further investigation of this observable, with a possible expansion in the explored phase-space.

6.3.1 Further Analysis of Current Experiment

As previously discussed, the experiment collected data at three photon beam energies: 8, 12, and 16 MeV. Experimental runs with circularly polarized photons were carried out for all three. Data was also collected with linearly polarized photons for the 8 and 16 MeV beam energies. This dissertation has presented the results of the measurement at 16 MeV with circular polarization. Analysis of the data at 8 MeV with circular polarization was been performed in parallel with this analysis, for presentation in a separate work. As such, further analysis of additional measurements is possible with the available data. The runs at 12 MeV with circular polarization and the runs at 8 and 16 MeV with linear polarization remain to be analyzed with the procedure outlined in this work. These measurements offer exciting new contributions to these investigations to provide insight into deuteron photodisintegration and the nuclear forces at play.

6.3.2 Potential Improvements to the Experimental Design

One of the challenges faced during the experimental run was the corruption of the collected data by the shifted pedestal effect discussed in Section 5.2.1. The electronics experienced some phenomenon that caused these shifted pedestals, generating skewed ADC measurements that were crucial to the analysis. While the exact cause of

this issue remains unknown, the distribution of this behavior amongst the detectors offers insight into possible ways to address it. The detectors closest to the beamline exhibited the most extreme cases of this problem, indicating a correlation to some high intensity beam effect.

A first possibility for mitigating this effect is the addition of more radiation shielding for the most exposed detectors. Some lead shielding had already been introduced downstream from the target to reduce the number of Compton scattered photons incident on the near-beam detectors. This shielding was positioned so as to shield these detectors without interrupting the trajectories of neutrons traveling from the analyzers to the counting detectors. Increasing the thickness of this shielding may provide detectors the protection they need to avoid detrimental beam effects.

Another method for mitigating beam effects is a modification to the geometry of the experimental setup. Increasing the distance of the detectors from the beam axis would offer additional protection from the high intensity beam. Positioning the analyzers at an increased radius from the target would move each station further from the beamline, hopefully out of the way of detrimental beam effects.

This same modification to the geometry could also help to decrease the uncertainty on the analyzing power of neutrons scattered in the analyzer. As described in Section 3.5.3, the relationship between the finite length of the target and the distance to the analyzers produced a range in possible analyzing powers, varying by up to a factor of 2. The calculation of effective analyzing powers from Monte Carlo simulation provided a means to extract a neutron polarization. Extending the distance between the target and the analyzers could drastically reduce the spread in neutron energies and scattering angles that led to uncertainty in the analyzing power. For example, increasing this distance from the current 40 cm to 1 m would decrease the uncertainty on A_y below 10%. However, this change would also decrease the statistics of analyzing events, as the solid angle of the analyzer decreases. Properly implementing a modification of the geometry would require balancing the reduction in systematic uncertainties with the change in the statistical uncertainties. Careful consideration of these parameters could offer a measurement with an uncertainty of $\delta P_y \sim 0.03$ or better, comparable to those of the presented results at $\theta_n = 90^\circ$ and 135°.

6.3.3 Possibilities for Future Measurements

Plenty of points of interest remain to investigate this observable near the photodisintegration threshold. For one, revisiting the measurement at $\theta_n = 45°$ with modifications to the experimental method would be beneficial to improve the precision of the measurement. The changes to the experimental setup identified earlier could offer significant reduction in the current ambiguity of the consistency between measurement and theory.

Extending the measurement to include a wider range of photon energies would offer more opportunity to study this observable near the photodisintegration threshold. Increasing the photon energy above $E_\gamma = 16$ MeV could investigate a region of the energy spectrum in which the data of Nath et al. demonstrated the largest discrepancies from theoretical predictions. While the theory predicts a finite magnitude for the neutron polarization up to 30 MeV, the experimental data indicates zero polarization for higher energies, starting at about 19 MeV. Higher beam energies would come with new considerations in the analysis, such as the emergence of photoneutrons from the disintegration of oxygen nuclei in a heavy water target. With careful experimental planning, further investigation of this observable could offer exciting new contributions to the story of the deuteron.

Chapter 7

Conclusion

This dissertation has presented the preparation, operation, analysis and results of an experiment to measure the neutron polarization in deuteron photodisintegration. The presented results include measurements taken with a circularly polarized photon beam of energy $E_\gamma = 16$ MeV, at neutron reaction angles of 45°, 90°, and 135° in the laboratory frame. These results are part of a series of measurements made by this experiment, performed at the High Intensity Gamma Source at TUNL. The goal of the experiment was to investigate this observable near the photodisintegration threshold after previous measurements have demonstrated notable discrepancies with theoretical calculations.

Two theoretical approaches were tested against the results: calculations performed by H. Arenhövel [11, 12] using the Bonn-OBEPR (One-Boson-Exchange Potential in R-space) model and those from S. I. Ando et al. using Pionless Effective Field Theory up to Next-to-Next-to-Leading Order (NNLO). Interpolations from the previous measurements taken at $\theta_n = 45°$ and $\theta_n = 90°$ by Nath et al. [10] were included for comparison as well. At $\theta_n = 90°$ and $\theta_n = 135°$, the results demonstrate consistency with both theoretical models, though aligning more closely with the EFT calculations. At $\theta_n = 90°$, the results also agree with the measurements by Nath et al. The result at $\theta_n = 45°$ is more ambiguous due to the challenges faced with the detector electronics during data collection. However, the available measurement is closer to being consistent with theory than it is with previous measurements. Overall, the results offer promising support for the theoretical models, with exciting prospects for future investigations into this observable.

The pursuit to understand the strong nuclear force is an ongoing endeavor, which benefits from coordinated efforts between experimental and theoretical research. Advancements in accelerator physics, particle detection, and spin polarization techniques continue to open up new frontiers in the field of nuclear physics, motivating the de-

velopment of nuclear theory. The measurements presented in this dissertation offer new contributions to the field, informing theoretical models of the nuclear force as it pertains to low-energy interactions between nucleons. The 2023 Long Range Plan for Nuclear Science, produced by the U.S. Nuclear Science Advisory Committee, emphasizes the importance of this topic, explaining "ultimately, an accurate description of the nuclear force is needed for a precise and predictive theory of nuclei." [75] The results of this work introduce new knowledge to this effort, taking a step forward towards a more complete understanding of the nuclear force.

Bibliography

[1] H. C. Urey, F. G. Brickwedde, and G. M. Murphy. "A Hydrogen Isotope of Mass 2". In: *Phys. Rev.* 39.1 (1932), pp. 164–165. DOI: 10.1103/physrev.39.164.

[2] J. Chadwick and M. Goldhaber. "A Nuclear Photo-effect: Disintegration of the Diplon by γ Rays". In: *Nature* 134 (1934), pp. 237–238. DOI: 10.1038/134237a0.

[3] H. Yukawa. "On the Interaction of Elementary Particles I". In: *Proc. Phys. Math. Soc. Jap.* 17 (1935), pp. 48–57. DOI: 10.1143/PTPS.1.1.

[4] D. H. Perkins. "Nuclear Disintegration by Meson Capture". In: *Nature* 159 (4030 Jan. 1947), pp. 126–127. DOI: 10.1038/159126a0.

[5] G. P. S. Occhialini and C. F. Powell. "Nuclear Disintegrations Produced by Slow Charged Particle of Small Mass". In: *Nature* 159 (4032 Feb. 1947), pp. 186–190. DOI: 10.1038/159186a0.

[6] S. D. Drell and A. C. Hearn. "Exact Sum Rule for Nucleon Magnetic Moments". In: *Physics Review Letters* 16 (1966), pp. 908–911. DOI: 10.1103/PhysRevLett.16.908.

[7] H. Dutz et al. "Experimental Check of the Gerasimov-Drell-Hearn Sum Rule for ^{1}H". In: *Phys. Rev. Lett.* 93 (3 July 2004), p. 032003. DOI: 10.1103/PhysRevLett.93.032003. URL: https://link.aps.org/doi/10.1103/PhysRevLett.93.032003.

[8] S. Hoblit et al. "Measurements of H-polarized D-polarized (gamma-polarized, pi) and Implications for Convergence of the GDH Integral". In: *Phys. Rev. Lett.* 102 (2009), p. 172002. DOI: 10.1103/PhysRevLett.102.172002. arXiv: 0808.2183 [hep-ex].

[9] V. I. Kukulin et al. "Photon-induced neutron polarization from the $^2H(\gamma, \vec{n})^1H$ reaction within the NN-force model with an intermediate dibaryon". In: *Phys. Rev. C* 77 (4 Apr. 2008), p. 041001. DOI: 10.1103/PhysRevC.77.041001. URL: https://link.aps.org/doi/10.1103/PhysRevC.77.041001.

[10] R. Nath, F. W. K. Firk, and H. L. Schultz. "Differential Polarization of Photoneutrons from Deuterium". In: *Nucl. Phys. A* 194 (1972), pp. 49–63. DOI: 10.1016/0375-9474(72)91051-2.

[11] H. Arenhövel and M. Sanzone. "Photodisintegration of the Deuteron: A Review of Theory and Experiment". In: *Few Body Syst. Suppl.* 3 (1991), pp. 1–183.

[12] H. Arenhövel. private communication.

[13] L. J. Drooks. "The Polarization of the Neutrons Produced by the Photodisintegration of Deuterium". PhD thesis. Yale University, 1976.

[14] R. J. Holt, K. Stephenson, and J. R. Specht. "Meson-Exchange Currents and the Reaction $^2H(\gamma, n_{pol})H$". In: *Phys. Rev. Lett.* 50 (1983), pp. 577–579. DOI: 10.1103/PhysRevLett.50.577.

[15] S. I. Ando et al. "Spin Polarization in $\gamma d \to \vec{n}p$". In: *EPJ Web Conf.* 20 (2012). Ed. by Hyun-Chul Kim and Seung-Il Nam, p. 02003. DOI: 10.1051/epjconf/20122002003.

[16] Y. H. Song, S. I. Ando, and C. H. Hyun. "Spin-Polarization Observables of Deuteron Photodisintegration at Low Energies in Pionless Effective-Field Theory". In: *Phys. Rev. C* 96 (1 July 2017), p. 014001. DOI: 10.1103/PhysRevC.96.014001. URL: https://link.aps.org/doi/10.1103/PhysRevC.96.014001.

[17] B. D. Sawatzky. "A Measurement of the Neutron Asymmetry in d(g,n)p Near Threshold". PhD thesis. Department of Physics, University of Virginia, 2005. DOI: 10.18130/V31Z6J.

[18] M. Blackston. "Precision Measurements of Deuteron Photodisintegration Using Linearly Polarized Photons of 14 and 16 MeV". PhD thesis. Duke University, 2007.

[19] S. Kucuker. "Photodisintegration of the Deuteron at 20 MeV". PhD thesis. University of Virginia, 2010.

[20] B. E. Norum, R. Pywell, and et. al. "Measurement of Neutron Recoil Polarization in Low Energy Photodisintegration of Deuterium". In: *Update to Proposal to the High Intensity Gamma-Ray Source (HIγS)* PAC-12 (2013).

[21] R. Machleidt. "Historical Perspective and Future Prospects for Nuclear Interactions". In: *International Journal of Modern Physics E* 26.11 (Nov. 2017). ISSN: 1793-6608. DOI: 10.1142/s0218301317300053. URL: http://dx.doi.org/10.1142/S0218301317300053.

[22] R. Machleidt. "Phenomenology and Meson Theory of Nuclear Forces". In: *Handbook of Nuclear Physics*. Ed. by Isao Tanihata, Hiroshi Toki, and Toshitaka Kajino. Singapore: Springer Nature Singapore, 2020, pp. 1–53. ISBN: 978-981-15-8818-1. DOI: 10.1007/978-981-15-8818-1_48-1. URL: https://doi.org/10.1007/978-981-15-8818-1_48-1.

[23] M. Naghdi. "Nucleon-Nucleon Interaction: A Typical/Concise Review". In: *Physics of Particles and Nuclei* 45.5 (Sept. 2014), pp. 924–971. ISSN: 1531-8559. DOI: 10.1134/s1063779614050050. URL: http://dx.doi.org/10.1134/S1063779614050050.

[24] M. A. Preston and R. K. Bhaduri. *Structure Of The Nucleus*. Avalon Publishing, 1993. ISBN: 9780201627299.

[25] S. S. M. Wong. *Introductory Nuclear Physics, 2nd Ed.* Wiley-VCH, 2004.

[26] L. van Dommelen. *Quantum Mechanics for Engineers*. 2004.

[27] M. Thomson. *Modern Particle Physics*. New York: Cambridge University Press, 2013. ISBN: 978-1-107-03426-6. DOI: 10.1017/CBO9781139525367.

[28] S. Navas et al. "Review of particle physics". In: *Phys. Rev. D* 110.3 (2024), p. 030001. DOI: 10.1103/PhysRevD.110.030001.

[29] F. Wilczek. "Hard-Core Revelations". In: *Nature* 445 (Jan. 2007), pp. 156–7.

[30] R. Machleidt, K. Holinde, and C. Elster. "The Bonn Meson-Exchange Model for the Nucleon—Nucleon Interaction". In: *Physics Reports* 149.1 (1987), pp. 1–89. ISSN: 0370-1573. DOI: https://doi.org/10.1016/S0370-1573(87)80002-9. URL: https://www.sciencedirect.com/science/article/pii/S0370157387800029.

[31] R. Machleidt. "High-Precision, Charge-Dependent Bonn Nucleon-Nucleon Potential". In: *Physical Review C* 63.2 (Jan. 2001). ISSN: 1089-490X. DOI: 10.1103/physrevc.63.024001. URL: http://dx.doi.org/10.1103/PhysRevC.63.024001.

[32] S. Okubo and R. E. Marshak. "Velocity Dependence of the Two-Nucleon Interaction". In: *Annals of Physics* 4.2 (1958), pp. 166–179. ISSN: 0003-4916. DOI: https://doi.org/10.1016/0003-4916(58)90031-9.

[33] R. B. Wiringa, V. G. J. Stoks, and R. Schiavilla. "Accurate Nucleon-Nucleon Potential with Charge-Independence Breaking". In: *Phys. Rev. C* 51 (1 Jan. 1995), pp. 38–51. DOI: 10.1103/PhysRevC.51.38. URL: https://link.aps.org/doi/10.1103/PhysRevC.51.38.

[34] R. B. Wiringa, R. A. Smith, and T. L. Ainsworth. "Nucleon-Nucleon Potentials With and Without $\Delta(1232)$ Degrees of Freedom". In: *Phys. Rev. C* 29 (4 Apr. 1984), pp. 1207–1221. DOI: 10.1103/PhysRevC.29.1207. URL: https://link.aps.org/doi/10.1103/PhysRevC.29.1207.

[35] A. M. Green and P. Haapakoski. "The Effect of the $\Delta(1236)$ in the Two-Nucleon Problem and in Neutron Matter". In: *Nucl. Phys. A* 221 (1974), pp. 429–449. DOI: 10.1016/0375-9474(74)90474-6.

[36] S. Weinberg. "Nuclear Forces from Chiral Lagrangians". In: *Phys. Lett. B* 251 (1990), pp. 288–292. DOI: 10.1016/0370-2693(90)90938-3.

[37] S. Weinberg. "Effective Chiral Lagrangians for Nucleon - Pion Interactions and Nuclear Forces". In: *Nucl. Phys. B* 363 (1991), pp. 3–18. DOI: 10.1016/0550-3213(91)90231-L.

[38] R. Machleidt and D.R. Entem. "Chiral Effective Field Theory and Nuclear Forces". In: *Physics Reports* 503.1 (2011), pp. 1–75. ISSN: 0370-1573. DOI: https://doi.org/10.1016/j.physrep.2011.02.001.

[39] H.-W. Hammer, S. König, and U. van Kolck. "Nuclear Effective Field Theory: Status and Perspectives". In: *Reviews of Modern Physics* 92.2 (June 2020). ISSN: 1539-0756. DOI: 10.1103/revmodphys.92.025004. URL: http://dx.doi.org/10.1103/RevModPhys.92.025004.

[40] H. Sazdjian. "Introduction to Chiral Symmetry in QCD". In: *EPJ Web Conf.* 137 (2017). Ed. by Y. Foka, N. Brambilla, and V. Kovalenko, p. 02001. DOI: 10.1051/epjconf/201713702001. arXiv: 1612.04078.

[41] G. F. Chew. "The Inelastic Scattering of High Energy Neutrons by Deuterons According to the Impulse Approximation". In: *Phys. Rev.* 80 (2 Oct. 1950), pp. 196–202. DOI: 10.1103/PhysRev.80.196.

[42] A. M. Green. "Nucleon Resonances in Nuclei". In: *Rept. Prog. Phys.* 39 (1976), pp. 1109–1190. DOI: 10.1088/0034-4885/39/12/001.

[43] W. Haeberli. "II.A - Polarization Experiments: II.A.1 Polarized Beams". In: *Nuclear Spectroscopy and Reactions, Part A*. Ed. by J. Cerny. Vol. 40. Pure and Applied Physics. Elsevier, 1974, pp. 151–191. DOI: https://doi.org/10.1016/B978-0-12-165201-2.50013-5. URL: https://www.sciencedirect.com/science/article/pii/B9780121652012500135.

[44] M. Tanifuji. *Polarization Phenomena in Physics*. WORLD SCIENTIFIC, 2018. DOI: 10.1142/10731. eprint: https://www.worldscientific.com/doi/pdf/10.1142/10731. URL: https://www.worldscientific.com/doi/abs/10.1142/10731.

[45] S. M. Ross. *Introduction to Probability Models*. Elsevier Science, 2014. ISBN: 9780124081215.

[46] D. J. C. Mackay. "Introduction to Monte Carlo Methods". In: *Learning in Graphical Models*. Ed. by M. I. Jordan. Springer Netherlands, 1998, pp. 175–204. ISBN: 978-94-011-5014-9. DOI: 10.1007/978-94-011-5014-9_7. URL: https://doi.org/10.1007/978-94-011-5014-9_7.

[47] S. Agostinelli et al. "GEANT4–A Simulation Toolkit". In: *Nucl. Instrum. Meth. A* 506 (2003), pp. 250–303. DOI: 10.1016/S0168-9002(03)01368-8.

[48] J. Allison et al. "Geant4 Developments and Applications". In: *IEEE Trans. Nucl. Sci.* 53 (2006), p. 270. DOI: 10.1109/TNS.2006.869826.

[49] J. Allison et al. "Recent Developments in Geant4". In: *Nucl. Instrum. Meth. A* 835 (2016), pp. 186–225. DOI: 10.1016/j.nima.2016.06.125.

[50] W. Pokorski and A. Ribon. *Tracking*. URL: https://indico.cern.ch/event/472305/contributions/1982331/attachments/1223729/1790331/Tracking.pdf. Feb. 2016.

[51] J. Apostolakis et al. "GEANT4 Physics Lists for HEP". In: *2008 IEEE Nuclear Science Symposium Conference Record*. 2008, pp. 833–836. DOI: 10.1109/NSSMIC.2008.4774655.

[52] J. Apostolakis et al. "Geometry and physics of the Geant4 toolkit for high and medium energy applications". In: *Radiation Physics and Chemistry* 78.10 (2009). Workshop on Use of Monte Carlo Techniques for Design and Analysis of Radiation Detectors, pp. 859–873. ISSN: 0969-806X. DOI: https://doi.org/10.1016/j.radphyschem.2009.04.026. URL: https://www.sciencedirect.com/science/article/pii/S0969806X09001650.

[53] T. Polischuk. private communication.

[54] T. Stammbach and R. L. Walter. "R -matrix Formulation and Phase Shifts for n- ^{4}He and p-^{4}He Scattering for Energies up to 20 MeV". In: *Nucl. Phys. A* 180 (1972), pp. 225–240. DOI: 10.1016/0375-9474(72)90166-2.

[55] H. R. Weller et al. "Research Opportunities at the Upgraded HIγS Facility". In: *Progress in Particle and Nuclear Physics* 62.1 (2009), pp. 257–303. ISSN: 0146-6410. DOI: https://doi.org/10.1016/j.ppnp.2008.07.001. URL: https://www.sciencedirect.com/science/article/pii/S0146641008000434.

[56] G. F. Knoll. *Radiation Detection and Measurement; 4th ed.* New York, NY: Wiley, 2010. URL: https://cds.cern.ch/record/1300754.

[57] G. Pridham. "Photodisintegration of the Deuteron at 18 MeV Using Linearly Polarized Photons". Master's thesis. University of Saskatchewan, 2014.

[58] J. A. Northrop, J. M. Gursky, and A. E. Johnsrud. "Further Work with Noble Element Scintillators". In: *IRE Transactions on Nuclear Science* 5.3 (1958), pp. 81–87. DOI: 10.1109/TNS2.1958.4315630.

[59] W. S. Wilburn et al. "Measurements at Low-Energies of the Polarization Transfer Coefficient $K_y^{y'}$ for the Reaction $^3H(\vec{p},\vec{n})^3He$ at 0°". In: *Few Body Syst.* 24 (1998), pp. 27–38. DOI: 10.1007/s006010050074. arXiv: nucl-ex/9710003.

[60] W. Tornow et al. "High-pressure 3He–Xe Gas Scintillators for Simultaneous Detection of Neutrons and Gamma Rays Over a Large Energy Range". In: *Nuclear Instruments and Methods in Physics Research Section A: Accelerators, Spectrometers, Detectors and Associated Equipment* 647.1 (2011), pp. 86–93. ISSN: 0168-9002. DOI: https://doi.org/10.1016/j.nima.2011.05.022. URL: https://www.sciencedirect.com/science/article/pii/S0168900211008965.

[61] B. Weller, S. Reich, and J. Ebert. "Principles and Geometry of Modular Steel-Glass Space Strcutures". In: *Challenging Glass, Conference on Architectural and Structural Applications of Glass*. Ed. by F. Bos, C. Louter, and F. Veer. IOS Press BV, 2008, pp. 145–154. ISBN: 9781586038663.

[62] K. J. Kasunic. "Structural Design—Optical Components". In: *Optomechanical Systems Engineering*. John Wiley and Sons, Ltd, 2015. Chap. 6, pp. 107–132. ISBN: 9781118809860. DOI: https://doi.org/10.1002/9781118809860.ch6.

[63] W. Tornow. private communication.

[64] R. Weil. "Reflectivity of Steel". In: *Nature* 159 (4035 Mar. 1947), p. 305. DOI: 10.1038/159305a0.

[65] J. S. Preston. "The Reflection Factor of Magnesium Oxide". In: *Transactions of the Optical Society* 31.1 (Dec. 1929), p. 15. DOI: 10.1088/1475-4878/31/1/303. URL: https://dx.doi.org/10.1088/1475-4878/31/1/303.

[66] P. Kozma and Č. Hradečný. "Diphenylstilbene as a Wavelength Shifter". In: *Nuclear Instruments and Methods in Physics Research Section A: Accelerators, Spectrometers, Detectors and Associated Equipment* 254.3 (1987), p. 639. ISSN: 0168-9002. DOI: https://doi.org/10.1016/0168-9002(87)90045-3.

[67] B. Bewer. "Development of a Gain Monitoring System for a Neutron Detector Array". Master's thesis. University of Saskatchewan, 2005.

[68] D. Murray and the Saskatchewan Accelerator Laboratory. *LUCID User's Guide*. University of Saskatchewan. 1995.

[69] R. Brun and F. Rademakers. "ROOT: An object oriented data analysis framework". In: *Nucl. Instrum. Meth. A* 389 (1997). Ed. by M. Werlen and D. Perret-Gallix, pp. 81–86. DOI: 10.1016/S0168-9002(97)00048-X.

[70] W. A. Wurtz. *RLucid, Version 0.4*. University of Saskatchewan. 2007.

[71] W. A. Wurtz. *Blowfish-ROOT Analysis Pacakge, Version 0.0*. University of Saskatchewan. 2008.

[72] R. Pywell. private communication.

[73] R.E. Pywell et al. "Light Output Response of BC-505 Liquid Scintillator". In: *Nuclear Instruments and Methods in Physics Research Section A: Accelerators, Spectrometers, Detectors and Associated Equipment* 565.2 (2006), pp. 725–730. ISSN: 0168-9002. DOI: https://doi.org/10.1016/j.nima.2006.05.087. URL: https://www.sciencedirect.com/science/article/pii/S0168900206009107.

[74] W. A. Wurtz. "Photodisintegration of Lithium Isotopes". PhD thesis. University of Saskatchewan, 2010.

[75] *A New Era of Discovery: The 2023 Long Range Plan for Nuclear Science*. Tech. rep. U.S. Nuclear Science Advisory Committee, 2023.

Appendix A

Input Parameters for Event Generation

Accurate results from the Monte Carlo simulation were crucial to the calculation of detector calibrations, background effects, and systematic corrections. The GEANT4 simulation package provided the necessary physics models to realistically simulate the interactions of neutrons and photons with detectors and materials as they travel through the experimental setup. However, the simulation still required proper initiation of the event generator with input parameters provided by the user.

A.1 Photodisintegration Differential Cross Section

The final state kinematics of the neutron from photodisintegration are defined by the differential cross section, which can be parameterized by the Legendre polynomial expansion

$$\frac{d\sigma}{d\Omega} = \frac{\sigma}{4\pi}\left[1 + \sum_{k=1}^{\infty} a_k P_k^0(\cos\theta) + \sum_{k=2}^{\infty} e_k P_k^2(\cos\theta)\cos 2\phi\right]. \tag{A.1}$$

Here, σ represents the total absolute cross section of the reaction, and the direction of final state momenta are defined in the center-of-momentum frame by θ and ϕ. The full Legendre polynomial expansion is used for linearly polarized photons. In the case of circularly polarized photons, the coefficients of the second summation of terms go to zero, $e_k = 0$, and the differential cross section is dependent only on the coefficients a_k.

For the Monte Carlo simulation of this experiment, the coefficients were obtained

from calculations by H. Arenhövel using the Bonn-OBEPR potential model. [11, 12]. At the photon energies of interest in this experiment, these coefficients have been experimentally verified, providing confidence in the accuracy of the event generation. The values of the coefficients applied to the simulation are listed in Table A.1.

E_γ (MeV)	8	12	16
a_1	1.0	1.0	1.0
a_2	-9.26353×10^{-2}	-1.21724×10^{-1}	-1.45159×10^{-1}
a_3	-9.55727×10^{-1}	-9.35665×10^{-1}	-9.06346×10^{-1}
a_4	9.06288×10^{-2}	1.16555×10^{-1}	1.35260×10^{-1}
a_5	-6.04823×10^{-3}	-1.00502×10^{-2}	-1.41870×10^{-2}
e_2	4.78105×10^{-1}	4.67254×10^{-1}	4.51007×10^{-1}
e_3	-1.51174×10^{-2}	-1.94447×10^{-2}	-2.25688×10^{-2}
e_4	5.06318×10^{-4}	8.43331×10^{-4}	1.17846×10^{-3}

Table A.1: Coefficients for Legendre Polynomial Expansion of Photodisintegration Cross Section. The coefficients used in the photodisintegration event generator were calculated by H. Arenhövel.

A.2 Gamma-Ray Beam Parameters

Physical properties of the incident photon beam on the target contribute to the distribution of neutrons generated in photodisintegration. These properties must be properly modeled in the event generator for the Monte Carlo simulation for accurate results to apply to experimental data. Table A.2 lists the parameters included for this experiment.

Parameter	Value
Beam Diameter	22 mm
Energy Spread	0.55%
Beam Attenuation	0.0228 cm^{-1}

Table A.2: Gamma-ray Beam Parameters Applied to Event Generator.

Appendix B

Analyzing Powers in n-^{4}He Elastic Scattering

The polarization of a neutron, P_y is related to the scattering asymmetry, A, in elastic scattering by the analyzing power of the reaction, A_y such that

$$A(\theta) = P_y A_y(\theta) \rightarrow P_y = \frac{A(\theta)}{A_y(\theta)}. \tag{B.1}$$

The analyzing power is a function of the neutron energy, E_n, and the laboratory scattering angle, θ_{Lab}. Theoretical analyzing powers for ^{4}He(n,n)^{4}He were obtained from calculations performed by Stammbach and Walter [54], labeled in their notation as "polarization". In elastic scattering, the polarization is equivalent to the analyzing power, as the two parameters are related by a time reversal transformation of the reaction. These calculations were input as parameters into the Monte Carlo simulation for modeling polarized neutron scattering. The simulation was used to calculate effective analyzing powers which provided the means to extract polarization from the experimental asymmetries. Effective analyzing powers used for the measurement at $E_\gamma = 16$ MeV are listed in Table B.1. The analyzing powers obtained from Stammbach and Walter are listed in Table B.2.

Station	A_y(Cell 1)	A_y (Cell 2)	A_y (Cell 3)
45°	-0.164 ± 0.019	-0.252 ± 0.022	-0.329 ± 0.028
90°	-0.210 ± 0.013	-0.312 ± 0.014	-0.336 ± 0.018
135°	-0.233 ± 0.010	-0.317 ± 0.011	-0.384 ± 0.014

Table B.1: Effective Analyzing Powers for $E_\gamma = 16$ MeV. Effective analyzing powers were calculated from Monte Carlo simulation to handle the variation of the true analyzing powers.

	E_n (MeV)											
$\theta_{Lab}(^\circ)$	1.000	2.000	2.500	3.000	3.500	4.000	4.500	5.000	6.000	7.000	8.000	9.000
10.0	0.021	-0.051	-0.084	-0.111	-0.128	-0.135	-0.135	-0.131	-0.119	-0.108	-0.099	-0.091
20.0	0.050	-0.099	-0.165	-0.219	-0.253	-0.268	-0.269	-0.263	-0.241	-0.219	-0.201	-0.185
30.0	0.097	-0.138	-0.237	-0.318	-0.372	-0.398	-0.403	-0.396	-0.368	-0.337	-0.310	-0.287
40.0	0.178	-0.160	-0.291	-0.400	-0.476	-0.517	-0.532	-0.529	-0.500	-0.463	-0.429	-0.400
50.0	0.317	-0.153	-0.314	-0.449	-0.550	-0.612	-0.643	-0.652	-0.633	-0.597	-0.560	-0.528
60.0	0.523	-0.092	-0.281	-0.440	-0.565	-0.655	-0.711	-0.742	-0.753	-0.731	-0.701	-0.669
70.0	0.730	0.047	-0.160	-0.334	-0.478	-0.594	-0.681	-0.742	-0.809	-0.827	-0.821	-0.805
80.0	0.797	0.274	-0.069	-0.099	-0.242	-0.364	-0.468	-0.555	-0.683	-0.763	-0.810	-0.834
90.0	0.703	0.539	0.381	0.252	0.145	0.053	-0.027	-0.097	-0.217	-0.312	-0.389	-0.449
100.0	0.556	0.735	0.679	0.621	0.575	0.538	0.513	0.494	0.471	0.461	0.455	0.452
110.0	0.424	0.799	0.857	0.876	0.881	0.884	0.888	0.894	0.910	0.929	0.948	0.965
120.0	0.320	0.750	0.886	0.959	0.991	0.999	0.997	0.990	0.973	0.958	0.944	0.933
130.0	0.240	0.641	0.807	0.903	0.939	0.939	0.922	0.898	0.849	0.808	0.775	0.749
140.0	0.176	0.511	0.670	0.764	0.796	0.788	0.762	0.731	0.672	0.626	0.590	0.563
150.0	0.124	0.378	0.508	0.587	0.610	0.600	0.574	0.545	0.492	0.452	0.422	0.399
160.0	0.079	0.249	0.339	0.394	0.410	0.400	0.381	0.359	0.321	0.292	0.271	0.255
170.0	0.039	0.123	0.169	0.198	0.205	0.200	0.189	0.178	0.158	0.143	0.132	0.125

Table B.2: Analyzing Powers in n-^{4}He Scattering ($E_{n,lab} = 1.0 - 9.0$ MeV). Theoretical calculations of A_y in n-^{4}He elastic scattering, obtained from Stammbach and Walter [54].

Appendix C

Data Tables of Presented Results

Day	P_y
1	-0.351 ± 0.296
2	-0.171 ± 0.253
3	-0.266 ± 0.248
4	-0.236 ± 0.247
5	-0.269 ± 0.210

Table C.1: Results at $\theta_n = 45°$ by Day. Data Table for Fig. 6.1a.

Day	P_y
1	-0.119 ± 0.087
2	-0.130 ± 0.052
3	-0.062 ± 0.060
4	-0.022 ± 0.051
5	-0.013 ± 0.055

Table C.2: Results at $\theta_n = 90°$ by Day. Data Table for Fig. 6.1b.

Day	P_y
1	-0.152 ± 0.104
2	-0.174 ± 0.072
3	-0.151 ± 0.084
4	-0.116 ± 0.071
5	-0.175 ± 0.071

Table C.3: Results at $\theta_n = 135°$ by Day. Data Table for Fig. 6.1c.

θ_n^{Lab}	$\cos(\theta_n)$	P_y
45°	0.7071	-0.2546 ± 0.1102
90°	0.000	-0.0627 ± 0.0259
135°	-0.7071	-0.1197 ± 0.0348

Table C.4: Preliminary Results. Data Table for Fig. 6.2.

θ_n^{Lab}	$\cos(\theta_n)$	P_y
45°	0.7071	-0.3578 ± 0.0593
90°	0.000	-0.0627 ± 0.0259
135°	-0.7071	-0.1197 ± 0.0348

Table C.5: Exploratory Results. Data Table for Fig. 6.3.